



**CAVITY GEOMETRIC FEATURES AND ENTRAINMENT  
CHARACTERIZATION RESULTING FROM A BALLISTICALLY INDUCED  
HYDRODYNAMIC RAM EVENT**

**DISSERTATION**

Andrew J. Lingenfelter, Captain, USAF

AFIT-ENY-DS-16-S-065

**DEPARTMENT OF THE AIR FORCE  
AIR UNIVERSITY**

***AIR FORCE INSTITUTE OF TECHNOLOGY***

**Wright-Patterson Air Force Base, Ohio**

**DISTRIBUTION STATEMENT A:  
APPROVED FOR PUBLIC RELEASE; DISTRIBUTION UNLIMITED**

The views expressed in this dissertation are those of the author and do not reflect the official policy or position of the United States Air Force, the Department of Defense, or the United States Government.

This material is declared a work of the U.S. Government and is not subject to copyright protection in the United States.

AFIT-ENY-DS-16-S-065

CAVITY GEOMETRIC FEATURES AND ENTRAINMENT CHARACTERIZATION  
RESULTING FROM A BALLISTICALLY INDUCED HYDRODYNAMIC RAM  
EVENT

DISSERTATION

Presented to the Faculty  
Graduate School of Engineering and Management  
Air Force Institute of Technology  
Air University  
Air Education and Training Command  
in Partial Fulfillment of the Requirements for the  
Degree of Doctorate of Philosophy in Aeronautical Engineering

Andrew J. Lingenfelter, B.S.M.E., M.E.I.E  
Captain, USAF

September 2016

DISTRIBUTION STATEMENT A:  
APPROVED FOR PUBLIC RELEASE; DISTRIBUTION UNLIMITED

AFIT-ENY-DS-16-S-065

CAVITY GEOMETRIC FEATURES AND ENTRAINMENT CHARACTERIZATION  
RESULTING FROM A BALLISTICALLY INDUCED HYDRODYNAMIC RAM  
EVENT

Andrew J. Lingenfelter, B.S.M.E., M.E.I.E  
Captain, USAF

Committee Membership:

David Liu, PhD  
Chair

Mark Reeder, PhD  
Member

Raymond Hill, PhD  
Member

ADEDEJI B. BADIRU, PhD  
Dean, Graduate School of Engineering and Management



**Abstract**

Hydrodynamic Ram can cause damage to industrial and aircraft systems. The resulting transient spray increases the probability of fire. To better understand the driving mechanisms behind transient spray, internal, and external measurements of the cavity geometry, and entrained flow field were accomplished. Research determined cavity contraction and separation are pre-cursors to the initiation of the transient spray phases. The entrained flow measurement required development of a new and novel technique using a continuous wave laser and atomized water particles. The peak mass flow correlated well with cavity geometric features, such as cavity contraction. Using the mass flow, cavity diameter at the orifice, and cavity length, projectile kinetic energy dissipation was related to cavity contraction. A relationship was developed for a range of impact velocities for the expected kinetic energy dissipation to occur prior to cavity contraction. Design of safer systems is possible by relating cavity contraction to the projectile's kinetic energy, and understanding how the transient spray is related to the cavity geometric features and the entrained mass flow.

*To my family – you are a part of me, and this research was performed at your expense. A thank you is not enough. To my wife – it's been a crazy ride...no reason to stop now...I love you! :)*

## **Acknowledgments**

I would like to acknowledge and thank the Joint Aircraft Survivability Program, Mr. Dennis Lindell, the 96<sup>th</sup> Test Group – AVSF, Mr. Eric Brickson, Mr. Craig Veatch, Mr. Keith Long, Mr. Jamie Smith, Mr. Josh Dewitt, Dr. Raymond Hill, Dr. Mark Reeder, and lastly my adviser, Major David Liu, PhD. Without the help, guidance, assistance, and encouragement, this research would not have happened, and this experience would be far different. To all – you have my deep gratitude and appreciation.

Andrew J. Lingenfelter

## Table of Contents

	Page
Abstract . . . . .	iv
Dedication . . . . .	v
Acknowledgments . . . . .	vi
Table of Contents . . . . .	vii
List of Figures . . . . .	x
List of Tables . . . . .	xxxi
List of Symbols . . . . .	xxxii
 I. Introduction . . . . .	 1
1.1 Motivation . . . . .	2
1.2 Research Goal . . . . .	3
1.2.1 Objective I . . . . .	4
1.2.2 Objective II . . . . .	4
1.2.3 Objective III . . . . .	5
 II. Previous Work . . . . .	 7
2.1 Brief HRAM History . . . . .	7
2.2 HRAM Cavity Dynamics . . . . .	8
2.3 Characterizing HRAM Cavity Formation . . . . .	10
2.3.1 Cavity Formation for Spherical Projectiles . . . . .	11
2.3.2 Cavity Formation Based on Projectile's Caliber-Radius-Head . . . . .	12
2.4 Characterizing HRAM Pressure-Volume Work and Cavity Collapse . . . . .	14
2.5 Hypothesis on the Effect of Different Projectile and Fluid Properties . . . . .	17
2.6 Characterizing the Transient Spray resulting from HRAM . . . . .	18
2.7 Measuring HRAM Cavity Dynamics . . . . .	19
2.8 HRAM Cavitation Mechanisms . . . . .	22
2.9 Computational Modeling of HRAM . . . . .	24
2.10 Orifice Flow Equations . . . . .	25
2.11 Summary . . . . .	30

	Page
III. Diagnostic Technique and Experimental Apparatus . . . . .	32
3.1 Investigative Research with the 96th Test Group . . . . .	33
3.2 Methodology for Imagery Acquisition for Cavity Volume and Projectile Position Measurements . . . . .	34
3.2.1 Imagery Analysis Process . . . . .	40
3.2.2 Feature Detection with Relative Constant Contrast . . . . .	41
3.2.3 Feature Detection and Tracking with Changing Contrast . . . . .	48
3.3 Orifice Entrainment Technique and Methodology . . . . .	50
3.3.1 Limitations of Developed Orifice Entrainment Technique . . . . .	54
3.4 Chapter III Conclusion . . . . .	58
IV. Analysis, Results, and Discussion . . . . .	59
4.1 The General Cavity Energy Model . . . . .	59
4.2 Entrained Flow through Penetration Orifice . . . . .	60
4.3 Relationship Between HRAM Cavity Geometric Features and the Transient Spray . . . . .	78
4.3.1 Observations from the 1,200 m/s Shot . . . . .	78
4.3.2 Observations from the 1,495 m/s Shot . . . . .	79
4.3.3 Observations from the 1,800 m/s Shot . . . . .	82
4.3.4 Overview of HRAM Cavity Observations . . . . .	85
4.4 Determination and Discussion of Important HRAM Cavity Relationships . . . . .	91
4.4.1 Volumetric Inflection Point . . . . .	91
4.4.2 Extrapolated Volumetric Data from research with the 96th Test Group . . . . .	93
4.4.3 HRAM Cavity Pressure Calculations . . . . .	96
4.4.4 Entrained Mass Flow Related to Cavity Geometry . . . . .	102
4.5 Predicting Cavity Contraction . . . . .	109
4.6 Discussion and Summary . . . . .	120
V. Findings, Implications for Practice, Additional Research, and Conclusions . . . . .	123
5.1 Summary of Findings . . . . .	123
5.1.1 Determine Cavity Composition . . . . .	123
5.1.2 Determine Cavity Dynamics Contributing to the Transient Spray . . . . .	124
5.1.3 Predicting Cavity Contraction . . . . .	125
5.1.4 Development of Empirical Model . . . . .	126
5.2 Implications for Practice . . . . .	127
5.3 Additional Research . . . . .	128
5.4 Conclusion . . . . .	129
Appendix A: Entrainment Imagery . . . . .	131

	Page
Appendix B: Entrained Mass and Velocity Plots . . . . .	157
Appendix C: Cavity Imagery . . . . .	208
Appendix D: Extrapolated Imagery from Research with 96th Test Group . . . . .	243
Bibliography . . . . .	284
Vita . . . . .	288

## List of Figures

Figure	Page
2.1 Design summary for bare 7075-T6 aluminum panels struck by single cubical fragments. Failure velocity versus panel thickness for various mass fragments, based on $\frac{v^2 D}{W} = 5.19 \frac{km^2}{s^2}$ where $D$ is the sphere diameter or cube edge and $W$ is the panel thickness. This figure was re-printed from “Fuel Tank Survivability for Hydrodynamic Ram Induced by High Velocity Fragments: Part I. Experimental Results and Design Summary” [16]. . . . .	15
2.2 Measured Position Information for specified muzzle velocities. . . . .	20
2.3 Velocity profile for axisymmetric slender body traveling through water [24]. The linear velocity decline supported the second-order nature of the position data collected for spheres for a short time duration after initial penetration. This figure is intellectual property and re-printed with permission from Cheng-Gong Zhao. . . . .	21
2.4 Cross section of rapidly expanding pipe used for reference for Eq. 2.14 through 2.24 modified from “Hydraulics and its Applications [30]”. . . . .	27
3.1 Overview Experimental Setup with the 96 <sup>th</sup> TG. . . . .	35
3.2 Overall experimental schematic to achieve the research objectives. . . . .	36
3.3 Overview of PAD used to complete HRAM tests. . . . .	37
3.4 Polycarbonate tank side view with LED lights reflecting on the photographic linen to generate the brightfield image technique used for imagery collection [34]. . . . .	38

Figure	Page
3.5 Selected images of leading-edge tracking of a 0.953 <i>cm</i> projectile penetrating water from 138.4 <i>cm</i> drop at 8,000 <i>Hz</i> . At 8,000 <i>Hz</i> , there was a 31.25 $\mu s$ mean time between each of the recorded images with an exposure time of 93.75 $\mu s$ . The + indicated the leading-edge of the projectile as determined by the developed algorithm [36]. . . . .	44
3.6 Cavity boundary tracking of a 0.953 <i>cm</i> projectile penetrating water from 138.4 <i>cm</i> drop at 8,000 <i>Hz</i> . At 8,000 <i>Hz</i> , there was a 31.25 $\mu s$ mean time between each of the recorded images with an exposure time of 93.75 $\mu s$ . The vertical white line indicated when no difference in boundary detection existed. The conformal white line indicated edge detection for cavity measurement [36]. . .	46
3.7 The right image was an enlarged subset image of Figure 3.5. The white horizontal line on the right subset image represented the cylinder's diameter used for volume calculations based on the assumption of axial symmetry about the projectile shot line [36]. . . . .	47
3.8 The right image was an enlarged subset image of Figure 3.5. The white rectangle was the horizontal white line displayed in Figure 3.7 illustrating the associated pixel height at the detected boundary. The height is needed to compute the small cylindrical calculations for each row of pixels [36]. . . .	47
3.9 A visual example of how the tensor was formed to create the image cube for flow analysis. Notice, instead of positional depth on the <i>z</i> axis, Frame Number is on the <i>z</i> axis. This subtle difference was not instinctive but is important to conduct position and velocity analysis at the desired $S_{n,r,c}$ . $S_{n,r,c}$ corresponded to row 130 of all images collected and formed together via Equation 3.8 to obtain Frame Number vs. Horizontal Position information. Time is obtained by using the frame number and the known camera's frame rate. . . . .	51



Figure	Page
3.10 Overall experimental schematic to obtain entrainment data [40]. . . . .	53
3.11 Example of a rectangular investigation region used for streak analysis to determine flow field velocity. The red arrow is the projectile shot line which also coincides with the orifice center line. The investigation region is larger than the projectile due to petaling of the aluminum creating a funnel larger than twice the projectile diameter on the exterior of the shot plate. The flow field velocity through the investigation region was used to determine the mass flow through the orifice. . . . .	56
4.1 PIV images utilizing atomized water as seed. Illumination source was a 532 nm, 12.5 W continuous wave laser sheet. Images are 800 by 1280 pixels and were taken at 10,000 fps with a 10 $\mu s$ exposure time. Notice the particle streaking visually decreasing between (c) and (d), when the flow begins to reverse direction and spurt is beginning. A shorter streak is indicative of a lower measured entrainment velocity. Initial projectile impact velocity is approximately 135 $m/s$ . See Fig. 4.3 for an example of the vector plots from the analyzed particle streaking [41]. . . . .	62
4.2 The above image processing sequence for a single image is applied to detect the streaks necessary for flow field characterization. First, the pixel values of the raw image, (a), are transformed using a log function to form Fig (b). Then, a convolution filter is applied to detect the edges of the streaks as shown in (c). After the convolution, a threshold is utilized to generate a binary shown in (d). The binary image is then filtered for aberrations and cropped to fit the investigation region. The detected streaks' length and orientation are recorded as flow field vectors. Examples of flow vectors at multiple instances in time are plotted in Fig. 4.3 [41]. . . . .	65

Figure	Page
4.3 Vector flow field results from streak analysis in the defined investigation region per Fig. 3.11. Images were collected at 10,000 frames per second with a $10\ \mu s$ exposure time [41]. . . . .	66
4.4 Depiction of the measured horizontal velocity profile data at different radial funnel positions at different instances in time. Notice the overall increase in the general velocity profile between (a) and (b) [41]. . . . .	67
4.5 A trapazoidal approximation of a volume of revolution was applied to the measured velocity profiles per Eq. 4.11 to obtain the mass flow rate through the orifice. The error bars represent the propagation of the error from the measured streak data. Notice the flow rate reaches a maximum around $1.5\ ms$ which corresponds to the initiation of cavity contraction at the orifice. The calculated mass flow continues to change and correlates well with cavity separation and conduit severance. . . . .	70
4.6 Time-resolved mass entrainment calculations for different impact velocities. The mass flow reaches a maximum approximately $1.5$ to $2\ ms$ after initial impact. The maximum mass flow rates correlated well with internal cavity dynamics. . . . .	71
4.7 HRAM cavity growth for $0.953\ cm$ steel sphere projectile at an impact velocity of approximately $176\ m/s$ . Imagery was collected at 20,000 frames per second with a $4\ \mu s$ exposure time at a resolution of 768 by 1024 pixels utilizing a brightfield technique [34]. The imagery displayed was cropped to a resolution of 130 by 865 pixels. . . . .	74

Figure	Page
4.8 HRAM cavity growth for 0.953 <i>cm</i> steel sphere projectile at an impact velocity of approximately 132 <i>m/s</i> . Imagery was collected at 20,000 frames per second with a 4 $\mu s$ exposure time at a resolution of 768 by 1024 pixels utilizing a brightfield technique [34]. The imagery displayed was cropped to a resolution of 110 by 625 pixels. . . . .	75
4.9 HRAM cavity growth for 0.953 <i>cm</i> steel sphere projectile at an impact velocity of approximately 114 <i>m/s</i> . Imagery was collected at 20,000 frames per second with a 4 $\mu s$ exposure time at a resolution of 768 by 1024 pixels utilizing a brightfield technique [34]. The imagery displayed was cropped to a resolution of 128 by 625 pixels. . . . .	77
4.10 Exterior view (EV) and Interior view (IV) of HRAM imagery data obtained with the 96 <sup>th</sup> Test Group Aerospace Vehicle Survivability Flight. The projectile was a 0.953 <i>cm</i> steel sphere with an impact velocity of approximately 1,200 <i>m/s</i> . The above images were obtained utilizing high-speed, synchronized cameras. Continuation of the event is seen in Fig 4.11. . . . .	80
4.11 Exterior view (EV) and Interior view (IV) of HRAM imagery data obtained with the 96 <sup>th</sup> Test Group Aerospace Vehicle Survivability Flight. The above images were obtained utilizing high-speed, synchronized cameras. The projectile was a 0.953 <i>cm</i> steel sphere with an impact velocity of approximately 1,200 <i>m/s</i> . . . . .	81
4.12 Exterior view (EV) and Interior view (IV) of HRAM imagery data obtained with the 96 <sup>th</sup> Test Group Aerospace Vehicle Survivability Flight. The projectile was a 0.953 <i>cm</i> steel sphere with an impact velocity of approximately 1,495 <i>m/s</i> . The above images were obtained utilizing high-speed, synchronized cameras. Continuation of the event is seen in Fig 4.13 [20]. . . . .	83

Figure	Page
4.13 Exterior view (EV) and Interior view (IV) of HRAM imagery data obtained with the 96 <sup>th</sup> Test Group Aerospace Vehicle Survivability Flight. The projectile was a 0.953 <i>cm</i> steel sphere with an impact velocity of approximately 1,495 <i>m/s</i> . The above images were obtained utilizing high-speed, synchronized cameras [20]. . . . .	84
4.14 Exterior view (EV) and Interior view (IV) of HRAM imagery data obtained with the 96 <sup>th</sup> Test Group Aerospace Vehicle Survivability Flight. The projectile was a 0.953 <i>cm</i> steel sphere with an impact velocity of approximately 1,800 <i>m/s</i> . The above images were obtained utilizing high-speed, synchronized cameras. Continuation of the event is seen in Fig 4.15. . . . .	86
4.15 Exterior view (EV) and Interior view (IV) of HRAM imagery data obtained with the 96 <sup>th</sup> Test Group Aerospace Vehicle Survivability Flight. The projectile was a 0.953 <i>cm</i> steel sphere with an impact velocity of approximately 1,800 <i>m/s</i> . The above images were obtained utilizing high-speed, synchronized cameras. . . . .	87

Figure	Page
4.16 Distinguishable cavity formation, contraction, separation, and collapse phases and features that occur during an HRAM event. Cavity formation, in Fig. 4.16(a), occurs when the projectile penetrates the body of fluid and creates a cavity. Cavity contraction, in Fig. 4.16(b), occurs when the cavity's diameter at the orifice begins to decrease and contract around the orifice. Cavity separation, in Fig. 4.16(c) occurs after cavity contraction and occurs when the cavity separates from the shot plate. The cavity conduit is also present during this phase. Cavity collapse, in Fig. 4.16(d) occurs as the cavity volume decreases and implodes on itself. Research can focus on cavity contraction and separation phase, which are pre-cursors to the transient spray, by breaking down Ball's overall HRAM cavity phase [4]. . . . .	90
4.17 Calculated cavity volumetric data from imagery for the test cases specified in Table 4.3 [20]. . . . .	92
4.18 Example of extrapolated image to permit cavity volume calculations. See Appendix D for all sets of extrapolated images. . . . .	94
4.19 Example of extrapolated image to permit cavity volume calculations. . . . .	95
4.20 Calculated partial pressure of air in HRAM cavity based on measured cavity volume data and entrained air through the orifice for the test cases specified in Table 4.1 and 4.4. The solid line at 2,340 Pa represents the vapor pressure of water at 20 degrees centigrade [44]. . . . .	98
4.21 Calculated partial pressure of entrained gases in HRAM cavity plotted versus calculated projectile cavitation number. Notice for the low cavitation numbers, the cavity pressure is significantly above the fluid's vaporization pressure of 2,340 Pa for the test cases specified in Tables 4.1 and 4.4 [44]. . . . .	101

Figure	Page
4.22 Example of image subset used to obtain measurements for $\beta_C$ calculations per Eq. 4.14 . . . . .	103
4.23 Maximum cavity diameter at the orifice for different impact velocities. . . . .	105
4.24 Example of the maximum cavity diameter measurements for calculation of $\beta_C(t)$ per Eq. 4.14. . . . .	106
4.25 Calculated mass flow through the orifice versus $[1 - \beta_C(t)^2]$ per Eq. 4.14. . . . .	107
4.26 Calculated mass flow plotted versus dimensionless cavity geometry per Eq. 4.16. As the dimensionless area ratio and penetration distance increased, the mass flow through the orifice increases approximately linearly. . . . .	109
4.27 Calculated mass flow plotted versus projectile dimensionless geometry per Eq. 4.16. Initiation of cavity contraction occurred approximately when the mass flow peaks through the orifice, as detailed in Section 4.2. For the test cases, this occurred around 6.5 grams per second. The solid line at 6.5 grams per second provides the visual representation for the expected bounds of $\psi$ corresponding cavity contraction. . . . .	111
4.28 Calculated dimensionless term $\psi$ plotted versus dimensionless term $\Delta KE'$ per Eq. 4.17. Initiation of cavity contraction occurred approximately when $\psi$ ranged between 1.0 to 1.125, as shown in Fig. 4.27. By using the bounds for $\psi$ , determination of the corresponding $\Delta KE'$ was possible and shown in (b). . . . .	113
4.29 Evolution of cavity contraction for impact velocity of 174 <i>m/s</i> at $\Delta KE'$ values ranging from 0.54 to 0.65 per Fig. 4.28. . . . .	114
4.30 Evolution of cavity contraction for impact velocity of 136 <i>m/s</i> at $\Delta KE'$ values ranging from 0.40 to 0.49 per Fig. 4.28. . . . .	116
4.31 Evolution of cavity contraction for impact velocity of 114 <i>m/s</i> at $\Delta KE'$ values ranging from 0.30 to 0.36 per Fig. 4.28. . . . .	117

Figure	Page
4.32 It is possible to predict cavity contraction for a range of velocities by plotting the dimensionless $\Delta KE'$ with regards to the impact velocity. The dashed lines provide the upper, lower, and average bounds determined by a least squares method for the range of $\Delta KE'$ determined by Fig. 4.27 and 4.28. Cavity contraction will occur within the determined range of $\Delta KE'$ . . . . .	118
4.33 Measured maximum cavity pressure work versus total projectile kinetic energy lost for the experimental velocities specified in Tables 4.1 and 4.4. . . . .	121
A.1 Collected images depicting the evolution of entrained velocity measurements for 113 <i>m/s</i> impact velocity from the first image prior to impact to 1.2 <i>ms</i> after impact. Continuation of the event is shown in Fig. A.2. . . . .	137
A.2 Collected images depicting the evolution of entrained velocity measurements for 113 <i>m/s</i> impact velocity from 1.3 to 2.6 <i>ms</i> after impact. Continuation of the event is shown in Fig. A.3. . . . .	138
A.3 Collected images depicting the evolution of entrained velocity measurements for 113 <i>m/s</i> impact velocity from 2.7 to 4.0 <i>ms</i> after impact. Continuation of the event is shown in Fig. A.4. . . . .	139
A.4 Collected images depicting the evolution of entrained velocity measurements for 113 <i>m/s</i> impact velocity from 4.1 to 4.8 <i>ms</i> after impact. . . . .	140
A.5 Collected images depicting the evolution of entrained velocity measurements for 114 <i>m/s</i> impact velocity from the first image prior to impact to 1.2 <i>ms</i> after impact. Continuation of the event is shown in Fig. A.6. . . . .	141
A.6 Collected images depicting the evolution of entrained velocity measurements for 114 <i>m/s</i> impact velocity from 1.3 to 2.6 <i>ms</i> after impact. Continuation of the event is shown in Fig. A.7. . . . .	142

Figure	Page
A.7 Collected images depicting the evolution of entrained velocity measurements for 114 <i>m/s</i> impact velocity from 2.7 to 4.0 <i>ms</i> after impact. Continuation of the event is shown in Fig. A.8. . . . .	143
A.8 Collected images depicting the evolution of entrained velocity measurements for 114 <i>m/s</i> impact velocity from 2.7 to 4.0 <i>ms</i> after impact. . . . .	144
A.9 Collected images depicting the evolution of entrained velocity measurements for 132 <i>m/s</i> impact velocity from the first image prior to impact to 1.2 <i>ms</i> after impact. Continuation of the event is shown in Fig. A.10. . . . .	145
A.10 Collected images depicting the evolution of entrained velocity measurements for 132 <i>m/s</i> impact velocity from 1.3 to 2.6 <i>ms</i> after impact. Continuation of the event is shown in Fig. A.11. . . . .	146
A.11 Collected images depicting the evolution of entrained velocity measurements for 132 <i>m/s</i> impact velocity from 2.7 to 3.7 <i>ms</i> after impact. . . . .	147
A.12 Collected images depicting the evolution of entrained velocity measurements for 135 <i>m/s</i> impact velocity from the first image prior to impact to 1.2 <i>ms</i> after impact. Continuation of the event is shown in Fig. A.13. . . . .	148
A.13 Collected images depicting the evolution of entrained velocity measurements for 135 <i>m/s</i> impact velocity from 1.3 to 2.6 <i>ms</i> after impact. Continuation of the event is shown in Fig. A.14. . . . .	149
A.14 Collected images depicting the evolution of entrained velocity measurements for 135 <i>m/s</i> impact velocity from 2.7 to 3.5 <i>ms</i> after impact. . . . .	150
A.15 Collected images depicting the evolution of entrained velocity measurements for 176 <i>m/s</i> impact velocity from the first image prior to impact to 1.2 <i>ms</i> after impact. Continuation of the event is shown in Fig. A.16. . . . .	151



Figure	Page
A.16 Collected images depicting the evolution of entrained velocity measurements for 176 <i>m/s</i> impact velocity from 1.3 to 2.6 <i>ms</i> after impact. Continuation of the event is shown in Fig. A.17. . . . .	152
A.17 Collected images depicting the evolution of entrained velocity measurements for 176 <i>m/s</i> impact velocity from 2.7 to 3.4 <i>ms</i> after impact. . . . .	153
A.18 Collected images depicting the evolution of entrained velocity measurements for 176 <i>m/s</i> impact velocity from the first image prior to impact to 1.1 <i>ms</i> after impact. Continuation of the event is shown in Fig. A.19. . . . .	154
A.19 Collected images depicting the evolution of entrained velocity measurements for 176 <i>m/s</i> impact velocity from 1.2 to 2.5 <i>ms</i> after impact. Continuation of the event is shown in Fig. A.20. . . . .	155
A.20 Collected images depicting the evolution of entrained velocity measurements for 176 <i>m/s</i> impact velocity from 2.6 to 3.4 <i>ms</i> after impact. . . . .	156
B.1 Mass flow plot for the 113 <i>m/s</i> shot obtained by performing a trapezoidal approximation of a volume of revolution around the projectile's shot-line. Each mass flow data point's corresponding velocity profile is shown in Fig. B.3 through B.8. . . . .	159
B.2 Entrained mass calculation of ambient air into the HRAM cavity used for partial pressure calculations in Section 4.4.3 for the 113 <i>m/s</i> shot. The entrained mass was calculated by performing a rectangular approximation of Fig. B.1's data to estimate the area under the curve. . . . .	159
B.3 Plotted horizontal component of the streak velocity across the funnel diameter 0.5 to 1.0 <i>ms</i> after impact for the 113 <i>m/s</i> impact velocity. . . . .	160
B.4 Plotted horizontal component of the streak velocity across the funnel diameter 1.1 to 1.6 <i>ms</i> after impact for the 113 <i>m/s</i> impact velocity. . . . .	161

Figure	Page
B.5 Plotted horizontal component of the streak velocity across the funnel diameter 1.7 to 2.2 <i>ms</i> after impact for the 113 <i>m/s</i> impact velocity. . . . .	162
B.6 Plotted horizontal component of the streak velocity across the funnel diameter 2.3 to 2.8 <i>ms</i> after impact for the 113 <i>m/s</i> impact velocity. . . . .	163
B.7 Plotted horizontal component of the streak velocity across the funnel diameter 2.9 to 3.4 <i>ms</i> after impact for the 113 <i>m/s</i> impact velocity. . . . .	164
B.8 Plotted horizontal component of the streak velocity across the funnel diameter 3.5 to 4.0 <i>ms</i> after impact for the 113 <i>m/s</i> impact velocity. . . . .	165
B.9 Mass flow plot for the 114 <i>m/s</i> shot obtained by performing a trapezoidal approximation of a volume of revolution around the projectile's shot-line. Each mass flow data point's corresponding velocity profile is shown in Fig. B.11 through B.16. . . . .	168
B.10 Entrained mass calculation of ambient air into the HRAM cavity used for partial pressure calculations in Section 4.4.3 for the 114 <i>m/s</i> shot. The entrained mass was calculated by performing a rectangular approximation of Fig. B.9's data to estimate the area under the curve. . . . .	168
B.11 Plotted horizontal component of the streak velocity across the funnel diameter 0.5 to 1.0 <i>ms</i> after impact for the 114 <i>m/s</i> impact velocity. . . . .	169
B.12 Plotted horizontal component of the streak velocity across the funnel diameter 1.1 to 1.6 <i>ms</i> after impact for the 114 <i>m/s</i> impact velocity. . . . .	170
B.13 Plotted horizontal component of the streak velocity across the funnel diameter 1.7 to 2.2 <i>ms</i> after impact for the 114 <i>m/s</i> impact velocity. . . . .	171
B.14 Plotted horizontal component of the streak velocity across the funnel diameter 2.3 to 2.8 <i>ms</i> after impact for the 114 <i>m/s</i> impact velocity. . . . .	172

Figure	Page
B.15 Plotted horizontal component of the streak velocity across the funnel diameter 2.9 to 3.4 <i>ms</i> after impact for the 114 <i>m/s</i> impact velocity. . . . .	173
B.16 Plotted horizontal component of the streak velocity across the funnel diameter 3.5 to 4.0 <i>ms</i> after impact for the 114 <i>m/s</i> impact velocity. . . . .	174
B.17 Mass flow plot for the 132 <i>m/s</i> shot obtained by performing a trapezoidal approximation of a volume of revolution around the projectile's shot-line. Each mass flow data point's corresponding velocity profile is shown in Fig. B.19 through B.24. . . . .	176
B.18 Entrained mass calculation of ambient air into the HRAM cavity used for partial pressure calculations in Section 4.4.3 for the 132 <i>m/s</i> shot. The entrained mass was calculated by performing a rectangular approximation of Fig. B.17's data to estimate the area under the curve. . . . .	177
B.19 Plotted horizontal component of the streak velocity across the funnel diameter 0.5 to 1.0 <i>ms</i> after impact for the 132 <i>m/s</i> impact velocity. . . . .	178
B.20 Plotted horizontal component of the streak velocity across the funnel diameter 1.1 to 1.6 <i>ms</i> after impact for the 132 <i>m/s</i> impact velocity. . . . .	179
B.21 Plotted horizontal component of the streak velocity across the funnel diameter 1.7 to 2.2 <i>ms</i> after impact for the 132 <i>m/s</i> impact velocity. . . . .	180
B.22 Plotted horizontal component of the streak velocity across the funnel diameter 2.3 to 2.8 <i>ms</i> after impact for the 132 <i>m/s</i> impact velocity. . . . .	181
B.23 Plotted horizontal component of the streak velocity across the funnel diameter 2.9 to 3.2 <i>ms</i> after impact for the 132 <i>m/s</i> impact velocity. . . . .	182
B.24 Plotted horizontal component of the streak velocity across the funnel diameter 3.3 to 3.5 <i>ms</i> after impact for the 132 <i>m/s</i> impact velocity. . . . .	183

Figure	Page
B.25 Mass flow plot for the 135 <i>m/s</i> shot obtained by performing a trapezoidal approximation of a volume of revolution around the projectile's shot-line. Each mass flow data point's corresponding velocity profile is shown in Fig. B.27 through B.31. . . . .	185
B.26 Entrained mass calculation of ambient air into the HRAM cavity used for partial pressure calculations in Section 4.4.3 for the 135 <i>m/s</i> shot. The entrained mass was calculated by performing a rectangular approximation of Fig. B.25's data to estimate the area under the curve. . . . .	186
B.27 Plotted horizontal component of the streak velocity across the funnel diameter 0.5 to 1.0 <i>ms</i> after impact for the 135 <i>m/s</i> impact velocity. . . . .	187
B.28 Plotted horizontal component of the streak velocity across the funnel diameter 1.1 to 1.6 <i>ms</i> after impact for the 135 <i>m/s</i> impact velocity. . . . .	188
B.29 Plotted horizontal component of the streak velocity across the funnel diameter 1.7 to 2.2 <i>ms</i> after impact for the 135 <i>m/s</i> impact velocity. . . . .	189
B.30 Plotted horizontal component of the streak velocity across the funnel diameter 2.3 to 2.8 <i>ms</i> after impact for the 135 <i>m/s</i> impact velocity. . . . .	190
B.31 Plotted horizontal component of the streak velocity across the funnel diameter 2.9 to 3.4 <i>ms</i> after impact for the 135 <i>m/s</i> impact velocity. . . . .	191
B.32 Mass flow plot for the 176 <i>m/s</i> shot obtained by performing a trapezoidal approximation of a volume of revolution around the projectile's shot-line. Each mass flow data point's corresponding velocity profile is shown in Fig. B.34 through B.45. . . . .	193

Figure	Page
B.33 Entrained mass calculation of ambient air into the HRAM cavity used for partial pressure calculations in Section 4.4.3 for the 176 <i>m/s</i> shot. The entrained mass was calculated by performing a rectangular approximation of Fig. B.32's data to estimate the area under the curve. . . . .	194
B.34 Plotted horizontal component of the streak velocity across the funnel diameter for 176 <i>m/s</i> impact velocity from 0.5 to 1.0 <i>ms</i> after impact. . . . .	195
B.35 Plotted horizontal component of the streak velocity across the funnel diameter 1.1 to 1.6 <i>ms</i> after impact. . . . .	196
B.36 Plotted horizontal component of the streak velocity across the funnel diameter 1.7 to 2.2 <i>ms</i> after impact. . . . .	197
B.37 Plotted horizontal component of the streak velocity across the funnel diameter 2.3 to 2.8 <i>ms</i> after impact. . . . .	198
B.38 Plotted horizontal component of the streak velocity across the funnel diameter 2.9 to 3.3 <i>ms</i> after impact. . . . .	199
B.39 Mass flow plot for the 176 <i>m/s</i> shot obtained by performing a trapezoidal approximation of a volume of revolution around the projectile's shot-line. Each mass flow data point's corresponding velocity profile is shown in Fig. B.41 through B.45. . . . .	202
B.40 Entrained mass calculation of ambient air into the HRAM cavity used for partial pressure calculations in Section 4.4.3 for the 176 <i>m/s</i> shot. The entrained mass was calculated by performing a rectangular approximation of Fig. B.39's data to estimate the area under the curve. . . . .	202
B.41 Plotted horizontal component of the streak velocity across the funnel diameter 0.6 to 1.1 <i>ms</i> after impact. . . . .	203

Figure	Page
B.42 Plotted horizontal component of the streak velocity across the funnel diameter 1.2 to 1.7 <i>ms</i> after impact. . . . .	204
B.43 Plotted horizontal component of the streak velocity across the funnel diameter 1.8 to 2.3 <i>ms</i> after impact. . . . .	205
B.44 Plotted horizontal component of the streak velocity across the funnel diameter 2.4 to 2.9 <i>ms</i> after impact. . . . .	206
B.45 Plotted horizontal component of the streak velocity across the funnel diameter 3.0 to 3.3 <i>ms</i> after impact. . . . .	207
C.1 Image slice at $S_{417}$ using the Image Cube technique detailed in Chapter III. The positional information resides on the horizontal while the frame number information resides on the vertical. The images composing the vertical were collected over a 4.0 <i>ms</i> duration after projectile impact. The position data pulled from this slice is shown in Table C.1. . . . .	209
C.2 Cavity volume calculations for the 111 <i>m/s</i> shot plotted at 20,000 <i>Hz</i> . The necessary volume data was extracted from the above figure and used to match the entrainment measurement rate of 10,000 <i>Hz</i> . Details on the process and assumptions to compute the cavity volume are provided in Chapter III and in “Development of Methods for Characterizing Hydrodynamic Ram Cavity Dynamics” [36]. . . . .	212
C.3 Raw cavity images for 111 <i>m/s</i> impact velocity for 0.0 to 0.5 <i>ms</i> after impact. .	213
C.4 Raw cavity images for 111 <i>m/s</i> impact velocity for 0.6 to 1.1 <i>ms</i> after impact. .	214
C.5 Raw cavity images for 111 <i>m/s</i> impact velocity for 1.2 to 1.7 <i>ms</i> after impact. .	215
C.6 Raw cavity images for 111 <i>m/s</i> impact velocity for 1.8 to 2.3 <i>ms</i> after impact. .	216
C.7 Raw cavity images for 111 <i>m/s</i> impact velocity for 2.4 to 2.9 <i>ms</i> after impact. .	217
C.8 Raw cavity images for 111 <i>m/s</i> impact velocity for 3.1 to 3.6 <i>ms</i> after impact. .	218

Figure	Page
C.9 Raw cavity images for 111 <i>m/s</i> impact velocity for 3.7 to 4.2 <i>ms</i> after impact. .	219
C.10 Image slice at $S_{432}$ using the Image Cube technique detailed in Chapter III. The positional information resides on the horizontal while the frame number information resides on the vertical. The images composing the vertical were collected over a 4.0 <i>ms</i> duration after projectile impact. The position data pulled from this slice is shown in Table C.2. . . . .	221
C.11 Cavity volume calculations for the 136 <i>m/s</i> shot plotted at 20,000 <i>Hz</i> . The necessary volume data was extracted from the above figure and used to match the entrainment measurement rate of 10,000 <i>Hz</i> . Details on the process and assumptions to compute the cavity volume are provided in Chapter III and in “Development of Methods for Characterizing Hydrodynamic Ram Cavity Dynamics” [36]. . . . .	223
C.12 Raw cavity images for 136 <i>m/s</i> impact velocity for 0.0 to 0.5 <i>ms</i> after impact. .	224
C.13 Raw cavity images for 136 <i>m/s</i> impact velocity for 0.6 to 1.1 <i>ms</i> after impact. .	225
C.14 Raw cavity images for 136 <i>m/s</i> impact velocity for 1.2 to 1.7 <i>ms</i> after impact. .	226
C.15 Raw cavity images for 136 <i>m/s</i> impact velocity for 1.8 to 2.3 <i>ms</i> after impact. .	227
C.16 Raw cavity images for 136 <i>m/s</i> impact velocity for 2.4 to 2.9 <i>ms</i> after impact. .	228
C.17 Raw cavity images for 136 <i>m/s</i> impact velocity for 3.1 to 3.6 <i>ms</i> after impact. .	229
C.18 Raw cavity images for 136 <i>m/s</i> impact velocity for 3.7 to 4.2 <i>ms</i> after impact. .	230
C.19 Image slice at $S_{428}$ using the Image Cube technique detailed in Chapter III. The positional information resides on the horizontal while the frame number information resides on the vertical. The images composing the vertical were collected over a 4.0 <i>ms</i> duration after projectile impact. The position data pulled from this slice is shown in Table C.3. . . . .	233

Figure	Page
C.20 Cavity volume calculations for the 174 <i>m/s</i> shot plotted at 20,000 <i>Hz</i> . The necessary volume data was extracted from the above figure and used to match the entrainment measurement rate of 10,000 <i>Hz</i> . Details on the process and assumptions to compute the cavity volume are provided in Chapter III and in “Development of Methods for Characterizing Hydrodynamic Ram Cavity Dynamics” [36]. . . . .	235
C.21 Raw cavity images for 174 <i>m/s</i> impact velocity for 0.0 to 0.5 <i>ms</i> after impact. .	236
C.22 Raw cavity images for 174 <i>m/s</i> impact velocity for 0.6 to 1.1 <i>ms</i> after impact. .	237
C.23 Raw cavity images for 174 <i>m/s</i> impact velocity for 1.2 to 1.7 <i>ms</i> after impact. .	238
C.24 Raw cavity images for 174 <i>m/s</i> impact velocity for 1.8 to 2.3 <i>ms</i> after impact. .	239
C.25 Raw cavity images for 174 <i>m/s</i> impact velocity for 2.4 to 2.9 <i>ms</i> after impact. .	240
C.26 Raw cavity images for 174 <i>m/s</i> impact velocity for 3.1 to 3.6 <i>ms</i> after impact. .	241
C.27 Raw cavity images for 174 <i>m/s</i> impact velocity for 3.7 to 4.2 <i>ms</i> after impact. .	242
D.1 Volume plot resulting from extrapolated images shown in Figs. D.4 through D.16.	244
D.2 Volume plot resulting from extrapolated images shown in Figs. D.17 through D.29.	245
D.3 Volume plot resulting from extrapolated images shown in Figs. D.30 through D.41.	245
D.4 Extrapolated cavity images for 1,200 <i>m/s</i> impact velocity for 0.0 to 0.1429 <i>ms</i> after impact. . . . .	246
D.5 Extrapolated cavity images for 1,200 <i>m/s</i> impact velocity for 0.2500 to 0.4643 <i>ms</i> after impact. . . . .	247
D.6 Extrapolated cavity images for 1,200 <i>m/s</i> impact velocity for 0.5714 to 0.7857 <i>ms</i> after impact. . . . .	248
D.7 Extrapolated cavity images for 1,200 <i>m/s</i> impact velocity for 0.8929 to 1.1071 <i>ms</i> after impact. . . . .	249



Figure	Page
D.8 Extrapolated cavity images for 1,200 <i>m/s</i> impact velocity for 1.2143 to 1.4286 <i>ms</i> after impact. . . . .	250
D.9 Extrapolated cavity images for 1,200 <i>m/s</i> impact velocity for 1.5357 to 1.7500 <i>ms</i> after impact. . . . .	251
D.10 Raw cavity images for 1,200 <i>m/s</i> impact velocity for 1.8571 to 2.3929 <i>ms</i> after impact. . . . .	252
D.11 Raw cavity images for 1,200 <i>m/s</i> impact velocity for 2.1786 to 2.3929 <i>ms</i> after impact. . . . .	253
D.12 Raw cavity images for 1,200 <i>m/s</i> impact velocity for 2.5000 to 3.0357 <i>ms</i> after impact. . . . .	254
D.13 Raw cavity images for 1,200 <i>m/s</i> impact velocity for 2.5000 to 3.0357 <i>ms</i> after impact. . . . .	255
D.14 Raw cavity images for 1,200 <i>m/s</i> impact velocity for 3.1429 to 3.6786 <i>ms</i> after impact. . . . .	256
D.15 Raw cavity images for 1,200 <i>m/s</i> impact velocity for 3.1429 to 3.6786 <i>ms</i> after impact. . . . .	257
D.16 Raw cavity images for 1,200 <i>m/s</i> impact velocity for 3.7857 to 3.8929 <i>ms</i> after impact. . . . .	258
D.17 Extrapolated cavity images for 1,485 <i>m/s</i> impact velocity for 0.0 to 0.1429 <i>ms</i> after impact. . . . .	259
D.18 Extrapolated cavity images for 1,485 <i>m/s</i> impact velocity for 0.2500 to 0.4643 <i>ms</i> after impact. . . . .	260
D.19 Extrapolated cavity images for 1,485 <i>m/s</i> impact velocity for 0.5714 to 0.7857 <i>ms</i> after impact. . . . .	261

Figure	Page
D.20 Extrapolated cavity images for 1,485 <i>m/s</i> impact velocity for 0.8929 to 1.1071 <i>ms</i> after impact. . . . .	262
D.21 Extrapolated cavity images for 1,485 <i>m/s</i> impact velocity for 1.2143 to 1.4286 <i>ms</i> after impact. . . . .	263
D.22 Extrapolated cavity images for 1,485 <i>m/s</i> impact velocity for 1.5357 to 1.7500 <i>ms</i> after impact. . . . .	264
D.23 Raw cavity images for 1,485 <i>m/s</i> impact velocity for 1.8571 to 2.0714 <i>ms</i> after impact. . . . .	265
D.24 Raw cavity images for 1,485 <i>m/s</i> impact velocity for 1.8571 to 2.3929 <i>ms</i> after impact. . . . .	266
D.25 Raw cavity images for 1,485 <i>m/s</i> impact velocity for 2.5000 to 2.7143 <i>ms</i> after impact. . . . .	267
D.26 Raw cavity images for 1,485 <i>m/s</i> impact velocity for 2.8214 to 3.0357 <i>ms</i> after impact. . . . .	268
D.27 Raw cavity images for 1,485 <i>m/s</i> impact velocity for 3.1429 to 3.3571 <i>ms</i> after impact. . . . .	269
D.28 Raw cavity images for 1,485 <i>m/s</i> impact velocity for 3.4643 to 3.6786 <i>ms</i> after impact. . . . .	270
D.29 Raw cavity images for 1,485 <i>m/s</i> impact velocity for 3.7857 to 3.8929 <i>ms</i> after impact. . . . .	271
D.30 Extrapolated cavity images for 1,800 <i>m/s</i> impact velocity for 0.0 to 0.1429 <i>ms</i> after impact. . . . .	272
D.31 Extrapolated cavity images for 1,800 <i>m/s</i> impact velocity for 0.2500 to 0.4643 <i>ms</i> after impact. . . . .	273

Figure	Page
D.32 Extrapolated cavity images for 1,800 <i>m/s</i> impact velocity for 0.5714 to 0.7857 <i>ms</i> after impact. . . . .	274
D.33 Extrapolated cavity images for 1,800 <i>m/s</i> impact velocity for 0.8929 to 1.1071 <i>ms</i> after impact. . . . .	275
D.34 Extrapolated cavity images for 1,800 <i>m/s</i> impact velocity for 1.2143 to 1.4286 <i>ms</i> after impact. . . . .	276
D.35 Extrapolated cavity images for 1,800 <i>m/s</i> impact velocity for 1.5357 to 1.7500 <i>ms</i> after impact. . . . .	277
D.36 Raw cavity images for 1,800 <i>m/s</i> impact velocity for 1.8571 to 2.0714 <i>ms</i> after impact. . . . .	278
D.37 Raw cavity images for 1,800 <i>m/s</i> impact velocity for 1.1786 to 2.3929 <i>ms</i> after impact. . . . .	279
D.38 Raw cavity images for 1,800 <i>m/s</i> impact velocity for 2.5000 to 2.7143 <i>ms</i> after impact. . . . .	280
D.39 Raw cavity images for 1,800 <i>m/s</i> impact velocity for 2.8214 to 3.0357 <i>ms</i> after impact. . . . .	281
D.40 Raw cavity images for 1,800 <i>m/s</i> impact velocity for 3.1429 to 3.3571 <i>ms</i> after impact. . . . .	282
D.41 Raw cavity images for 1,800 <i>m/s</i> impact velocity for 3.4643 to 3.6786 <i>ms</i> after impact. . . . .	283

## List of Tables

Table	Page
4.1 Projectile Parameters for Entrainment Data . . . . .	72
4.2 Time elapsed after projectile impact until the detected Transient Spray Events .	88
4.3 Projectile Parameters for HRAM Cavity Inflection Point Experiments . . . . .	92
4.4 Projectile Parameters for HRAM Volumetric Experiments . . . . .	96
4.5 Projectile Parameters for Entrainment Data . . . . .	98
C.1 Projectile Position Data for 111 m/s shot . . . . .	210
C.2 Projectile Position Data for 136 m/s shot . . . . .	222
C.3 Projectile Position Data for 174 m/s shot . . . . .	234

## List of Symbols

Symbol	Definition
$A$	Area
$\beta$	Dimensionless diameter ratio
$C$	Degrees Centigrade
$C_d$	Coefficient of drag
$C_p$	Coefficient of pressure drag
$g$	Acceleration due to gravity
$H$	Head loss
$K$	Flow resistance factor
$\lambda$	Dimensionless cavity length ratio
$\mu$	Dynamic Viscosity
$m$	mass
$N$	Camera frame rate constant
$n$	Number of vectors in an image
$\Omega$	Dimensionless area ratio
$P_c$	Pressure in cavity
$P_o$	Pressure at shot line to include atmosphere and static head
$P_v$	Fluid vapor pressure
$Q$	Number of successful $\dot{m}_o$ measurements
$\rho_f$	Fluid density
$r$	Radius
$\sigma$	Cavitation number
$\tau$	Characteristic response time for particle latency
$\Theta$	Contrast gradient

Symbol	Definition
$\theta$	Contrast gradient component
$T$	Temperature
$t$	time
$V$	Velocity
$\bar{V}$	Volume
$\psi$	Dimensionless cavity geometry parameter
$W$	Specific weight
$Y$	Expansion factor
$\epsilon$	Error
$ms$	milliseconds
$\mu s$	microseconds
$m/s$	meters per second
$cm$	centimeters
$J$	Joules
$Pa$	Pascals
$g/s$	grams per second
$d$	diameter
$W_C$	Cavity pressure-volume work
$W_E$	Maximum cavity pressure-volume work potential due to entrainment

#### *Subscripts*

$C$	Cavity
$f$	Fluid
$F$	Funnel
$i$	Numerical Index

Symbol	Definition
--------	------------

$L$	Liquid
-----	--------

$O$	Orifice
-----	---------

$0$	Initial conditions
-----	--------------------

$P$	Projectile
-----	------------

$x$	Horizontal component
-----	----------------------

$y$	Vertical component
-----	--------------------

$v$	Gaseous vapor
-----	---------------

### *Superscripts*

$'$	Dimensionless quantity
-----	------------------------

$3$	Cubed
-----	-------

$2$	Squared
-----	---------

# CAVITY GEOMETRIC FEATURES AND ENTRAINMENT CHARACTERIZATION RESULTING FROM A BALLISTICALLY INDUCED HYDRODYNAMIC RAM EVENT

## I. Introduction

**H**YDRODYNAMIC ram (HRAM) refers to the large fluid, vapor, and entrained gas pressures from cavitation in a fluid-filled device. In general, cavitation in fluids is caused by various types of mechanisms such as pumps, fluid flow separation, and high kinetic energy projectiles. Typically the bubble composition during cavitation occurring on a propeller or pump is assumed to consist primarily of vaporized local fluid. In an HRAM event, involving projectiles, the cavity may consist of a mixture of vaporized local fluid and ambient gases entrained through the penetration orifice. Additionally, the fluid ejecting from the orifice has distinguishable properties and phases. Discussion of the internal geometric features and the associated transient spray will follow.

During an HRAM event, the cavity has distinguishable geometric features. The geometric features dynamically change as the HRAM event progresses in time. The focus of this research is on the HRAM cavity features and their dynamics resulting from a high kinetic energy projectile penetrating a body of fluid. The projectile can have any shape or form as long as the projectile has sufficient kinetic energy to generate a gaseous low pressure region in the wake of the projectile. This low pressure region permits the transfer or entrainment of ambient air through the orifice, which generates a gaseous cavity resulting in a large pressure difference between the cavity and the fluid-filled apparatus. Upon cavity collapse, this large pressure difference can result in equipment failure, industrial safety



hazards, catastrophic structural damage to an aircraft, or cause atomized liquid spurt via the penetration orifice [1].

The liquid spurt resulting from an HRAM event is commonly referred to as transient spray. The transient spray can increase the probability of fire on-board aircraft under the appropriate circumstances [2]. The objective of this research is to focus on the cavity dynamics contributing to the transient spray and characterize the properties and associated mechanisms to improve aircraft safety.

## **1.1 Motivation**

Current modeling and simulation capabilities do not have sufficient understanding of the physical mechanisms to model ballistically induced HRAM accurately or with sufficient fidelity. The capability to accurately predict the probability of ballistically-induced dry bay fires as a result of HRAM is still a work in progress [2]. The underlying equations in the modeling and simulation software are based on empirical HRAM observations for a specific ballistic scenario. The physics-based models and mechanisms to describe HRAM cavity dynamics are not well developed to account for the different phases of an HRAM event observed through testing [3].

An HRAM event causes aircraft damage via two mechanisms. First is the structural damage generated by the large pressure in the closed fluid-filled container [4, 5]. Second, combustible fluid inside the tank can spray into the dry bay after an HRAM event. This spray can create a high potential for a fire event [1, 2]. This research will focus on the HRAM cavity geometric features contributing to the resultant spray after the projectile has entered the container. Aircraft survivability is improved by better understanding the cavity's geometric features and the associated transient spray resulting from an HRAM event.

## 1.2 Research Goal

The overall research goal is to determine the relationship and driving mechanism between HRAM cavity features to the resulting transient spray via the penetration orifice. This goal is divided into focused objectives contributing to the completion of the overall research goal. The objectives are: *determine entrainment portion of cavity composition, determine cavity features and characteristics contributing to the transient spray, develop a physics and empirical-based relationship to the cavity parameters contributing to the transient spray*. Completion of all objectives will utilize spherical projectiles for data collection and analysis.

Literature review and preliminary experiments identified specific measurements for this research. Experimental observations showed the cavity had very distinguishable features such as cavity volume, diameter, and length, while corresponding changes in projectile velocity were calculated. Furthermore, mass entrainment, cavity contraction, and cavity separation were observed at specific times within the experiment. Measuring these features provided insight between the HRAM cavity dynamics and transient spray relationship ultimately completing the research objectives.

Velocity and projectile mass significantly affected cavity formation. The formed cavity volume also changed as projectile velocity and mass varied. Additionally, the projectile's geometry was fixed as a sphere to generate axial symmetric cavities along the projectile shot-line. Axial symmetric cavities are needed to lend credence to the assumption of axial symmetry for the cavity. By assuming axial symmetry, cavity volume is then calculated from a single image.

Flat-nosed and ogive projectiles are more prone to tumble, causing the projectile to veer from the shot line. Deviation from the shot line results in non-symmetric cavities, which are difficult to measure accurately, even with more than one camera. Measurement of the properties necessary to complete the overall research goal is detailed below.

### ***1.2.1 Objective I.***

The vapor composition of an HRAM cavity prior to this research was unknown. To calculate the cavity composition, the development of an image acquisition technique to measure the entrainment flow field velocity was needed. Accurately measuring the flow field velocity was required to calculate the volumetric and mass flow rate into the HRAM cavity. Since the time-resolved PIV techniques for obtaining the data had not been applied to this problem, or any similar flow field problems, development and implementation of these techniques were part of the overall contribution to this field of study.

Once the time-resolved PIV technique was implemented, it was possible to infer the entrained flow field via the orifice from the measurements. Application of Antoine Lavoisier's conservation of mass law reveals the gaseous mass in the cavity has the potential to come from two sources: vaporized surrounding fluid or entrained ambient air from outside the tank. Orifice flow equations were used to calculate the entrained mass of ambient air assuming negligible density changes at the penetration orifice. Utilizing the ideal gas law and conservation of mass, a calculation was possible for determining the cavity composition and its partial pressure. Under the appropriate circumstances, approximating the cavity pressure from the entrained air provided additional information with regards to vaporization of the surrounding fluid.

### ***1.2.2 Objective II.***

Previous research had not collected synchronized imagery for the purpose of correlating interior cavity dynamics and the resulting transient spray. Partnerships with the 96<sup>th</sup> Test Group enabled collecting qualitative HRAM data to scope the research and identify the necessary cavity dynamics to model or predict. The research determined which HRAM cavity dynamics or features must occur prior to the transient spray event. Based on the qualitative findings, the research focused on the cavity contraction and separation phases of the HRAM event.

Testing further identified the volumetric inflection point as indicative of the maximum cavity growth rate. Mathematically, the volumetric inflection point corresponded to when the cavity growth rate changes sign. Physically, the volumetric inflection point indicated when something in the system changed to limit the growth rate. Complete cavity contraction at the orifice occurred after the inflection point.

Additionally, entrainment data from Objective I, when combined with internal cavity imagery, provided further insight into the mass flow properties and the influence of cavity geometry. Treating HRAM as a fluid flow problem has its advantages and disadvantages. An advantage is fluid flow research is well established and developed with regards to velocity profiles, mass continuity, and cavitation. HRAM is a transient event and is far from reaching any form of steady state. Hence, high-speed imagery over the duration of the event permitted the ability to analyze the fluid flow as a transient system during the HRAM event. Therefore, the need exists to identify consistent cavity properties and features to relate the transient flow across the HRAM cavity domain regardless of impact velocity. Finding consistent HRAM cavity properties and relationships provide researchers with the ability to focus resources and improved understanding of the phenomenon.

### ***1.2.3 Objective III.***

Empirical models predicted transient spray using mathematical techniques to curve fit the empirical data. Computational models attempt to account for the physical changes in the system but use broad generic assumptions such as cavity mass composition. The model, based on initial projectile properties, applies to a relatively narrow set of HRAM conditions. By utilizing the results from the aforementioned objectives, an empirical model was developed to predict HRAM cavity's geometric features. This empirical model utilized projectile kinetic energy as a basis for prediction. Additionally, the process of relating cavity pressure work back to projectile kinetic energy was introduced and the additional terms to complete the relationship were identified. Developing an energy

transmission relationship between the projectile kinetic energy to cavity pressure work will form the basis for understanding the physical mechanisms and potentially move away from empirically fit models.

When the projectile impacts the tank, it begins to exchange its kinetic energy with its surroundings. As the projectile travels through the fluid, a low pressure cavity is formed in its wake. Using a first-principles approach may provide the foundation for continued research to expand the model and account for a broader range of impact parameters. By measuring the cavity's volume and utilizing measurements from Objective II, the cavity's energy, or pressure work, is calculated.

HRAM research has characterized the cavity formation and some of the dynamics of the cavity event [6–8]. However, cavity contraction and collapse research is needed to further understand the physics of the event and its relationship to the transient spray. Measurement of cavity dynamics included the projectile kinetic energy, cavity volume, cavity energy, and mass flow through the orifice. Measuring these parameters provided an overview of the observed event and permitted analysis of additional measurements to complement and determine the driving mechanisms.

In summary, the overall research goal is to determine the relationship between HRAM cavity entrainment, cavity dynamics, and the resulting transient spray phases. Through the research process, discoveries were made contributing the advancement of the HRAM knowledge. These findings enable the development of physical and empirical relationships between cavity geometry, mass flow, and projectile kinetic energy to predict cavity contraction at the orifice for a range of impact velocities.

## II. Previous Work

THE work proposed here is based on a foundation of previous studies completed by other researchers in various and related fields. Research on hydrodynamic ram (HRAM) spans the spectrum from numerical modeling to empirically collected and analyzed data. Understanding the process of cavity formation is critical to understanding the dynamics of cavity collapse. This literature review will provide details on HRAM history, cavity formation, cavity dynamics, and experimental processes developed for measuring a cavity during an HRAM event. The goal of this chapter is to convey the completed research and remaining areas of research needed to advance the science and complete the objectives stated in Chapter I.

### 2.1 Brief HRAM History

HRAM causes damage to aircraft via two damage mechanisms: pressure fluctuations damaging critical aircraft structures and the atomized liquid spurt creating a higher probability of on-board fire. Historically, HRAM events were investigated to prevent catastrophic failure of aircraft fuel cells subjected to ballistic impact [6]. The structural damage resulting from the pressure fluctuations was the primary concern during an HRAM event. Several researchers have characterized the pressure fluctuations resulting from HRAM and have designed aircraft systems to mitigate the damage [5, 9, 10].

The transient spray from an HRAM event has distinct phases and was first characterized by Disimile *et al.* [1]. Recently developed requirements to determine the relationship of an HRAM event to the transient spray have become a priority. The requirement to understand this phenomenon is needed for both military and commercial applications. Tragic accidents from military aircraft to civilian aircraft, such as the

Concorde accident in 2000, potentially have HRAM as contributing factors in their loss [11].

For example, HRAM was a possible contributing factor on 25 July 2000 when Air France flight 4950, and all on board perished. A DC-10, while taking off, left a piece of debris on the same runway as Concorde flight 4950 used for takeoff. The piece of debris ruptured the Concorde's tire sending large chunks of rubber into the underside of the aircraft's wing at speeds exceeding  $100\text{ m/s}$ . The impacting rubber caused large pressure fluctuations in the tank potentially causing fuel leakage and contributing to the aircraft's fire. Ultimately the pilot and the crew could not overcome the circumstances to safely recover the aircraft and its passengers [11].

## 2.2 HRAM Cavity Dynamics

Ball separates the HRAM event into 3 phases: *entry phase*, *drag phase*, and *cavity phase* [4]. However, for this research effort, the cavity phase is further separated into 4 additional phases: *cavity formation phase*, *cavity contraction phase*, *cavity separation phase*, and *cavity collapse phase*. The cavity formation phase begins when the projectile enters the fluid. During the cavity formation phase, the cavity's diameter at the orifice increases until it reaches its maximum and begins to decrease and transition to the cavity contraction phase. The cavity contraction phase begins when the cavity begins to constrict and close around the penetration orifice. When the cavity constricts around the orifice, it forms a re-entrant jet where the water mixes with the incoming air mass flow. The cavity separation phase occurs after the cavity has constricted the flow at the orifice and begins to separate and move away from the orifice. After cavity separation, the cavity collapses and sends pressure waves through the fluid [5]. The cavity contraction and separation phases are critically important when predicting the transient spray in addition to understanding the entrained mass flow characteristics [20, 41]. The introduction of the additional cavity

phases identified distinct internal cavity characteristics and features for precise discussion during this research effort.

Research by Campbell and Hilborne focused on the air entrainment in artificially inflated cavities. The research was conducted in a water tunnel, by pumping air through a disk cavitator. The resulting cavity, in the moving water, had an internal pressure above the atmospheric pressure. This setup and research is different than an HRAM event, but important ideas about cavity composition translate to the HRAM regime [12].

Campbell and Hilborne's research yielded volumetric flow data to generate stable cavities for a range of cavitation numbers. The cavity pressure also varied based on the air's volumetric flow rate into the cavity. Depending on the air's volumetric flow rate, and the cavity's pressure, different cavity behaviors were observed. For a relatively high cavity pressure, the cavity closure behaved like a trailing vortex. For a relatively low cavity pressure, the cavity closure behaved like a re-entrant jet [12].

Campbell and Hilborne's research is similar to HRAM research in air is also entrained into both types of cavities. The researchers controlled the air's volumetric flow rate behind the cavitator and measured the corresponding pressure. However, during the HRAM event, the entrainment is not controlled through the penetration orifice. Although these differences exists, this research showed cavity composition and pressure affects the cavity closure. Therefore, cavity composition can influence cavity dynamics.

Previous research has predicted cavity formation in terms of size relative to impact parameters. The Guo *et al.* cavity model reasonably predicted the cavity formation phase and the beginning of cavity pinch off and correlated the timing back to the experimentally observed data [6]. However, it is not known if the model accurately predicts the entire cavity contraction phase. Also, the Guo *et al.* model did not make any prediction on the transient spray phases as described by Disimile et al [1]. Therefore, additional research to determine the relationship between the cavity contraction and separation phases is needed.



HRAM cavity dynamics are reasonably well understood from the entry phase to the cavity formation phase. Beyond the cavity formation phase, little is understood and published on the cavity contraction phase and the separation phase. Consequently, additional research is needed to determine the fluid discharge properties and the associated physics and driving mechanisms resulting from the cavity collapse. Therefore, this research attempted to determine the physics and mechanisms driving the cavity contraction and subsequent separation phase, as well as how those phases contributed to the transient spray.

### 2.3 Characterizing HRAM Cavity Formation

An HRAM event for a given projectile velocity will vary based on the impact conditions and the fluid in the tank. However, the link between cavitation, HRAM events, and the different areas of research is the cavitation number. The cavitation number, represented by  $\sigma$ , is related specifically to the fluid's vapor pressure and is shown in Eq. 2.1 [13]

$$\sigma = \frac{P_0 - P_v}{\frac{1}{2}\rho_f V_f^2} \quad (2.1)$$

where  $P_0$  represents the atmospheric and fluid pressure at the impact location,  $P_v$  is the fluid's vapor pressure,  $\rho_f$  is the fluid density, and  $V_f$  is the characteristic fluid velocity, which is typically assumed as the projectile velocity. Therefore, the cavitation number provides a dimensionless parameter to relate HRAM events in water to HRAM events in other fluids.

The process of developing a cavity is related to the projectile impact velocity, density, shape, and coefficient of drag. Researchers have developed numerically simulated and empirically correlated models based on the underlying physics of the problem. The connecting factor between models is the cavitation number as shown in Eq. 2.1. However, what is unknown is the cavity composition resulting from an HRAM event. It is assumed the cavity consists of a mixture of entrained ambient air and vaporized local fluid [14].

Various models developed by researchers applied the cavitation parameter differently. Hoerner showed how the coefficient of drag,  $C_d$ , is a function of cavitation number such that:

$$C_d = C_{do}(1 + \sigma) \quad (2.2)$$

where  $C_{do}$  is the drag coefficient of the projectile at entry. However, an HRAM event occurs at very high impact velocities such the cavitation number had negligible influence on the drag coefficient per Eq. 2.2. This resulted because  $V_f^2$  was of sufficient magnitude the overall cavitation number is very small and usually much less than 0.1. Hence, the drag coefficient is approximately equal to  $C_{do}$ . Previous research has successfully used Eq. 2.2 to predict projectile position and velocity changes, but only assumed the energy transfer from the projectile to cavity was sufficient to generate the cavity. The in-depth analysis to determine the projectile energy transfer rate to cavity pressure-volume work was not accomplished [13–15].

### 2.3.1 Cavity Formation for Spherical Projectiles.

A physics based model for spherical projectiles entering a horizontal tank was developed by Lecysyn *et al.* [6]. The model was verified with experimental data through the use of high-speed imagery. The Lecysyn *et al.* model provided the time rate of growth for the cavity and is shown in Eq. 2.3 below:

$$r_c(t + dt) = r_c(t) + \Delta t \sqrt{A \frac{u_{p0}^2}{r_c^2(1 + Bt)^2} - 2gh} \quad (2.3)$$

where  $r_c$  is the radius of the cavity,  $u_{p0}$  is the projectile velocity before impact, and  $h$  is the height of liquid at shot level. A and B are constants defined below in Eq. 2.4, Eq. 2.5 [6].

$$A = \frac{d_p^2}{4(1 + \sqrt{\rho_l/\rho_p})} \quad (2.4)$$

$$B = \frac{3u_{p0}C_d\rho_l}{4\rho_pd_p} \quad (2.5)$$

where  $d_p$  is the projectile diameter, and  $\rho_l$  and  $\rho_p$  are the respective liquid and projectile densities.

The Lecysyn *et al.* model essentially used the projectile's initial kinetic energy, and fluid properties to predict the cavity's radial growth. The model provided critical information applicable to the current research. First, the model provided the cavity dimensions for a spherical projectile. Second, the model showed cavity dimensions are related to the projectile and fluid properties. Understanding the cavity dimensions, and the rate of growth of the cavity ( $\mu_c$ ), is critical before attempting to determine the cavity contraction relationship. The experimental setup utilized high-speed imagery and a light diffusing screen to measure crater diameters. This experimental setup provided a reasonable foundation for the equipment required to measure cavity dimensions. Section 2.7 provides additional information on the type of equipment and techniques needed to measure the HRAM events.

### **2.3.2 Cavity Formation Based on Projectile's Caliber-Radius-Head.**

Guo *et al.* developed a cavity model based on cylindrical projectiles with different nose shapes [7, 8]. The different nose shapes were characterized via the projectiles' caliber-radius-head (CRH) value. CRH values varied based on the curvature of the projectiles nose. For example, a CRH value of zero correlated to a flat nose projectile. A CRH value of  $\frac{1}{2}$  correlated to a hemispherical nose projectile.

The CRH value was a significant factor in the overall drag coefficient,  $C_d$ , for the projectile as presented in Eq. 2.9. Change in the  $C_d$  affected the velocity and deceleration of the projectile as it moved through the fluid. The change in  $C_d$  resulted in different cavity growth rates,  $\mu_c$ , and cavity dimensions at different instances in time. However, it is not clear if the Guo *et al.* model shown in Eq. 2.6 is applicable or capable of modeling cavity formation from spherical projectiles as accomplished by Lecysyn *et al.* [6]. The primary

reason is the coefficient of pressure drag ( $C_p$ ) was different for a sphere as compared to a cylindrical rod with different nose shapes.

Equations 2.6 through 2.8 represents the Guo *et al.* cavity formation model [8].

$$R^2 = \alpha R_0^2 + 2R_0 \sqrt{A + B \exp(-2\beta x_p)} K v_0 (t - t_0) - K^2 v_0^2 (t - t_0)^2 \quad (2.6)$$

where  $\alpha$  is a correction factor for different nose shapes,  $R_0$  is the projectile radius, and  $v_0$  is the initial projectile velocity.  $K$  is the cavity size at the projectile head.  $A$  and  $B$  are two points in the fluid, where  $A$  is at the cavity surface and  $B$  is far away where there is no fluid motion at penetration distance  $x_p$  as shown in Eq. 2.7:

$$x_p = \frac{1}{\beta} \ln(1 + \beta v_0 t) \quad (2.7)$$

where  $x_p$  is a function of the projectile impact velocity,  $v_0$ , and projectile properties represented by  $\beta$  shown in Eq. 2.8:

$$\beta = \frac{\rho A_0 C_d}{2m} \quad (2.8)$$

where  $\rho$  is the projectile density,  $A_0$  is the effective projectile area,  $m$  is the projectile mass, and  $C_d$  is the effective coefficient of drag as shown in Eq. 2.9:  $C_d$  is obtained via Eq. 2.9:

$$C_d = (D_1 + D_2 \exp(-D_3 \Pi)) \left( 1 + (D_4 + D_5 \Pi) \frac{v_0^2}{v_c^2} \right) \quad (2.9)$$

where  $D_1$ ,  $D_2$ ,  $D_3$ , and  $D_4$  are experimentally determined constants resulting from fitting the drag coefficient data using a least squares method.  $\Pi$  is the CRH value,  $v_0$  is the initial projectile velocity, and  $v_c$  is the speed of sound in the fluid.

This model can theoretically predict the cavity radius and position ( $x_p$ ) at any point along the shot line. This was accomplished through adjusting the reference time scale by using the associated velocity at the desired reference point. However, the parameters  $D_1$  through  $D_4$  are experimentally determined. Therefore, the model's  $C_d$  in Eq. 2.9 is forced to fit the experimental data without an understanding of the physics behind  $D_1$  through  $D_4$ .

Hence, caution is needed when applying the model outside of the experimentally tested conditions.

The different cavity models provided insight into the different ways characterization of HRAM cavity dynamics was accomplished. It is critical to understand the differences and applications of the cavity models to competently apply them to the proposed research. Each of the models focused on the dimensions of the cavity rather than the work performed by the projectile on the system. Additionally, the models used empirically determined coefficients from experimental data without a full description of the parameters' physical significance.

To understand the pressure-volume work, a measurement of the cavity composition was needed. Therefore, the models presented here adequately functioned within the bounds for which they were created but do not provide insight into the overall relationship between the projectile kinetic energy and the pressure-volume work performed on the liquid. Hence, the techniques required to take the time resolved orifice entrainment measurement needed development to approximate the cavity composition.

## **2.4 Characterizing HRAM Pressure-Volume Work and Cavity Collapse**

The collapse of an HRAM cavity is a relatively new research area in the fluids field. Initial research into the HRAM cavity was focused on predicting the resultant pressure waves and associated damage to the fluid filled structure, but did not focus on the energy it takes to form the cavity. Bless, Cardea, and Fourest *et al.* assumed the kinetic energy was transferred from the projectile to the fluid and caused the observed HRAM cavity [15–17]. Each researcher took different approaches to predict the cavity collapse and how the pressure can cause damage to the surrounding structure.

Bless utilized empirical data to compute failure constants related to tank and projectile impact conditions as shown in Fig. 2.1. In Fig. 2.1 the failure and safe regions for two different projectile masses and two different impact velocities were plotted. The region

below the extrapolated line is considered safe while the region above the line corresponds to tank failure. Fitting the curve between the data points permitted calculation of constants to build a model to approximate conditions for tank failure due to HRAM effects. These predictions provided a focus for tank design to mitigate the HRAM pressure effects [16].

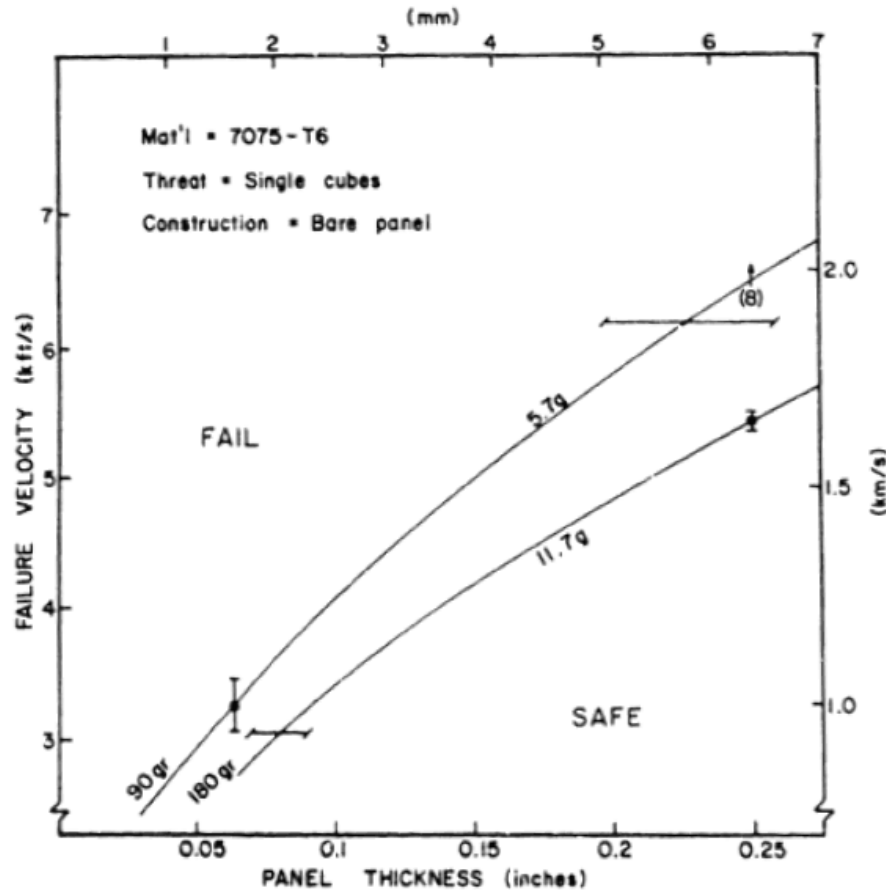


Figure 2.1. Design summary for bare 7075-T6 aluminum panels struck by single cubical fragments. Failure velocity versus panel thickness for various mass fragments, based on  $\frac{v^2 D}{W} = 5.19 \frac{km^2}{s^2}$  where  $D$  is the sphere diameter or cube edge and  $W$  is the panel thickness. This figure was re-printed from “Fuel Tank Survivability for Hydrodynamic Ram Induced by High Velocity Fragments: Part I. Experimental Results and Design Summary” [16].

Cardea's research drew a relationship between underwater explosion models and observed HRAM cavities. The proven underwater explosion models were used to show the projectile had sufficient kinetic energy to form the observed cavities. Additionally, the underwater explosion models were also used to predict the oscillations of the HRAM cavity's collapse, subsequent rebound and the associated radii.

Other research used a computational approach to describe the HRAM cavity. Fourest *et al.* used the confined Rayleigh-Plesset equation to predict cavity dimensions during HRAM cavity collapse and rebound [17]. To improve the computational models, knowledge of the system behavior, such as mass flow, is needed. More so, knowledge of the energy transmission rates from the projectile into the cavity pressure-volume work can provide higher fidelity results in both the experimental and computational research.

The previous research showed the projectile's kinetic energy lost to the fluid is sufficient to cause the observed HRAM cavity. Although the cavity composition is unknown, earlier work predicted the cavity collapse for a given cavity energy. However, a disconnect existed between the energy transmission rate from the projectile to the formed cavity. More simply put, the rate the projectile's kinetic energy is converted into pressure-volume work was unknown and requires additional research.

Disimile *et al.*'s research quantified the fluid's pressure profile during an HRAM event. The research focus was to determine the pressure profile and determine potential HRAM mitigation solutions in industrial and aircraft tank design. However, during the research, it appeared a pressure transducer measured the internal pressure of the HRAM cavity. The plots showed a negative relative pressure measurement indicating measurement of the internal HRAM cavity's pressure. Disimile *et al.* did not specifically write about the negative pressure measurement since the focus of the article was measuring the relatively large pressure fluctuations causing tank damage [5].

Interestingly, the negative pressure measurement spawned the idea to treat the HRAM cavity as pressure-volume work resulting from the projectile's kinetic energy. To determine the pressure-volume work performed on the system, the cavity composition and pressure are needed. Previous research did not make an attempt to predict HRAM pressure-volume work. A technique to measure the entrained flow rate via the penetration orifice was developed to overcome this experimental hurdle and provide insight into the cavity composition [41]. If the previous research had orifice entrainment measurements, computation of the entrained gas's mass would have been possible and may have provided further insight into the energy transmission rate.

## **2.5 Hypothesis on the Effect of Different Projectile and Fluid Properties**

Research has shown projectile geometry and kinetic energy affected the size and rate of cavity formation during an HRAM event [6, 8, 16]. Cavity contraction was expected to have a direct relationship to the kinetic energy of the projectile and the rate it transferred the energy to the fluid. However, previous work has not determined the energy transfer mechanism between the projectile's kinetic energy to the cavity's pressure-volume work. It is not clear how the different projectile geometries and fluid properties would impact the overall physics and driving mechanism during the cavity formation, contraction, and separation phases but the different geometries and fluid properties were expected to have an influence based on work by May [14, 18].

Consistent cavity formation was needed for experimental purposes to generate axial symmetric cavities for measurement. Symmetric cavities were needed to initiate the determination of the energy transfer process. It is expected the projectile's kinetic energy, the overall system  $C_d$ , and fluid properties will relate to the cavity contraction and separation phase because each of these parameters affected the drag forces and hence the overall kinetic energy depletion rate. Additional undetermined mechanisms may have driven the rate of cavity contraction, separation, and collapse such as fluid momentum,



pressure head, vapor pressure, and fluid motion. Since prior research had not addressed the relationship between projectile kinetic energy and the cavity phases, this work focused on determining the basic relationship while acknowledging additional research into projectile and fluid properties is needed.

## **2.6 Characterizing the Transient Spray resulting from HRAM**

Prior research indicated the transient spray event will begin around 3 to 15 *ms* after projectile impact [1, 5, 19, 20]. The difference in timing is expected to depend on the cavity dynamics mentioned in the aforementioned research. The remaining transient spray phases were expected to occur or overlap as observed by Disimile *et al.* [1].

Traditional testing of the relationship between HRAM and transient spray utilized precision timing, high-speed cameras, and various projectile properties and impact conditions. Researchers varied properties such as projectile size, density, velocity, and angle of obliquity and measured the timing of the subsequent transient spray events. However, the cavity dynamics occurring inside the tank relative to the transient spray outside the tank is unknown [2].

Part of this research effort was to move away from the time domain and measure what was happening inside the tank while observing the transient spray outside the tank. Shifting the reference frame away from the time domain enabled research on specific cavity properties and enabled discovery of the driving mechanisms behind the HRAM cavity dynamics. Projectile kinetic energy was one of the anticipated driving mechanisms behind the cavity dynamics contributing to the transient spray. Additionally, prior research did not measure entrained gas composition in the cavity.

This research will focus on measuring the cavity's entrained gas composition. A deeper understanding regarding the pressure-volume work relationship between the projectile and the cavity is obtained by measuring the entrained gas composition.

Understanding the pressure-volume work and kinetic energy relationship will enable a quasi link to the cavity's geometry and mass entrainment during the HRAM event.

## 2.7 Measuring HRAM Cavity Dynamics

Measuring HRAM cavitation events was not insignificant with projectile velocities upto 176  $m/s$ . High-speed imagery for data collection was an appropriate method. However, attention to detail for developing the proper triggering, timing, back-lighting, and laser illumination was just as important in order to collect useful data. The Lecysyn *et al.* and the Guo *et al.* experimental processes used high-speed imagery with sectioned back lighting [6, 8]. This application produced results necessary to characterize the cavity formation. Additionally, developments requiring brightfield imaging and time-resolved PIV were needed to measure the projectile position and entrained flow field velocity.

Calculating the projectile's kinetic energy was accomplished by measuring the projectile's relative position to the orifice in the high-speed imagery. The projectile's position was measured by using the pixel location and the necessary camera calibration images to relate the pixel values to units of length. The camera's frame rate was used as the source for time. The position information was detected using a multi-dimensional tensor along the projectile's shot line [21]. The position information was recorded and used to fit a second-order polynomial to issues associated with pixel locking. Pixel locking occurs when the signal is biased towards the nearest pixel value [22]. For example, the true projectile position location is a continuous signal, however the position measurements refer to a pixel location where the leading edge of the projectile is detected. Since the true projectile position can occur between or within pixels, pixel locking occurs when the true position is rounded up or down to the nearest pixel and provides an integer response for an otherwise continuous signal.

A second-order polynomial was selected after observing the trend in the raw positional data as shown in Fig. 2.2. The fitted polynomial adequately predicted the position data

with R-squared values exceeding 96%. Curve fitting to discrete pixel values is a practiced PIV technique to avoid pixel locking for integer responses [22] and enables continuous calculations and derivatives from the measured positional data. The fitted function avoids problems with pixel locking and permits the continuous derivation of the positional data to determine the projectile's velocity and acceleration. Realistically, the second-order polynomial cannot predict the entire projectile position and velocity profiles. Regardless, the polynomial was sufficient for predicting the projectile kinematics within the relatively narrow window of time where cavity formation, contraction, and separation occur.

The position plots in Fig. 2.2 indicated over the cavity formation phase, the velocity decay was linear and the acceleration was relatively constant. Figure 2.3 by Zhao shows the velocity of an axisymmetric slender body traveling through water indicating a relatively linear velocity decay. The linear velocity decay of the slender body supports the second-order form of the measured position data. Additionally, similar findings corroborating the second-order nature of the projectile positional data were accomplished by Aristoff and Zhao [23, 24].

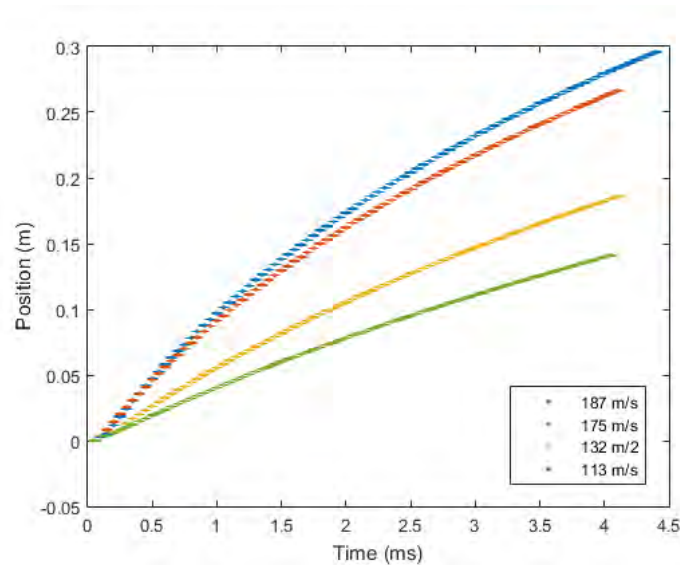


Figure 2.2. Measured Position Information for specified muzzle velocities.

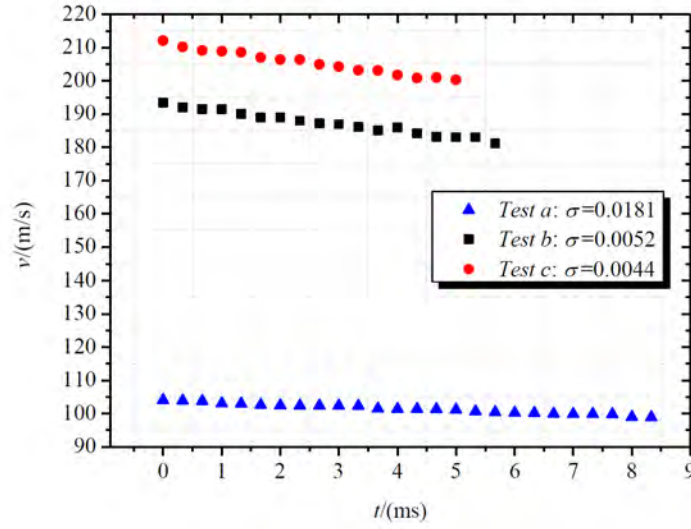


Figure 2.3. Velocity profile for axisymmetric slender body traveling through water [24]. The linear velocity decline supported the second-order nature of the position data collected for spheres for a short time duration after initial penetration. This figure is intellectual property and re-printed with permission from Cheng-Gong Zhao.

Using the measured positional information and the calculated velocity decay, the initial kinetic energy of the projectile was:

$$KE(0) = \frac{1}{2}m_p V_P(0)^2 = KE_0 \quad (2.10)$$

where  $V_P(0)$  is the initial penetration velocity of the projectile, and  $m_p$  is the mass of the projectile. The kinetic energy of the projectile at any time,  $t$ , is shown in Eq. 2.11 by using the vector equation, along the Cartesian coordinate system, for kinetic energy

$$KE(t) = \frac{1}{2}m_p[V_{P_x}(t)^2 + V_{P_y}(t)^2 + V_{P_z}(t)^2] \quad (2.11)$$

where  $V_p$  is the velocity of the projectile along the respective  $x$ ,  $y$ ,  $z$  components of the Cartesian coordinate system at any time  $t$ . By rearranging Eq. 2.10 and 2.11 the change in kinetic energy was obtained as shown in Eq. 2.12

$$\Delta KE(t) = \frac{1}{2}m_p V_P(0)^2 - \frac{1}{2}m_p[V_{P_x}(t)^2 + V_{P_y}(t)^2 + V_{P_z}(t)^2] \quad (2.12)$$

where the change in kinetic energy shown in Eq. 2.12 represents the total amount of kinetic energy dissipated to the surrounding fluid.

Experiments were designed to use spherical projectiles to generate axisymmetric cavities and minimize the  $y$  and  $z$  component of the projectile velocity vector. Since the  $y$  and  $z$  component were not utilized during this analysis, many of the above equations simplify. Utilizing the  $x$  component of Eq. 2.12 and the change in velocity information along the horizontal axis, the total kinetic energy dissipated to the system was simplified and shown in Eq. 2.13

$$\Delta KE(t) = \frac{1}{2}m_p V_0^2 - \frac{1}{2}m_p V_P(t)^2 \quad (2.13)$$

where  $\Delta KE(t)$  is the amount of kinetic energy lost by the projectile to the fluid. Now the changing projectile's kinetic energy is studied with respect to the cavity's volume and entrained mass calculations.

## 2.8 HRAM Cavitation Mechanisms

By definition, cavitation is the formation of vapor cavities in liquid [13]. In mechanical systems, such as pumps and propellers, the location of cavitation is isolated such the cavity's composition is assumed to consist primarily of vaporized local liquid. Cavitation during an HRAM event is unique because the formed cavity can source its mass from two locations: local fluid or ambient gases through the penetration orifice [14, 25].

Brandner *et al.*'s research saw sheet vaporization of local fluid for spheres in a water tunnel start at cavitation numbers as high as 1 and became more pronounced as the cavitation number decreased [26, 27]. The free stream velocity in the water tunnel was 12.6  $m/s$ , which is much lower than the 111 to 176  $m/s$  projectile velocities in the HRAM event indicating cavitation from fluid separation is possible. The cavitation bubbles generated by sheet cavitation collapsed within a few diameters of formation and were unable to sustain its volume relative to a much larger observed HRAM cavity volume. HRAM cavitation numbers typically were very low and much less than unity indicating

local fluid vaporization was possible for the impact conditions. However, the cavity volume differences between Brandner *et al.*'s research and an HRAM cavity are significant indicating additional mass sources were needed to compose the HRAM cavity.

Mass entrainment via the penetration orifice was another mass source, other than local fluid vaporization, for cavity composition [14]. Mass entrainment for artificially inflated cavities was dependent on projectile dynamics, cavity pressure, and ambient air pressure [14, 18]. Campbell and Hilborne's experiments used disk cavitators submerged in water tunnels at velocities ranging from 4.2 to 7.6  $m/s$ , where air was supplied at known pressures to generate a trailing cavity. The cavitation number ranged from 0.04 to 0.125 for disks ranging in diameter from 0.5 to 1.0 inch. Generally, as the cavitation number decreased, an increase in the mass flow rate was needed to inflate the cavity [12]. The cavities formed had similar sizes and closure properties as compared to HRAM cavities. Applying the research to HRAM cavities, as the velocity of the projectile increased, the mass needed to satisfy cavity growth must increase. However, the mass flow of gases for a ballistically-induced cavity must flow through an orifice created by the projectile. Consideration of orifice flow characteristics, limitations, and properties needs additional research.

Thinking about ballistically-induced HRAM as a transient event, a qualitative prediction of the process is formulated. Upon entry, the pressure region behind the projectile is the lowest pressure source in the system. Projectile velocities generated the fluid separation conditions to vaporize local fluid based on cavitation number and previous work [13, 26–28]. The vaporized fluid alone was not sufficient to generate the observed cavity volumes. Entrained gases provided additional mass necessary to form the observed cavity volumes at pressures potentially much larger than the fluid's vaporization pressure [25]. If the entrained air mass can raise the total cavity pressure above the fluid's vaporization pressure, the cavity would likely consist of primarily entrained air and vaporized local liquid caused by fluid separation near the projectile. If the entrained

air mass cannot bring the cavity pressure above the fluid's vapor pressure, vaporization of the local fluid could occur across the liquid-cavity interface in addition to the liquid vaporized from separation near the projectile surface. Determination of the flow through the projectile penetration orifice is needed to determine the relative mass composition, and the associated partial pressure for the HRAM events. Using published research, a hypothesis is generated for the 3 mechanisms of mass transfer into the HRAM cavity. The 3 mechanisms are: orifice entrainment, vaporization of the local fluid across the liquid-cavity interface, and vaporization of the local fluid from separation cavitation occurring close to the projectile's surface as detailed by Brandner *et al.* and Washio [26–28].

## 2.9 Computational Modeling of HRAM

Computational HRAM modeling research has focused on characterizing the pressure fluctuations and associated tank deformations. Varas *et al.* collected pressure data from an HRAM event and built the associated models using the empirical pressure measurements as a reference [9, 10, 29]. The application of these models is sufficient at predicting tank pressures and deformations within the experimental bounds. One model even considered the transfer of energy from the projectile to the fluid and then from the fluid to the tank [29]. However, the model showed most of the energy was related to the fluid's velocity. Additionally, the internal composition of the cavity was assumed to consist of primarily air and was modeled using a linear polynomial equation of state [9]. Varas *et al.*'s pressure models did not predict the physics of liquid spurt or the causes of the transient spray. Also, the model did not measure the energy transmission mechanisms, or attempt to predict any of the cavity formation, contraction, separation phases.

Only recently has the modeling and simulation community focused on predicting the transient spray [3]. Current research efforts need additional data to refine the ability to model the multiphase fluids to completely solve for the conservation of mass and increase the fidelity of the models. For simulated 300 *m/s* impact velocities, the cavity was below

the fluid's vapor pressure, and the vaporization of liquid proceeded via the cavity liquid interface [3].

The simulated transient spray results occurred at times,  $0.2\text{ ms}$ , much shorter time duration than other published data, which occurred in the range of 2 to  $15\text{ ms}$  [1, 3]. Additionally, the cavity contraction and separation phases also occurred much quicker than the observed experiments [3]. By measuring and providing the mass flow of entrained air, an additional parameter was provided for the modeling and simulation community to include in their research.

The computation modeling of the HRAM phenomenon also used various codes such as Smooth Particle Hydrodynamics (SPH), Arbitrary Lagrangian Eulerian (ALE), and Multiphase and Multiphysics Code (CFD-ACE+) [3, 9]. Each code made different assumptions or approximations for internal cavity composition. However, only Yang *et al.* attempted to predict the initiation of the transient spray phases [3]. Additionally, each model used different approximations as to the internal cavity composition and mass. Therefore, any data providing the entrained mass flow rate can enhance the models results and potentially improve their fidelity.

## **2.10 Orifice Flow Equations**

Little research is published on the flow of ambient air through an orifice formed by projectile penetration and into the HRAM cavity. Some research was completed on the tank pressure generated by projectiles, but the focus of the research was not on the pressure or gas composition inside the HRAM cavity [5]. Additionally, the composition of the cavity with respect to air and vaporized liquid also requires additional research. Therefore, the experimental process was developed to obtain the time resolved flow field measurements from external ambient air, through the orifice, and into the HRAM cavity. To utilize these measurements, and make sense of the data relative to orifice flow, empirical formulas and relationships for similar orifice and pipe flow conditions are utilized.



An orifice is typically used in a pipe to measure pressure loss to facilitate flow velocity or mass flow computations. The orifice reduces the cross-sectional area of the pipe but usually the pipe diameter is the same upstream and downstream of the orifice. In some cases, the pipe has a gradual contraction and expansion, such as a venturi, to minimize system losses. Orifice flow during an HRAM event did not follow these typical characteristics. During an HRAM experiment, the flow across the orifice experienced a sudden contraction and sudden expansion. Losses due to sudden contraction were derived from conservation of momentum and continuity of flow for incompressible fluids [30]. Gibson's relationship was derived to provide the system losses in terms of head loss rather than a resistance coefficient. Gibson's derivation determined the head loss coefficient in terms of an area ratio for a rapidly expanding pipe in Fig. 2.4 and is shown in Eq. 2.14 through Eq. 2.24.

The following is Gibson's derivation for head loss in a rapidly expanding pipe modified from "Hydraulics and its Applications [30]". The fluid velocity, pressure, and area in the small and large cross sections of pipe in Fig. 2.4 are represented by  $V_1$ ,  $A_1$ ,  $P_1$  and  $V_2$ ,  $A_2$ ,  $P_2$ , respectively.  $P'$  is the pressure on the end of the pipe approximately at cross section EE shown in Fig. 2.4. Neglecting frictional effects and compressibility of the fluid, the force to produce a momentum change in the direction of flow is represented by Eq. 2.14.

$$P_1 A_1 + P'(A_2 - A_1) - P_2 A_2 = \frac{W A_2 V_2^2}{g} - \frac{W A_1 V_1^2}{g} \quad (2.14)$$

where  $g$  is the acceleration due to gravity, and  $W$  is the weight of the fluid. Gibson assumed  $P'$  over the face of the plate was equal to  $P_1$  based on experimental data. Equation 2.14 is now simplified to:

$$(P_1 - P_2) A_2 = \frac{W}{g} (A_2 V_2^2 - A_1 V_1^2) \quad (2.15)$$

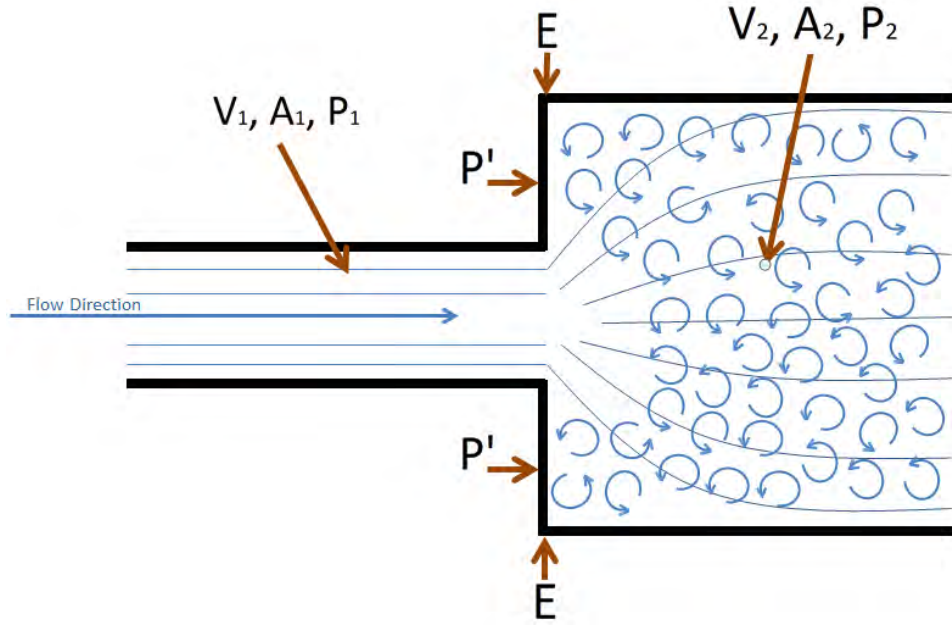


Figure 2.4. Cross section of rapidly expanding pipe used for reference for Eq. 2.14 through 2.24 modified from “Hydraulics and its Applications [30]”.

The continuity equation solved for  $V_1$  for incompressible flow is shown in Eq. 2.16

$$V_1 = \frac{A_2 V_2}{A_1} \quad (2.16)$$

Using Eq. 2.16 and substituting for  $V_1$ , Eq. 2.15 becomes:

$$(P_1 - P_2)A_2 = \frac{W}{g} \left( 1 - \frac{A_2}{A_1} \right) V_2^2 A_2 \quad (2.17)$$

If the Bernoulli equation were used while neglecting gravity, and using  $H$  to represent the head loss at the expansion of the pipe, the equation takes the form:

$$\frac{P_1}{W} + \frac{V_1^2}{2g} = \frac{P_2}{W} + \frac{V_2^2}{2g} + H \quad (2.18)$$

Once again, using Eq. 2.16 and substituting for  $V_1$  and solving Eq 2.18 for  $H$  yields:

$$\frac{P_1 - P_2}{W} + \frac{V_2^2 A_2^2}{2A_1^2 g} - \frac{V_2^2}{2g} = H \quad (2.19)$$

Eq. 2.17 is solved for  $\frac{P_1 - P_2}{W}$  and substituted into Eq. 2.19 to obtain:

$$H = \frac{1}{g} \left( 1 - \frac{A_2}{A_1} \right) V_2^2 + \frac{V_2^2 A_2^2}{2A_1^2 g} - \frac{V_2^2}{2g} \quad (2.20)$$

Expanding Eq. 2.20 yields:

$$H = \frac{V_2^2}{g} - \frac{V_2^2 A_2}{A_1 g} + \frac{V_2^2 A_2^2}{2A_1^2 g} - \frac{V_2^2}{2g} \quad (2.21)$$

Gathering terms and pulling out a  $\frac{V_2^2}{2g}$  yields:

$$H = \frac{V_2^2}{2g} \left( 1 - \frac{2A_2}{A_1} + \frac{A_2^2}{A_1^2} \right) \quad (2.22)$$

Using  $\Omega$  as the area ratio for  $\frac{A_2}{A_1}$ , the parenthetical term simplifies to provide:

$$H = \frac{V_2^2}{2g} (\Omega - 1)^2 \quad (2.23)$$

Using the continuity equation one last time to determine the head loss for the upstream flow conditions:

$$H = \frac{V_1^2}{2g} \left( 1 - \frac{1}{\Omega} \right)^2 \quad (2.24)$$

Let  $\beta$  represent the diameter ratio between  $A_1$  and  $A_2$  respectively, the parenthetical term in Eq. 2.24 becomes:

$$\left( 1 - \frac{1}{\Omega} \right)^2 = (1 - \beta^2)^2 \quad (2.25)$$

Crane Company used Gibson's area ratio relationship from Eq. 2.24 and developed a resistance factor per Eq. 2.26 based on the diameter ratio term  $\beta$ .

$$K = \frac{(1 - \beta^2)^2}{\beta^4} \quad (2.26)$$

where  $\beta$  is the ratio of orifice diameter to cavity diameter at the orifice. It is important to note the cavity diameter at the orifice was changing during an HRAM event. The cavity even separated from the orifice while still maintaining an appreciable outer diameter as the orifice diameter became reduced. This is why it is important to distinguish the subtleties

between overall cavity diameter and cavity diameter at the orifice. Additionally, Eq. 2.26 was developed using pipes with significant length as to not influence the flow. During an HRAM event, the projectile was creating an effective pipe for the entrained gases to flow through.

Remember, Gibson's derivation assumed incompressible flow. Empirical research into the relationship between a measured  $K$  and the expansion factor  $Y$  for compressible fluids at a known pressure ratio permitted the use of the general mass flow equations while accounting for the fluid's changing density [31]. The mass flow through an orifice using the modified Darcy formula for compressible flow is provided in Eq. 2.27.

$$\dot{m}_O = YA \sqrt{\frac{2\Delta P \rho_{Air}}{K}} \quad (2.27)$$

where  $\dot{m}_O$  is the mass flow rate through the orifice,  $Y$  is the experimentally determined expansion factor for compressible fluids,  $K$  is the resistance coefficient for geometric flow conditions.  $A$  is the area of the orifice,  $\Delta P$  is the pressure difference across the orifice, and  $\rho$  is the density of the upstream gas.

For compressible fluids, the maximum flow through the orifice becomes choked when the fluid's speed approaches the speed of sound. For isentropic processes at atmospheric conditions, flow through a 0.375 inch diameter smooth orifice required an approximate pressure difference of 50,000 Pa to become choked. However, with significant amounts of resistance in the system per Eq. 2.27, the resulting mass flow was reduced for the same observed pressure difference.

To obtain an estimation if the projectile can potentially choke the flow during an HRAM event, the pressure difference at the rear of the projectile was calculated using the  $C_p$  equation:

$$\Delta P = C_p \frac{1}{2} \rho_L V_P^2 \quad (2.28)$$

where  $V_P$  is the projectile velocity at penetration. Using the  $C_p$  data from Achenbach, the  $\Delta P$  for a 50 m/s projectile moving through a dense medium such as water resulted

in a negative absolute pressure difference indicating the flow through the orifice could potentially become choked [32]. May also theorized the flow of air approaching sonic values during initial research of vertical projectile water entry [18].

The potential existed to create a pressure gradient to choke the flow. Looking back at Eq. 2.27, it was expected the mass flow would change with respect to the resistance coefficient ( $K$ ) during the HRAM experiments. As the resistance coefficient changes, the mass flow is expected to change assuming the pressure gradient remained relatively the same. The flow resistance during an HRAM experiment will have similarities with regard to the developed orifice flow equations and coefficients. The aforementioned subtleties between flow through pipes and orifices and an HRAM event was expected to cause differences in the observed flow rate versus the developed equations for orifice flow. The pressure gradient across the orifice may generate mass flow values significantly less than maximum choked mass flow values isentropic conditions due to the resistances in the system [31, 33].

## **2.11 Summary**

Scholars have initiated research into the driving mechanisms behind the HRAM event. However, requirements to understand HRAM cavity dynamics are relatively recent and have pushed the research into new areas. Aspects of HRAM not addressed by current research are the pressure-volume work on the fluid by the projectile, cavity composition, and orifice flow characteristics. By researching these areas, the findings will contribute to the overall understanding of HRAM knowledge.

Centuries ago, fluid dynamics and properties were the forefront of research efforts. Decades ago, cavitation on pumps, propellers, rocket engines, and torpedoes was beginning. Research into the driving mechanisms and underlying physics behind the cavity formation and transient spray is fewer than 20 years old. Recent HRAM research developments is due to recent improvements in high-speed imagery. Another part is due to

the increase in computer and processing power to conduct the numerical simulations and model verification. Regardless, development of physics-based models of HRAM cavity dynamics is necessary to improve aviation safety.

### III. Diagnostic Technique and Experimental Apparatus

THIS chapter will describe the equipment and resources used for data collection, measuring the HRAM cavity volume, and the techniques developed for measuring the orifice entrainment. Additionally, this chapter will cover the experimental data analysis techniques, limitations, and methodologies necessary to post process the imagery to obtain the volume data, projectile position, entrainment velocity, and mass flow calculations used during research. Discussion of the techniques and their limitations is meant to convey the experimental basis and techniques used for the upcoming results and conclusions.

It is important to note the 3 different experimental setups were used to collect the imagery data. Although there are 3 experimental setups, only 2 different experimental locations were utilized. The first experimental location was the 96<sup>th</sup> Test Group's (TG) range complex. This is an Air Force certified test range where projectile velocities can exceed 1,800 *m/s*. AFIT provided some high-speed cameras to supplement the test range's capabilities. Support and consult from the 96<sup>th</sup> TG was instrumental in completion of this research. Full description of the test setup is shown in Section 3.1

The second and third setups were built and executed at AFIT's laboratories. The Projectile velocities up to 176 *m/s*, considerably less than the 96<sup>th</sup> TG, were used and sufficient to generate a much smaller HRAM event. Until this research, HRAM experiments were not conducted at AFIT. Development of novel high-speed imagery acquisition was needed to complete the research, and working on a test range for months was cost prohibitive. Hence, to have the freedom of research and experimentation for the development of the technique, experiments at AFIT were needed. The second experimental setup to measure the projectile's position and cavity's volume is shown in Section 3.2. The third experimental setup to measure the entrained flow field via the penetration orifice is shown in Section 3.3.

### 3.1 Investigative Research with the 96<sup>th</sup> Test Group

During the literature review, it was noticed prior research has not investigated internal and external HRAM characteristics simultaneously. To bound the research in an attempt to determine which cavity dynamics are of interest, HRAM testing in conjunction with the 96<sup>th</sup> TG provided an opportunity to collect data with synchronized high-speed cameras focused on simultaneous internal and external views of the tank. The experimental setup used 30 *mm* powder cartridge to accelerate the 0.375 inch diameter steel projectile to velocities ranging from 1,200 *m/s* to 1,800 *m/s*. The steel ball bearing pierced through the aluminum shot plate on the tank's front and then traveled through water. Three of the tank's sides were composed of polycarbonate sheets on the side walls for imagery access.

All shots had an approximate 0 degrees of azimuth and elevation. The tank's back wall was 64 inches deep from the shot plate to the rear of the tank. Additionally, there was 24 inches of water head above the shot line while the polycarbonate wall was approximately 30 inches from the shot line. Panel size, thickness, and material was held constant at for all impact conditions. Panel size was 24 x 24 inches at 0.06 inches thick of 2024-T3 Aluminum.

The primary goal of the experiments for the 96<sup>th</sup> TG was to characterize the time to transient spray for the different ballistic parameters. An accelerometer was placed on the shot panel with its voltage monitored by an oscilloscope. The oscilloscope sent a 5V TTL signal to the cameras once it detected a voltage rise from the accelerometer resulting from projectile impact. Using the Phantom Camera Control software, the appropriate pre-trigger was set to capture the HRAM event prior to projectile impact.

By combining AFIT's and the 96<sup>th</sup> TG's camera resources, synchronized high-speed imagery was collected with less than a 200 nanosecond variance between image pairs. Figure 3.1 is a diagram of the experimental setup. The goal of the experiments was to provide insight into the cavity features or dynamics required for initiation of the transient



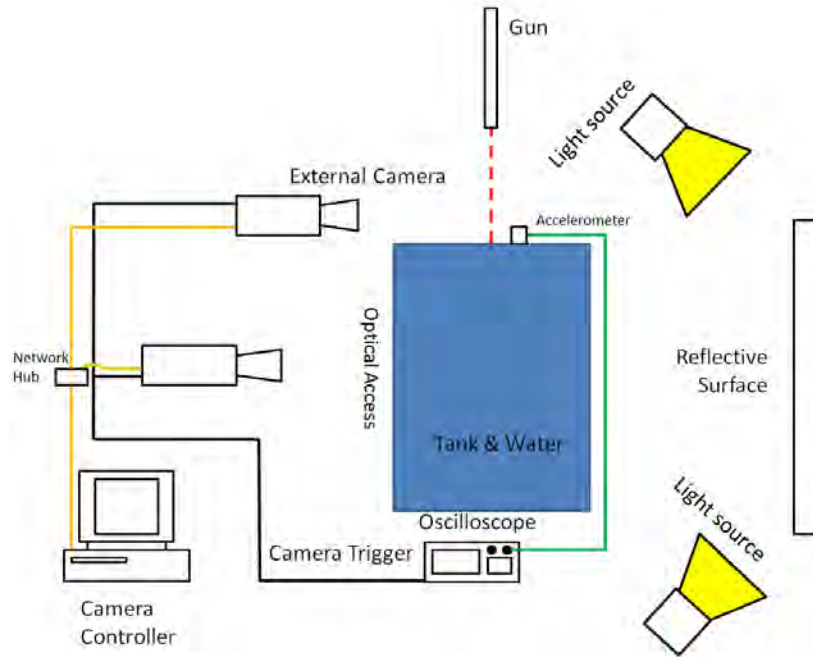
spray phases. The results of the experiment are detailed in Chapter IV. A secondary goal was to collect and analyze cavity volume data as a function of time and compare findings to lower velocity conditions.

Having the capability and opportunity to collect internal and external measurements at the high frame rates with the 200 nanosecond variance paid huge dividends in bounding the research. The 96<sup>th</sup> TG can provide detailed descriptions of the tank dimensions, test setup, its limitations, and capabilities upon request.

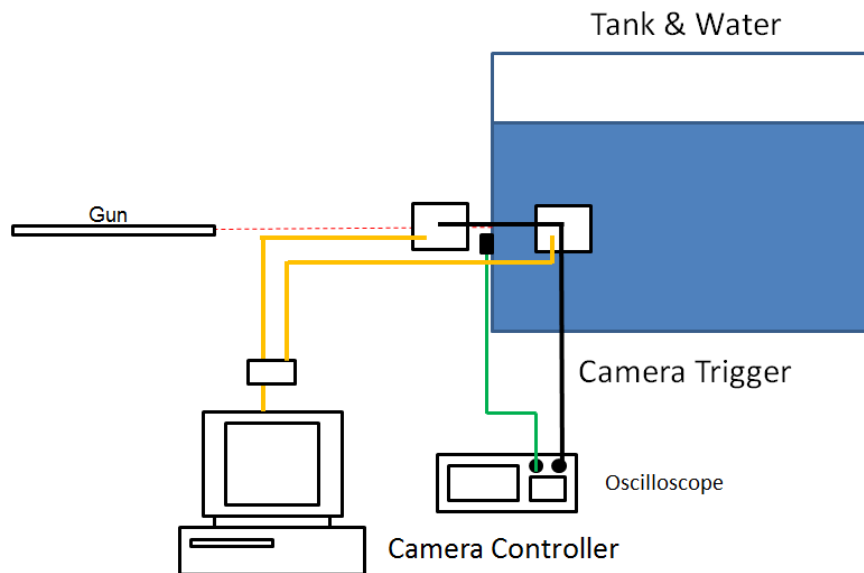
### **3.2 Methodology for Imagery Acquisition for Cavity Volume and Projectile Position Measurements**

AFIT did not have an existing laboratory to conduct HRAM experiments. The laboratory space was sequestered, the necessary equipment was purchased or borrowed, and the mandatory safety review was conducted to certify the lab space operated within AFIT and WPAFB requirements. Total cost to construct the laboratory was less than \$6,000. However, more than \$500,000 dollars worth of cameras, lasers, lenses, oscilloscopes, and other equipment was used at moments to collect the necessary data. The approved experimental setup is illustrated in Fig. 3.2.

Some of the equipment AFIT built or purchased for this research was the nitrogen projectile acceleration device (PAD), polycarbonate tank, high-speed cameras, optical support equipment, and triggering equipment. The PAD is constructed from stainless steel and aluminum support structure and is capable of 12.4 megapascal maximum operating pressure. The PAD's actuation, or firing mechanism, is controlled by a fast acting, 0.5 inch NPT solenoid. Multiple barrels were sized to accommodate projectile diameters of 0.450, 0.953, and 1.032 *cm* projectiles. Currently 190 *m/s*, is the approximate maximum projectile velocity from the PAD. However, the PAD could not consistently achieve the 190



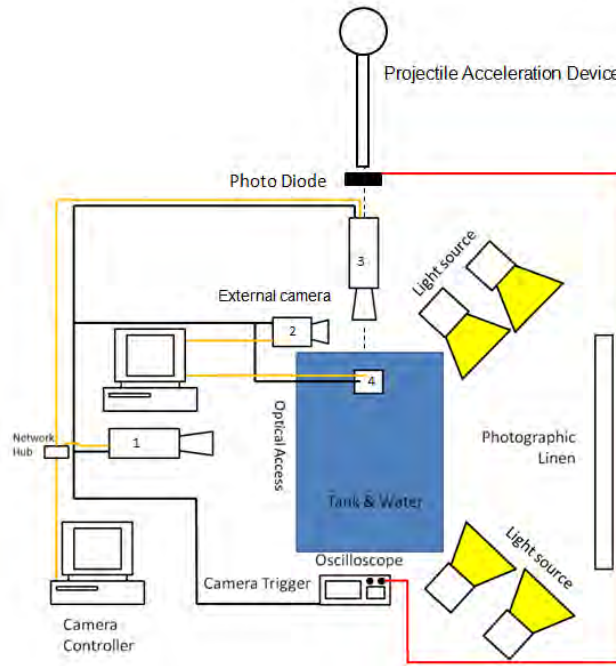
(a) Top view of the experimental setup at the 96<sup>th</sup> TG's Range



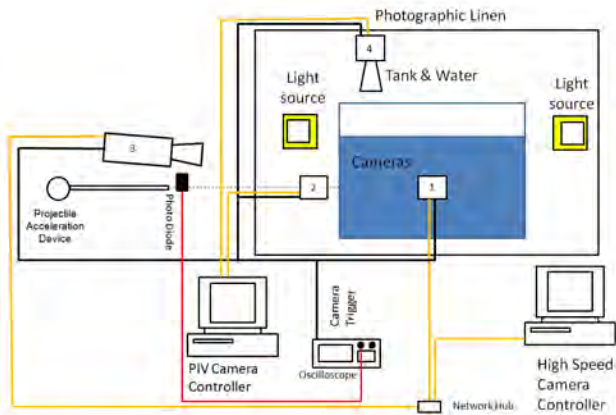
(b) Side view of the experimental setup at the 96<sup>th</sup> TG's Range

Figure 3.1. Overview Experimental Setup with the 96<sup>th</sup> TG.

$m/s$  maximum velocity. Therefore, the pressure in the PAD was lowered and the maximum repeatable velocity occurred around  $175\text{ m/s}$  for a charge pressure of 3.45 megapascal.

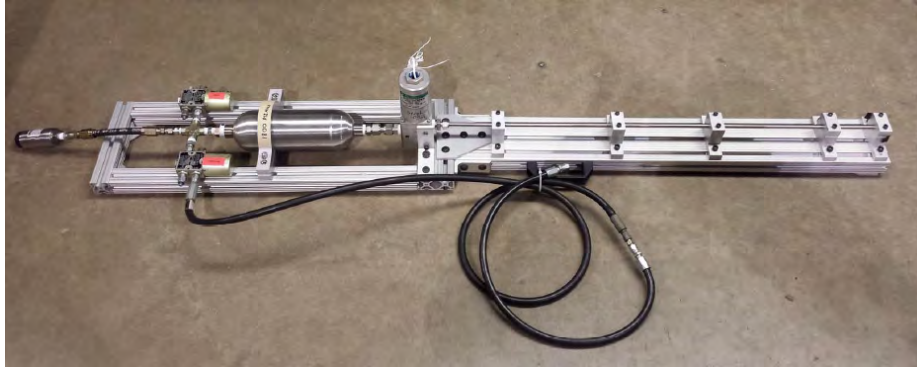


(a) Top view of experimental setup

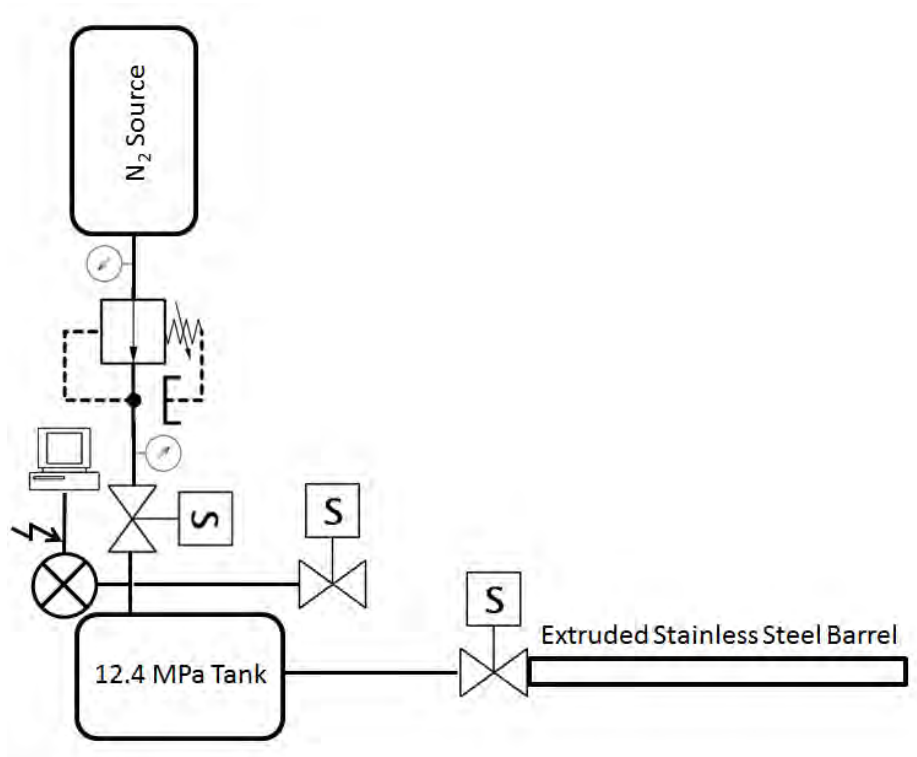


(b) Side view of experimental setup

Figure 3.2. Overall experimental schematic to achieve the research objectives.



(a) Projectile acceleration device (PAD)



(b) Schematic of PAD

Figure 3.3. Overview of PAD used to complete HRAM tests.

The tank is approximately  $33 \times 35.6 \times 61$  cm and shown in Fig. 3.4. It is constructed out of 2.54 cm thick polycarbonate sheets to resist bending due to the pressure fluctuations at projectile impact. The tank can withstand shots from 0.450, 0.953, and 1.032 cm aluminum, steel, and tungsten projectiles with interior extruded aluminum energy absorbent backing shown at the rear of the tank in Fig. 3.4. Nevertheless, to significantly increase the size or velocity of the projectiles would require a significant investment to re-design the tank and laboratory to withstand the larger projectiles. The projectiles traveled from the PAD to a replaceable 0.81 mm thick aluminum shot plate. An aluminum shot plate was chosen to minimize the kinetic energy required to penetrate the fluid filled tank, while maintaining a barrier does not deform due to the static water pressure in the tank.

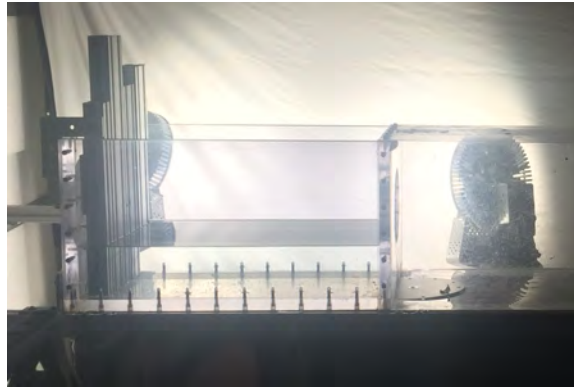


Figure 3.4. Polycarbonate tank side view with LED lights reflecting on the photographic linen to generate the brightfield image technique used for imagery collection [34].

Data was extracted from high-speed imagery for position and volume measurements. Obtaining clear imagery of the HRAM event is necessary to facilitate post processing measurements. Many imagery lighting techniques were tried such as schlieren, direct lighting, and flash lighting, but ultimately brightfield imaging proved the most promising method to collect the imagery at high frame rates [34–36].

The LED lights in Fig. 3.4 emit 23,000 lumens each at an approximate 5,000 Kelvin temperature profile. The light was sufficient to capture the event with a  $4\ \mu s$  exposure time. Theoretically, with a  $4\ \mu s$  exposure time, the light was sufficient to capture the event at frame rates up to 250,000  $Hz$ . However, to maximize the resolution of the cameras, frame rates between 20,000 to 40,000  $Hz$  were utilized. The disadvantage of brightfield imaging is it requires greater amounts of light, as compared to direct lighting, to collect the high-speed images due to the scattering of the light off the photographic linen. The advantage of using brightfield imaging is the relatively uniform contrast in the collected imagery, easing image processing and post data analysis.

AFIT possesses cameras capable of a variety of frame rates at differing resolutions. It is necessary to understand potential sources of error and how the trade space between error, resolution, and frame rates works. Since the measurements made from the imagery were positional in nature, the error associated with the measurement was within 1 pixel. If an image of the same subject matter was obtained with a higher resolution, the positional error associated with the measurement decreased. The Phantom cameras used in this research generally decreased in resolution as frame rates increased. Therefore, frame rates were selected to minimize the positional error, while maintaining the frame rates necessary to capture the overall HRAM event with sufficient fidelity. The ideal camera settings occurred between 20,000 and 40,000  $Hz$  with a  $4\ \mu s$  exposure time. The images collected at 20,000  $Hz$  had a resolution of 786 by 1024 while the images at 40,000  $Hz$  had a resolution of 512 by 256.

Spherical projectiles were chosen for data collection purposes due to their symmetric cavity formation and lower probability of deviation from the projectile shot line. Development of the analysis tools was accomplished at low-speed vertical drops to increase repetition of data necessary for tool validation. This process enabled the development of appropriate diagnostic tools and image processing techniques in a simplified setting

and was addressed in detail in Lingenfelter and Liu [36] and also shown in Section 3.2.2 for reference. The developed tools were still applicable at projectile velocities up to and exceeding 180  $m/s$ .

The experimental setup utilized laser gated photo diodes monitored by an oscilloscope to measure the projectile velocity after it left the PAD. A pair of Thor Labs, model DET10A, photo-diodes were used and monitored on a Tektronix DPO 4104 digital oscilloscope. The photo diodes were placed on the end of the PAD and separated by 3.25 inches along the projectile shot-line. When the projectile interrupted the laser beam, the oscilloscope measured the resulting voltage drop on each photo diode. The distance between the photo diodes was divided by the measured time difference between the two voltage drops.

To achieve maximum performance (nanosecond response times for voltage drops) on the photo diodes, the voltage is measured across a 50 ohm resistance. The selected oscilloscope defaulted to 1 mega-ohm resistance when measuring the voltages of the photo diodes. At the higher resistance, the photo diodes functioned when the light was interrupted by slow moving objects, such as a hand, but did not function fast enough to detect the projectile as it exits the PAD's barrel. Once the oscilloscope was changed to 50 ohm resistance, the photo diodes operated at their published nanosecond response time and provided the associated voltage drops for projectile velocity calculations. In all cases, the projectile muzzle velocity and the initial penetration velocity are not the same. The energy to penetrate the aluminum shot plate lowers the projectile's kinetic energy resulting in a lower penetration velocity. In the research, the shot velocity is referencing to the projectile muzzle velocity. The penetration velocity and kinetic energy are referencing the projectile velocity after piercing through the shot plate, unless otherwise noted.

### ***3.2.1 Imagery Analysis Process.***

When detecting the desired features, two regimes were identified. This section was broken into multiple sub-sections to describe the analysis tools developed to detect

features with different contrast backgrounds. The first sub-section discusses the process for detecting desired features with relatively constant background contrast. The second section discusses the process for detecting desired features with changing or variable background contrast.

### ***3.2.2 Feature Detection with Relative Constant Contrast.***

The desired data resides in the images' features and is presented to the user as a two-dimensional contrast of a three-dimensional activity. Data extraction from the imagery was dependent on developing the mathematical algorithms needed to detect the desired features within the image, while not detecting undesired features. Utilizing published processing techniques, data for the projectile leading-edge and cavity's gas-liquid interface were extracted from the imagery for further analysis [37]. Below is the description of the processes used to collect the desired data from the imagery.

Detecting the leading-edge of the projectile was determined by using a Sobel edge detection algorithm. A script, using the Sobel algorithm and the necessary linear algebra, was written in MatLab to expedite image processing. This method required imagery with relatively small or undetectable aberrations.

When processing any images, it is important to understand the operations behind the techniques and algorithms. Sobel approximated a derivative between neighboring pixel values to provide an estimate of the contrast gradient. Setting a threshold for the contrast gradient converted a raw gray-scale image to a binary image at the specified threshold limit. Equations 3.1 through 3.5 demonstrate the Sobel edge detection technique initially developed by Irwin Sobel [37].

Each pixel in a digital image has eight neighbors, except for the first and last row, and first and last column positions. For example, given a matrix  $M$ , shown in Eq. 3.1, a 3 by 3



subset of the raw gray-scale image taken where  $l$  is the pixel of interest.

$$M = \begin{bmatrix} h & i & j \\ k & l & m \\ n & o & p \end{bmatrix} \quad (3.1)$$

We define  $\theta$  as the magnitude of the directional derivative of pixel  $l$  with respect to its neighbors as seen in Eq. 3.2.

$$\theta = \frac{\text{density difference}}{\text{distance to neighbor}} \quad (3.2)$$

For example, the value of  $\theta$  for pixel  $l$  to pixel  $j$  is shown in Eq. 3.3.

$$\theta = \frac{j - l}{\sqrt{2}} \quad (3.3)$$

where  $j$  and  $l$  are pixel values associated with the pixel locations  $j$  and  $l$  from Eq. 3.1. The  $\sqrt{2}$  in the denominator is a result of the Pythagorean theorem to account for the distance between pixel  $l$  to pixel  $j$ .

Now, considering the  $x$  and  $y$  vector components of contrast, while applying similar methodology of Eq. 3.3 across all eight neighbors, a vector for pixel  $l$  was obtained based on the gradient and the known position of the pixels relative to the pixel of interest. The gradient vector *Theta* is mathematically represented in Eq. 3.4.

$$\Theta = [\theta_x, \theta_y] = \left[ \frac{(j-n)-(h-p)}{4} + \frac{m-k}{2}, \quad \frac{(j-n)+(h-p)}{4} + \frac{i-o}{2} \right] \quad (3.4)$$

where the  $\theta_x$  component of  $\Theta$  is the horizontal component gradient calculation across pixel  $l$  and the  $\theta_y$  component of  $\Theta$  is the vertical component gradient calculation across pixel  $l$ .  $\Theta$ 's magnitude as written in Eq. 3.4 is actually four times the true contrast gradient's value since  $\Theta$  includes the gradients in the  $\pm x$  and  $\pm y$  directions. For the Sobel algorithm,  $\Theta$  was multiplied by four to preserve memory, which generated a vector estimate 16 times greater than the true average contrast gradient.

$$l = \begin{cases} 1 & \text{if } T \geq 4\theta_x \text{ or } 4\theta_y \\ 0 & \text{if } T < 4\theta_x \text{ and } 4\theta_y \end{cases} \quad (3.5)$$

where  $l$  is the pixel of interest from Eq. 3.1,  $T$  is the contrast threshold set by the user. The user determined threshold value is applied universally across the horizontal and vertical components of  $G$ . If one of the vector component's obtained in Eq. 3.5 was greater than the threshold, the algorithm placed a 1 in pixel  $l$ 's location, otherwise 0. Applying this method across the desired pixel range converted the raw image to a binary image with desired edge features displayed for projectile tracking. Since  $\Theta$  was now a vector 16 times larger than the original contrast vector,  $\Theta$  provided the user a wide threshold range of adjustment to block out undesirable aberrations without losing track of the projectile. A wide threshold range was only possible when strong contrast between projectile and the cavity was much stronger than the undesired aberrations.

Now the leading-edge of the projectile was determined and the resulting binary image was created. Location of the leading edge was determined by starting on the row or column opposite of where the projectile first entered the tank and the first instance where a 1 was detected, while progressing towards the penetration location, was recorded. This process was repeated for image and time between each image was provided by the camera's frame rate as shown in Fig. 3.5 [36]. The "+" in Figure 3.5 is the detected leading-edge of the projectile from the Sobel edge detection technique. Figure 3.5 also illustrates the accuracy of the developed projectile tracking algorithm. The developed image processing techniques also minimize image processing time when compared with taking optical measurements via visual inspection.

Sobel edge detection algorithm was also used to determine the cavity dimensions. Processing the cavity dimensions requires slightly different mathematics than the projectile position algorithm. Instead of measuring the leading edge of the projectile, the upper and

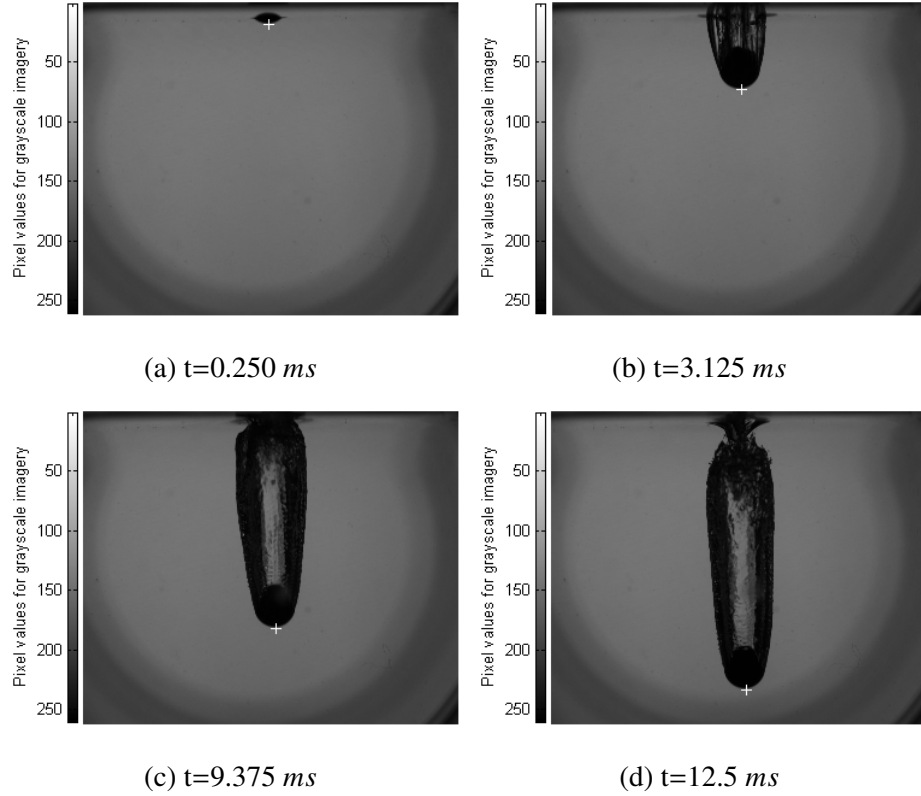


Figure 3.5. Selected images of leading-edge tracking of a  $0.953\text{ cm}$  projectile penetrating water from  $138.4\text{ cm}$  drop at  $8,000\text{ Hz}$ . At  $8,000\text{ Hz}$ , there was a  $31.25\text{ }\mu\text{s}$  mean time between each of the recorded images with an exposure time of  $93.75\text{ }\mu\text{s}$ . The + indicated the leading-edge of the projectile as determined by the developed algorithm [36].

lower edge of the cavity was detected and its position was recorded. The distance between the upper and lower cavity boundaries was determined by the difference between pixel locations. Assuming axial symmetry of the cavity, the distance between pixels was utilized as the diameter of a cylinder with a thickness of 1 pixel. A small cylinder volume was computed based on circular area measurements for each row of imagery data. The total volume of the cavity was then a summation of all the small cylinder volumes detected in each row of imagery data [36].

The images in Fig. 3.6 are derived from the images displayed in Fig. 3.5 except processed through the cavity boundary detection algorithm. The vertical white line on the left of the image does not have a physical meaning. This line occurred when the algorithm did not detect a significant contrast difference, and there was no distance across the cavity. A more detailed example is shown in Fig 3.7 and 3.8, where each image is an enlarged cavity portion of Figure 3.5(d). Nonetheless, the results were very useful for extracting data from the imagery.

The error associated with using digital imagery primarily lies within the accuracy of the technique to measure the true cavity boundary versus the detected cavity boundary. Similar to pixel locking, the cavity's boundary is only measured to the nearest pixel value, when in reality the boundary is continuous. Since pixel values were integer responses, versus a continuous response, there was error between the measured cavity boundary versus the true cavity boundary. Therefore, the true cavity boundary is contained within  $\pm 1/2$  pixel of the measured cavity boundary. The  $\pm 1/2$  a pixel error is associated with each time there is a boundary. For the cavity volume, the edge detection was applied on the upper and lower bounds of the cavity. Hence, the total error for each detected cavity diameter is  $\pm 1$  pixel.

The smallest portion of the cavity is approximately the diameter of the projectile. The smallest portion is chosen since it is the most sensitive to error. For example, the projectile diameter encompassed approximately 25 pixels. Since the error is  $\pm 1$  pixel of the 25 pixel diameter, this computes to an error of 4%. Conversely, as the cavity increased in diameter, the relative error percentage decreased. The cavity maximum diameter for the 111 *m/s* shot was approximately 95 pixels. Again the error is  $\pm 1$  pixel of the 95 pixel diameter, and this computes to an error of 1.05%.

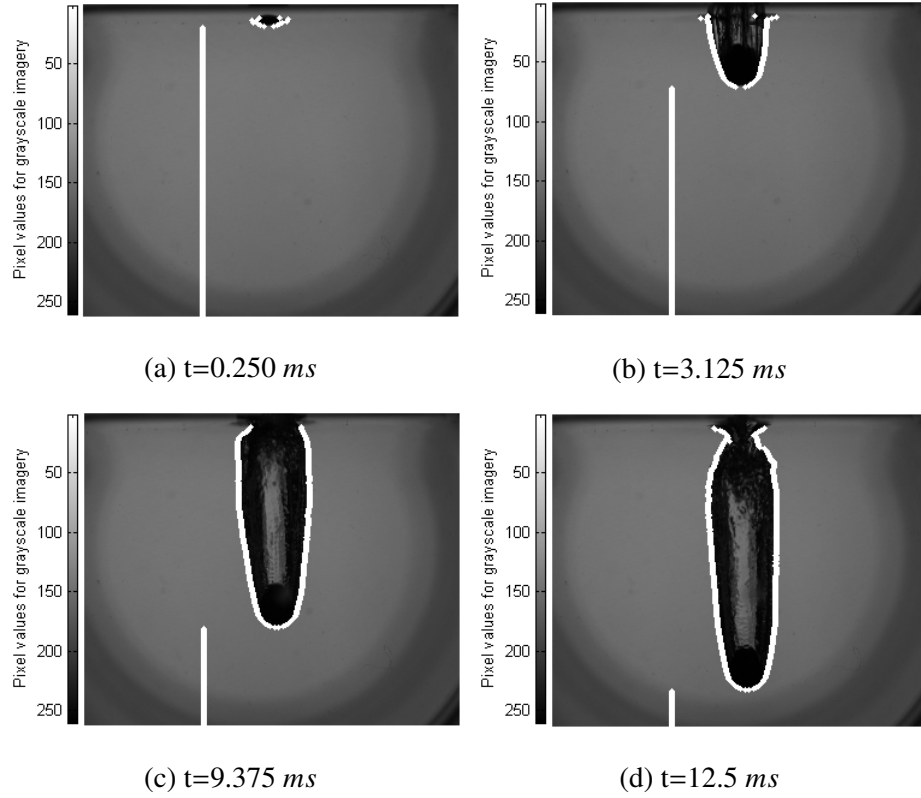


Figure 3.6. Cavity boundary tracking of a  $0.953\text{ cm}$  projectile penetrating water from  $138.4\text{ cm}$  drop at  $8,000\text{ Hz}$ . At  $8,000\text{ Hz}$ , there was a  $31.25\text{ }\mu\text{s}$  mean time between each of the recorded images with an exposure time of  $93.75\text{ }\mu\text{s}$ . The vertical white line indicated when no difference in boundary detection existed. The conformal white line indicated edge detection for cavity measurement [36].

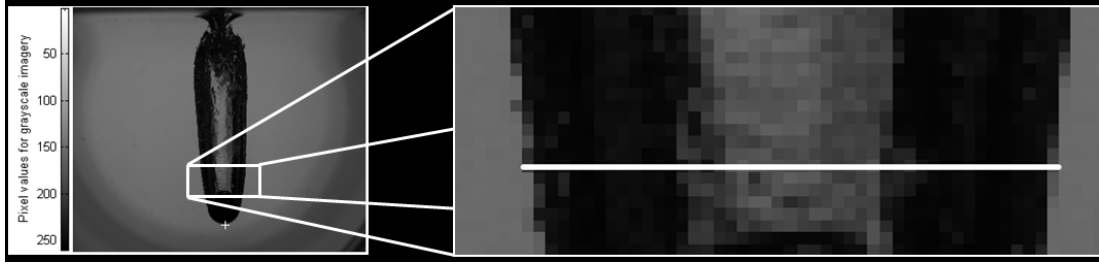


Figure 3.7. The right image was an enlarged subset image of Figure 3.5. The white horizontal line on the right subset image represented the cylinder's diameter used for volume calculations based on the assumption of axial symmetry about the projectile shot line [36].

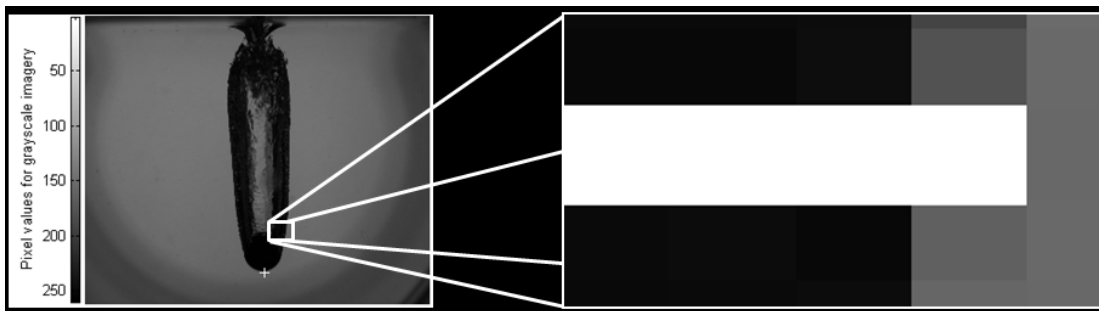


Figure 3.8. The right image was an enlarged subset image of Figure 3.5. The white rectangle was the horizontal white line displayed in Figure 3.7 illustrating the associated pixel height at the detected boundary. The height is needed to compute the small cylindrical calculations for each row of pixels [36].

### ***3.2.3 Feature Detection and Tracking with Changing Contrast.***

A tensor is a mathematical object with components and obeys certain transformation rules. Tensors are able to generalize scalars, vectors, and matrices, up to any number of indices [38]. For the developed image processing technique, a three dimensional tensor is generated from the collected imagery. The first two indices correspond to the horizontal and vertical spatial component of the collected imagery. By “stacking” the imagery together in sequential order, the third index corresponds to time over which the imagery was collected.

A multidimensional tensor image processing technique was developed to track and measure items of interest, such as the transient and non steady HRAM flow field. Similar techniques are used to visualize hyper-spectral imagery [39]. The entrained HRAM flow field had changing contrast, where traditional edge detection techniques do not work well. Additionally, the tensor technique was also useful to track features with nearly constant contrast, such as the projectile’s leading-edge. The following technique was developed and published in the Journal of Physics: Conference Series [21].

As the cavity began to contract around the penetration orifice, water started to mix with the entrained flow field and generated a water fluid mixture. The water fluid mixture’s contrast changed as it progressed through the cavity’s interior. Predicting the contrast gradient for use in edge detection algorithms to detect multiple fronts was computationally intensive due to the transient and unsteady nature of the flow field. However, the formation of a multidimensional tensor enabled flow field detection, where traditional techniques have failed. Hence the development of the “image cube” for detection and analysis of multiphase flows during an HRAM event.

An image,  $A_{n,r,c}$ , represented by Eq. 3.6, is an  $r \times c$  matrix composed of pixel values as shown in Eq. 3.6

$$A_{n,r,c} = \begin{bmatrix} a_{n,1,1} & a_{n,1,2} & \cdots & a_{n,1,c} \\ \vdots & \vdots & \ddots & \vdots \\ a_{n,r,1} & a_{n,r,2} & \cdots & a_{n,r,c} \end{bmatrix} \quad (3.6)$$

where  $a_{n,r,c}$  are the pixel values from the specified image frame number,  $n$ , at the corresponding row,  $r$ , and column,  $c$ .  $A_{n,r,c}$  represents a typical image, where vertical position was on the  $y$ -axis and horizontal position was on the  $x$ -axis. An image cube is a multidimensional tensor as shown in Eq. 3.7

$$\text{ImageCube} = \left[ A_{1,r,c} \dots A_{n,r,c} \right] \quad (3.7)$$

where all the two dimensional images from frame number 1 to  $n$  reside on the  $z$ -axis. A pictorial showing an example of the image cube is shown in Figure 3.9(a).

To determine the flow field's velocity, an image slice,  $S_{n,r,c}$  via Equation 3.8

$$S_{n,r,c} = \begin{bmatrix} A_{(1,r,1)} & A_{(1,r,2)} & \cdots & A_{(2,r,c)} \\ A_{(2,r,1)} & A_{(2,r,2)} & \cdots & A_{(2,r,c)} \\ \vdots & \vdots & \ddots & \vdots \\ A_{(n,r,1)} & A_{(n,r,2)} & \cdots & A_{(n,r,c)} \end{bmatrix} \quad (3.8)$$

where  $r$  is the specified row of interest.  $S_{n,r,c}$  is a two-dimensional plane extracted from the multidimensional tensor represented by Eq. 3.7.  $S_{n,r,c}$  therefore is composed of all pixel values from image 1 to  $n$ , column 1 to  $c$ , for the user specified row value,  $r$ . The user must specify  $r$  based on the row location of the flow field of interest in  $A_n$ .



For example, the the row with close proximity to the projectile shot line was chosen to generate  $S_{n,130,c}$ . The composition of  $S_{n,130,c}$  is shown in Eq. 3.9 below:

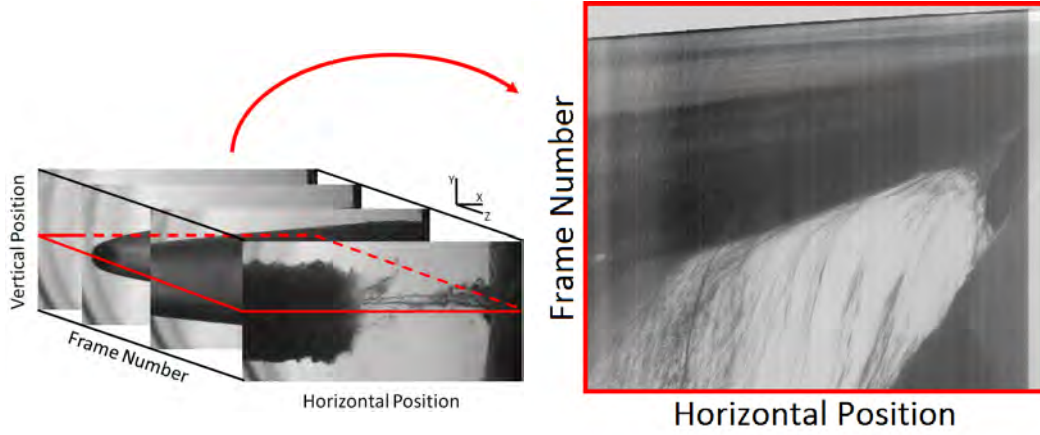
$$S_{n,130,c} = \begin{bmatrix} A_{(1,130,1)} & A_{(1,130,2)} & \cdots & A_{(2,130,c)} \\ A_{(2,130,1)} & A_{(2,130,2)} & \cdots & A_{(2,130,c)} \\ \vdots & \vdots & \ddots & \vdots \\ A_{(n,130,1)} & A_{(n,130,2)} & \cdots & A_{(n,130,c)} \end{bmatrix} \quad (3.9)$$

where  $r$  was set to row 130. The box placed around the image cube in Figure 3.9(a) corresponded to row 130 for all the images composing  $S_{n,130,c}$ . Therefore,  $S_{n,130,c}$  formed a horizontal plane across the tensor and contains the frame number versus horizontal position data utilized for velocity analysis of the flow field for row 130.

Vertical position and velocity analysis was possible by looking at the vertical plane of the tensor. To detect velocities in multiple directions, correlation of the flow field between the multiple tensor planes was necessary. However, the horizontal velocity was much larger than the vertical velocity in this experiment. Since the dominant flow was in the horizontal direction for this experiment, only the horizontal plane of the tensor was utilized for the position measurements. The technique was very useful for measuring the projectile position. For the above example, the raw projectile position and time information was displayed as the very top line in Fig 3.9(b). Using the necessary tools, a second-order polynomial was fit to the positional data for use in the Chapter IV analysis as stated in Chapter II. Details of the position measurements, the data, and the image slice information for each impact condition is detailed in Appendix C.

### 3.3 Orifice Entrainment Technique and Methodology

Development of a technique to illuminate particles and measure the entrainment of ambient gases through the orifice and into the cavity was needed to calculate the mass flow . Given the experiential limitations and hazardous nature of the experiment, development



(a) Image Cube per Eq. 3.7

(b) Slice 130 ( $S_{n,130,c}$ ) of Image Cube

Figure 3.9. A visual example of how the tensor was formed to create the image cube for flow analysis. Notice, instead of positional depth on the  $z$  axis, Frame Number is on the  $z$  axis. This subtle difference was not instinctive but is important to conduct position and velocity analysis at the desired  $S_{n,r,c}$ .  $S_{n,r,c}$  corresponded to row 130 of all images collected and formed together via Equation 3.8 to obtain Frame Number vs. Horizontal Position information. Time is obtained by using the frame number and the known camera's frame rate.

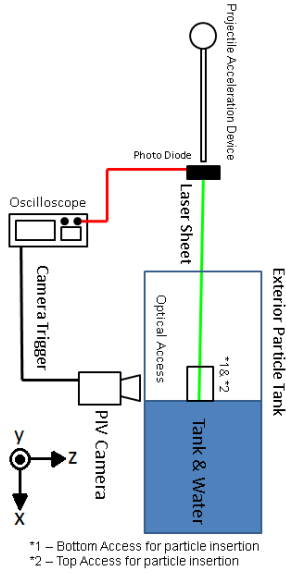
of this technique was not trivial. The first experimental limitation was time. The duration of the event from projectile impact to first spurt was usually less than 4  $ms$ . It was anticipated the orifice flow field would have a non-constant velocity over the 4  $ms$  time frame. Therefore, a continuous wave laser was used as the illumination source. The high hazards from the projectile and resulting spurt drove experimental trade offs to protect the equipment. These experimental trade offs such as increasing camera distance from the shot line and construction of a particle tank resulted in less than ideal situations for flow field measurements. Full detail of the lessons learned and the development of the technique were published in the “Methodology Development of Orifice Entrainment

Velocity Characterization during a Hydrodynamic Ram Event [40]”. Details on the utilized technique, its applications, results, and limitations in Lingenfelter *et al.* are reiterated below [41].

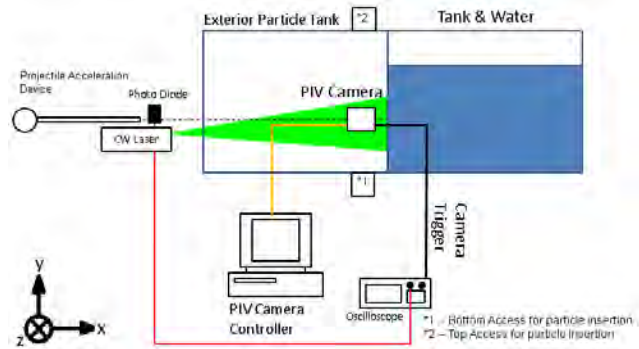
To seed the flow, a particle tank was constructed on the front exterior of the main water tank. The particle tank served two purposes. It enabled flow seeding in a localized region and protected the camera from liquid damage resulting from the seed particles and the transient spray. The protection of the particle tank permitted closer placement of the camera, as if the flow was open to the atmosphere. The data acquisition system was triggered by an oscilloscope measuring the voltage across a pair of photo diodes at the end of the PAD. When the projectile exited the PAD’s barrel, it blocked the laser beam projected onto the photo diode causing a voltage drop. Once the oscilloscope measured the corresponding voltage drop, a 5 volt digital transistor-transistor logic signal which triggered the cameras. The experimental setup is shown in Fig. 3.10.

The best experimental setup developed to date utilized a Coherent V12 solid state laser. The laser was a 12.5 watt, 532 nanometer, continuous wave (CW) laser used to illuminate atomized water particles. The Phantom V16 camera used a 200 *mm* macro lens, with the f-stop set to 4, to capture the flow field. A 300 f(*mm*) cylindrical lens was used to optically change the laser beam from a point to a sheet. The laser sheet had a height of approximately 7 *cm* with a width of 0.5 *cm*.

The atomized water particles seeded the flow more uniformly and were significantly larger than atomized propylene glycol particles. Most importantly, the atomized water adequately reflected the laser light permitting streak measurements. With the 12.5 watt laser and water particles, an exposure time of 10  $\mu s$  was achieved, which was a considerable improvement over the 99  $\mu s$  exposure time obtained by using other particles [40]. Ideally, lower exposure times, or double exposure images, would better capture the flow field, but a laser with the power and repetition rate was not available to capture the non-constant



(a) Top view of experimental setup



(b) Side view of experimental setup

Figure 3.10. Overall experimental schematic to obtain entrainment data [40].

flow field. Hence, the particle motion over the  $10 \mu s$  exposure time generated a streak in the imagery. The velocity was then the length of the streak divided by the exposure time for the captured image. Frame rates of  $10,000 \text{ Hz}$  were utilized to maximize the camera resolution at 800 by 1280 pixels.

The  $200 \text{ mm}$  macro lens was necessary to increase the particle size on the camera's sensor at standoff distances necessary to keep the optical equipment safe. The lens' depth of field at these distances was thinner than the actual laser sheet and reflected laser light from the tank and aluminum shot plate. Therefore, particles out of the focal plane appeared as large aberrations with lower intensity. Post processing and filtering of the image removed a majority of these aberrations and provided the streaks necessary for velocity calculations and analysis.

### 3.3.1 Limitations of Developed Orifice Entrainment Technique.

There are limitations of this entrainment measurement. Streak analysis still has the pixel error associated with detecting and measuring its length on the images. In addition to streak error, the potential existed for particle latency to under represent the flow field velocity. Using the *Springer Handbook of Experimental Fluid Mechanics*, particle latency was represented by the characteristic response time,  $\tau$ , in Eq. 3.10 [42].

$$\tau = \frac{2}{9}a^2\frac{\rho_p - \rho_f}{\mu} \quad (3.10)$$

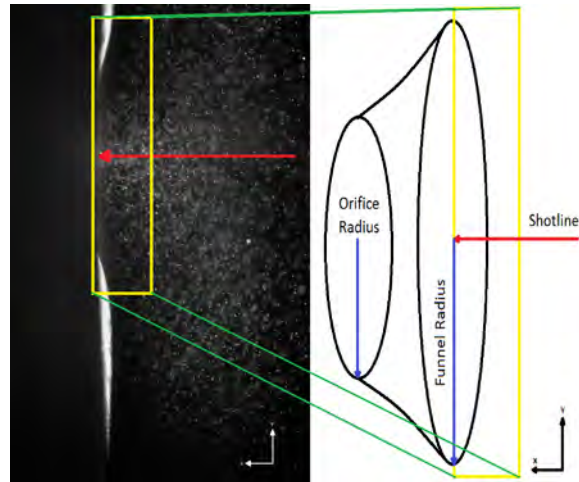
where  $a$  is the particle radius,  $\rho_p$  is the particle's density,  $\rho_f$  is the fluid's density, and  $\mu$  is the dynamic viscosity of the fluid. The atomizer was operated at lower operating pressures than published specifications. Interpolated published specifications of particle diameter converged around 10 to 15  $\mu m$ . Using the 15  $\mu m$  interpolated particle value in Eq. 3.10, a characteristic response time of 0.7  $ms$  was calculated. The response time assumes the particle volume was 100% water for a worse case prediction. The true volume percentage could range from approximately 20 to 100 percent water with the remaining volume consisting of air. Any reduction in the particle's volume percentage or particle size would reduce the calculated response time of 0.7  $ms$  since  $\rho_p$  would decrease per Eq. 3.10. The calculated response time did not mean the data from impact to 0.7  $ms$  was not usable, rather the measured flow field may have slightly under represented the actual flow field. Since the flow field was usually obscured during the first 0.5  $ms$ , only a few of the initial mass flow calculations were potentially under represented due to particle latency.

The streak analysis was also limited by the physical size and dispersion of the particles. To gather enough streaks, an investigation region was needed to approximate the flow field velocity outside the tank but near the orifice. The hole generated by the projectile caused the aluminum shot plate to petal forming a funnel shape. For the research conducted, the

flow field investigation region was located adjacent to the hole and across the funnel to measure the flow field velocity.

Application of an investigation region was not considerably different from traditional PIV analysis techniques. Traditional PIV does not have the ability to predict flow normal to a thin plane. Instead PIV relies on the flow velocity within sub regions to characterize and approximate the flow through the plane of interest. PIV analysis may use cross correlation of image sub-regions to determine the particle phase change in the image. For example, to conduct the desired correlation technique, two images separated by a known time delay are acquired. Then each image is divided into sub regions of known pixel sizes for analysis to determine particle location. The cross correlation technique is applied to the surrounding sub-regions to determine the phase change of the particles between these regions [43]. Streak analysis simply uses the length of the streak in a single image divided by the camera's exposure time within the identified investigation region. An example of the investigation region is shown in Fig. 3.11. The advantage of streak velocimetry is obtaining time-resolved data over a relatively short time duration with a modestly powered continuous wave laser. The available resources and the nature of the HRAM event drove the application of a streak velocimetry data collection technique.

The investigation was critical when attempting to calculate the mass flow through the orifice. The rectangular region in Fig. 3.11 is approximately 21.16 *mm* in height and 5.72 *mm* in width. Comparatively, the projectile is 9.525 *mm* in diameter. The streaks detected in the investigation region were assumed to represent the flow velocity through the funnel's opening, even though the investigation region had a width of 5.72 *mm*. The measured streaks at the rear of the investigation region were projected across the funnel's diameter to provide the velocity profile data necessary to calculate the mass flow. It was assumed the flow through the funnel was symmetric about the projectile's shotline. Therefore, the measured two-dimensional axial flow was integrated with respect to the funnel radius to



(a) Expanded view of the investigation region.



(b) Isometric view of projectile  
shot plate

Figure 3.11. Example of a rectangular investigation region used for streak analysis to determine flow field velocity. The red arrow is the projectile shot line which also coincides with the orifice center line. The investigation region is larger than the projectile due to petaling of the aluminum creating a funnel larger than twice the projectile diameter on the exterior of the shot plate. The flow field velocity through the investigation region was used to determine the mass flow through the orifice.

obtain the overall mass flow. Applying the streak analysis technique to this data set had its limitations and nuances.

The vertical portion of the investigation region was set because the aluminum deformed and petaled during projectile impact and created a funnel on the exterior with approximately twice the diameter of the original projectile. The objective was to use the velocity data to calculate a mass flow through the orifice by using the horizontal component of the measured streak data. Therefore, the diameter of the funnel was where streak measurements were possible since the actual orifice opening was masked by the tank's wall. Theoretically, the investigation region could extend beyond the exterior of the funnel diameter and accurately compute the mass flow because the horizontal velocity component should reach zero when outside the diameter of the funnel. However, the horizontal velocity component at the far ends of the investigation region did not reach zero for each test case due to the particle diameter.

As expected, streak length decreased as the vertical distance from the orifice center line increased. Since the technique was designed to measure streak length, the overall effectiveness and applicability of the technique decreased as the length of the streak decreased. For example, at the regions outside the funnel diameter, there was detected particle motion in the horizontal direction, albeit very small, due to the particle's diameter and the investigation region's width. The detected small horizontal velocity became an issue due to the assignment of a horizontal velocity through an area much larger than the true funnel area when computing the associated mass flow. Therefore, the height and the width of the investigation region had competing interests. If the width of the detection region was too thin, the streak data became sparse. If its too large, the computed mass flow was potentially under represented. Thus, the height of the investigation region is set appropriately to measure the velocity through the desired funnel area to compute the mass flow.



Not surprisingly, if the investigation region was increased in diameter, aligning roughly with the projected increase in funnel diameter and offset from the shot plate accordingly, the calculated mass flow through the region was an average of 3% difference as compared to the calculated mass flow from the original investigation region.

In summary, understanding the limitations of the developed technique was necessary to effectively apply the technique to the problem. The height and width of the investigation region required attention and management to effectively use the technique. Improper sizing of the investigation region could potentially result in data contributing to computations under or over representing the mass flow.

### **3.4 Chapter III Conclusion**

In summary, this chapter provides insight regarding the experiences gained in imagery acquisition, test setup, and utilizing available resources necessary to provide the foundation for research. The test setups covered ranged from synchronized cameras capturing HRAM events from super-sonic projectiles, to collecting imagery for cavity volume calculations. Techniques also incorporated the development of image processing tools to capture the projectile position data, and the development of techniques to measure the entrained flow field. Additionally, the limitations of each technique and the associated error was also discussed. Development and application of these diagnostic techniques and experimental apparatuses were needed to collect the data to complete the research objectives.

## IV. Analysis, Results, and Discussion

**T**HIS chapter addresses the analysis and results of the data gathered. The chapter is broken into multiple sections providing details regarding each measurement, its data, and contribution to the understanding of the HRAM problem. An overall summary of each measurement, associated conclusions, and discussion of future work are provided in the next chapter.

### 4.1 The General Cavity Energy Model

The general equation for work done on gas by a piston is shown in Eq. 4.1 [44]

$$W(\bar{V}) = \int_{\bar{V}_1}^{\bar{V}_2} P d\bar{V} \quad (4.1)$$

where  $W$  is done on gas by a piston,  $dV$  is the change in volume, and  $P$  is the pressure within the changing volume. Thinking of the HRAM event as a pressure-volume work system, where the projectile is analogous to the piston with the cavity's changing volume, the projectile does work to form the cavity. The work is in the form of causing gases to flow through the orifice, or vaporize local fluid. Equation 4.1 was modified to form a general HRAM energy model in Eq. 4.2

$$W_C(t) = [P_o - P_C(t)] \bar{V}_C(t) - \epsilon \quad (4.2)$$

where  $W_C$  is the pressure work the projectile performs on the system to form the cavity,  $P_o$  is the static pressure at the shot line,  $P_C(t)$  is the internal cavity pressure,  $\bar{V}_C(t)$  is the cavity's volume, and  $\epsilon$  is the measurement error. At time,  $t = 0$ ,  $\bar{V}_C(t) = 0$ , and since there is no cavity,  $P_C(t) = 0$ . By treating the cavity formation as a pressure work function, a relationship between projectile kinetic energy depletion is theoretically possible. This simplified model assumes the pressure is applied uniformly throughout the volume when the true pressure varies across the cavity's volume. Projectile position measurements

were used to calculate the projectile velocity, and kinetic energy, as shown in Eq. 2.13. Therefore, it is assumed the cavity pressure-volume work in Eq. 4.2 is a function of the kinetic energy lost by the projectile shown in Eq. 4.3

$$W_C(t) = f(\Delta KE(t)) - \epsilon \quad (4.3)$$

where  $\Delta KE$  is the kinetic energy of the projectile transferred to the surrounding fluid. The kinetic energy transmission rate to perform  $W_C(t)$  is not currently known, but by separating the cavity pressure into its individual mass components, the general pressure work equation takes the form:

$$W_C(t) = P_o \bar{V}_C(t) - \int_0^t \dot{m}_O(t) R_{Air} T dt - \int_0^t \dot{m}_v(t) R_{Water} T dt - \epsilon = [P_o - P_C(t)] \bar{V}_C(t) - \epsilon \quad (4.4)$$

where  $\dot{m}_O(t)$  is the mass flow through the orifice,  $\dot{m}_v(t)$  is the mass vaporization rate of water,  $R_{Air}$  and  $R_{Water}$  are the gas constants for air and water vapor, respectively, and  $T$  is the absolute temperature.

By looking at Eq. 4.4, and recalling published literature, it was noticed cavity composition needed additional research [5–8, 15, 18, 25]. Measuring  $\dot{m}_O(t)$  directly is currently not possible, but measuring a velocity flow field through the penetration orifice is achievable. Hence, experiments were set up to obtain orifice velocity measurements to calculate  $\dot{m}_O(t)$  initiated the process for determining the energy transfer rate, and also provided insight into the overall HRAM problem.

## 4.2 Entrained Flow through Penetration Orifice

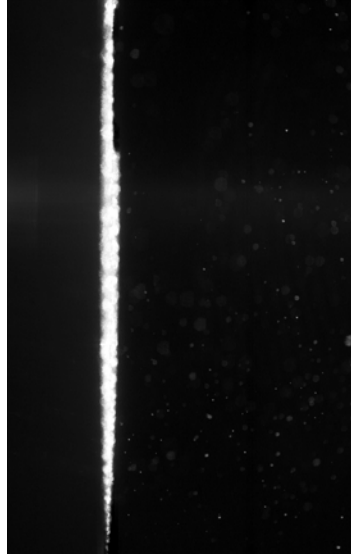
This section will provide the analysis process to measure the flow field velocity and detail the mass flow calculations. The entrained mass flow via the penetration orifice follows similar trends for the different impact velocities. Initially, this observation was counterintuitive. Since higher impact velocities generated larger cavities, it was expected they also would have a larger mass flow rate than the relatively lower impact velocities.

The similar trends in the mass flow rates for the different impact velocities indicate a relationship between the various impact conditions is possible. Utilizing the experimental setup detailed in Chapter III, experiments to measure the entrained flow field used spherical projectiles at various impact velocities.

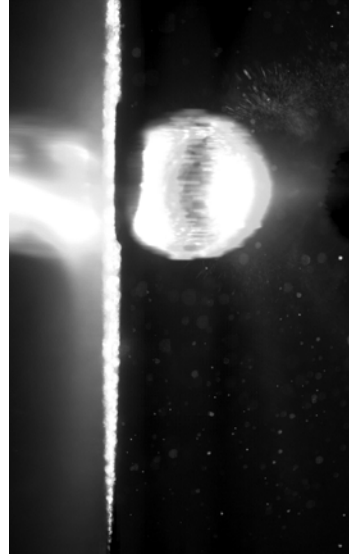
A subset of the collected images are shown in Fig. 4.1 for one case with a projectile velocity of  $135\text{ m/s}$ . Figure 4.1(a) shows the seeded flow field prior to impact. At projectile impact, in Fig. 4.1(b), the seeded flow was dissipated due to the turbulent nature of the flow around the sphere. For approximately the first  $0.5\text{ ms}$  after impact the, particles from the shot plate obscured the region of interest and the streak data did not have sufficient fidelity for velocity profile measurements. As the particles from the shot plate streamline with the flow, streak measurements were possible as shown in Fig. 4.1(c). The velocity measurement was complete once the indication of spurt was present as shown in Fig. 4.1(d). The entire raw image sequences, for impact velocities of 113, 114, 132, 135, and two cases of  $176\text{ m/s}$  are shown in Appendix A.

Since the penetration mechanism of the aluminum causes a petaling in the direction of projectile travel, the actual orifice location is masked by the exterior tank wall. Instead of measuring the particles at the orifice, visible particles are measured through a large “funnel-like” opening created by the petaling aluminum causing the flow to converge to the orifice. The funnel’s presence is evident by the shot plate curvature as seen in Fig. 3.11. Determining the flow field velocity is accomplished by measuring the streak of the seed particles over the  $10\text{ }\mu\text{s}$  exposure time. However, the seed particle density and the streak’s length on the image requires an investigation region also shown in Fig. 3.11.

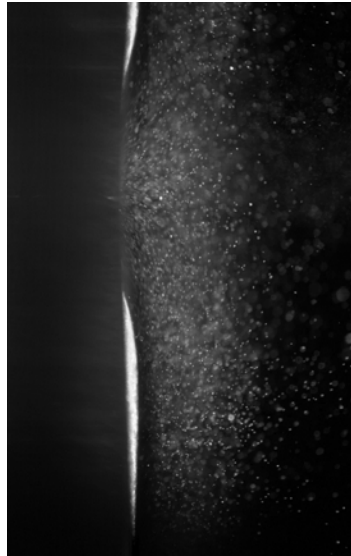
For the selected example, the investigation region is placed on the projectile shot line, which also coincides with the orifice centerline. The height of the investigation region is determined by the funnel diameter. Width of the investigation region is selected based on the particle density. Due to unevenness in particle density, detection of the flow field



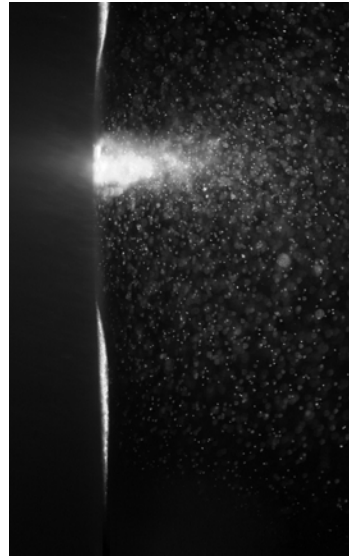
(a) Seed prior to impact



(b) Projectile at impact



(c) 1.0 *ms* after impact



(d) 3.6 *ms* after impact

Figure 4.1. PIV images utilizing atomized water as seed. Illumination source was a 532 nm, 12.5 W continuous wave laser sheet. Images are 800 by 1280 pixels and were taken at 10,000 fps with a  $10\ \mu s$  exposure time. Notice the particle streaking visually decreasing between (c) and (d), when the flow begins to reverse direction and spurt is beginning. A shorter streak is indicative of a lower measured entrainment velocity. Initial projectile impact velocity is approximately  $135\ m/s$ . See Fig. 4.3 for an example of the vector plots from the analyzed particle streaking [41].

becomes difficult to determine at times. If the investigation region is too small, the region will lack the necessary particles to fully represent the flow. If the investigation region is too large, the increased distance from the orifice results in particle motion measurements further away from the desired point of interest. Further distance from the point of interest may result in lower velocity measurements and an under-representation of the overall mass flow. Therefore, the height of the investigation region is set based on outer diameter of the funnel and the width is set based on particle density. For the conducted tests this was about 0.4 to 0.5 projectile diameters away from the orifice.

The post processing tools used the raw gray-scale image, as exemplified in Fig. 4.1, and performed a log transform on the measured pixel values. The log transform adjusted the contrast of the raw image in Fig. 4.2(a), resulting in a quasi-normal distribution of pixel values and is shown in Fig. 4.2(b). After the log transform, a spatial convolution filter, shown in Fig. 4.2(c) further separates the streak's signal from the background noise and enhances streak brightness [45]. After a binary threshold is applied to the filtered image, shown in Fig. 4.2(d), the streak length, location, and angle data are measured and recorded.

Figure 4.3 is the plot of the detected and measured vectors in the specified investigation region. Notice the horizontal component of the vectors becoming larger towards the center of the image as expected for flow through an orifice [46]. Not only does the velocity vary with radial distance from the orifice centerline, but it also varies with time as indicated by the difference between vector density and length between Fig. 4.3(a), (b), (c), and (d). Also notice the spread of the vectors between Fig. 4.3(a) through(d). The spread and distribution is accounted for by recording the location of the vector relative to the projectile shot-line. Since the primary focus is to measure the entrainment velocity, only the horizontal component of the streaks in the investigation region are needed. A plot, showcasing the analysis from a couple images, is shown in Fig. 4.4(a) and (b). The error bars in this plot is based on the detection of the streak length within  $\pm 1$  pixel of the true streak length. If

the measured streak's length is off by 1 pixel, this results in an error ranging from 30% to under 3% based on the length of the streak data collected.

To obtain the mass flow, an integral of each image's velocity profile is performed across the funnel's diameter. The general orifice flow equations assuming minimal density changes across the investigation region are utilized as a guide to calculate the mass flow through the orifice and shown in Eq. 4.5.

$$\dot{m}_O(t) = \int_0^r \rho_{Air} V_F(r, t) 2\pi r dr \quad (4.5)$$

where  $\dot{m}_O(t)$  is the mass flow through the orifice,  $\rho_{Air}$  is the density of air at atmospheric conditions,  $V_F(r, t)$  is the velocity measurement across the funnel at time  $t$  at radial component  $r$ , which ranges from 0 (orifice centerline) to the outer radius of the funnel. The raw measured velocity profile shown in Fig. 4.3, yields individual velocity vectors at radial component  $r$ , as shown in Fig. 4.4. Hence,  $V_F(r, t)$  is not a continuous function, and application of Eq 4.5 is not possible.

The profile velocity generally decreased as the distance from the orifice centerline increased across the funnel as shown in Fig. 4.4 as expected for flow through an orifice. Additionally, notice the velocity profile increasing from Fig. 4.4(a) to (b) indicating the mass flow rate is changing from image to image. Since the velocity profile varies with time, it is expected the mass flow rate would also change with time to satisfy the non-constant cavity growth rates discovered in previous research [5–7, 20].

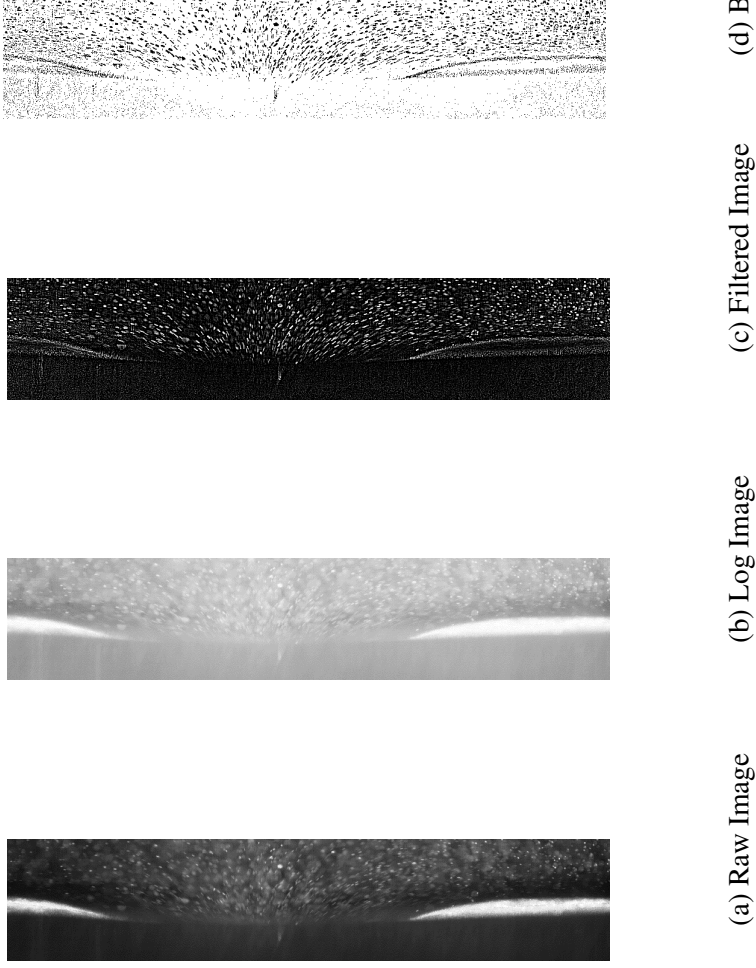
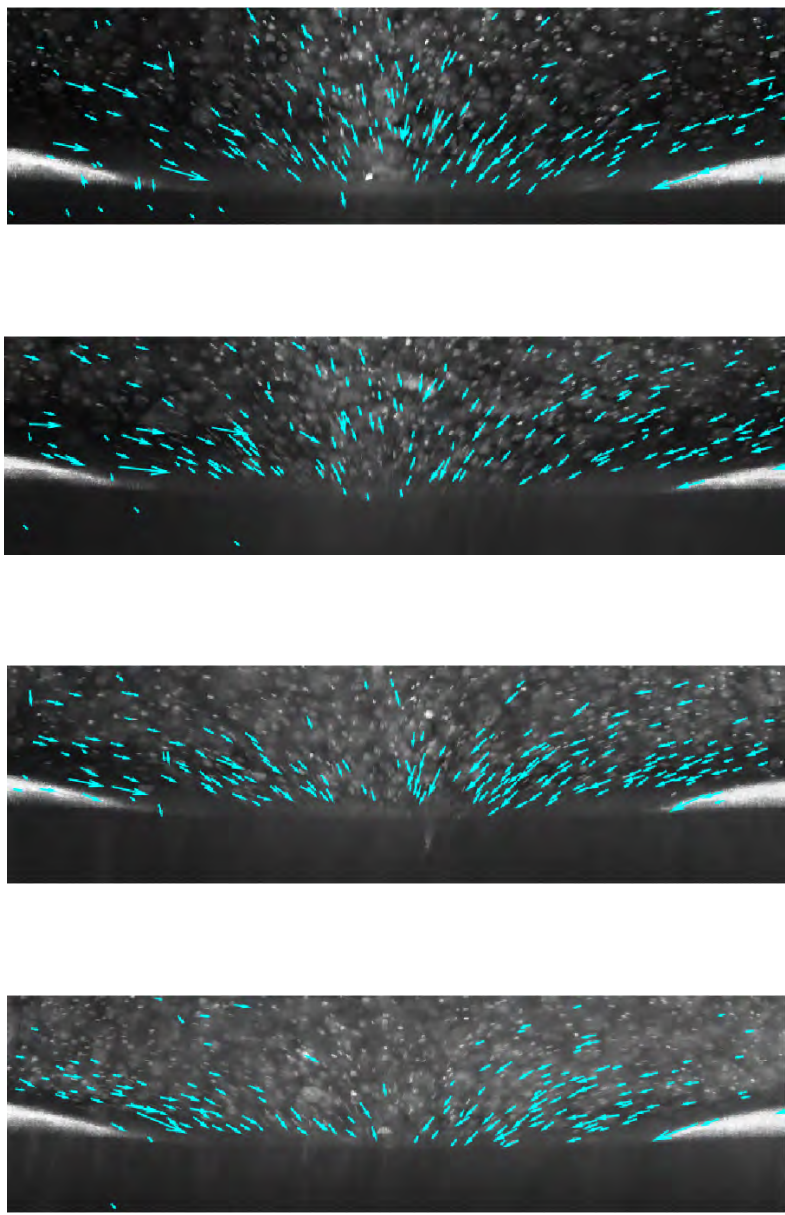


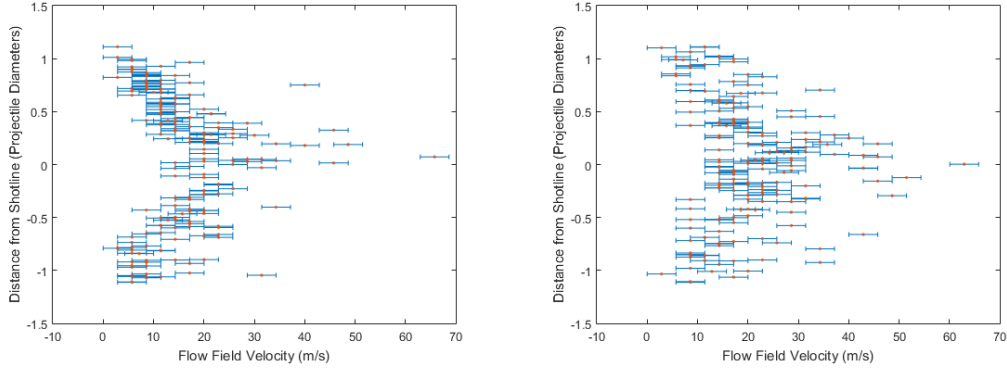
Figure 4.2. The above image processing sequence for a single image is applied to detect the streaks necessary for flow field characterization. First, the pixel values of the raw image, (a), are transformed using a log function to form Fig (b). Then, a convolution filter is applied to detect the edges of the streaks as shown in (c). After the convolution, a threshold is utilized to generate a binary shown in (d). The binary image is then filtered for aberrations and cropped to fit the investigation region. The detected streaks' length and orientation are recorded as flow field vectors. Examples of flow vectors at multiple instances in time are plotted in Fig. 4.3 [41].





(a) 0.7 *ms* after impact      (b) 1.0 *ms* after impact      (c) 1.5 *ms* after impact      (d) 2.0 *ms* after impact

Figure 4.3. Vector flow field results from streak analysis in the defined investigation region per Fig. 3.11. Images were collected at 10,000 frames per second with a 10  $\mu s$  exposure time [41].



(a)  $V_F$  profile across funnel 1.0  $ms$  after impact      (b)  $V_F$  profile across funnel 2.0  $ms$  after impact

Figure 4.4. Depiction of the measured horizontal velocity profile data at different radial funnel positions at different instances in time. Notice the overall increase in the general velocity profile between (a) and (b) [41].

A trapezoidal approximation for a volume of revolution is used to approximate the volume under the measured piecewise velocity profile. In a traditional application of the trapezoidal rule, the distance between the length of the trapezoid's base,  $\Delta r$ , is controlled. In this experiment, control over  $\Delta r$  is not possible since  $\Delta r$  is essentially the vertical distance between seed particles. Therefore, linear interpolation between neighboring horizontal velocity vectors was necessary since the slope of the trapezoid changes. Computation of the volume of revolution between each horizontal velocity vector is possible by accounting for the slope of the trapezoid as the radial distance from the orifice centerline changes. The linearly interpolated piecewise equation between each horizontal velocity vector to determine the slope of the trapezoid is shown in Eq. 4.6.

$$V_F(r, t) = z_i r + b_i \quad (4.6)$$

where  $V_F(r, t)$  is continuous from  $r_i$  to  $r_{i+1}$ , and  $z_i$  and  $b_i$  are defined in Eq. 4.7 and 4.8, respectively.

$$z_i = \frac{V_F(r_i, t) - V_F(r_{i+1}, t)}{r_i - r_{i+1}} \quad (4.7)$$

$$b_i = V_F(r_i, t) - \frac{V_F(r_i, t) - V_F(r_{i+1}, t)}{r_i - r_{i+1}} r_i \quad (4.8)$$

Equation 4.5 becomes a piecewise continuous function over  $r_i$  to  $r_{i+1}$ , and the mass flow rate through the corresponding sub-area has the form:

$$\dot{m}_{O_i}(t) = \int_{r_i}^{r_{i+1}} \rho_{Air} [z_i r + b_i] 2\pi r dr = 2\pi \rho_{Air} \left[ \frac{z_i r_{i+1}^3}{3} - \frac{z_i r_i^3}{3} + \frac{b_i r_{i+1}^2}{2} - \frac{b_i r_i^2}{2} \right] \text{ for } r_i \in [0, r] \quad (4.9)$$

where  $\dot{m}_{O_i}(t)$  is a portion of the of the total mass flow rate occurring through the funnel sub-area between radial positions  $r_i$  to  $r_{i+1}$ ,  $i$  ranges from 1 to  $n - 1$ ,  $n$  is the total number of velocity vectors in the image collected at time  $t$ ,  $z_i$  and  $b_i$  are the coefficients determined from linearly interpolating between  $V_F(r_i, t)$  and  $V_F(r_{i+1}, t)$ . Equation 4.9 assumes axisymmetric flow and  $r_i \in [0, r]$ . In the data collected,  $r_i \in [-r, r]$  requiring modification of Eq. 4.9, so the volume of revolution around the funnel isn't counted twice.

$$\dot{m}_{O_i}(t) = \pi \rho_{Air} \left[ \frac{z_i r_{i+1}^3}{3} - \frac{z_i r_i^3}{3} + \frac{b_i r_{i+1}^2}{2} - \frac{b_i r_i^2}{2} \right] \text{ for } r_i \in [-r, r] \quad (4.10)$$

Each  $\dot{m}_{O_i}(t)$  is a subset of the mass flow through the applicable funnel sub-area, the summation of each piecewise mass flow rate is necessary to obtain the overall mass flow rate across the entire funnel as shown in Eq. 4.11. Therefore, the mass flow, for each image, through the funnel is obtained using Eq. 4.11 by summing the piecewise mass flow rate at the calculated  $i^{th}$  funnel sub-volume based on the measured velocity vectors obtained in images like those found in Fig. 4.3.

$$\dot{m}_O(t) = \sum_{i=1}^{n-1} \dot{m}_{O_i}(t) \quad (4.11)$$

To obtain the mass flow for each impact condition, the velocity profile data for each image was collected and analyzed from the first image after projectile impact until the

reversal of the flow direction. As stated earlier, a pressure wave from the projectile impact dissipated particles on the shot plate and obscured the flow field for the first few images after impact. These obstructions resulted in a time delay after impact to when mass flow calculations are possible.

For the selected test case, directly after impact, the flow field is obstructed for the first 0.5 *ms*. As the obstructions dissipated, and the flow field became established, the length of the streaks were detected. As expected, bulk velocity flow measured through the orifice initially starts slow, at roughly 47 *m/s*, relative to the projectile impact velocity of 135 *m/s*. After initial penetration, the HRAM cavity volume is small, not much larger than the projectile. Measurements show as the cavity grows, air entrainment from outside the tank occurs. The resulting entrained mass flow rate was found to increase with time as shown in Fig. 4.5. The mass flow increases to a maximum until approximately 1.5 to 2.0 *ms* after impact, at which time the cavity contracts around the orifice causing the mass flow to drop.

The experimental process was repeated with the same size sphere at different projectile velocities referenced in Table 4.1. Comprehensive details for the measured velocity profiles and entrainment calculations are provided in Appendix B, while the resultant mass flow rates are summarized in Fig. 4.6. The observed mass entrainment trends appear largely independent of impact velocity. Qualitative results regarding the calculated mass flow rate were obtained by observing the corresponding internal cavity geometric features for tests at similar impact conditions.

Here it is advantageous to briefly introduce and discuss the cavity contraction and cavity separation phase, and examine these phases as they correlate to the entrained mass flow calculations. Cavity contraction and separation are pre-cursors for the initiation of the transient spray phases. The specific geometric features were determined by research conducted with the 96<sup>th</sup> TG. An in-depth discussion on the research behind each cavity geometric phase takes place in Section 4.3.

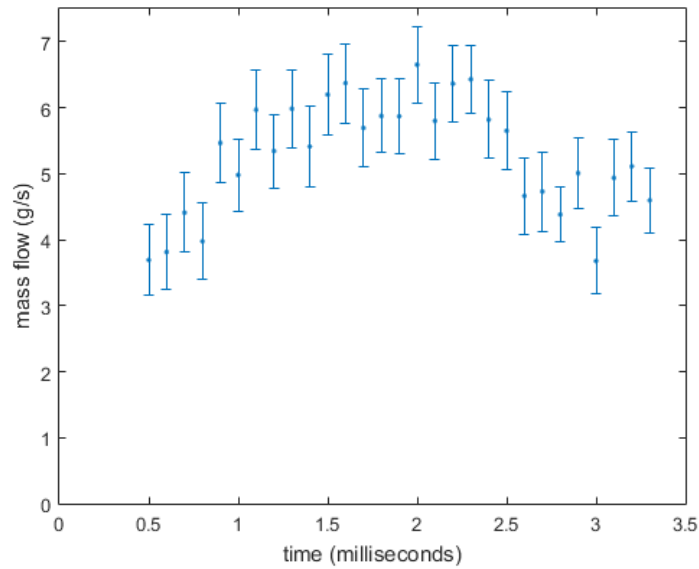
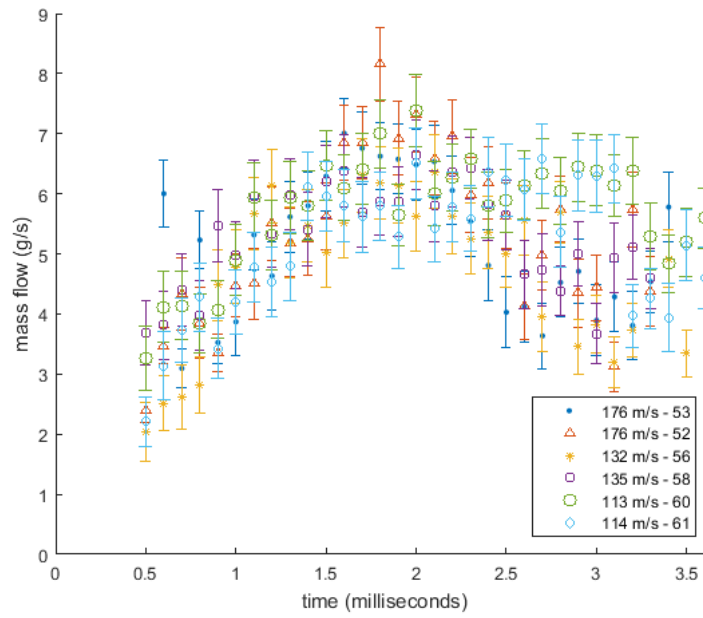
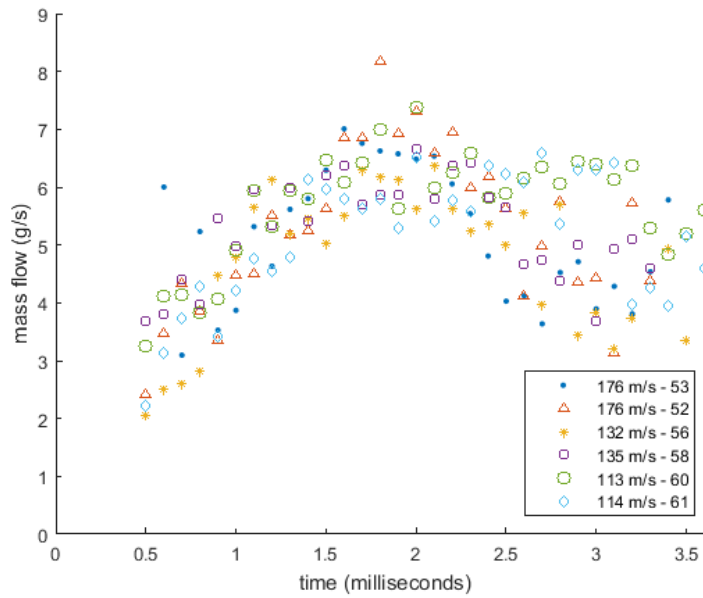


Figure 4.5. A trapazoidal approximation of a volume of revolution was applied to the measured velocity profiles per Eq. 4.11 to obtain the mass flow rate through the orifice. The error bars represent the propagation of the error from the measured streak data. Notice the flow rate reaches a maximum around 1.5 *ms* which corresponds to the initiation of cavity contraction at the orifice. The calculated mass flow continues to change and correlates well with cavity separation and conduit severance.



(a) Mass flow rate data with error bars.



(b) Mass flow rate data without error bars.

Figure 4.6. Time-resolved mass entrainment calculations for different impact velocities. The mass flow reaches a maximum approximately 1.5 to 2 *ms* after initial impact. The maximum mass flow rates correlated well with internal cavity dynamics.

Table 4.1. Projectile Parameters for HRAM Entrainment Experiments

Reference Number	Material	Diameter (cm)	Impact Velocity (m/s)
53	Steel	0.953	176
52	Steel	0.953	176
56	Steel	0.953	132
58	Steel	0.953	135
60	Steel	0.953	113
61	Steel	0.953	114

Cavity contraction phase occurs when the cavity diameter at the orifice began to contract. The cavity formed a re-entrant jet when the cavity contracted around the orifice. Cavity separation phase occurs after cavity contraction when the cavity separated from the shot plate. During cavity separation, a conduit is formed linking the cavity to the orifice. Discussion on the A discussion of the cavity's evolution and the corresponding calculated mass flow is presented below.

Figure 4.7 through 4.9 shows the evolution of cavity geometry for each of the different impact velocities. Looking at cavity evolution provides the ability to visualize how the cavity is behaving in conjunction with the changing mass flow rate. Looking at the 176 *m/s* show, at impact the cavity is small, as shown in Fig. 4.7(a). The mass flow rate is not calculated due to the aforementioned obstructions. The cavity gets larger while it is attached to the orifice, as shown in Fig. 4.7(b), the mass flow also increases per Fig. 4.6.

For the 176 *m/s* shot, the maximum mass flow rate coincides approximately with the initiation of cavity contraction at the orifice, as shown in Fig. 4.7(c). As the cavity contracts around the orifice, it forms a re-entrant jet at the rear of the cavity, where the water mixes with the incoming entrained air as shown in Fig. 4.7(d), (e), and (f). The introduction

of the additional mass mixing with the incoming entrained air constricts the orifice flow and resulted in the mass flow rate drop seen in Fig. 4.6 after 2.0 *ms*. As the re-entrant jet continues to form, the cavity begins to separate from the shot plate and creates a conduit between the cavity and the orifice, also seen in Fig. 4.7(d), (e), and (f). The conduit forms due to the significant low-pressure region in the cavity well below atmospheric pressure and is sufficient to draw ambient air through the orifice, albeit at a reduced rate. As the cavity continues to separate from the shot plate, the conduit extends until it is severed in Fig. 4.7(g), and the orifice mass flow begins its reversal. Once the flow reverses, the fluid spurts out of the tank as shown in Fig. 4.1(d).

For the medium velocity shots, the cavity is very small at impact as shown in Fig. 4.8(a). At an approximate impact velocity of 132 *m/s*, the mass flow rate also increased as the cavity grew in size while it was attached to the orifice as shown in Fig. 4.8(b). The maximum flow rate, per Fig. 4.6, also coincided with the cavity contraction around the orifice around 1.5 *ms* shown in Fig. 4.8(c). A conduit also forms connecting the orifice to the cavity's rear as the re-entrant begins to supply a water/vapor mixture to the cavity displayed in Fig. 4.8(d), (e), and (f). Similarly, entrained gases continue to flow through the orifice and the conduit, but at a reduced rate similar to the 176 *m/s* impact velocities. Once the conduit severs in Fig. 4.8(g), the flow begins its reversal and the liquid spurt is observed.

Figure 4.9(a) shows the small cavity at projectile impact. At an approximate impact velocity of 114 *m/s*, the low velocity shot's mass flow rate increased per Fig. 4.6 as the cavity grew in size while it was attached to the orifice as shown in Fig. 4.9(b). The maximum flow rate also coincided with the cavity contraction around the orifice around 1.5 *ms* as shown in Fig. 4.9(c). As the cavity separated from the shot plate, the conduit formed in Fig. 4.9(d), (e), and (f) is similar to the conduit formed in the 132 and 176 *m/s* shots. However, the lower velocity shot's conduit takes longer to sever. This is most likely





(a) At impact



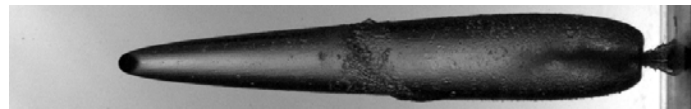
(b) 1.00 *ms* after impact



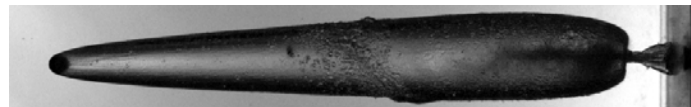
(c) 1.50 *ms* after impact



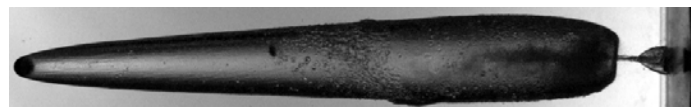
(d) 2.00 *ms* after impact



(e) 2.75 *ms* after impact

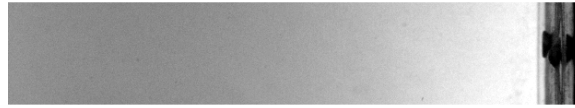


(f) 3.30 *ms* after impact



(g) 3.60 *ms* after impact

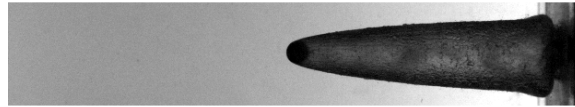
Figure 4.7. HRAM cavity growth for 0.953 *cm* steel sphere projectile at an impact velocity of approximately 176 *m/s*. Imagery was collected at 20,000 frames per second with a 4  $\mu s$  exposure time at a resolution of 768 by 1024 pixels utilizing a brightfield technique [34]. The imagery displayed was cropped to a resolution of 130 by 865 pixels.



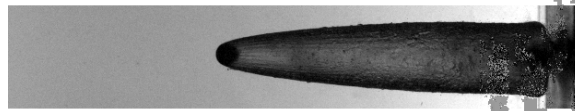
(a) At impact



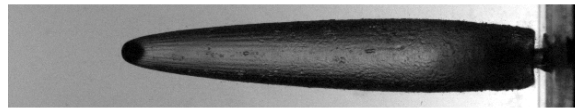
(b) 1.00 *ms* after impact



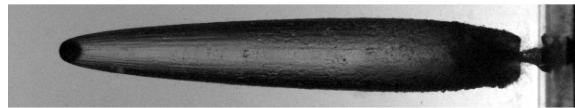
(c) 1.50 *ms* after impact



(d) 2.00 *ms* after impact



(e) 2.75 *ms* after impact



(f) 3.30 *ms* after impact

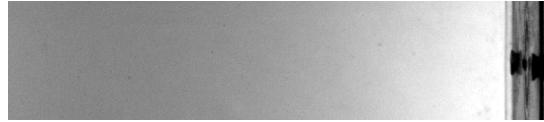


(g) 3.60 *ms* after impact

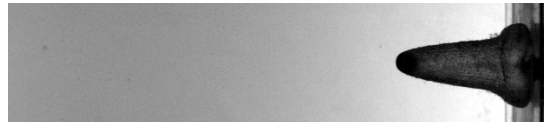
Figure 4.8. HRAM cavity growth for 0.953 *cm* steel sphere projectile at an impact velocity of approximately 132 *m/s*. Imagery was collected at 20,000 frames per second with a 4  $\mu$ s exposure time at a resolution of 768 by 1024 pixels utilizing a brightfield technique [34]. The imagery displayed was cropped to a resolution of 110 by 625 pixels.

due to the rate of cavity separation from the shot plate, which is also likely related to the projectile's velocity. The conduit taking longer to sever also explains why the mass flow rate for the lower impact velocities does not fall as rapidly as compared to the faster impact velocities as seen in Fig. 4.6. Eventually, the conduit is severed in Fig. 4.9(g) and the flow begins its reversal.

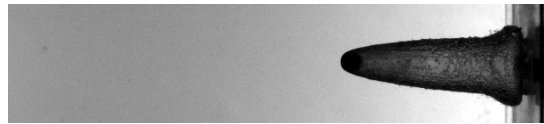
For the data collected, the internal cavity dynamics correlate well with the mass flow diagrams. The transient spray via the orifice occurred at different times for different impact velocities, as expected, and approximately correlated well with the severance of the conduit from the cavity. Synchronized imagery of both the internal and external views of the tank were collected in the following research. Some of the results from the synchronized imagery were already presented for complete and thorough discussion of the calculated mass flow with regards to cavity contraction, separation and the conduit. Further results and discussion of the synchronized image research is necessary to present the cavity geometric features occurring prior to the initiation of the transient spray phases and to bound the cavity features of interest.



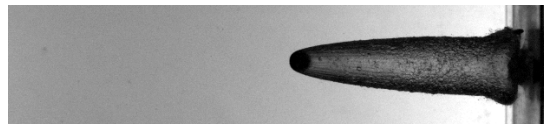
(a) At impact



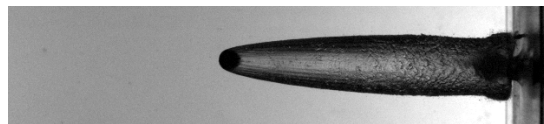
(b) 1.00 *ms* after impact



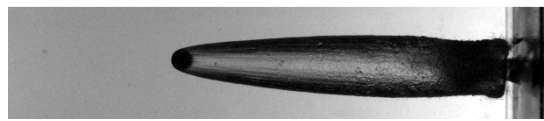
(c) 1.50 *ms* after impact



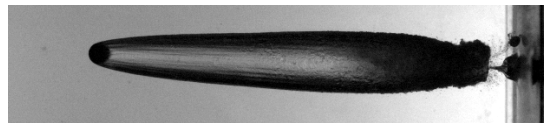
(d) 2.00 *ms* after impact



(e) 2.75 *ms* after impact



(f) 3.30 *ms* after impact



(g) 4.35 *ms* after impact

Figure 4.9. HRAM cavity growth for 0.953 *cm* steel sphere projectile at an impact velocity of approximately 114 *m/s*. Imagery was collected at 20,000 frames per second with a 4  $\mu$ s exposure time at a resolution of 768 by 1024 pixels utilizing a brightfield technique [34]. The imagery displayed was cropped to a resolution of 128 by 625 pixels.

### 4.3 Relationship Between HRAM Cavity Geometric Features and the Transient Spray

A partnership with AFIT and the 96<sup>th</sup> TG permitted the sharing of high-speed cameras to collect synchronized imagery on the tank's interior and exterior. The focus of the research was to determine which internal cavity geometric features contributed to the transient spray. The cameras operated at 28,000 *Hz* with a 35  $\mu s$  exposure time except for the 1,200 *m/s* external view which used a 20  $\mu s$  exposure time. Each camera was synchronized within 200 nanoseconds of each other and were triggered via an oscilloscope monitored accelerometer. The synchronized high-speed cameras captured some interesting results and are shown in Fig. 4.10 through 4.15. Tests were conducted at a nominal velocity of 1,200, 1,495, and 1,800 *m/s*, which is approximately 10 times faster than the shots conducted at AFIT as detailed in Section 4.2. Experiments conducted in 96<sup>th</sup> TG's facility yielded qualitative observations of the cavity's geometric features and their relationship to the transient spray.

#### 4.3.1 Observations from the 1,200 *m/s* Shot.

The exterior view of Fig. 4.10 and 4.11 used a 20  $\mu s$  exposure time versus the 35  $\mu s$  exposure time for the internal view. The different exposure times explains why the projectile is seen, just prior to impact, streaking through Fig. 4.10(a) while initial penetration of the tank is seen in the corresponding internal Fig. 4.10(b). Only the 1,200 *m/s* shots had different exposure times. All other exposure times were 35  $\mu s$ . After impact, the flash dissipates radially outward in Fig. 4.10(c) as the first stages of cavity formation is observed in Fig. 4.10(d). Notice the conical shape of the cavity and the increasing cavity diameter at the penetration orifice.

For the 1,200 *m/s* shot, no evidence of pre-spurt was observed externally, as depicted in Fig. 4.10(e), even though the cavity contracted around the orifice and formed a re-entrant jet as shown in Fig. 4.10(f). Pre-spurt was observed during cavity contraction for both the

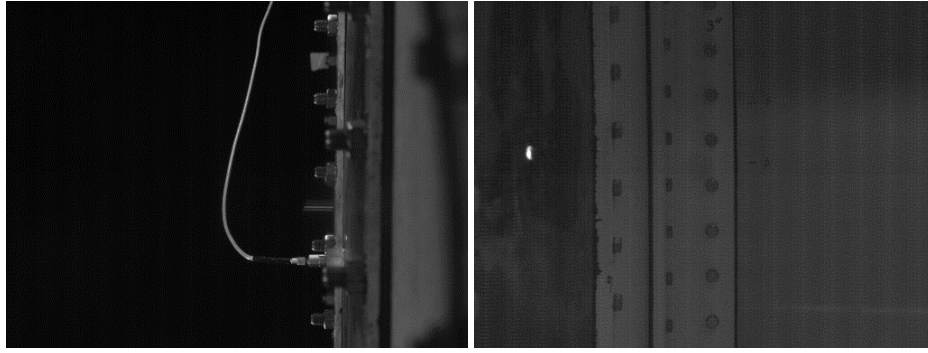
1,495 and 1,800  $m/s$  impact velocities. The lack of repeatable pre-spurt observations was noticed in previous research for replicated experiments [1]. Every instance when pre-spurt was detected, cavity contraction was observed. However, every time cavity contraction was observed, pre-spurt was not always detected, as discussed during the 1,200  $m/s$  shot. These observations indicate cavity contraction is a pre-cursor for the transient spray phases, but additional parameters such as petaling of the shot plate and the opposing jets caused by cavity seal at the orifice need consideration [14, 18, 23, 47, 48].

Since no pre-spurt was observed, no fluid is seen in Fig. 4.11(a). The conduit was formed, highlighted by the arrow in Fig. 4.11(b), as the cavity separated from the shot plate. The first instance of liquid ejecting from the tank was highlighted by the ellipse shown in Fig. 4.11(c) as the conduit became severed, as shown in Fig. 4.11(d). Past research potentially would label this liquid discharge as pre-spurt because it is the first instance of fluid ejecting from the orifice. However, because the data collected permitted synchronized internal and external imagery analysis, it is shown the ejecta in Fig. 4.11(c) and (e) is due to the severance of the conduit which correlated well with main spurt observations at the 1,495 and 1,800  $m/s$  impact velocities. As the event continued, the main spurt continued to flow away from the orifice as the cavity continued to separate from the shot plate as shown in Fig. 4.11(e) and (f), respectively.

In summary, the pre-spurt did not occur for the 1,200  $m/s$  shot after cavity contraction at the orifice which is in-line with difficulties in repeatable pre-spurt observations documented in previous research [1]. Main spurt occurred after the conduit became severed once the cavity separated from the shot plate. Initiation of the main spurt is very similar between the 1,200, 1,495, and 1,800  $m/s$  impact velocities.

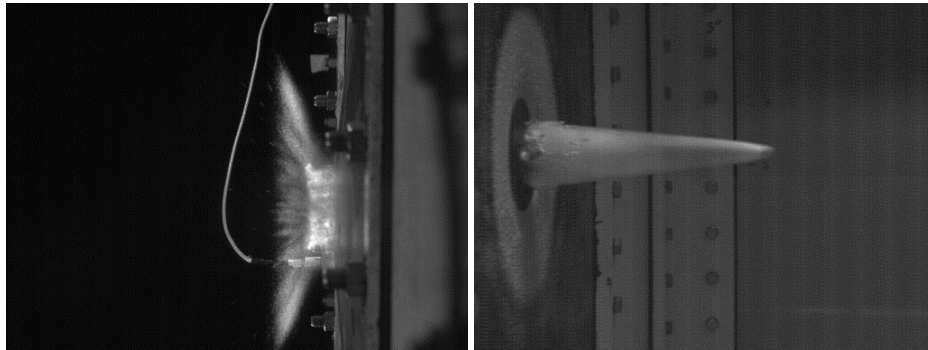
#### ***4.3.2 Observations from the 1,495 $m/s$ Shot.***

The pre-spurt and main spurt phases were observed for the 1,495  $m/s$  shot. When the projectile impacted the shot plate, it exchanged kinetic energy and created a flash, and



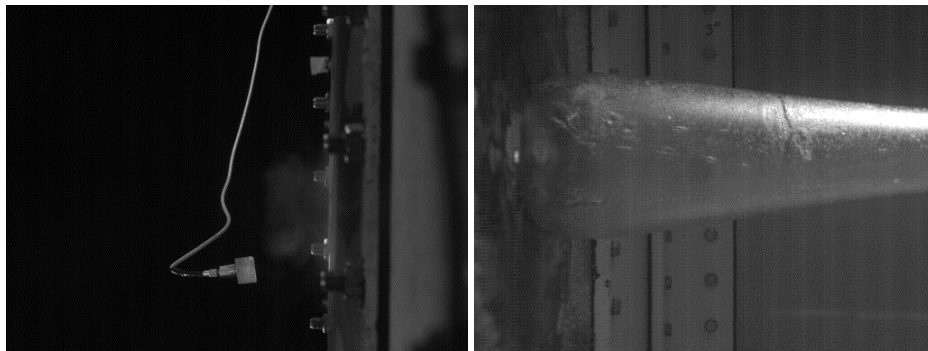
(a) EV at  $t=0\text{ ms}$

(b) IV at  $t=0\text{ ms}$



(c) EV at  $t=0.357\text{ ms}$

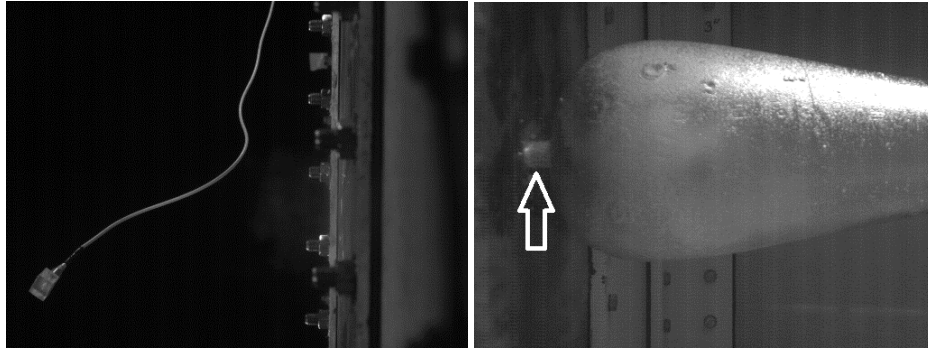
(d) IV at  $t=0.357\text{ ms}$



(e) EV at  $t=3.036\text{ ms}$

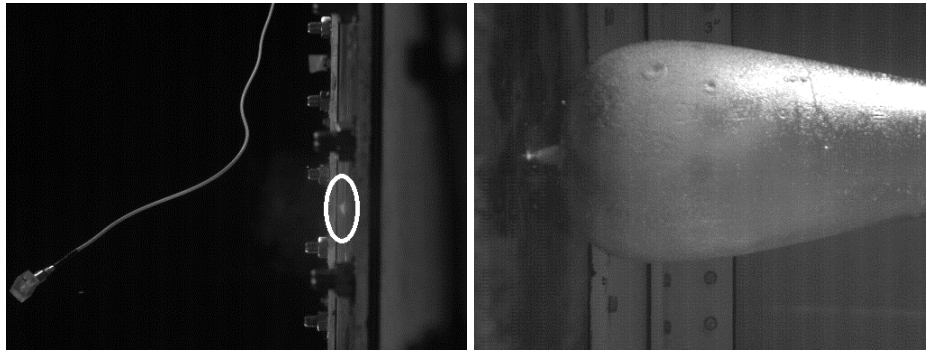
(f) IV at  $t=3.036\text{ ms}$

Figure 4.10. Exterior view (EV) and Interior view (IV) of HRAM imagery data obtained with the 96<sup>th</sup> Test Group Aerospace Vehicle Survivability Flight. The projectile was a 0.953 *cm* steel sphere with an impact velocity of approximately 1,200 *m/s*. The above images were obtained utilizing high-speed, synchronized cameras. Continuation of the event is seen in Fig 4.11.



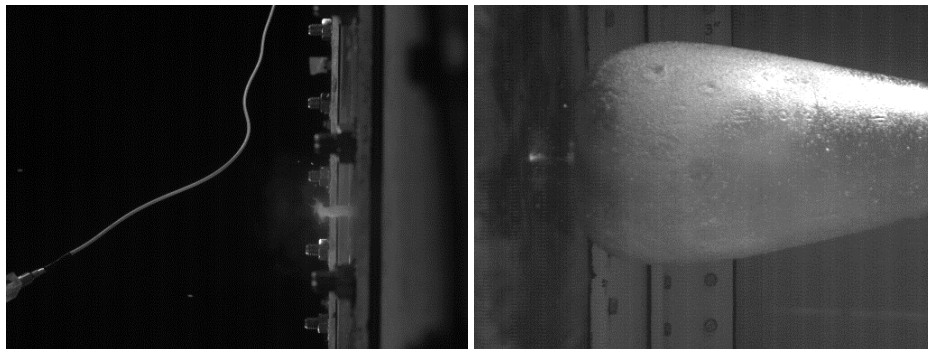
(a) EV at  $t=9.107\text{ ms}$

(b) IV at  $t=9.107\text{ ms}$



(c) EV at  $t=9.714\text{ ms}$

(d) IV at  $t=9.714\text{ ms}$



(e) EV at  $t=10.250\text{ ms}$

(f) IV at  $t=10.250\text{ ms}$

Figure 4.11. Exterior view (EV) and Interior view (IV) of HRAM imagery data obtained with the 96<sup>th</sup> Test Group Aerospace Vehicle Survivability Flight. The above images were obtained utilizing high-speed, synchronized cameras. The projectile was a 0.953 cm steel sphere with an impact velocity of approximately 1,200 m/s.



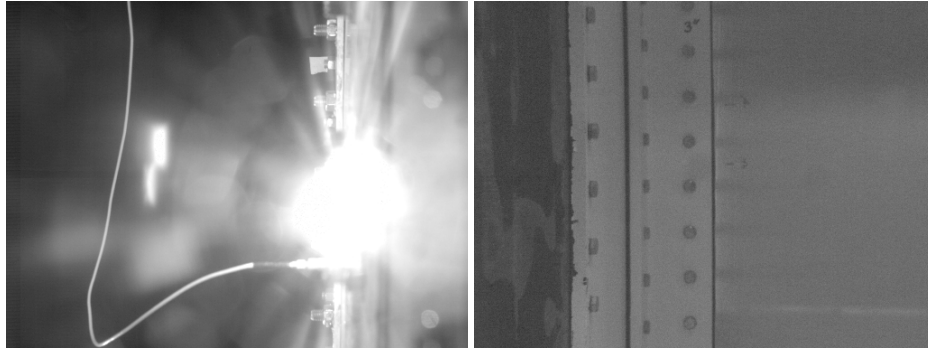
over saturated the camera's sensor, as shown in Fig. 4.12(a). As expected, no penetration or cavity is seen in the corresponding Fig. 4.12(b). Figure 4.12(c) is taken 0.321 *ms* after impact while the flash appears to dissipate radially away from the impact point. As the flash is moving away from the orifice, initial cavity formation is shown in Fig. 4.12(d) with increasing cavity diameter at the orifice. Eventually, the cavity diameter reaches its maximum and begins to contract. The pre-spurt is observed, as shown in Fig. 4.12(e), once the cavity contracts at the orifice as shown in Fig. 4.12(f).

In Fig. 4.13(a) and (b), the pre-spurt continued to move away from the orifice as the cavity contracted and formed a re-entrant jet at the rear of the cavity. A conduit between the orifice and the cavity is formed as the cavity separated from the shot plate. The main spurt was observed, highlighted by the ellipse shown in Fig. 4.13(c), once the conduit became severed, as highlighted by the arrow in Fig. 4.13(d). As the HRAM event progressed, the main spurt continued to flow away from the orifice as the conduit retracted towards the cavity as shown in Fig. 4.13(e) and (f), respectively.

Recall, the objective of analyzing synchronized imagery was to determine the driving mechanism of the transient spray phases, to focus research efforts. For the 1,495 *m/s* shot, the pre-spurt occurred after the cavity contracted at the orifice. Main spurt occurred after the conduit became severed once the cavity separated from the shot plate as also observed during the 1,200 *m/s* shot. The observation of these HRAM cavity features correlate very well to the initiation of each transient spray phase.

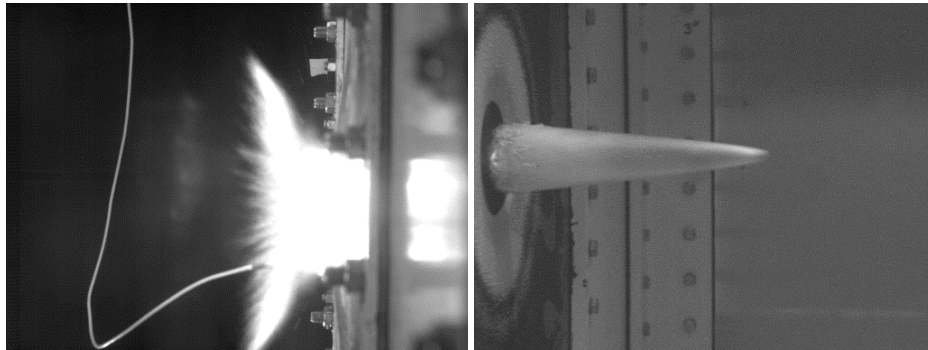
### ***4.3.3 Observations from the 1,800 m/s Shot.***

The projectile is seen just prior to impact in Fig. 4.14(a) and thus no cavity is seen in Fig. 4.14(b). Nine frames later, the flash is still present in Fig. 4.14(c), and cavity formation is also observed as shown in Fig. 4.14(d). Notice at the different impact velocities, the initial cavity formation appears very similar between the 1,200, 1,495, and 1,800 *m/s* shots. The cavity continues its formation, and the cavity's diameter at the orifice eventually reaches



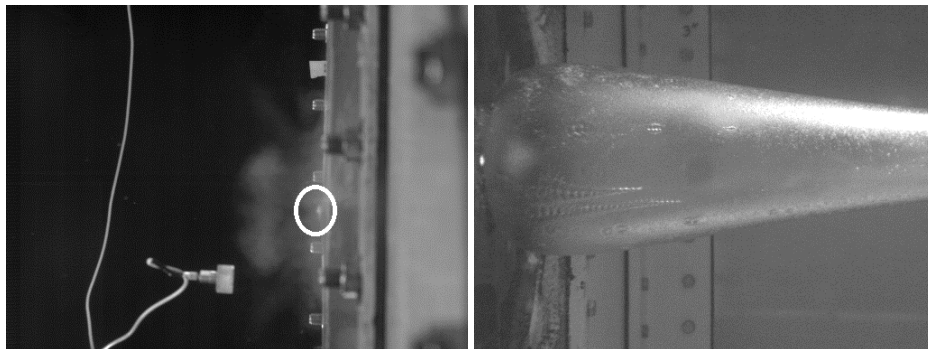
(a) EV at  $t=0\text{ ms}$

(b) IV at  $t=0\text{ ms}$



(c) EV at  $t=0.321\text{ ms}$

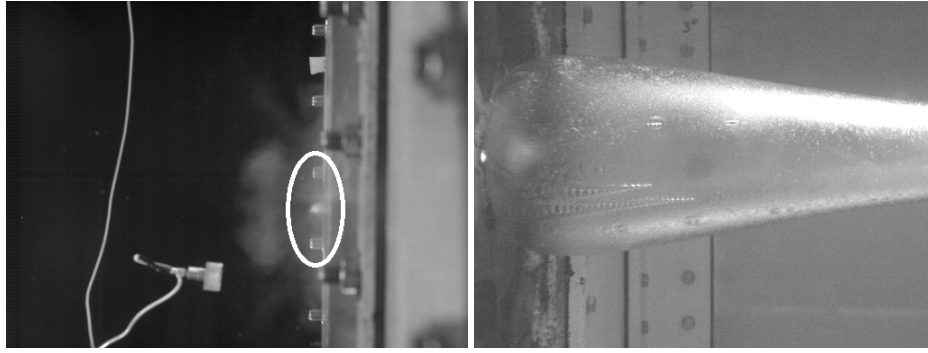
(d) IV at  $t=0.321\text{ ms}$



(e) EV at  $t=3.286\text{ ms}$

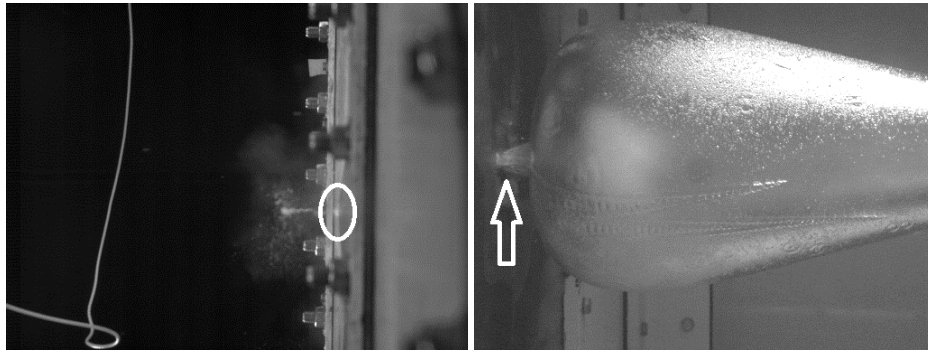
(f) IV at  $t=3.286\text{ ms}$

Figure 4.12. Exterior view (EV) and Interior view (IV) of HRAM imagery data obtained with the 96<sup>th</sup> Test Group Aerospace Vehicle Survivability Flight. The projectile was a 0.953 *cm* steel sphere with an impact velocity of approximately 1,495 *m/s*. The above images were obtained utilizing high-speed, synchronized cameras. Continuation of the event is seen in Fig 4.13 [20].



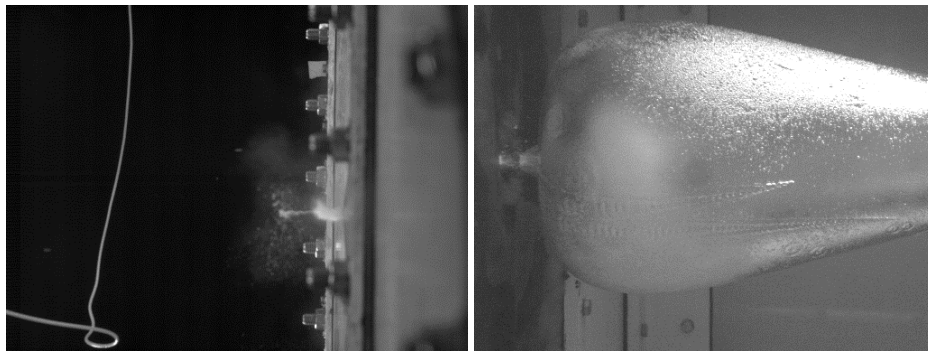
(a) EV at  $t=3.286\text{ ms}$

(b) IV at  $t=3.286\text{ ms}$



(c) EV at  $t=9.750\text{ ms}$

(d) IV at  $t=9.750\text{ ms}$



(e) EV at  $t=10.250\text{ ms}$

(f) IV at  $t=10.250\text{ ms}$

Figure 4.13. Exterior view (EV) and Interior view (IV) of HRAM imagery data obtained with the 96<sup>th</sup> Test Group Aerospace Vehicle Survivability Flight. The projectile was a 0.953 cm steel sphere with an impact velocity of approximately 1,495 m/s. The above images were obtained utilizing high-speed, synchronized cameras [20].

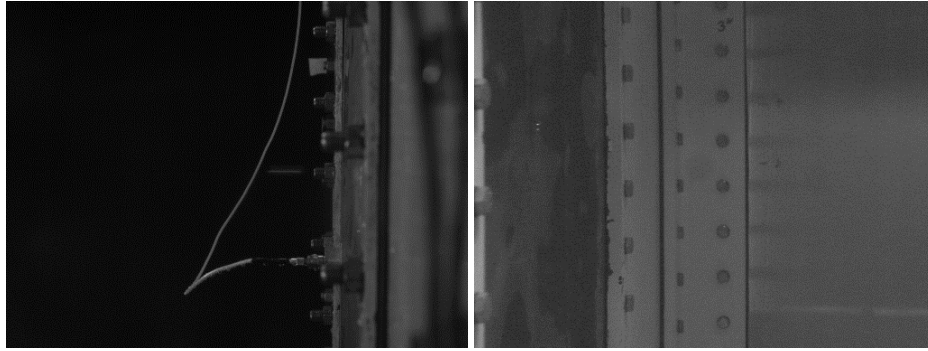
its maximum and it then begins to contract. The first instance of pre-spurt is highlighted by the ellipse shown in Fig. 4.14(e) as the cavity contracts around the orifice as shown in Fig. 4.14(f).

The pre-spurt continued to flow away from the orifice as the cavity contraction progressed and formed the re-entrant jet at the rear of the cavity as shown in Fig. 4.15(a) and (b), respectively. Once again, a conduit is formed as the cavity separates from the shot plate. The first sign of main spurt is observed within Fig. 4.15(c)'s ellipse region once the conduit is severed, as displayed in Fig. 4.15(d). The main spurt continued to flow away from the orifice as the conduit contracted towards the cavity as shown in Fig. 4.15(e) and (f), respectively.

In summary, the pre-spurt occurred after cavity contraction at the orifice as also observed in the 1,495  $m/s$  shot. Main spurt occurred after the conduit became severed once the cavity separated from the shot plate for all velocities tested. Initiation of each different transient spray phase is very similar between the 1,495 and 1,800  $m/s$  impact velocities.

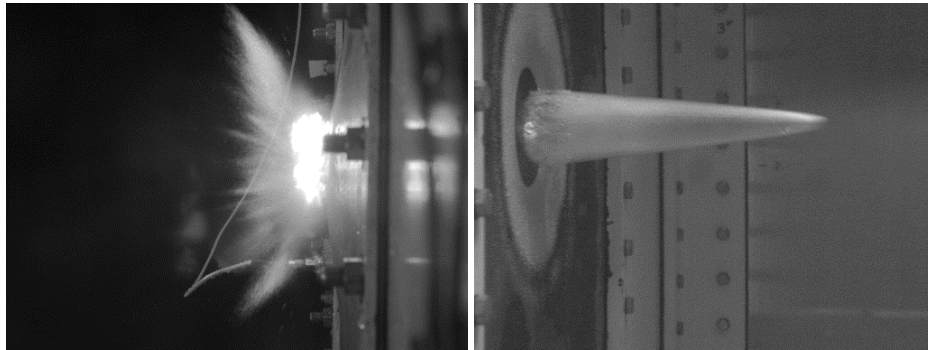
#### ***4.3.4 Overview of HRAM Cavity Observations.***

This section will provide an overview of the HRAM experiments and connect the important observations between the tested velocities, their geometric features, and the initiation of each different transient spray phase. The first observation, with regards to the transient spray, occurred after cavity formation. After the cavity's diameter reached its maximum, it began to contract around the orifice and form a re-entrant jet. For the 1,495 and 1,800  $m/s$  cases, the first signs of pre-spurt are observed once the rear of the cavity fully contracts around the orifice as shown in Fig. 4.12(e) and 4.14(e). Timing of the pre-spurt was at 2.964 and 2.464  $ms$  for the respective 1,495 and 1,800  $m/s$  shots. The pre-spurt phase was not observed for the 1,200  $m/s$  shot.



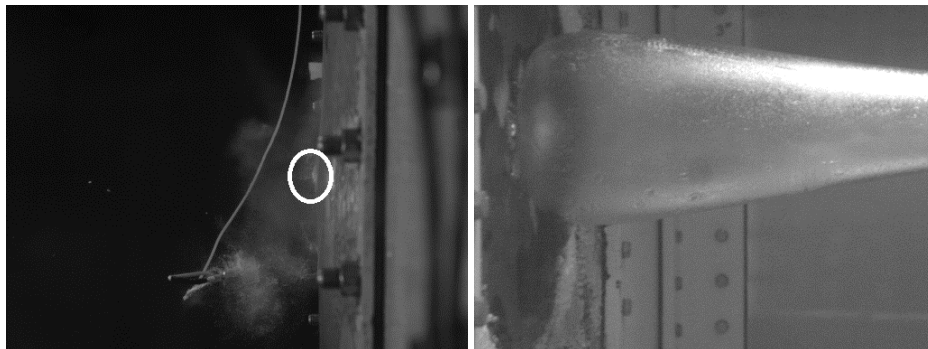
(a) EV at  $t=0$

(b) IV at  $t=0$



(c) EV at  $t=0.321\text{ ms}$

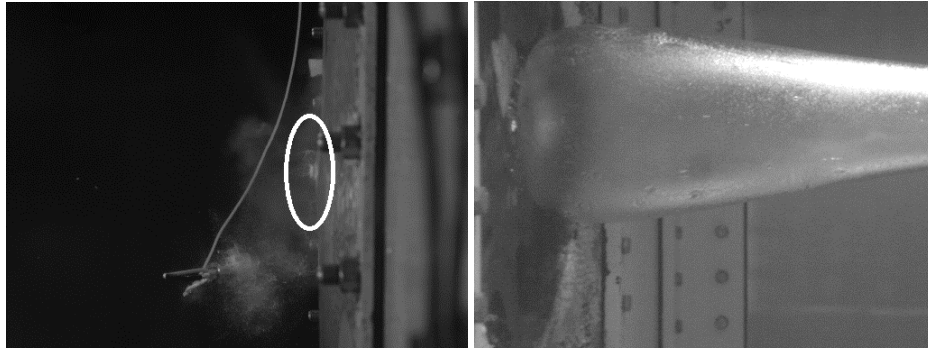
(d) IV at  $t=0.321\text{ ms}$



(e) EV at  $t=2.464\text{ ms}$

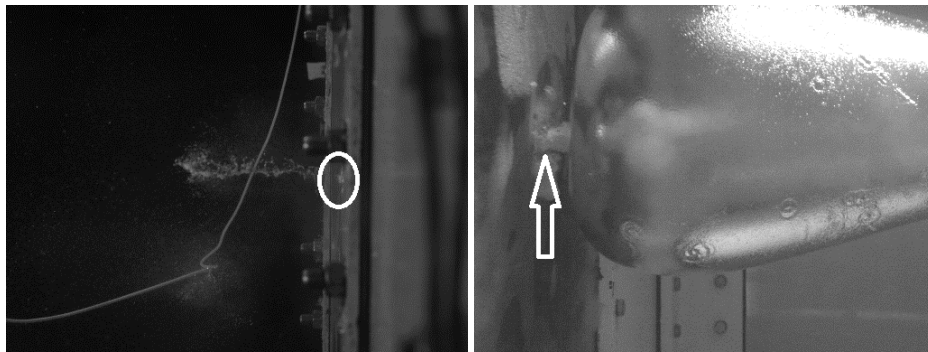
(f) IV at  $t=2.464\text{ ms}$

Figure 4.14. Exterior view (EV) and Interior view (IV) of HRAM imagery data obtained with the 96<sup>th</sup> Test Group Aerospace Vehicle Survivability Flight. The projectile was a 0.953 *cm* steel sphere with an impact velocity of approximately 1,800 *m/s*. The above images were obtained utilizing high-speed, synchronized cameras. Continuation of the event is seen in Fig 4.15.



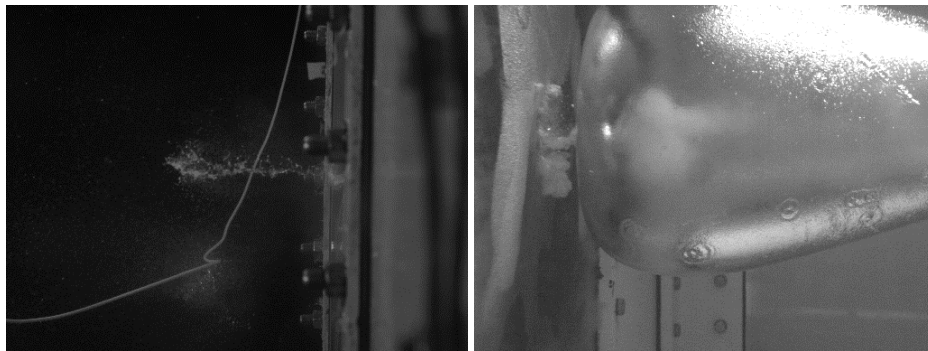
(a) EV at  $t=2.642\text{ ms}$

(b) IV at  $t=2.642\text{ ms}$



(c) EV at  $t=9.536\text{ ms}$

(d) IV at  $t=9.536\text{ ms}$



(e) EV at  $t=10.250\text{ ms}$

(f) IV at  $t=10.250\text{ ms}$

Figure 4.15. Exterior view (EV) and Interior view (IV) of HRAM imagery data obtained with the 96<sup>th</sup> Test Group Aerospace Vehicle Survivability Flight. The projectile was a 0.953 cm steel sphere with an impact velocity of approximately 1,800 m/s. The above images were obtained utilizing high-speed, synchronized cameras.

Once the cavity contracted around the orifice, it began to separate from the tank's wall. This separation created a conduit between the penetration orifice and the cavity as shown in Fig. 4.11(b), 4.13(d), and 4.15(d) for the 1,200, 1,495, and 1,800  $m/s$  shots, respectively. The conduit is formed due to the low pressure cavity continuing to draw air via the orifice at a reduced rate due to the cavity contraction and the mixing of water into the entrained air stream [41]. As the cavity continued to separate from the orifice, the conduit became severed and the main spurt is observed in Fig. 4.11(c), 4.13(c), and 4.15(c) for the 1,200, 1,495, and 1,800  $m/s$  shots, respectively. Main spurt was observed at 9.750, 9.536, and 9.714  $ms$  for the respective 1,496, 1,800, and 1,200  $m/s$  shots. A summary of the timing between the transient spray events is provided in Table 4.2.

Table 4.2. Time elapsed after projectile impact until the detected Transient Spray Events.

Velocity (m/s)	Pre-Spurt (ms)	Main Spurt (ms)	Time between Pre-Spurt and Main Spurt (ms)
1,200	–	9.714	–
1,495	2.964	9.750	6.786
1,800	2.464	9.536	7.072

In summary, the research focused on the cavity dynamics contributing to the pre-spurt and main spurt phases of the transient spray. It is advantageous to further expand Ball's cavity phase into four additional phases: *Cavity Formation Phase*, *Cavity Contraction Phase*, *Cavity Separation Phase*, and *Cavity Collapse Phase* as shown in Fig. 4.16 [4]. The cavity formation phase, in Fig. 4.16(a), occurs after projectile entry until the cavity's volume reaches its maximum. Cavity contraction, in Fig. 4.16(b), occurs when the cavity's diameter begins to constrict and close around the penetration orifice. Cavity separation

phase, in Fig. 4.16(c), occurs after the cavity has fully contracted around the orifice and has begun to separate from the shot plate. Cavity collapse, in Fig. 4.16(d), phase occurs after cavity separation and occurs when the cavity's volume starts to decrease and implode on itself. By breaking the cavity phase into the four separate phases and qualitatively looking at the cavity dynamic features contributing to the transient spray, follow-on HRAM research can now focus the mechanisms causing cavity contraction, separation, and collapse.



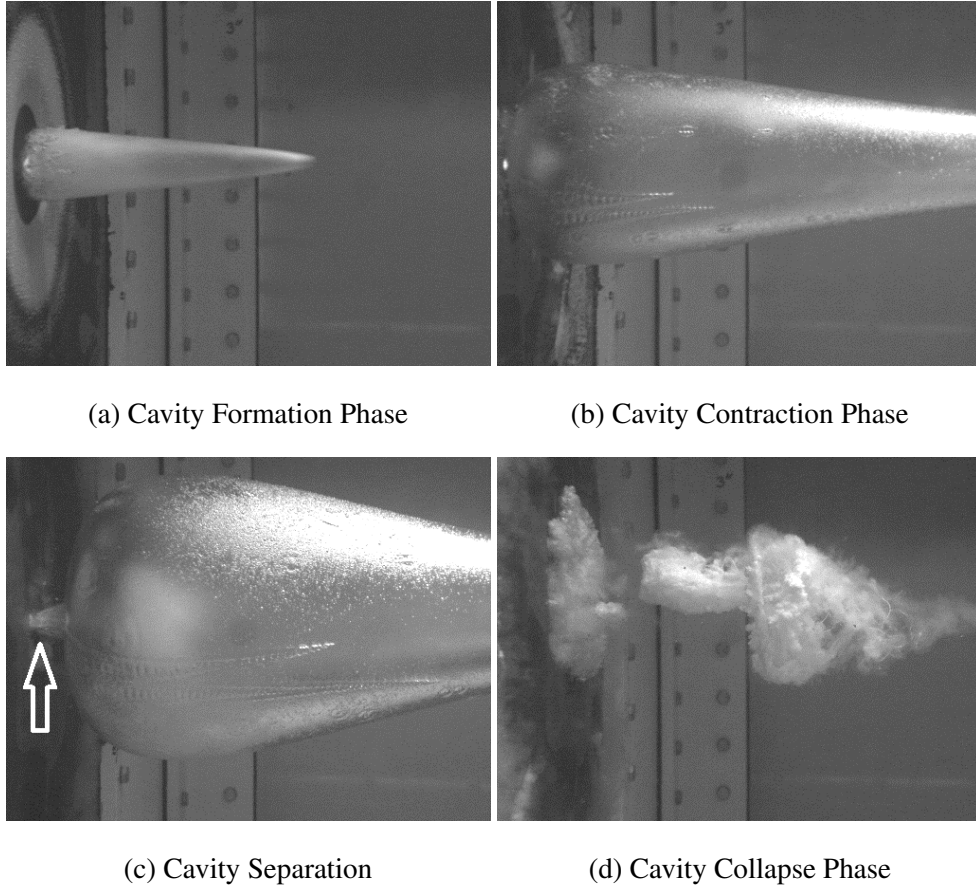


Figure 4.16. Distinguishable cavity formation, contraction, separation, and collapse phases and features that occur during an HRAM event. Cavity formation, in Fig. 4.16(a), occurs when the projectile penetrates the body of fluid and creates a cavity. Cavity contraction, in Fig. 4.16(b), occurs when the cavity's diameter at the orifice begins to decrease and contract around the orifice. Cavity separation, in Fig. 4.16(c) occurs after cavity contraction and occurs when the cavity separates from the shot plate. The cavity conduit is also present during this phase. Cavity collapse, in Fig. 4.16(d) occurs as the cavity volume decreases and implodes on itself. Research can focus on cavity contraction and separation phase, which are pre-cursors to the transient spray, by breaking down Ball's overall HRAM cavity phase [4].

#### **4.4 Determination and Discussion of Important HRAM Cavity Relationships**

This section is broken into multiple subsections to focus the discussion on specific topics of the HRAM cavity relationships. In particular, the relationships between the volumetric inflection point, cavity partial pressure, and mass entrainment rate with respect to cavity geometry is discussed in detail. Once the individual discussion of HRAM cavity topics is complete, a broad conversation on their overall contribution will ensue.

##### ***4.4.1 Volumetric Inflection Point.***

Research into HRAM cavity relationships was accomplished when the importance of cavity contraction was determined as detailed in Section 4.3. The goal of the research was to identify physical and predictable mechanisms driving or contributing to the cavity contraction. Utilizing the experimental setup in Chapter III, data were collected and analyzed at different projectile impact velocities. When calculating the total volume of the cavity, the inflection point of the curve was found to coincide with cavity contraction. Details of the data collected, and the cavity volume plots, are shown in Table 4.3 and in Fig. 4.17.

Each curve in Fig. 4.17 follows a similar trend regardless of impact velocity or projectile density. At the higher impact velocities, represented by Test 1 and 2, the volume is larger as compared to the lower impact velocities (Test 3 through 6) at similar instants in time. This makes sense due to the projectile's higher kinetic energy creating a larger volume. The volumetric growth rate is also greater for cavities from higher impact velocities. However, regardless of impact velocity, the cavity volume eventually collapses indicating the volumetric growth rate changes with time. Therefore, the inflection point indicates when the volumetric growth rate peaks.

Table 4.3. Reference Table for Projectile Parameters for HRAM Cavity Inflection Point Experiments

Reference Number	Material	Diameter (cm)	Impact Velocity (m/s)	Kinetic Energy (J)	Volumetric Inflection Point (ms)
1	Steel	0.953	142	36	1.200
2	Steel	0.953	137	33.5	1.225
3	Tungsten	0.953	80	21.4	1.150
4	Tungsten	0.953	92	28.4	1.350
5	Steel	0.953	87	13.5	1.200
6	Steel	0.953	87	13.5	1.175

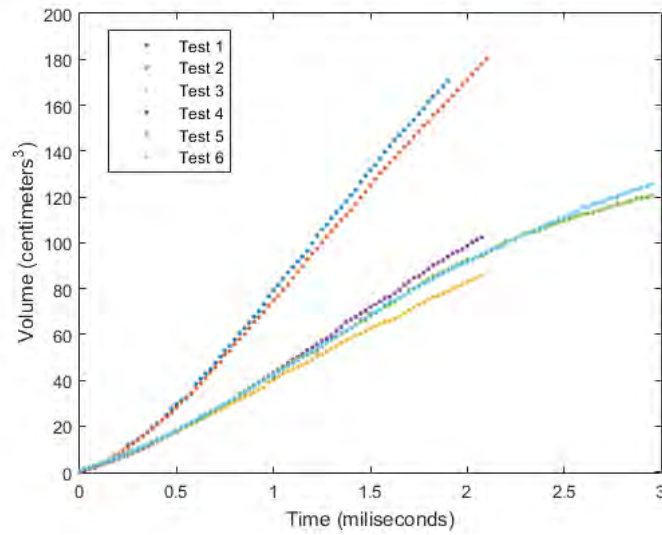


Figure 4.17. Calculated cavity volumetric data from imagery for the test cases specified in Table 4.3 [20].

From a qualitative standpoint, the inflection point in the volume versus time plots, in Fig. 4.17, makes sense for predicting cavity contraction. Inflection points indicate when a change in the system occurred. By definition, an inflection point is the second derivative of a function and is emblematic as to when the rate of change peaks or bottoms for the original function. In this case, the data in Fig. 4.17 are presented in  $cm^3$ . The cavity rate of growth rate has units of  $cm^3/s$ . Therefore, the inflection point possess units of  $cm^3/s^2$ , and represents when the cavity growth rate peaks. After the inflection point, the volumetric growth rate declines, resulting in the cavity volume increasing albeit at a slower rate.

Interestingly, the inflection point occurs just prior to the orifice mass flow reaching its maximum. Once the flow reaches its maximum, this acts as a de-facto limit on the cavity growth rate. When the flow cannot increase proportionately to accommodate the volumetric increase, the cavity growth rate peaks and then began its decrease. Currently, the flow through the orifice is measured as a function of time after projectile impact, which is useful when drawing a relationship between the different impact velocities. More discussion on the orifice flow characteristics with respect to the projectile's kinetic energy or cavity geometry is completed in Section 4.4.4.

#### ***4.4.2 Extrapolated Volumetric Data from research with the 96th Test Group.***

The imagery presented in Section 4.3 does not contain the entire cavity volume while the contraction and separation phases are occurring. Findings in Section 4.4.1 highlighted the importance of the volumetric inflection point. However, an inflection point calculation is possible by extrapolating the 1,200, 1495, and 1,800  $m/s$  imagery data and calculating the extrapolated volume over the series of images. For the 1,200  $m/s$  shot, the entire cavity volume was in the camera's field of view from 0 to 0.7857  $ms$ , while data was extrapolated from 0.8929 to 3.8929  $ms$ . For the 1,495  $m/s$  shot, the entire cavity volume was in the camera's field of view from 0 to 0.6786  $ms$ , while data was extrapolated from 0.7857 to

3.8929 *ms*. For the 1,800 *m/s* shot, the entire cavity volume was in the camera's field of view from 0 to 0.4643 *ms*, while data was extrapolated from 0.5714 to 3.6786 *ms*.

The imagery data was extrapolated by predicting projectile position and extrapolating the cavity's boundaries to the predicted location of the projectile, as shown in Fig. 4.18. The calculated cavity volume from the extrapolated images is shown in Fig. 4.19. Using the generated extrapolated imagery, cavity volume calculations were performed using similar processing techniques as detailed in Chapter III. Therefore, the accuracy of the cavity volume calculation is dependent on the accuracy of the projectile position, which is unknown. The full range of extrapolated images is shown in Appendix D.

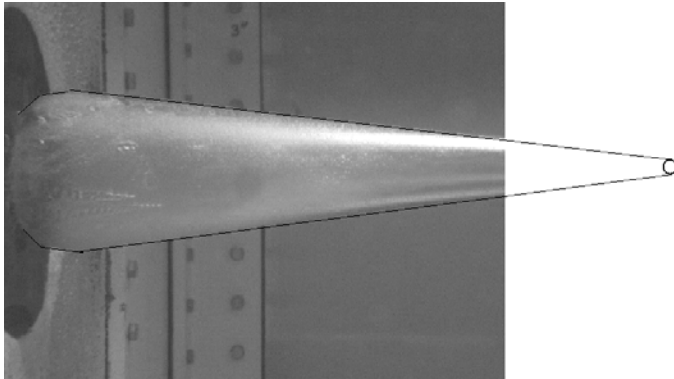


Figure 4.18. Example of extrapolated image to permit cavity volume calculations. See Appendix D for all sets of extrapolated images.

Regardless, important observations were made between the cavities generated by projectiles at velocities ranging between 111 to 176 *m/s* to the cavities generated by projectiles ranging between 1,200 to 1,800 *m/s*. As expected, the projectiles with higher impact velocity generated a larger cavity, as shown in Fig. 4.17 and Fig. 4.19. However, cavity geometry, with regards to cavity contraction and separation, were similar for the various impact conditions. Additionally, an inflection point was also calculated for the

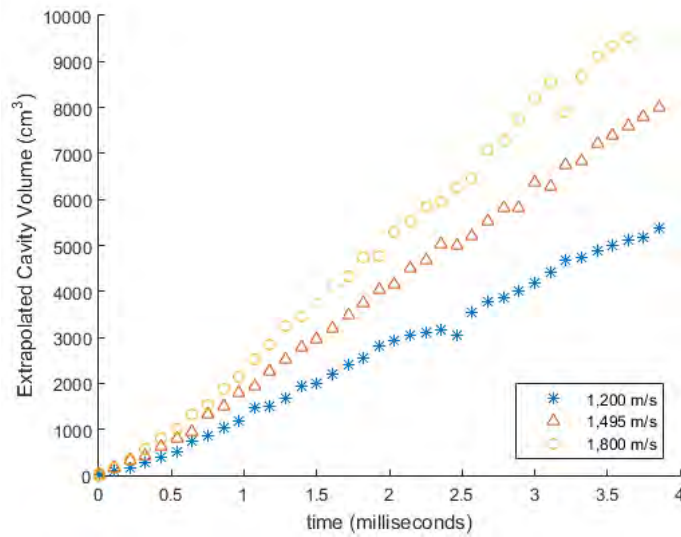


Figure 4.19. Example of extrapolated image to permit cavity volume calculations.

extrapolated volumetric data. The 1,200, 1,495, and 1,800  $m/s$  shots had inflection points of 1.653, 1.881, and 1.954  $ms$ , respectively, which are within the same order of magnitude as the inflection points for the low velocity cases shown in Table 4.4. The inflection points were found by fitting a 3<sup>rd</sup> order polynomial and solving for the associated derivatives.

As stated before, the inflection point is indicative of something changing in the system. The similarities with regards to the inflection points is very interesting. Analysis between the inflection point and the corresponding cavity geometry for the 111 to 176  $m/s$  shots will continue in Section 4.4.4. However, mass entrainment for the 1,200 to 1,800  $m/s$  shots is not currently available. Continued development of the entrainment technique detailed in Chapter III is needed to collect the data at these higher velocities. In summary, volumetric calculations for the 1,200 to 1,800  $m/s$  shots were accomplished by extrapolating the collected images. Although the velocity difference is very large between the experiments in Section 4.3 and Section 4.4.1 similarities were found between cavity geometry and the volumetric inflection points by comparing the low-velocity data to the high-velocity extrapolated data.

#### 4.4.3 HRAM Cavity Pressure Calculations.

Once determination of the volumetric inflection point as indicative of cavity contraction, additional analysis is needed as to precisely why the inflection point occurs. By utilizing the mass flow information, in conjunction with the measured volumetric data, the partial pressure is calculated for entrained gases in the HRAM cavity. Information about the vaporization mechanism is possible by looking at the partial pressure of the cavity.

To calculate the partial pressure, volumetric data were collected at similar impact velocities using the same steel, 0.953 cm, spherical, projectiles as the entrainment data specified in Table 4.1. The measured impact velocities for the volumetric data are shown in Table 4.4. The entrained mass composition of the cavity is obtained by summing the calculated mass flow rate multiplied by the appropriate change in time between each calculated mass flow rate shown in Eq. 4.11. The total mass of entrained air in the cavity at any time is now represented by Eq. 4.12.

Table 4.4. Projectile Parameters for HRAM Volumetric Experiments to Match Mass Entrainment Experiment Velocities per Table 4.1

Reference Number	Impact Velocity (m/s)	Inflection Point Location (ms)
65	174	1.3
66	136	1.5
67	111	1.4

$$m_o(t) = \sum_{i=1}^Q \dot{m}_o(i) \frac{1}{N} \quad (4.12)$$

where  $i$  ranges from 1 to  $Q$  for different impact velocities and corresponds to specific  $\dot{m}_O$  values at specific instances in time.  $Q$  is a set quantity representing the total total calculated  $\dot{m}_O$  data points at each different impact velocity shown in Fig 4.6. Table 4.5 contains the start times for the initiation of  $\dot{m}_O(t)$  calculations and the corresponding set values for  $Q$ . The time interval between each  $\dot{m}_O$  calculations is determined by the camera's frame rate, which was 10,000  $Hz$  for each entrainment test. Therefore, a rectangular approximation is used by summing the individual products of  $\dot{m}_O(i)$  and  $\frac{1}{N}$  at the corresponding instances in time over the desired interval. The unknown mass flow is approximated as error since the mass flow rate calculations were delayed from  $t$  equals 0 to the first measurement as indicated by the start times in Table 4.5. Once the calculated mass is obtained, it is combined with the measured cavity volume data and the partial pressure is calculated with the ideal gas law as shown in Eq. 4.13

$$P_{Air}(t) = \frac{\dot{m}_O(t)R_{Air}T}{\bar{V}_C(t)} \quad (4.13)$$

where  $P_{Air}(t)$  is the partial pressure of entrained gases in the cavity,  $\bar{V}_C(t)$  is the measured cavity volume,  $R_{Air}$  is the gas constant for air, and  $T$  is temperature and assumed constant for this process. The results are shown in Fig. 4.20. In Appendix C, images used for the volume calculations for the 111, 136, and the 174  $m/s$  shots are shown. Furthermore, details and plots for  $\dot{m}_O(t)$  and  $\bar{V}_C(t)$  are provided.

For the partial pressure calculations, it was assumed the entrained mass was evenly distributed throughout the cavity's volume. Therefore, the value from partial pressure calculation is applied globally throughout the entire cavity volume. The true cavity pressure is a gradient across the cavity volume, where the pressure varies from low to high beginning behind the projectile and ending at the orifice, respectively. Even though the partial pressure



Table 4.5. Projectile Parameters for HRAM Entrainment Experiments

Reference Number	Projectile Velocity (m/s)	Measurement Start Time (ms)	Q
53	176	0.6	27
52	176	0.6	27
58	135	0.4	26
56	132	0.5	31
61	114	0.6	30
60	113	0.5	31

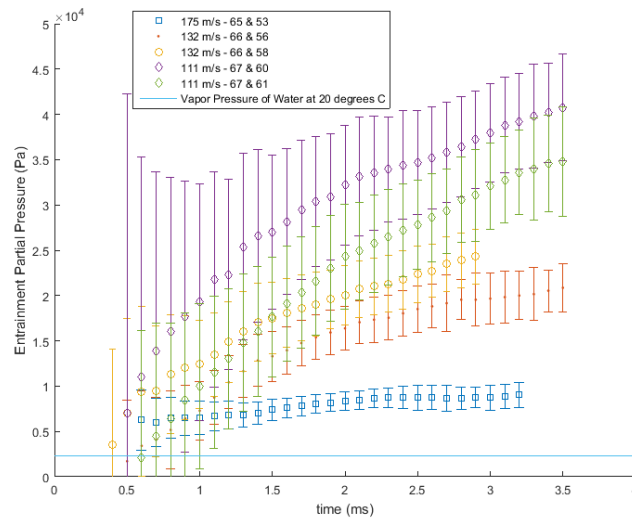


Figure 4.20. Calculated partial pressure of air in HRAM cavity based on measured cavity volume data and entrained air through the orifice for the test cases specified in Table 4.1 and 4.4. The solid line at 2,340 Pa represents the vapor pressure of water at 20 degrees centigrade [44].

calculation represents the global pressure, some inferences about the HRAM cavity are observed and are shown in Fig 4.20.

Figure 4.20 indicates the global partial pressure is potentially low enough to choke the flow. A choked flow may describe the similar trends for the mass flow data, as shown in Fig. 4.6. However, the total cavity pressure was not measured, nor was the ballistically formed orifice discharge coefficient. Hence, additional data is needed to definitively claim choked orifice flow for the impact conditions tested.

In Fig. 4.20, the cavity's global partial pressure is potentially below the fluid's vapor pressure for a short time after impact. The errorbars decreased as time increased since the unknown amount of mass, from  $t$  equals 0 to the first measurement, composed a decreasing amount of the total cavity mass. Regardless, the partial pressure of air exceeded the fluid's vapor pressure for a majority of the entrainment event per Fig. 4.20 Furthermore, as projectile velocity increased, the global partial air pressure in the cavity volume decreased. This relationship is due to the similar mass flow rates at each impact velocity per Fig. 4.6; however, higher-velocity projectiles generated larger cavity volumes. Therefore, the entrained mass occupied a larger cavity volume for higher velocity impacts. Additional mass from separation cavitation is possible which would increase the total pressure of the cavity.

Brandner *et al.* conducted research on cavitation inception on spheres [26, 27]. The research showed cavitation began near the sphere's surface for cavitation numbers as high as 1.0. As the cavitation number decreased, the vapor cloud generally became larger [26, 27]. Additionally, work by Washio detected cavitation inception occurring in flows around cylinders in water at velocities starting at 15  $m/s$  [28]. Missile water entry research by May theorized cavity composition would consist of a vaporized liquid and entrained ambient air mixture [14, 18]. The cavitation numbers in this research are significantly less than 1.0, as shown in Fig. 4.21, indicating possible vaporization of the

fluid very close to the projectile's surface is combining with the entrained air to compose the overall mass of the cavity.

Here is important to discuss the potential mechanisms of mass transfer into the HRAM cavity. The three mass transfer mechanisms are: orifice entrainment, vaporization of the local fluid across the liquid-cavity interface, and vaporization of the local fluid from separation cavitation occurring close to the projectile's surface as detailed by Brandner *et al.* and Washio [26–28]. Anecdotally, the cavitation numbers ranged from approximately 0.02 to 0.3 for the conducted experiments.

Notice how the global partial pressure for most data points quickly exceeds the fluid's vaporization pressure of water at 2,340 Pa as shown in Fig. 4.21. Considering the pressure in the cavity is a gradient, the potential does exist to vaporize water across the liquid-cavity interface right after projectile penetration and possibly for a region near the projectile, where the local pressure may be below the fluid's vapor pressure. However, the global partial pressure calculation does not account for the potential additional mass due to vaporized fluid close to the projectile's surface as detailed by Brandner *et al.* [26, 27]. This potential increase in mass raises the local pressure near the projectile, where the highest probability exists for vaporization across the liquid-cavity interface. Additionally, any increase in the cavity's mass will raise the global cavity pressure calculation making vaporization across the liquid-cavity interface less likely. This plot indicates, although vaporization of the local fluid across the liquid-cavity interface is possible, the cavity's global partial pressure quickly exceeds the fluid's vapor pressure based on the air entrainment measurements and the potential for additional mass from fluid vaporization close to the projectile's surface. Therefore, it appears of the three potential mass transfer mechanisms, air entrainment and vaporization of fluid close to the projectile's surface potentially dominate the mass transfer process for the range of impact velocities tested. Determination of the vaporized liquid's mass is not possible without direct cavity pressure

measurements, which were not collected as part of this research. Once the time resolved pressure measurements are obtained, a decomposition of the mass transfer mechanisms is possible.

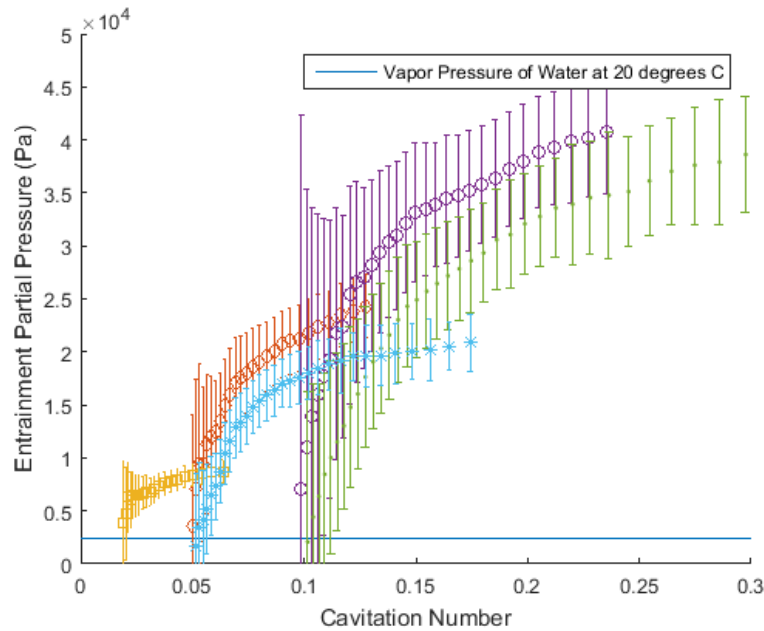


Figure 4.21. Calculated partial pressure of entrained gases in HRAM cavity plotted versus calculated projectile cavitation number. Notice for the low cavitation numbers, the cavity pressure is significantly above the fluid's vaporization pressure of 2,340 Pa for the test cases specified in Tables 4.1 and 4.4 [44].

In summary, the above analysis indicated the mass entrained via the orifice is sufficient to bring the cavity's partial pressure well above the water's vapor pressure for all but the earliest times. The partial pressure measurements above 2,340 Pa was observed for cavitation numbers greater than 0.02. Additional research is needed to determine the cavitation number range which corresponds to fluid vaporization across the liquid-cavity interface begins to dominate the mass transfer process. Of the 3 potential mass transfer

mechanisms, air entrainment and vaporization of fluid close to the projectile's surface potentially dominate the mass transfer process for the range of impact velocities tested. Simplifying the mass transfer mechanisms for a range of cavitation numbers focuses the follow on research into mass contributions of  $\dot{m}_v(t)$ . Precise composition of the cavity is not possible without the direct cavity pressure measurements.

#### ***4.4.4 Entrained Mass Flow Related to Cavity Geometry.***

As expected, the mass flow is related to the internal cavity geometry. Previous work by Gibson, ASME, and the Crane Company determined flow through pipe and orifices is limited, or restricted, by their respective geometries [30, 31, 33]. By using the orifice diameter and the measured maximum cavity diameter at the orifice, the non-dimensional term  $\beta_C$ , per Eq. 4.14, is formed

$$\beta_C(t) = \frac{d_o}{\max(d_{c_o}(t))} \quad (4.14)$$

where  $d_o$  is the orifice diameter, and  $d_{c_o}$  is the cavity diameter at the orifice.  $\beta_C$  is similar to the non-dimensional term  $\beta$  commonly used in fluid flow handbooks and derived in Chapter II [30, 31]. The main difference between the traditional non-dimensional diameter ratio,  $\beta$ , and  $\beta_C$ , is due to the changing cavity diameter at the orifice during an HRAM event. Equation 4.14 is valid from projectile entry to cavity separation from the shot plate. Once the cavity contracts and separates from the shot plate,  $d_{c_o}$  becomes difficult to detect, and a calculation of  $\beta_C$  becomes convoluted with the formation of the cavity's re-entrant jet and the conduit.

The cavity's maximum diameter was determined by using similar image processing techniques used to detect and calculate the cavity's volume. Instead of looking at the whole image, a cropped subset image at the orifice was used, and then the appropriate functions were applied to the detected cavity boundary to measure the maximum  $d_{c_o}$ . An example of the image subset used for determining  $d_{c_o}$  is shown in Fig. 4.22. A plot of the cavity's

maximum diameter is plotted in Fig. 4.23. It is easy to see how Eq. 4.14 would change as the diameter of the cavity changes with time.

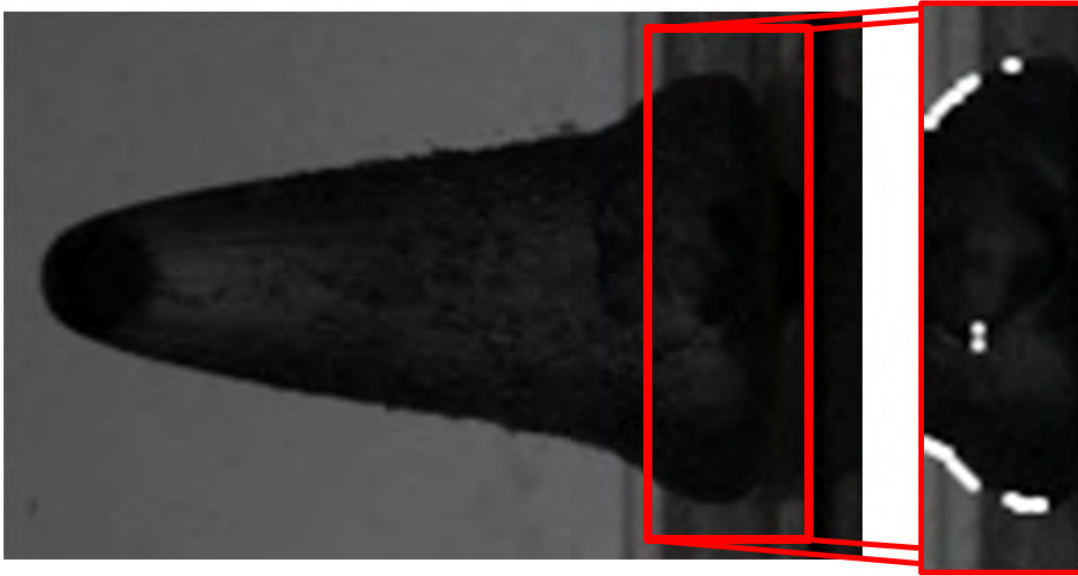


Figure 4.22. Example of image subset used to obtain measurements for  $\beta_C$  calculations per Eq. 4.14

Figure 4.24(a) shows the projectile at impact penetrating the aluminum shot plate on the far right of the image. After penetration, the cavity's diameter at the orifice is almost  $2.5\text{ cm}$ , over 2.5 times larger than the projectile diameter, as shown in Fig. 4.24(b). From Fig 4.24(b) to (c), the cavity diameter continued to grow and reached its approximate  $3\text{ cm}$  maximum around  $1.5\text{ ms}$  after impact. By Fig. 4.24(c) the cavity had begun to form the re-entrant jet. As the cavity separated from the shot plate, the conduit and cavity make detection of the diameter at the orifice difficult as shown in Fig. 4.24(d). Once the cavity had fully contracted, separated, and formed the conduit, as shown in Fig. 4.24(d), detection of the mas cavity diameter becomes difficult, and effective utilization of Eq. 4.14 is not advisable.

Interestingly, the cavity diameter increased very similarly for the first millisecond after impact for the 3 different impact velocities as shown in Fig. 4.23. Using the measured maximum cavity diameter information, the mass flow was plotted versus  $[1 - \beta_C(t)^2]$  instead of  $\beta_C(t)^2$  to stay consistent with parameters derived by Gibson used by the Crane Company. The plot of the mass flow versus  $[1 - \beta_C(t)^2]$  is shown in Fig. 4.25. Although the measured mass flow occurs within a range of  $[1 - \beta_C(t)^2]$ , the dimensionless term does not fully characterize the mass flow as evident of the data spread. The high-velocity shots tend to have smaller  $[1 - \beta_C(t)^2]$  terms while the low-velocity shots tend to have larger  $[1 - \beta_C(t)^2]$  terms even though the high velocity shots generated a larger volume. Therefore, when the mass flow was plotted versus  $[1 - \beta_C(t)^2]$ , a bias occurs and the data is almost universally spread by impact velocity in Fig. 4.25. Generally speaking, higher velocity shots produce larger volumes per Fig. 4.17, while relatively slower velocity shots produce larger diameters per Fig. 4.23. Perhaps  $[1 - \beta_C(t)^2]$  is not the only geometric limitation to the mass flow.

Looking again at Fig. 4.23, as impact velocity increased, the cavity contraction time at the orifice decreased. This is attributed to the longer and larger cavity created by the faster moving projectile, causing the cavity to contract and separate from the shot plate. Hence, the projectile formed cavity acts as a temporary “pipe” with a cross sectional area and length for the entrained gases to flow through, which is different from how orifice and pipe flow coefficients are determined.

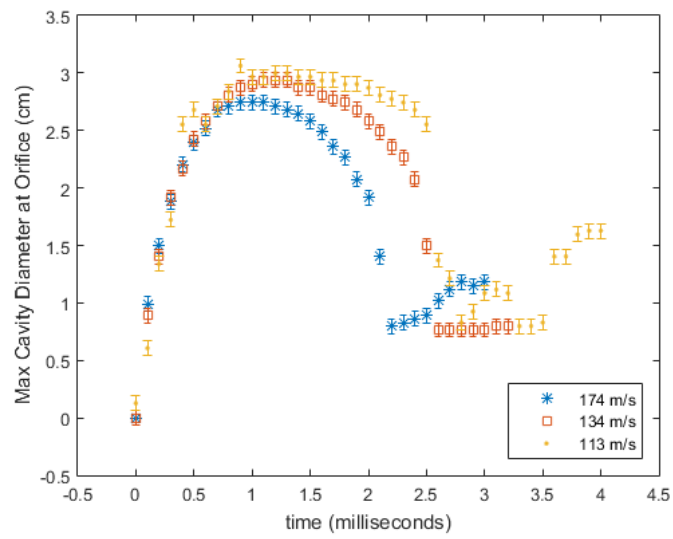


Figure 4.23. Maximum cavity diameter at the orifice for different impact velocities.



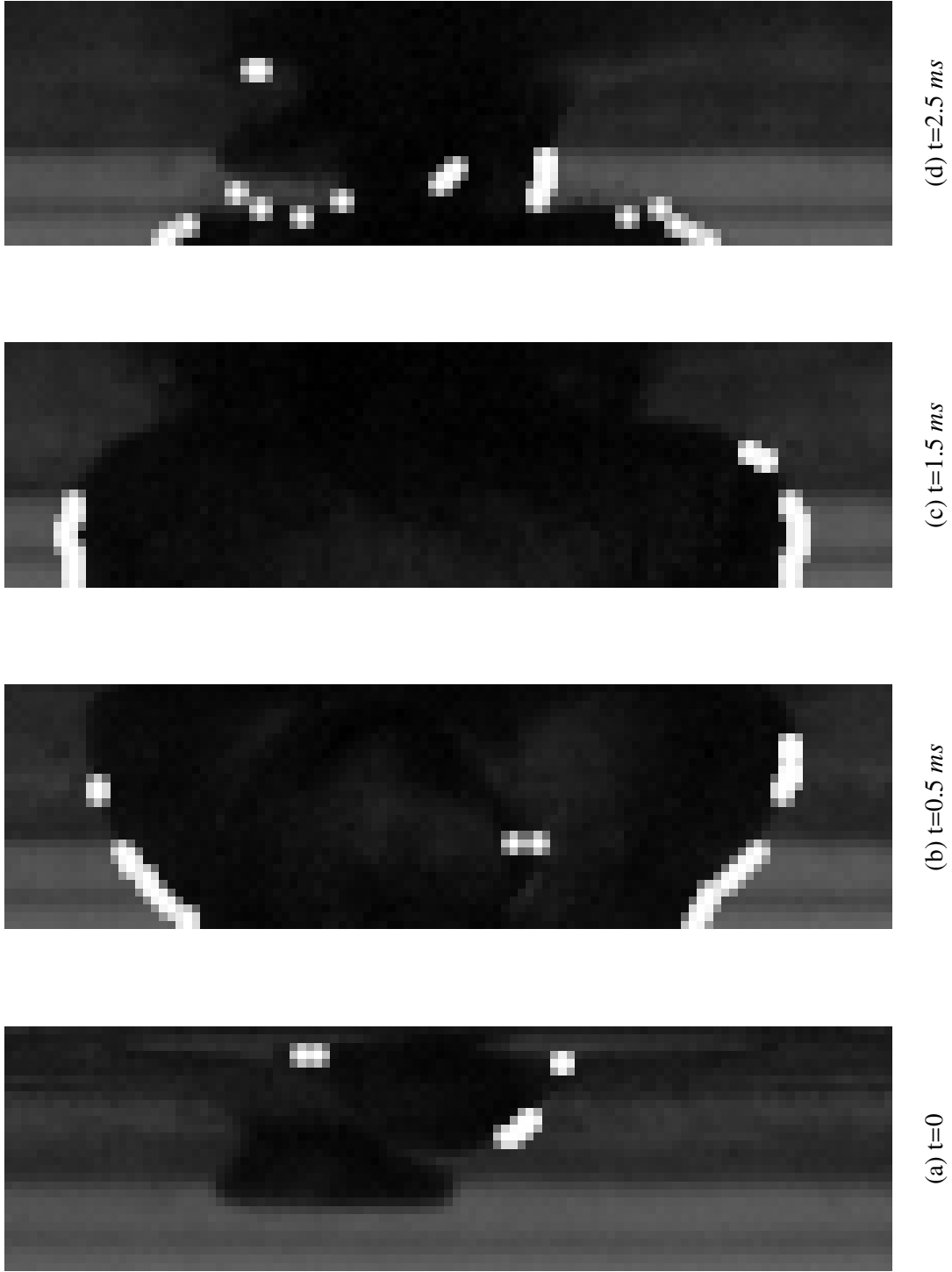


Figure 4.24. Example of the maximum cavity diameter measurements for calculation of  $\beta_c(t)$  per Eq. 4.14.

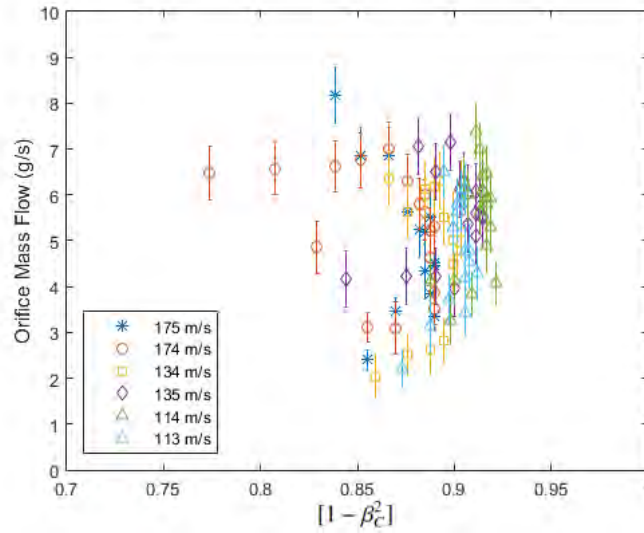


Figure 4.25. Calculated mass flow through the orifice versus  $[1 - \beta_C(t)^2]$  per Eq. 4.14.

Orifice and pipe flow measurements, and their respective coefficients, were derived for steady, established flow in a stable pipe structure. An HRAM event was very transient compared to pipe or orifice flow. The cavity is analogous to a “pipe” as the projectile transitions through the fluid, as shown in Fig. 4.8. To better fit, the mass flow to HRAM cavity geometry, a projectile position-ratio was created.

The position ratio acted as a dimensionless pipe length, which the entrained mass flows through. Since the projectile penetration distance changed with time, the length ratio also changed as the HRAM event occurred. Hence, the projectile position ratio was defined as the projectile distance from the orifice after penetration divided by the projectile penetration distance at the volumetric inflection point, for each corresponding impact condition. The equation for the projectile position ratio is displayed in Eq. 4.15

$$\lambda(t) = \frac{\lambda_o(t)}{\lambda_C} \quad (4.15)$$

where  $\lambda_o(t)$  was projectile penetration distance from the orifice, and  $\lambda_C$  was the projectile penetration distance corresponding to each impact condition’s inflection point. The

inflection points for each impact condition are shown in Table 4.4 and the corresponding image for the 136 *m/s* shot is shown in Fig. 4.8(c).

Initially,  $\lambda_C$  arbitrarily used the projectile penetration distance at 2.0 *ms* after impact. Arbitrarily setting  $\lambda_C$  resulted in a parameters not easily extrapolated or relatable for additional research at different impact conditions. For example, the penetration distance at 2.0 *ms* is much different at a 1,800 *m/s* versus a 176 *m/s* impact velocity. Instead, the penetration distance corresponding to the cavity's volumetric inflection point was used for  $\lambda_C$ . Remember the cavity's volumetric inflection point is indicative of the cavity's peak volumetric growth rate. Since the volumetric inflection point occurred just prior to peak mass flow rate in time, it provides a good parameter to normalize penetration distance across the different impact velocities. Additionally, the volumetric inflection is point calculable at a wide range impact velocities as shown in Section 4.4.1 and 4.4.2, and by obtaining the corresponding penetration distance allows follow on research to relate mass flow calculations to the data presented in Fig. 4.26.

The evolution of projectile penetration distance for the different velocity shots is shown in Fig. 4.7 through 4.9. By using Eq. 4.14 and 4.15, the dimensionless term  $\psi$  was created to predict mass flow per Eq. 4.16

$$\psi(t) = [1 - \beta_C(t)^2]\lambda(t) \quad (4.16)$$

where the combination of  $\beta_C(t)$  and  $\lambda(t)$  resembles a quasi dimensionless geometric volume accounting for the limitations of the mass flow associated with cavity and orifice geometry. As  $\psi$  increased the mass flow also increased as illustrated in Fig. 4.26.

The term  $[1 - \beta_C^2]$  is used versus  $\beta_C^2$  to stay consistent with parameters derived by Gibson and used by the Crane Company [30, 31]. The range of  $\psi$  in Fig. 4.26 is approximately 0.25 to 1.3 since the mass flow data for the approximately the first 0.5 *ms* is suspect, and since  $\lambda(t)$  can exceed 1.0. Currently, the application of  $\psi$  is limited since only a projectile geometry of 0.953 *cm* was used. However,  $\psi$  provided a research foundation

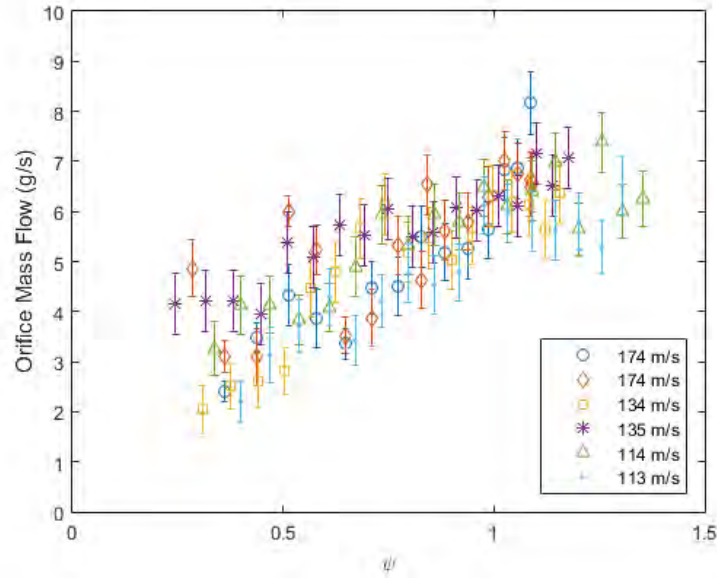


Figure 4.26. Calculated mass flow plotted versus dimensionless cavity geometry per Eq. 4.16. As the dimensionless area ratio and penetration distance increased, the mass flow through the orifice increases approximately linearly.

to generally relate the entrainment data with Guo and Lecysyn's cavity growth models to predict the mass flow of entrained gases. The ability to predict mass flow provided an estimate for cavity composition and partial pressure and provide additional insight into the HRAM event. Previous research had indicated the importance of orifice diameter to flow field properties [30, 31, 33]. Once again, since the experiments were limited to 0.953 *cm* for steel spheres, additional research is needed to determine the influence of projectile diameter on  $\psi$ , the mass flow rate, and the overall cavity composition.

#### 4.5 Predicting Cavity Contraction

The cavity energy model per Eq. 4.4 led to the identification of the orifice mass flow as potentially contributing to the cavity mass composition. In Fig. 4.6, the mass flow followed similar trends regardless of impact velocity. By referencing published flow relationships,

the dimensionless term  $\psi$  was developed to relate orifice flow based on cavity geometry. The mass flow rate for each test case in Fig. 4.5 peaks between 1.7 and 2.0 *ms* after projectile impact. The average of the collected mass flow data points between 1.7 to 2.0 *ms* is 6.46 grams per second, rounded up to 6.5 grams per second.

Applying the 6.5 grams per second peak flow rate to Fig. 4.26,  $\psi$  ranged approximately between 1.0 to 1.125 as shown in Fig. 4.27. By definition,  $\psi$  was composed of an area ratio multiplied by a length ratio and thus, it acted as a quasi-dimensionless volume. Looking back at Eq. 4.4, the cavity volume was a critical component of the cavity's pressure work. For an HRAM event, pressure work is a transmission of the projectile's kinetic energy into the displacement of liquid the cavity occupies. Therefore, it made sense to relate  $\psi$  to the projectile's kinetic energy.

The projectile's total kinetic energy loss to the system was shown in Eq. 2.13. To better relate each experimental case, the dimensionless kinetic energy is created per Eq. 4.17 by dividing the overall energy lost to the system by the initial projectile kinetic energy at penetration.

$$\Delta KE'(t) = \frac{\Delta KE(t)}{KE_0} = \frac{KE_0 - KE(t)}{KE_0} \quad (4.17)$$

where  $\Delta KE'(t)$  is the normalized change in kinetic energy. Investigating  $\psi$ , with regards to Eq. 4.17, provided the corresponding geometry to projectile kinetic energy lost relationship shown in Fig. 4.28. Therefore, it is useful to apply Eq. 4.17 and re-write Eq. 4.3

$$W_C(t) = f(\Delta KE') - \epsilon \quad (4.18)$$

where the  $W_C(t)$  term is now a function of the normalized projectile kinetic energy as described in Eq. 4.17.

In Fig. 4.28,  $\psi$  is plotted versus  $\Delta KE'(t)$ . Using the range of  $\psi$  for the expected maximum mass flow rate from Fig. 4.27,  $\Delta KE'(t)$  is now bounded for each impact condition as shown in Fig. 4.28(b). The vertical solid green lines in Fig. 4.28(b) represent the bounds

for the low velocity shots. The vertical solid orange lines in Fig. 4.28(b) represent the bounds for the medium velocity shots. The vertical solid blue lines in Fig. 4.28(b) represent the bounds for the high velocity shots. Bounding the  $\Delta KE'(t)$  provided the ability to predict the kinetic energy dissipation prior to cavity contraction for a range of impact conditions as shown in Fig. 4.32.

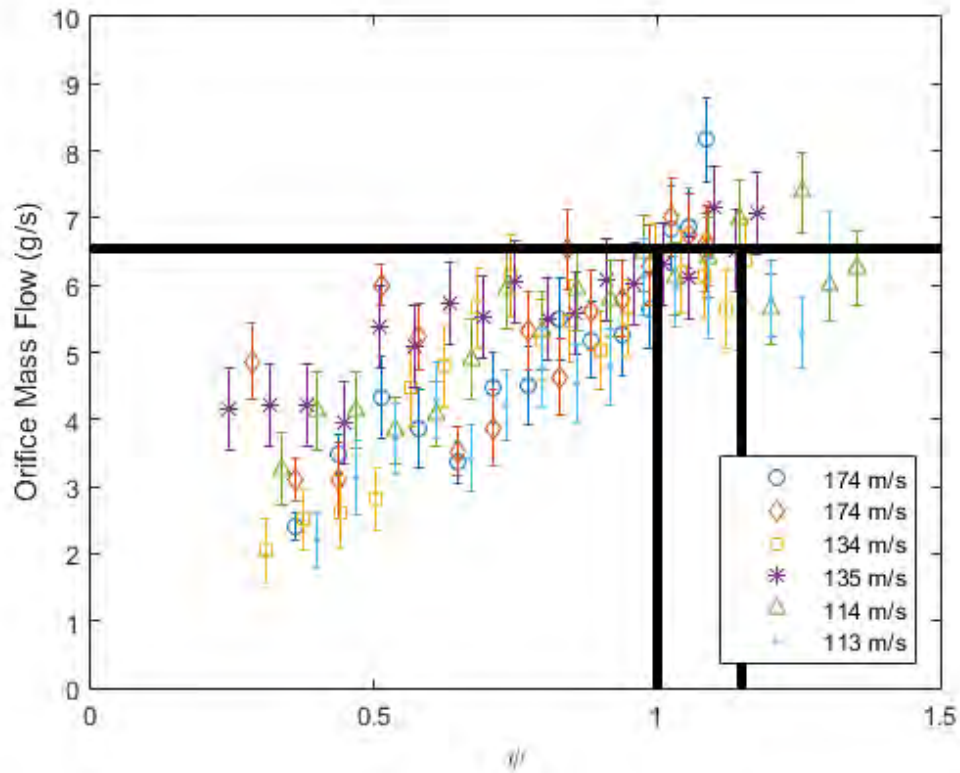


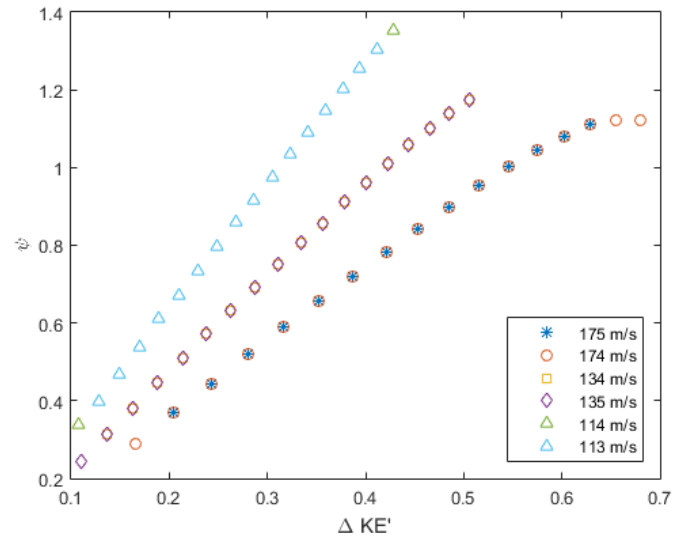
Figure 4.27. Calculated mass flow plotted versus projectile dimensionless geometry per Eq. 4.16. Initiation of cavity contraction occurred approximately when the mass flow peaks through the orifice, as detailed in Section 4.2. For the test cases, this occurred around 6.5 grams per second. The solid line at 6.5 grams per second provides the visual representation for the expected bounds of  $\psi$  corresponding cavity contraction.

The extrapolated volumetric data from the 1,200 to 1,800  $m/s$  shots in Section 4.4.2 is not included in Fig. 4.27 because the corresponding mass entrainment data was not collected. Since the extrapolated data has volumetric inflection points, calculation of the associated  $\psi$  values is possible, but without entrainment mass flow data calculation of the cavity composition, partial pressure, or prediction of peak mass flow is not possible. The similarities in the volumetric inflection point between the 111 to 176  $m/s$  and 1,200 to 1,800  $m/s$  shots indicate correlation and potential congruence for future calculations and data analysis. Regardless, the process for plotting the mass flow rate, bounding the kinetic energy dissipation, and the development of the pressure-volume work model is detailed in the following paragraphs and is applied to the 111 to 176  $m/s$  shots, where the necessary cavity geometry and mass entrainment data was available.

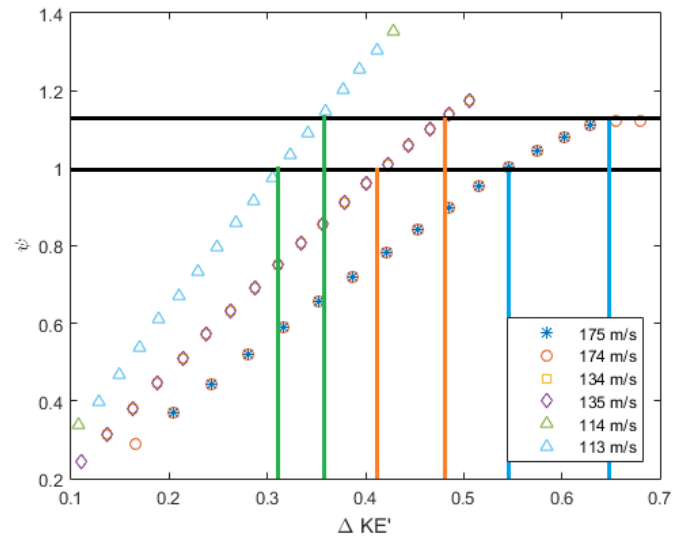
In Fig. 4.28(b) the  $\Delta KE'(t)$ 's values ranged from 0.54 to 0.65 for the 174  $m/s$  impact velocity. The 136  $m/s$  impact velocity's corresponding  $\Delta KE'$  ranged from 0.41 to 0.48, and the 114  $m/s$  impact velocity's corresponding  $\Delta KE'$  ranged from 0.31 to 0.36. The corresponding pictures for the  $\Delta KE'$  range are shown in Fig. 4.29 through 4.31.

For the 174  $m/s$  impact velocity, shown in Fig. 4.29, the 0.54 to 0.65 range of  $\Delta KE'$  corresponded to 1.50 to 1.90  $ms$  after impact. For Fig. 4.29(a), cavity contraction has begun. From Fig. 4.29(b) through (e) the re-entrant jet is formed and the cavity begins to separate from the shot plate. It is clear cavity contraction has occurred within the range of  $\Delta KE'$ .

The 135  $m/s$  impact velocity yielded similar results as shown in Fig. 4.30. For the 135  $m/s$  impact,  $\Delta KE'$  ranged from 0.41 to 0.48 which corresponded to 1.60 to 2.0  $ms$  after impact. The cavity has not yet completely contracted in Fig. 4.30(a). As the kinetic energy continued to dissipate to the fluid, the cavity became longer as shown in Fig. 4.30(b) through (d). Eventually the cavity contracted and the beginnings of the re-entrant jet are



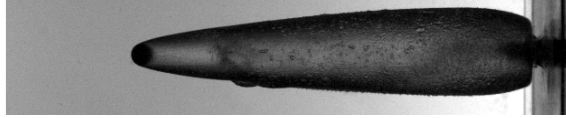
(a)  $\psi$  versus  $\Delta KE'$



(b) Bounded  $\psi$  versus  $\Delta KE'$

Figure 4.28. Calculated dimensionless term  $\psi$  plotted versus dimensionless term  $\Delta KE'$  per Eq. 4.17. Initiation of cavity contraction occurred approximately when  $\psi$  ranged between 1.0 to 1.125, as shown in Fig. 4.27. By using the bounds for  $\psi$ , determination of the corresponding  $\Delta KE'$  was possible and shown in (b).

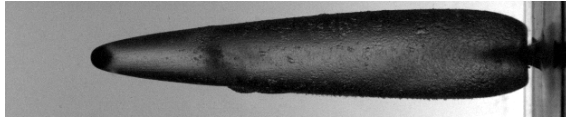




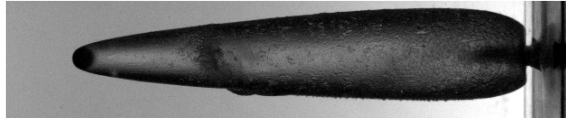
(a) Image taken at  $\Delta KE'$  of approximately 0.54 which corresponded to 1.50 *ms* after impact.



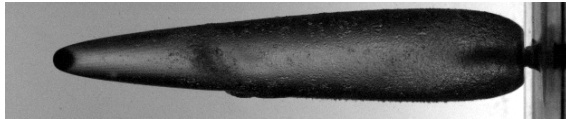
(b) Image taken at  $\Delta KE'$  of approximately 0.57 which corresponded to 1.60 *ms* after impact.



(c) Image taken at  $\Delta KE'$  of approximately 0.60 which corresponded to 1.70 *ms* after impact.



(d) Image taken at  $\Delta KE'$  of approximately 0.63 which corresponded to 1.80 *ms* after impact.



(e) Image taken at  $\Delta KE'$  of approximately 0.65 which corresponded to 1.90 *ms* after impact.

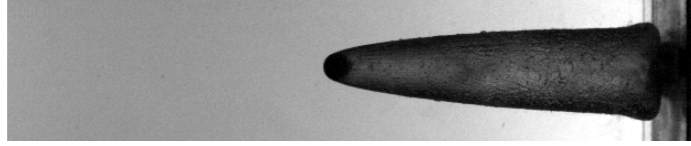
Figure 4.29. Evolution of cavity contraction for impact velocity of 174 *m/s* at  $\Delta KE'$  values ranging from 0.54 to 0.65 per Fig. 4.28.

shown in Fig. 4.30(e). As expected, the cavity contraction occurred within the range of projectile kinetic energy dissipation to the fluid.

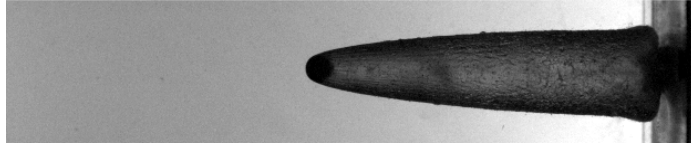
The 114 *m/s* impact velocity provided similar results as compared to the 136 and 174 *m/s* impact velocities. Cavity contraction occurred within the range of 0.31 to 0.36 for  $\Delta KE'$  which approximately corresponded to a range of 1.50 to 1.80 *ms*. In Fig. 4.31(a) the cavity diameter at the orifice has reached its maximum. The maximum diameter is held through Fig. 4.31(c) until Fig. 4.31(d), where contraction and separation have started. In summary, cavity contraction and separation is observed within the bounds of  $\Delta KE'$  per Fig. 4.32 for each of the tested impact conditions.

Figure 4.32 was a culmination of Fig. 4.27 and 4.28 relating cavity contraction via kinetic energy depletion back to initial impact velocity. The dashed lines in Fig. 4.32 were fit using a least squares method through the upper, lower, and average of the  $\Delta KE'$  bounded values at each impact velocity. The diamond symbols are the approximate location of the cavity's volumetric inflection point. As stated earlier, the volumetric inflection points was detected just prior to peak mass flow in the time domain. Since the volumetric inflection point indicates peak volumetric growth rate, it makes sense the the volumetric inflection point would also occur just prior when related to  $\Delta KE'$ . Additionally, by bounding and plotting  $\Delta KE'$ , it is possible to determine the expected energy loss required for cavity contraction at different impact velocities within the range tested. Relating cavity contraction to  $\Delta KE'$  is essentially treating the event as a function of the projectile performing pressure work on the system.

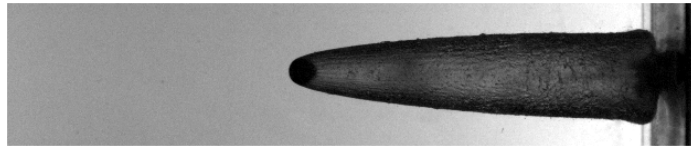
In Fig. 4.32, as the projectile impact velocity increases, the amount of kinetic energy depleted to the system also increases prior to cavity contraction. This relationship makes sense due to the larger cavity formed by the higher kinetic energy projectiles and presumably performing larger amounts of pressure work. Additionally, the bounds for  $\Delta KE'$  also increase as projectile velocity increases.



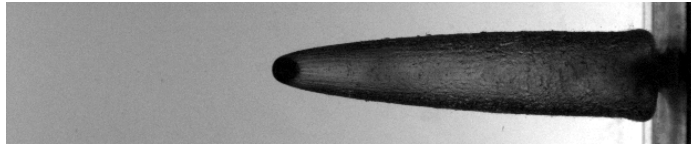
(a) Image taken at  $\Delta KE'$  of approximately 0.40 which corresponded to 1.60 *ms* after impact.



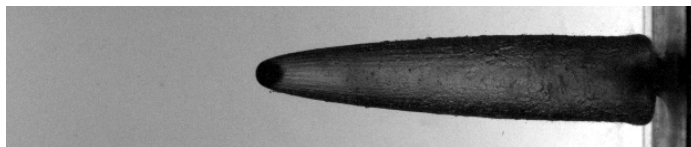
(b) Image taken at  $\Delta KE'$  of approximately 0.42 which corresponded to 1.70 *ms* after impact.



(c) Image taken at  $\Delta KE'$  of approximately 0.44 which corresponded to 1.80 *ms* after impact.



(d) Image taken at  $\Delta KE'$  of approximately 0.46 which corresponded to 1.90 *ms* after impact.



(e) Image taken at  $\Delta KE'$  of approximately 0.49 which corresponded to 2.0 *ms* after impact.

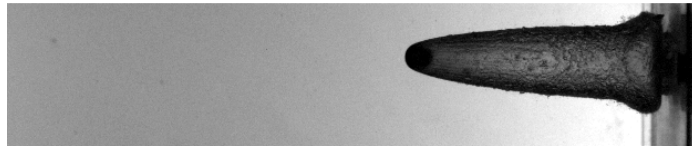
Figure 4.30. Evolution of cavity contraction for impact velocity of 136 *m/s* at  $\Delta KE'$  values ranging from 0.40 to 0.49 per Fig. 4.28.



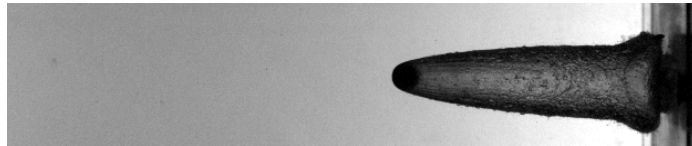
(a) Image taken at  $\Delta KE'$  of approximately 0.30 which corresponded to 1.50 *ms* after impact.



(b) Image taken at  $\Delta KE'$  of approximately 0.32 which corresponded to 1.60 *ms* after impact.



(c) Image taken at  $\Delta KE'$  of approximately 0.34 which corresponded to 1.70 *ms* after impact.



(d) Image taken at  $\Delta KE'$  of approximately 0.36 which corresponded to 1.80 *ms* after impact.

Figure 4.31. Evolution of cavity contraction for impact velocity of 114 *m/s* at  $\Delta KE'$  values ranging from 0.30 to 0.36 per Fig. 4.28.

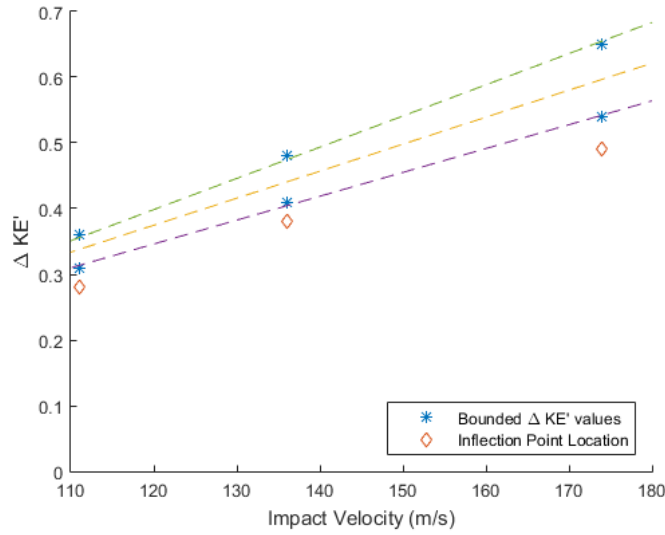


Figure 4.32. It is possible to predict cavity contraction for a range of velocities by plotting the dimensionless  $\Delta KE'$  with regards to the impact velocity. The dashed lines provide the upper, lower, and average bounds determined by a least squares method for the range of  $\Delta KE'$  determined by Fig. 4.27 and 4.28. Cavity contraction will occur within the determined range of  $\Delta KE'$ .

The widening of the bounds is most likely attributed to 3 confounding factors. First, the previously discussed limitations and error associated with the entrainment velocity technique may cause the bounds to widen as projectile impact velocity increases. Any improvement in the mass flow calculation or measurement technique may improve or help further explain the spread relative to projectile impact velocity. The second potential contributing factor is related to the cavity geometric characteristics represented by  $\psi$ . The dimensionless parameter utilized the term  $[1 - \beta_C(t)^2]$  and the created  $\lambda$  dimensionless length terms. The dimensionless length ratio when combined with  $[1 - \beta_C^2(t)]$  adequately described the mass flow but a better dimensionless term to describe the mass flow may exist. Lastly, thermodynamic losses in the system are potentially more prevalent as impact velocity increases. Each of these aforementioned factors may contribute to the bounded

spread, but identifying and characterizing precisely which factor is causing the spread is not possible with the collected data.

Previous research had not adequately predicted the energy depletion mechanism for projectiles during an HRAM event, as discussed in Chapter II. Hence, the kinetic energy depletion rate between the projectile and the surrounding fluid was unknown for a given set of impact conditions. As stated earlier, the projectile's kinetic energy was the primary source of energy performing pressure work on the system. Hence, Eq. 4.4 becomes a function of the projectile's kinetic energy lost. Predicting the elapsed time required for the dissipation of  $\Delta KE'$  would provide useful results. However, relating  $\Delta KE'$  back to the time domain is not currently feasible with the current collected data. Internal cavity pressure measurements, when combined with the measured cavity volume, provide the additional data to calculate the cavity pressure work. A transmission rate calculation is possible by using the change in projectile kinetic energy and the cavity pressure work calculations. Understanding the transmission rates may provide the necessary information to relate  $\Delta KE'$  back to the time domain.

Looking again to Eq. 4.4, the time-resolved cavity pressure work ( $W_C$ ) was unknown, because  $\dot{m}_v(t)$  or  $P_C(t)$  is currently unknown. Until  $\dot{m}_v(t)$  or  $P_C(t)$  is calculated or measured, relating the kinetic energy lost back to the time domain was not possible. However, a maximum pressure work potential using the partial pressures from Section 4.4.3 is possible and shown in Eq. 4.19. Equation 4.19 is simply Eq. 4.4 without  $\dot{m}_v(t)$  term. Using Eq. 4.19 provides an introductory and cursory glance at the process and the future research needed.

$$W_E(t) = W_C(t) + \int_0^t \dot{m}_v(t) R_{Water} T dt = P_o \bar{V}_C(t) - \int_0^t \dot{m}_O(t) R_{Air} T dt - \epsilon \quad (4.19)$$

where  $W_E(t)$  is the maximum pressure work potential due to entrainment. Equation 4.19 is simply Eq. 4.4 without the  $\dot{m}_v(t)$  term. Equation 4.19 represents the maximum pressure

work potential since any additional mass in the cavity, provided by the  $\dot{m}_v(t)$  term, would lower the overall pressure work in the system.

To illustrate the process, Fig. 4.33 showed what the potential energy transmission relationship may look like. Figure 4.33 only contains the entrained mass, but plotting the maximum pressure work potential versus  $\Delta KE'$  illustrates the first step in the process to determine the energy transmission relationship. Notice the different line slopes in Fig. 4.33 indicating different energy transmission rates. To fully understand the energy transmission mechanism, time-resolved measurement of the cavity's internal pressure is needed. Until this research, the importance of the cavity's internal pressure was not known as detailed in Section 4.4.3. Once the pressure measurement is made, calculation of transmission rates of projectile kinetic energy to cavity pressure work is possible. Understanding the transmission rates will further the understanding of the HRAM cavity formation, contraction, and separation. Regardless, by measuring the entrained flow field, great strides in determining and predicting cavity contraction was accomplished. Additionally, Fig. 4.32 provides a relatively simple way to bound the depleted projectile kinetic energy required for cavity contraction for a range of impact velocities.

## **4.6 Discussion and Summary**

The technique development process for measuring the entrained flow field proved challenging. Nevertheless, obtaining the measurement provided a great deal of information and understanding to the HRAM problem. The entrained flow field followed similar trends for projectile velocities ranging from 114 to 176 *m/s*. Relating the measured mass flow rate to cavity geometry provided insight into internal cavity dynamics associated with peak mass flow. The peak entrained mass flow also correlated well with internal cavity dynamics such as the inflection point, cavity contraction, and cavity separation.

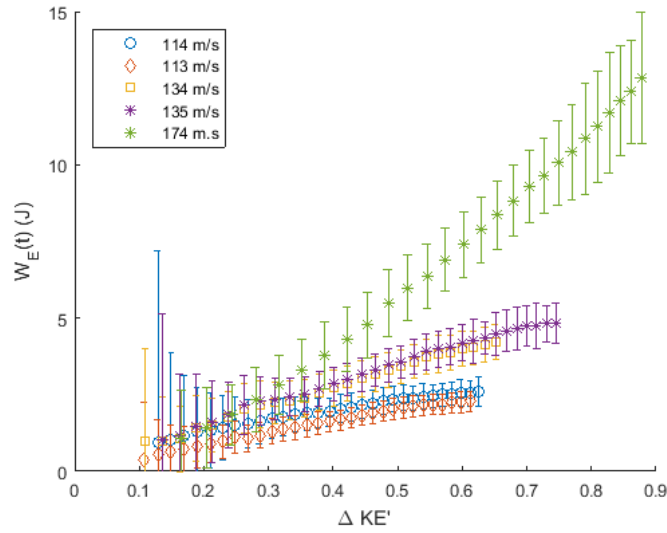


Figure 4.33. Measured maximum cavity pressure work versus total projectile kinetic energy lost for the experimental velocities specified in Tables 4.1 and 4.4.

Work with the 96<sup>th</sup> TG determined cavity contraction and separation were precursors to the initiation of the transient spray phases. Although the research was conducted at velocities from 1,200 to 1,800 *m/s*, similarities in cavity contraction and separation between the 111 to 174 *m/s* shots were observed. Cavity contraction and separation are pre-cursor events prior to the initiation of the transient spray phases.

To relate the mass flow to cavity geometry, a dimensionless term  $\psi$  was created. By using the dimensionless geometric term  $\psi$ , and the measured mass flow rates, predicting cavity contraction was possible by bounding  $\psi$  and the dimensionless kinetic energy,  $\Delta KE'$ . Bounding these parameters enabled prediction of the kinetic energy dissipated to the system prior to cavity contraction. Estimating the kinetic energy dissipation forms the basis for predicting the cavity contraction, which is a precursor to the transient spray phases. Additional research is needed to determine the overall energy transfer mechanism, since the importance of internal cavity pressure measurement was not known prior to conducting experiments.



Furthermore, measurement of the cavity's volume and entrained flow field enables partial pressure calculations for a range of cavitation numbers. For the range of cavitation numbers tested, the cavity partial pressure was significantly above the fluid's vaporization pressure. A cavity partial pressure above the fluid's vapor pressure indicates little to no vaporization of the local fluid across the cavity water boundary. However, prior research also suggests fluid vaporization was still likely as the flow separates close to the projectile's surface [28]. Measurement of the cavity's internal pressure was required to resolve the total cavity mass composition. The vaporized mass component of the cavity is resolved by subtracting out the entrained partial pressure from the total measured pressure. Then calculations for the vaporized water mass is then approximated by using the ideal gas law.

The importance of the entrainment measurement cannot be understated. Without the entrainment measurement, observing the cavity features, and calculating the cavity volume does not provide any additional insight into the HRAM event. Combining the cavity volume with the entrainment measurement enabled the aforementioned calculations and the development of the presented relationships between cavity geometry.

## V. Findings, Implications for Practice, Additional Research, and Conclusions

**T**HIS chapter will summarize the research findings, provide the implications for using the research in practice, and offer recommendations for future work.

### 5.1 Summary of Findings

#### 5.1.1 *Determine Cavity Composition.*

Objective I was completed directly by measuring the flow field velocity across the orifice and computing the entrained mass flow rate. The partial pressure of air was calculated using the mass flow calculations and the measured cavity volume. The partial pressure of air in the cavity ranged from 5,000 to 45,000 Pa for cavitation numbers ranging from 0.02 to 0.3, respectively.

For cavitation numbers ranging from 0.02 to 0.3, the cavity's global partial pressure of entrained gases was well above the fluid's vapor pressure for a majority of the test points collected. Possible vaporization across the liquid-cavity interface may occur for a short instance after impact, or in a cavity region close to the projectile. However, the global partial pressure does not account for the potential for additional vaporized liquid mass introduced into the cavity via fluid separation as described by Brandner *et al.* [26, 27]. Hence, of the 3 potential mass transfer mechanisms, air entrainment and vaporization of fluid close to the projectile's surface likely dominate the mass transfer process for the range of cavitation numbers and impact velocities tested. Simplifying the mass transfer mechanisms for a range of cavitation numbers focuses the follow on research into mass contributions of  $\dot{m}_v(t)$ . Taking the orifice mass flow calculations based on velocity measurements was the first instance an approximation of cavity composition and mass sources possible for a ballistically induced HRAM event. To determine the actual mass of entrained gases and vaporized water, measurement of the cavity pressure is required.

### ***5.1.2 Determine Cavity Dynamics Contributing to the Transient Spray.***

Research with the 96<sup>th</sup> TG provided the opportunity to collect synchronized HRAM and transient spray data at projectile impact velocities from 1,200 to 1,800 *m/s*. By synchronizing the cameras, a qualitative assessment of the internal cavity dynamics and the associated transient spray was possible. In addition, cavity volumes were estimated as a function of time. Cavity contraction and separation, near the orifice, are pre-cursor events prior to the initiation of the transient spray phases.

The collected imagery provides the qualitative data for the various impact velocities. The cavity contraction and separation phases occurred at inconsistent times with respect to their impact velocity, indicating time was not the applicable domain for measuring or predicting transient spray. This research portion bounded the progression of research to focus on the mechanisms behind cavity contraction and separation.

Research into the cavity dynamics at lower velocities in AFIT's laboratories uncovered the volumetric inflection point as it coincided with cavity contraction. Additionally, the inflection point occurred just prior to the orifice mass flow reaching its maximum value. The flow cannot increase proportionately to accommodate the volumetric increase, and therefore the cavity growth rate changed sign. The flow through the orifice was initially measured as a function of time after projectile impact, which was not useful to draw a relationship among the different impact velocities. Additional research on cavity geometry determined the mass flow rate was approximately linearly related to the non-dimensional geometric term  $\psi$ .

It was not possible at this time to collect the mass flow data for the test shots with the 96<sup>th</sup> TG. Therefore, correlations between internal cavity dynamics and the orifice mass flow were obtained by collecting internal cavity imagery at lower velocities at AFIT's laboratories. Observations were made by combining the mass flow data and the internal cavity imagery data at the lower velocities.

The peak mass flow rate coincided approximately in time with the initiation of cavity contraction at the orifice. As the cavity contracted around the orifice, it formed a re-entrant jet at the rear of the cavity, where the water most likely mixed with the incoming orifice air. The mixture of water and entrained air due to the re-entrant jet likely results in the measured drop in mass flow rate. As the re-entrant jet continued to form, the cavity began to separate from the shot plate and created a conduit between the cavity and the orifice. The conduit probably formed due to the cavity's low-pressure region and is sufficient to draw ambient air through the orifice, albeit at a reduced rate. While the cavity continued to separate from the shot plate, the conduit extended until it was severed and the fluid spurted out of the tank.

### ***5.1.3 Predicting Cavity Contraction.***

Using the volumetric inflection point as a starting position, the dimensionless geometry term  $\psi$  was used to predict the mass flow adequately for a range of impact velocities. Bounding  $\psi$  yielded a range of geometric conditions corresponding to the peak mass flow. Since the cavity formation was considered pressure work on the system, relating  $\psi$  to the projectile kinetic energy provided the information needed to predict cavity contraction for the range of impact velocities.

By combining the geometric and mass flow data, a relationship is formed between the ratio of the reduction in projectile kinetic energy to the projectile's initial kinetic energy, referred to as ( $\Delta KE'$ ), and the projectile's impact velocity. As the projectile impact velocity increased, the amount of kinetic energy depleted to the system also increased prior to cavity contraction. Bounding  $\Delta KE'$  provided the range of the expected kinetic energy dissipation prior to cavity contraction for various impact velocities.

Predicting the elapsed time required for the dissipation of  $\Delta KE'$  would provide useful results. However, relating  $\Delta KE'$  back to the time domain requires additional research since the total cavity pressure for the range of impact velocities was not measured. Previous

research has not adequately predicted the energy depletion mechanism. Hence, for a set of impact conditions, the kinetic energy depletion rate for the projectile, to the surrounding fluid, remains unknown. As stated earlier, the projectile's kinetic energy is the main source of energy leading to pressure-volume work on the fluid, and therefore cavity contraction becomes a function of the projectile's kinetic energy dissipated.

#### ***5.1.4 Development of Empirical Model.***

A model was developed to illustrate the process to relate the projectile's kinetic energy to the cavity's characteristics. Since the cavity's internal pressure was not directly measured, only the partial pressure of entrained gases was calculated. Therefore, the using the partial pressure calculations, a maximum pressure potential,  $W_E(t)T$ , was calculated to illustrate the process of relating the projectile's kinetic energy to the cavity pressure work. Model development identified the  $\dot{m}_v(t)$  and  $P_C(t)$  terms, which need measured, to provide the data necessary to complete the cavity pressure work model. Nevertheless, the model illustrated the process to develop a kinetic energy to pressure work relationship.

Furthermore, measuring the orifice discharge coefficient and internal cavity pressure will also provide the needed data to unravel the entertainment mass flow limitations. By measuring the orifice discharge coefficient and internal cavity pressure will provide additional insight into the mechanisms limiting the flow of entrained gasses. Additionally, this data may provide the parameters necessary to determine the cavity composition on a mass basis. Once the total cavity pressure is obtained, a pressure work calculation by combining the cavity's volume is possible. The relationship between the cavity mass composition, pressure work, and projectile kinetic energy will provide additional insight into the HRAM problem. Prior to this research, the importance and need to measure these terms was not known.

## 5.2 Implications for Practice

This research benefits the scientific community in at least four areas. The first area is for a range of cavitation numbers, the fluid vaporized via the cavity water interface is likely minimal. This finding simplifies and eliminates a vaporization mechanism through the cavity water boundary for cavitation numbers higher than 0.02. These results are useful in the empirical as well as the computational research communities.

Secondly, the entrained mass flow characteristics provided a physical relationship to solve previously unknown mass flow properties in computational research. Previous research had successfully predicted cavity geometry without accounting or knowing the mass entrainment portion of the HRAM event. By relating the mass flow to cavity geometry, the foundation was provided for incorporating the orifice mass flow into computational research.

Further delineation of Ball's cavity phase into the cavity formation, contraction, separation, and collapse phase broke the HRAM event into separate dynamic events as they relate to the transient spray phases [4]. Particularly, cavity contraction and separation are pre-cursors to the initiation of the pre-spurt and main spurt phases. Additional research can now focus on cavity contraction and separation phases once their relationships to the transient spray phases were determined.

Finally, prediction of cavity contraction, using the projectile's kinetic energy dissipation, is useful for indicating the initiation of the transient spray phases. Furthermore, the development of the cavity pressure model uncovered the orifice discharge coefficient and cavity time resolved pressure as important parameters when determining the evolution of the cavity. Measuring the orifice discharge coefficient and cavity pressure provides the data necessary to determine the limiting mass flow mechanism. Further understanding of the HRAM problem is obtained by determining the transmission mechanism and relating the cavity pressure work to the projectile's kinetic energy. Ultimately, a better

understanding of the underlying physics of HRAM is expected to lead to tank designs with improved aircraft survivability characteristics.

### **5.3 Additional Research**

This research attempted to construct a cavity energy model based on the entrained mass of air via the orifice and cavity volume measurements. The results of the analysis yielded additional terms needed to resolve the transmission of projectile kinetic energy into cavity pressure work. Although the analysis did not yield the overall energy transfer rates for placement into the dissertation, the process was introduced, and the identified terms provided a great segue for additional research.

Additional research is required to measure the internal, time-resolved, cavity pressure. The development of the pressure measurement technique has its unique set of challenges given the cavity's size and the relatively short time duration of the event. Regardless, obtaining the data is within the realm of possible. The next objective is obtaining an orifice discharge coefficient for the ballistically generated holes. Obtaining the internal pressure data and the orifice coefficient can provide further insight on the orifice flow limitations and complete the development of the cavity pressure work model.

Extending the methods to greater impact velocities will provide the means to continue the research and add further insight into functioning of the mass transfer mechanisms. The impact velocities in which the corresponding HRAM cavity is below the fluid's vapor pressure is unknown but must approach the fluid's vapor pressure as projectile impact velocity increases. This research could provide data regarding where the approximate cavitation number exists for the vaporization mechanism across the liquid-cavity interface can play a significant role in the mass transfer process.

Any improvement of the entrainment technique should focus on reducing the sources of error. Eliminating the 0.5 *ms* delay after projectile impact would reduce an error source and provide further insight into the orifice flow characteristics. Additionally, using a 10,000

*Hz* double pulsed laser or an optical chopper would also reduce the error associated with streak measurements. Regardless, the improvement of the technique is also needed to extend the research to greater impact velocities.

The effect of fluid properties on the projectile kinetic energy transmission into pressure work needs further development. Fluid properties, such as viscosity, would effect the overall drag on the projectile, as it traverses the fluid, and therefore effect the dissipation rate of the projectile's kinetic energy. Once the cavity energy model is refined, the research can focus on the energy transmission mechanism. It is hypothesized the projectile drag properties will influence the overall energy transmission mechanism.

Since the mass flow rate was dependent on cavity and projectile geometry, additional research on mass flow with different projectile diameters may provide further insight into the limiting mass flow mechanism. Typically, HRAM events do not generate axial symmetric cavities. Extending the research to non axial symmetric cavities may also provide interesting results, furthering the knowledge and understanding of HRAM. Additionally, computational research and simulations may augment or provide resources for “tumbling” projectiles. In particular, Monte Carlo simulations are potentially useful to predict the different energy dissipation rates due to the variable cross sectional areas the projectile presents when tumbling.

The mass flow rate results provide additional data potentially useful for modeling and simulation. Additional modeling and simulation research to incorporate mass flow characteristics may produce higher fidelity models when attempting to predict the transient spray or pressure fluctuations. A higher fidelity model based on physics may reduce expensive empirical data collection.

## **5.4 Conclusion**

The overall research goal was to determine the relationship and driving mechanism between HRAM cavity features and the resulting transient spray via the penetration



orifice. This goal was divided into focused objectives contributing to the completion of the overall research goal. The objectives were: *determine entrainment portion of cavity composition, determine cavity features and characteristics contributing to the transient spray, and develop a physics and empirical-based relationship to the cavity parameters contributing to the transient spray.*

The completed research objectives accomplished the overall research goal of predicting the events necessary to occur prior to the initiation of the transient spray phases. Additionally, the prediction of cavity contraction was related to the projectile kinetic energy dissipation. The findings further the knowledge for use in additional research. Furthermore, application of these results further the knowledge of HRAM, and ultimately will lead to safer industrial design practices, and safer aircraft.

## Appendix A: Entrainment Imagery

A total of 6 entrainment shots were taken at 3 velocities to provide a replicate at each velocity. Each shot behaved very similarly with regards to detection of the flow. Application of the investigation region, as detailed in Chapter II, was necessary due to differences in the seed density.

The projectile acceleration device could repeatedly achieve velocities around  $176\text{ m/s}$  or lower. Above  $176\text{ m/s}$ , repeating and measuring the velocity accurately became difficult. Using a longer barrel and applying higher voltage across the solenoid may help achieve repeatable higher velocities.

Once testing at the entrainment velocities was completed, internal tank shots at similar velocities were accomplished to capture the cavity volume and projectile position data. The internal cavity imagery for each case is shown in Appendix B.

### A.1 113 m/s impact velocity

Referred to as Test 60 in Table 4.1, the  $113\text{ m/s}$  shot provided good data. The entire event is displayed in Fig. A.1 through A.4. The collected raw imagery was a 1280 by 800 pixel image. Each image was cropped to 1001 by 201 pixels around the funnel area to decrease image processing time. The seeded flow field prior to impact is seen in Fig. A.1(a). Projectile impact is shown in Fig. A.1(b). The flow field is obstructed for the first  $0.5\text{ ms}$  after impact, Figs. A.1(c) through (f). Some streaks are visualized, in Figs. A.1(c) through (f) but the streak data is not sufficient to make a reasonable mass flow calculation. Additionally, the potential for particle lag exists during this time window after impact based on the characteristic response time calculations, also detailed in Chapter II.

For Fig. A.1(f) through Fig. A.3(j), the velocity flow field data was extracted from the raw images. A log transform, convolution filter and a binary threshold was equally applied

to each image for streak detection and measurement. The measured velocity profile for each image is shown in Section B.1. Looking back at Fig. 4.6, the mass flow increases from 0.5 *ms* to approximately 2.0 *ms*. The velocity slows through the orifice as expected once the cavity contracts, separates, and forms the conduit. The flow eventually slows down to the point where the particles do not sufficiently streak and the image processing algorithm would falsely assign streak values based on the diameter of the particles. The diameter of the slowing particles are shown in Fig. A.3(k) through (n).

## **A.2 114 m/s impact velocity**

Referred to as Test 61 in Table 4.1, the 114 *m/s* shot provided good data. The entire event is displayed in Fig. A.5 through A.8. The collected raw imagery was a 1280 by 800 pixel image. Each image was cropped to 1001 by 201 pixels around the funnel area to decrease image processing time. The seeded flow field prior to impact is seen in Fig. A.5(a). Projectile impact is shown in Fig. A.5(b). The flow field is obstructed for the first 0.5 *ms* after impact, Figs. A.5(c) through (f). Some streaks are visualized, in Figs. A.5(c) through (f) but the streak data is not sufficient to make a reasonable mass flow calculation. Additionally, the potential for particle lag exists during this time window after impact based on the characteristic response time calculations, also detailed in Chapter II.

For Fig. A.5(f) through Fig. A.7(j), the velocity flow field data was extracted from the raw images. A log transform, convolution filter and a binary threshold was equally applied to each image for streak detection and measurement. The measured velocity profile for each image is shown in Section B.2. Looking back at Fig. 4.6, the mass flow increases from 0.5 *ms* to approximately 2.0 *ms*. The velocity slows through the orifice as expected once the cavity contracts, separates, and forms the conduit. The flow eventually slows down to the point where the particles do not sufficiently streak and the image processing

algorithm would falsely assign streak values based on the diameter of the particle as shown in Fig. A.7(k) through (n).

### **A.3 132 m/s impact velocity**

Referred to as Test 56 in Table 4.1, the 132 *m/s* shot provided good data. The entire event is displayed in Fig. A.9 through A.11. The collected raw imagery was a 1280 by 800 pixel image. Each image was cropped to 1001 by 201 pixels around the funnel area to decrease image processing time. The seeded flow field prior to impact is seen in Fig. A.9(a). The leading edge of the projectile is shown in Fig. A.9(b) just prior to impact. The flow field is obstructed for the first 0.5 *ms* after impact, Figs. A.9(c) through (f). Some streaks are visualized, in Figs. A.9(c) through (f) but the streak data is not sufficient to make a reasonable mass flow calculation. Additionally, the potential for particle lag exists during this time window after impact based on the characteristic response time calculations, also detailed in Chapter II.

For Fig. A.9(f) through Fig. A.11(f), the velocity flow field data was extracted from the raw images. A log transform, convolution filter and a binary threshold was equally applied to each image for streak detection and measurement. The measured velocity profile for each image is shown in Section B.3. Looking back at Fig. 4.6, the mass flow increases from 0.5 *ms* to approximately 2.0 *ms*. The velocity slows through the orifice as expected once the cavity contracts, separates, and forms the conduit. The flow eventually slows down to the point where the particles do not sufficiently streak and the image processing algorithm would falsely assign streak values based on the diameter of the particle as shown in Fig. A.11(f) through (k).

#### **A.4 135 m/s impact velocity**

Referred to as Test 58 in Table 4.1, the 135 *m/s* shot provided good data. The entire event is displayed in Fig. A.12 through A.14. The collected raw imagery was a 1280 by 800 pixel image. Each image was cropped to 801 by 201 pixels around the funnel area to decrease image processing time. The seeded flow field prior to impact is seen in Fig. A.12(a). The projectile is shown in Fig. A.12(b) at impact. The flow field is obstructed for the first 0.5 *ms* after impact, Figs. A.12(c) through (f). Some streaks are visualized, in Figs. A.12(c) through (f), but the streak data is not sufficient to make a reasonable mass flow calculation. Additionally, the potential for particle lag exists during this time window after impact based on the characteristic response time calculations, also detailed in Chapter II.

For Fig. A.12(f) through Fig. A.14(f), the velocity flow field data was extracted from the raw images. A log transform, convolution filter and a binary threshold was equally applied to each image for streak detection and measurement. The measured velocity profile for each image is shown in Section B.4. Looking back at Fig. 4.6, the mass flow increases from 0.5 *ms* to approximately 2.0 *ms*. The velocity slows through the orifice as expected once the cavity contracts, separates, and forms the conduit. The flow eventually slows down to the point where the particles do not sufficiently streak and the image processing algorithm would falsely assign streak values based on the diameter of the particle as shown in Fig. A.14(d) through (j). This may attribute to the increase in calculated mass flow for the high velocity shots after 3.0 *ms*.

#### **A.5 176 m/s impact velocity**

Referred to as Test 52 in Table 4.1, the 176 *m/s* shot provided good data. The entire event is displayed in Fig. A.15 through A.17. The collected raw imagery was a 1280 by 800 pixel image. Each image was cropped to 801 by 201 pixels around the funnel

area to decrease image processing time. The seeded flow field prior to impact is seen in Fig. A.15(a). The projectile is shown in Fig. A.15(b) at impact. The flow field is obstructed for the first 0.5 *ms* after impact, Figs. A.15(c) through (f). Some streaks are visualized, in Figs. A.15(c) through (f), but the streak data is not sufficient to make a reasonable mass flow calculation. Additionally, the potential for particle lag exists during this time window after impact based on the characteristic response time calculations, also detailed in Chapter II.

For Fig. A.15(f) through Fig. A.17(f), the velocity flow field data was extracted from the raw images. A log transform, convolution filter and a binary threshold was equally applied to each image for streak detection and measurement. The measured velocity profile for each image is shown in Section B.5. Looking back at Fig. 4.6, the mass flow increases from 0.5 *ms* to approximately 2.0 *ms*. The velocity slows through the orifice as expected once the cavity contracts, separates, and forms the conduit. The flow eventually slows down to the point where the particles do not sufficiently streak and the image processing algorithm would falsely assign streak values based on the diameter of the particle as shown in Fig. A.17(d) through (h). This may attribute to the increase in calculated mass flow for the high velocity shots after 3.0 *ms*.

## **A.6 176 m/s impact velocity**

Referred to as Test 53 in Table 4.1, the 176 *m/s* shot provided good data. The entire event is displayed in Fig. A.18 through A.20. The collected raw imagery was a 1280 by 800 pixel image. Each image was cropped to 1001 by 201 pixels around the funnel area to decrease image processing time. The seeded flow field prior to impact is seen in Fig. A.18(a). The flow field shown 0.2

*ms*

in Fig. A.18(a) was displayed to depict the flow field prior to impact since Fig. A.18(b) prominently shows the projectile just prior to impact. The flow field just after impact is shown in Fig. A.18(c). The flow field is obstructed for the first 0.5 *ms* after impact, Figs. A.18(c) through (f). Some streaks are visualized, in Figs. A.18(c) through (f), but the streak data is not sufficient to make a reasonable mass flow calculation. Additionally, the potential for particle lag exists during this time window after impact based on the characteristic response time calculations, also detailed in Chapter II.

For Fig. A.18(f) through A.20(f), the velocity flow field data was extracted from the raw images. A log transform, convolution filter and a binary threshold was equally applied to each image for streak detection and measurement. The measured velocity profile for each image is shown in Section B.6. Looking back at Fig. 4.6, the mass flow increases from 0.5 *ms* to approximately 2.0 *ms*. The velocity slows through the orifice as expected once the cavity contracts, separates, and forms the conduit. The flow eventually slows down to the point where the particles do not sufficiently streak and the image processing algorithm would falsely assign streak values based on the diameter of the particle as shown in Fig. A.20(d) through (i). This may attribute to the increase in calculated mass flow for the high velocity shots after 3.0 *ms*.

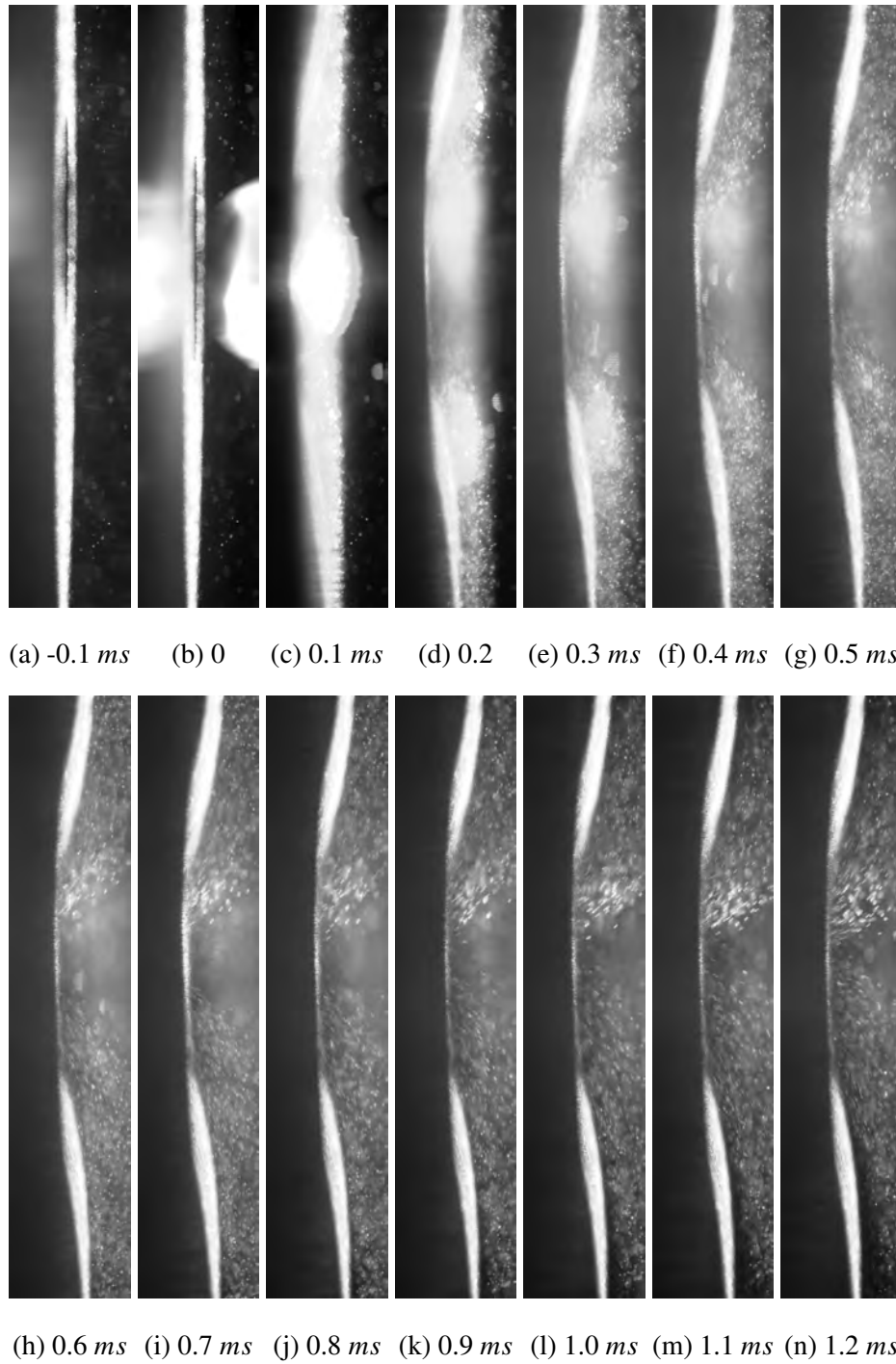
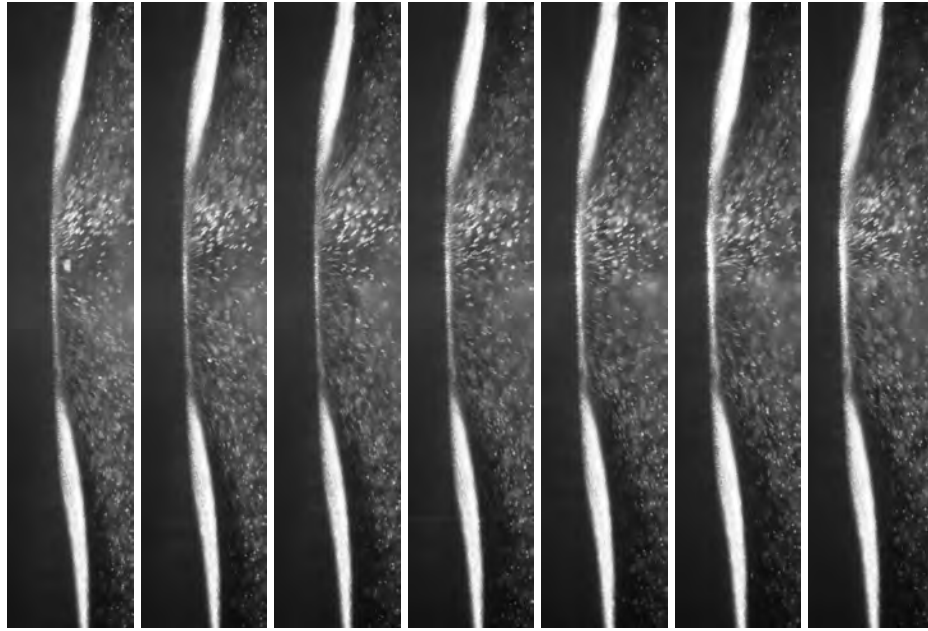
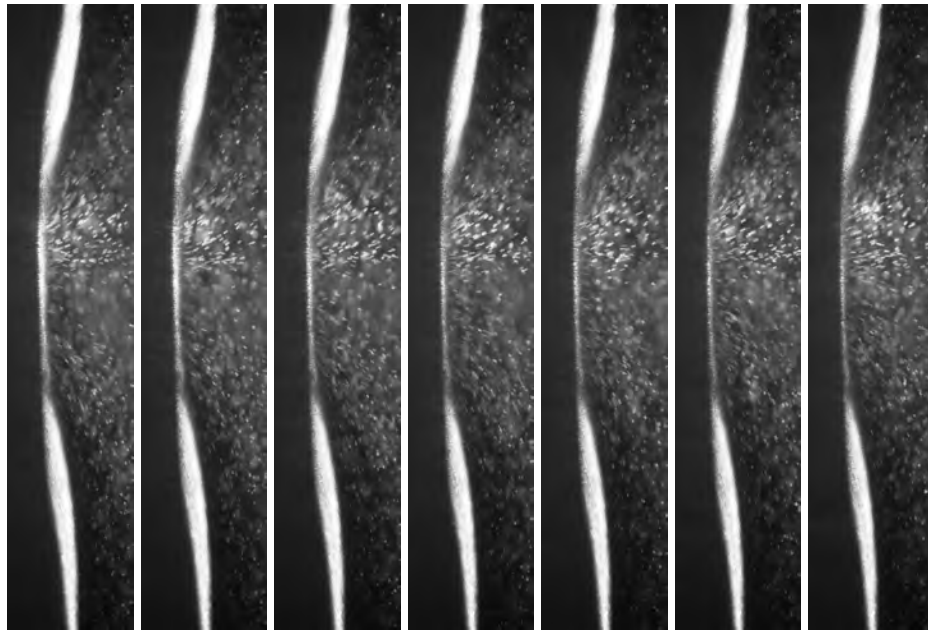


Figure A.1. Collected images depicting the evolution of entrained velocity measurements for  $113\text{ m/s}$  impact velocity from the first image prior to impact to  $1.2\text{ ms}$  after impact. Continuation of the event is shown in Fig. A.2.



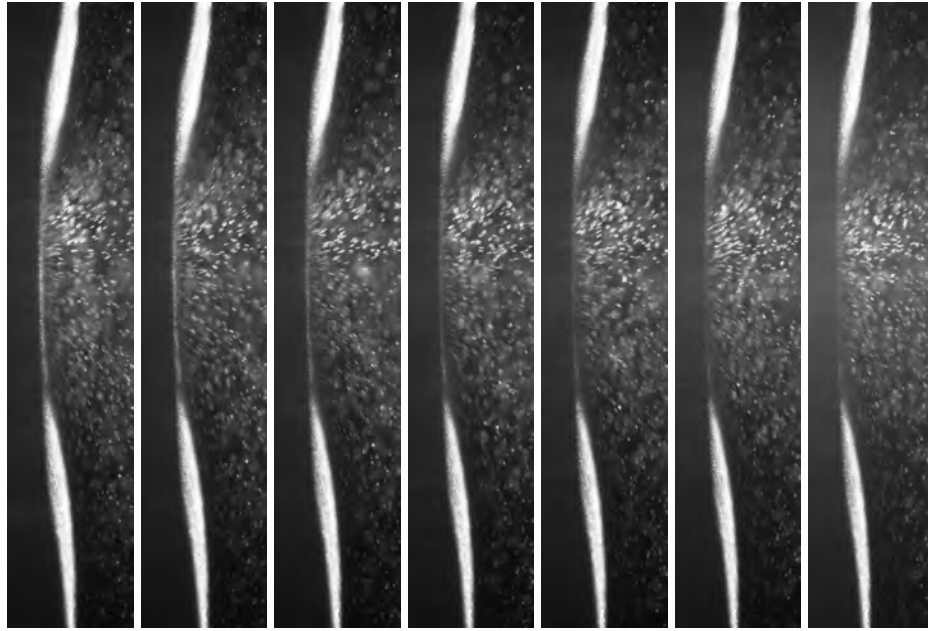


(a) 1.3 *ms* (b) 1.4 *ms* (c) 1.5 *ms* (d) 1.6 *ms* (e) 1.7 *ms* (f) 1.8 *ms* (g) 1.9 *ms*

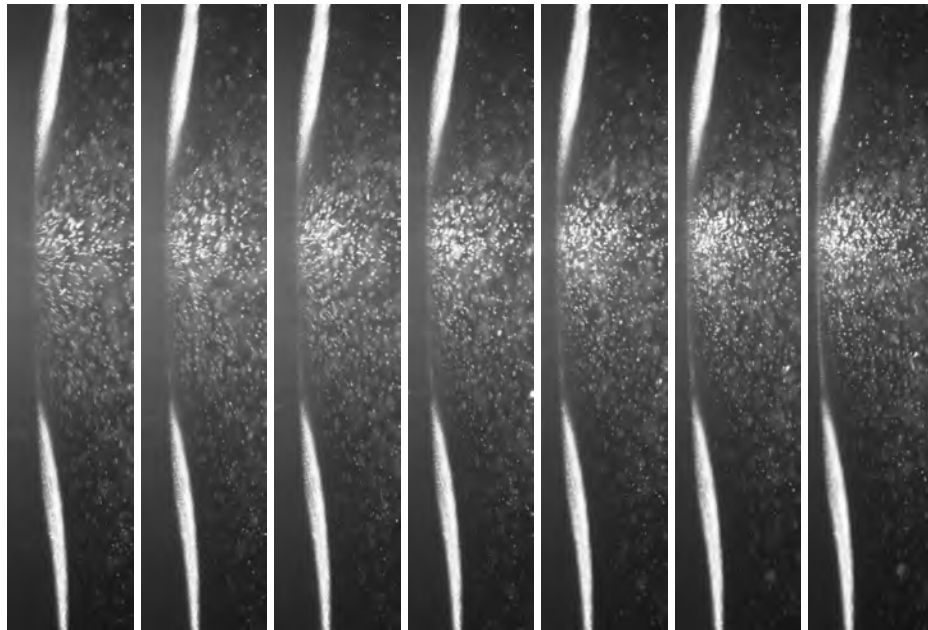


(h) 2.0 *ms* (i) 2.1 *ms* (j) 2.2 *ms* (k) 2.3 *ms* (l) 2.4 *ms* (m) 2.5 *ms* (n) 2.6 *ms*

Figure A.2. Collected images depicting the evolution of entrained velocity measurements for 113 *m/s* impact velocity from 1.3 to 2.6 *ms* after impact. Continuation of the event is shown in Fig. A.3.

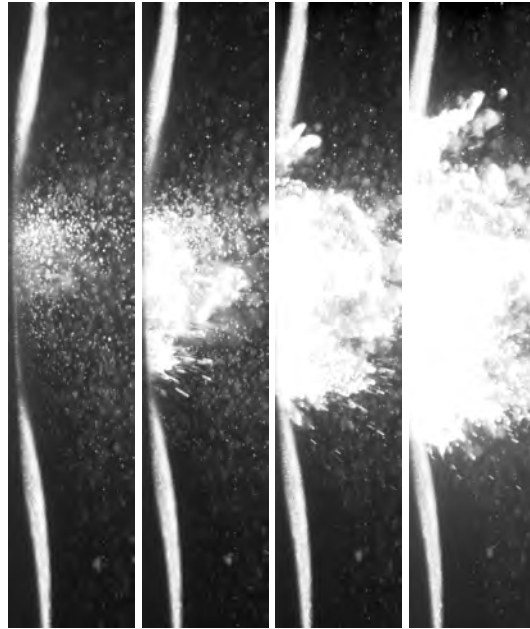


(a) 2.7 *ms* (b) 2.8 *ms* (c) 2.9 *ms* (d) 3.0 *ms* (e) 3.1 *ms* (f) 3.2 *ms* (g) 3.3 *ms*

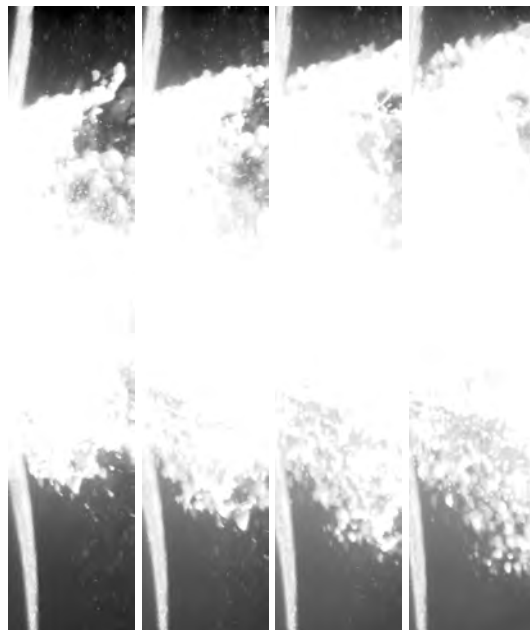


(h) 3.4 *ms* (i) 3.5 *ms* (j) 3.6 *ms* (k) 3.7 *ms* (l) 3.8 *ms* (m) 3.9 *ms* (n) 4.0 *ms*

Figure A.3. Collected images depicting the evolution of entrained velocity measurements for 113 *m/s* impact velocity from 2.7 to 4.0 *ms* after impact. Continuation of the event is shown in Fig. A.4.



(a) 4.1 *ms* (b) 4.2 *ms* (c) 4.3 *ms* (d) 4.4 *ms*



(e) 4.5 *ms* (f) 4.6 *ms* (g) 4.7 *ms* (h) 4.8 *ms*

Figure A.4. Collected images depicting the evolution of entrained velocity measurements for 113 *m/s* impact velocity from 4.1 to 4.8 *ms* after impact.

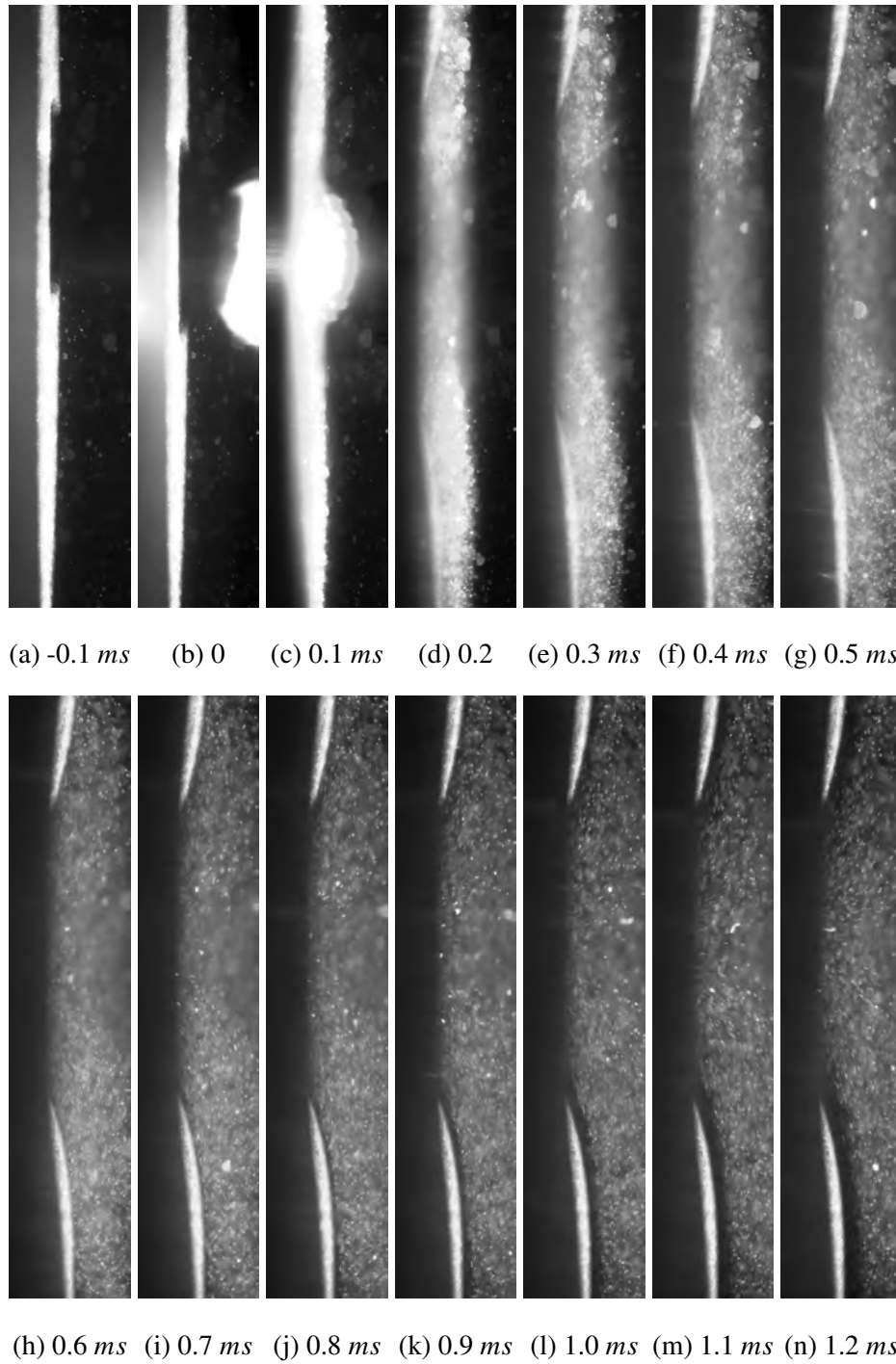
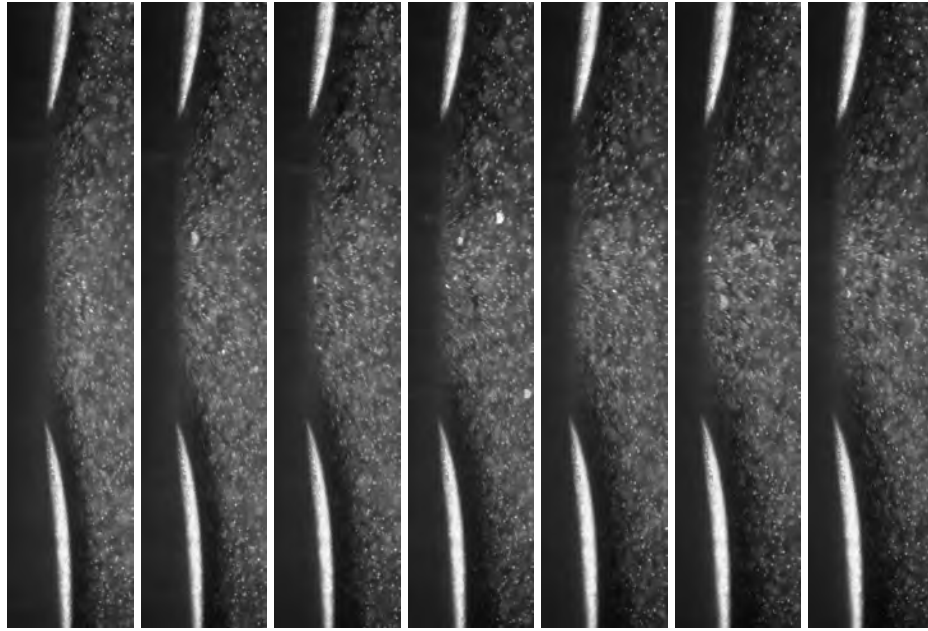
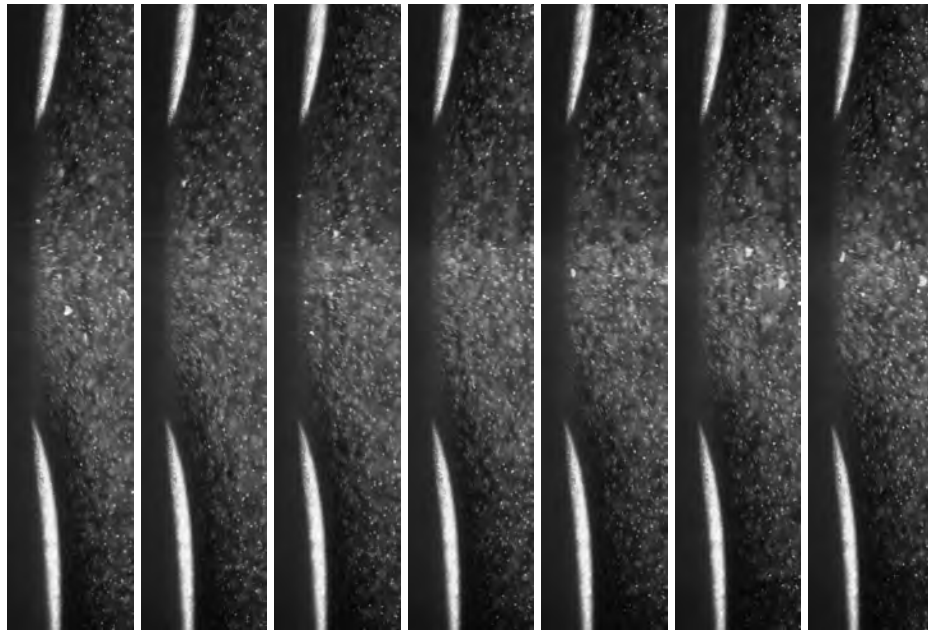


Figure A.5. Collected images depicting the evolution of entrained velocity measurements for  $114\text{ m/s}$  impact velocity from the first image prior to impact to  $1.2\text{ ms}$  after impact. Continuation of the event is shown in Fig. A.6.

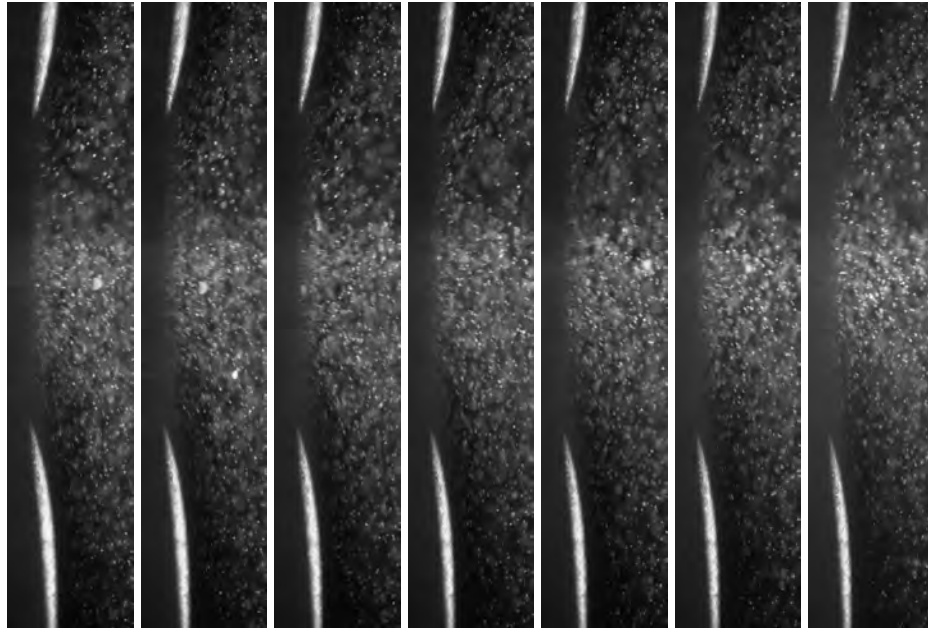


(a) 1.3 *ms* (b) 1.4 *ms* (c) 1.5 *ms* (d) 1.6 *ms* (e) 1.7 *ms* (f) 1.8 *ms* (g) 1.9 *ms*

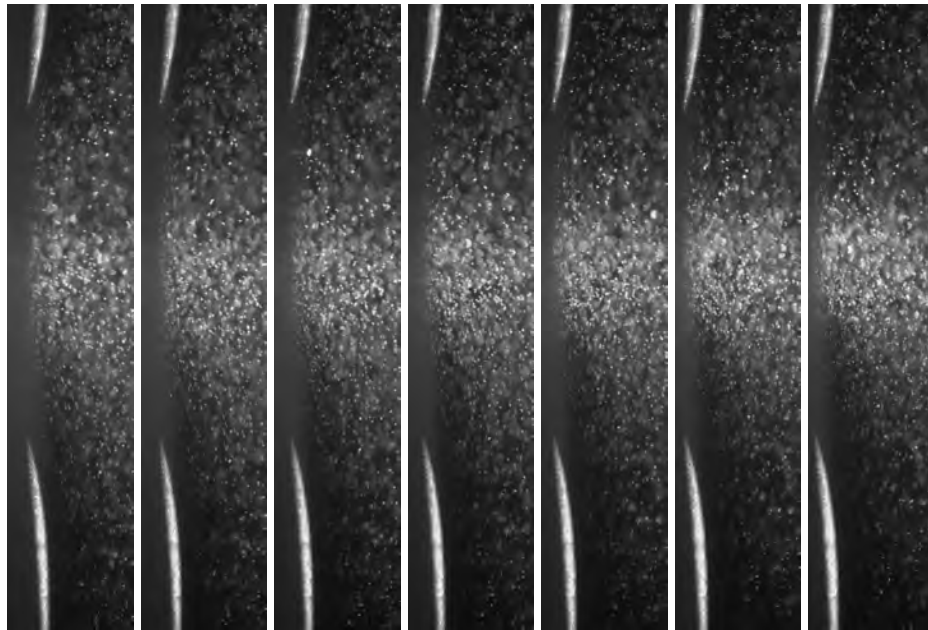


(h) 2.0 *ms* (i) 2.1 *ms* (j) 2.2 *ms* (k) 2.3 *ms* (l) 2.4 *ms* (m) 2.5 *ms* (n) 2.6 *ms*

Figure A.6. Collected images depicting the evolution of entrained velocity measurements for 114 *m/s* impact velocity from 1.3 to 2.6 *ms* after impact. Continuation of the event is shown in Fig. A.7.

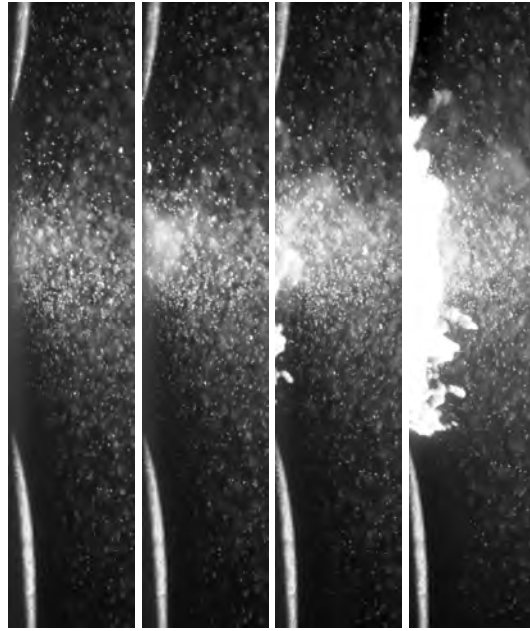


(a) 2.7 *ms* (b) 2.8 *ms* (c) 2.9 *ms* (d) 3.0 *ms* (e) 3.1 *ms* (f) 3.2 *ms* (g) 3.3 *ms*

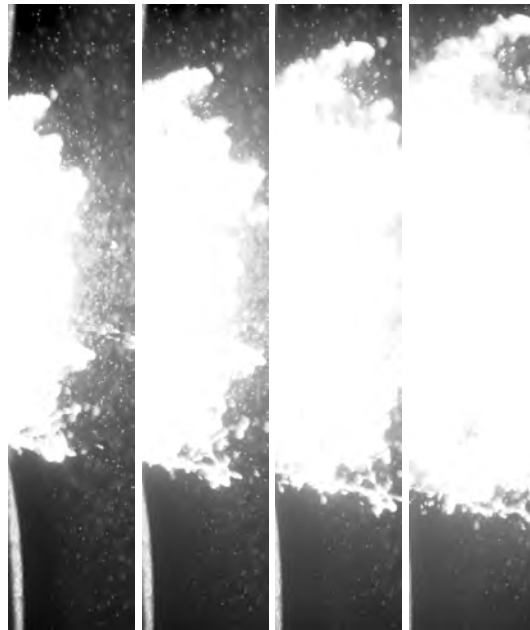


(h) 3.4 *ms* (i) 3.5 *ms* (j) 3.6 *ms* (k) 3.7 *ms* (l) 3.8 *ms* (m) 3.9 *ms* (n) 4.0 *ms*

Figure A.7. Collected images depicting the evolution of entrained velocity measurements for 114 *m/s* impact velocity from 2.7 to 4.0 *ms* after impact. Continuation of the event is shown in Fig. A.8.



(a) 4.1 *ms* (b) 4.2 *ms* (c) 4.3 *ms* (d) 4.4 *ms*



(e) 4.5 *ms* (f) 4.6 *ms* (g) 4.7 *ms* (h) 4.8 *ms*

Figure A.8. Collected images depicting the evolution of entrained velocity measurements for 114 *m/s* impact velocity from 2.7 to 4.0 *ms* after impact.

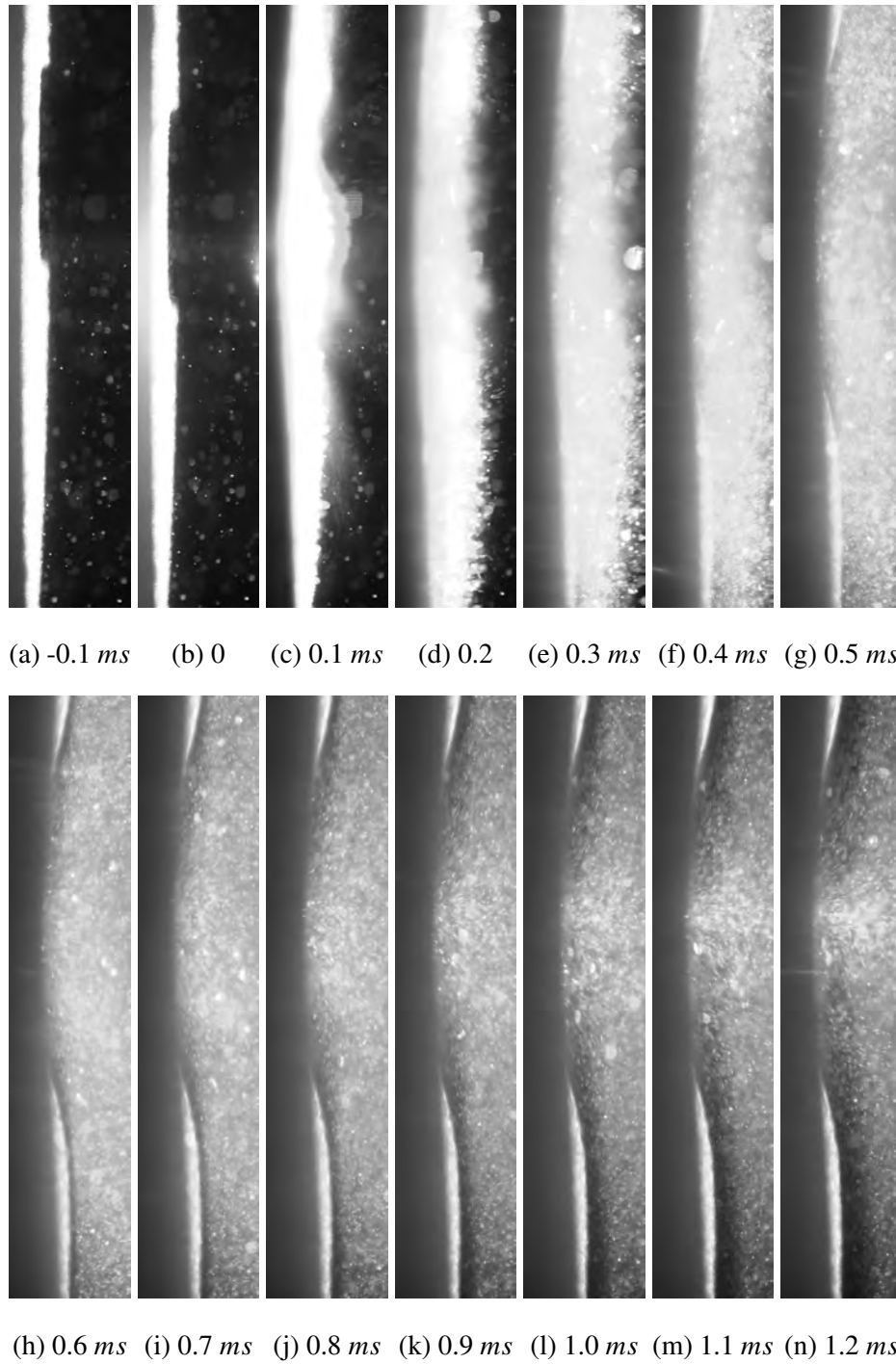
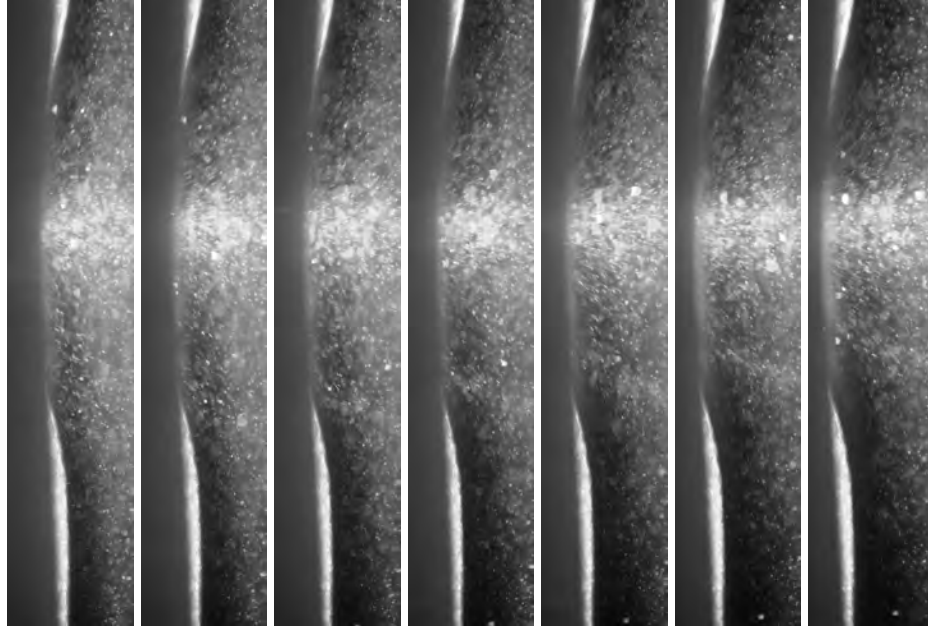
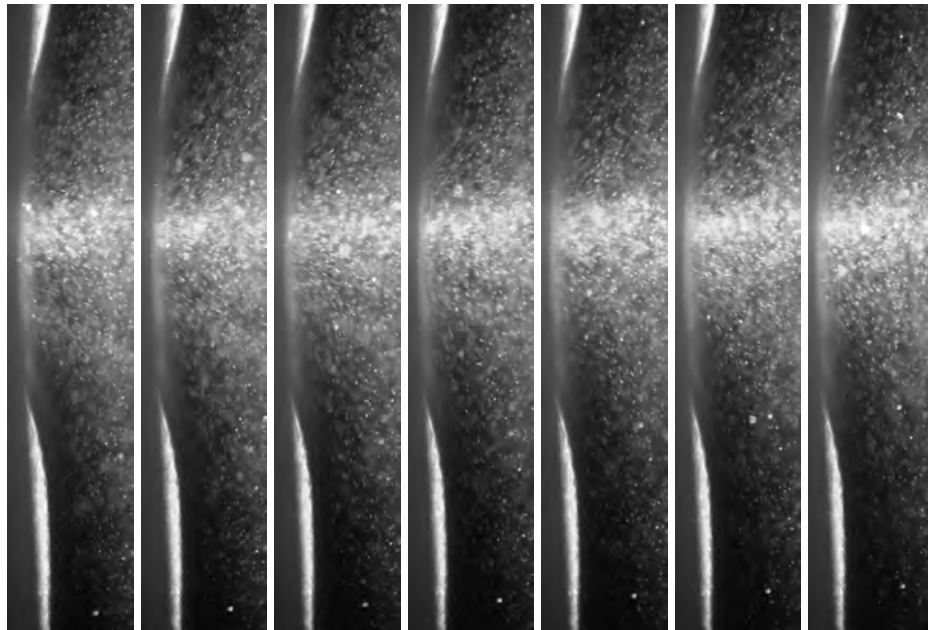


Figure A.9. Collected images depicting the evolution of entrained velocity measurements for  $132\text{ m/s}$  impact velocity from the first image prior to impact to  $1.2\text{ ms}$  after impact. Continuation of the event is shown in Fig. A.10.



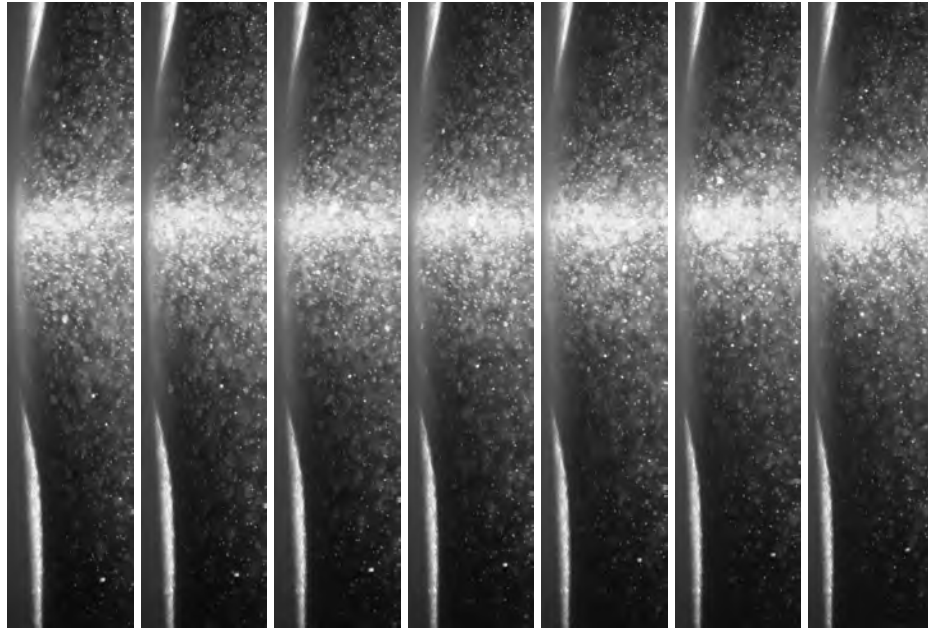


(a) 1.3 *ms* (b) 1.4 *ms* (c) 1.5 *ms* (d) 1.6 *ms* (e) 1.7 *ms* (f) 1.8 *ms* (g) 1.9 *ms*

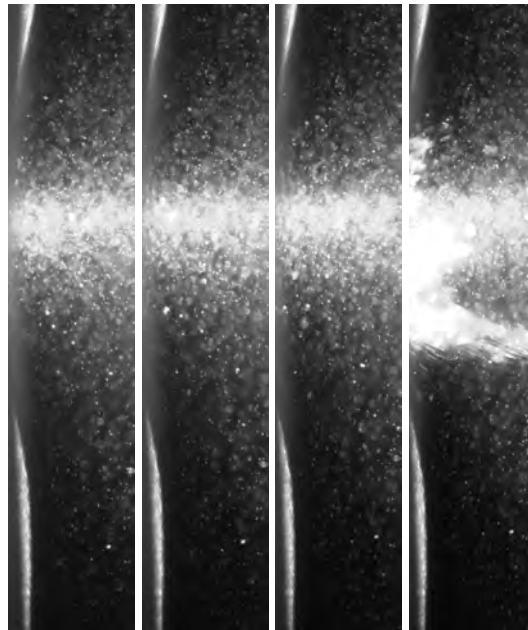


(h) 2.0 *ms* (i) 2.1 *ms* (j) 2.2 *ms* (k) 2.3 *ms* (l) 2.4 *ms* (m) 2.5 *ms* (n) 2.6 *ms*

Figure A.10. Collected images depicting the evolution of entrained velocity measurements for 132 *m/s* impact velocity from 1.3 to 2.6 *ms* after impact. Continuation of the event is shown in Fig. A.11.



(a) 2.7 *ms* (b) 2.8 *ms* (c) 2.9 *ms* (d) 3.0 *ms* (e) 3.1 *ms* (f) 3.2 *ms* (g) 3.3 *ms*



(h) 3.4 *ms* (i) 3.5 *ms* (j) 3.6 *ms* (k) 3.7 *ms*

Figure A.11. Collected images depicting the evolution of entrained velocity measurements for 132 *m/s* impact velocity from 2.7 to 3.7 *ms* after impact.

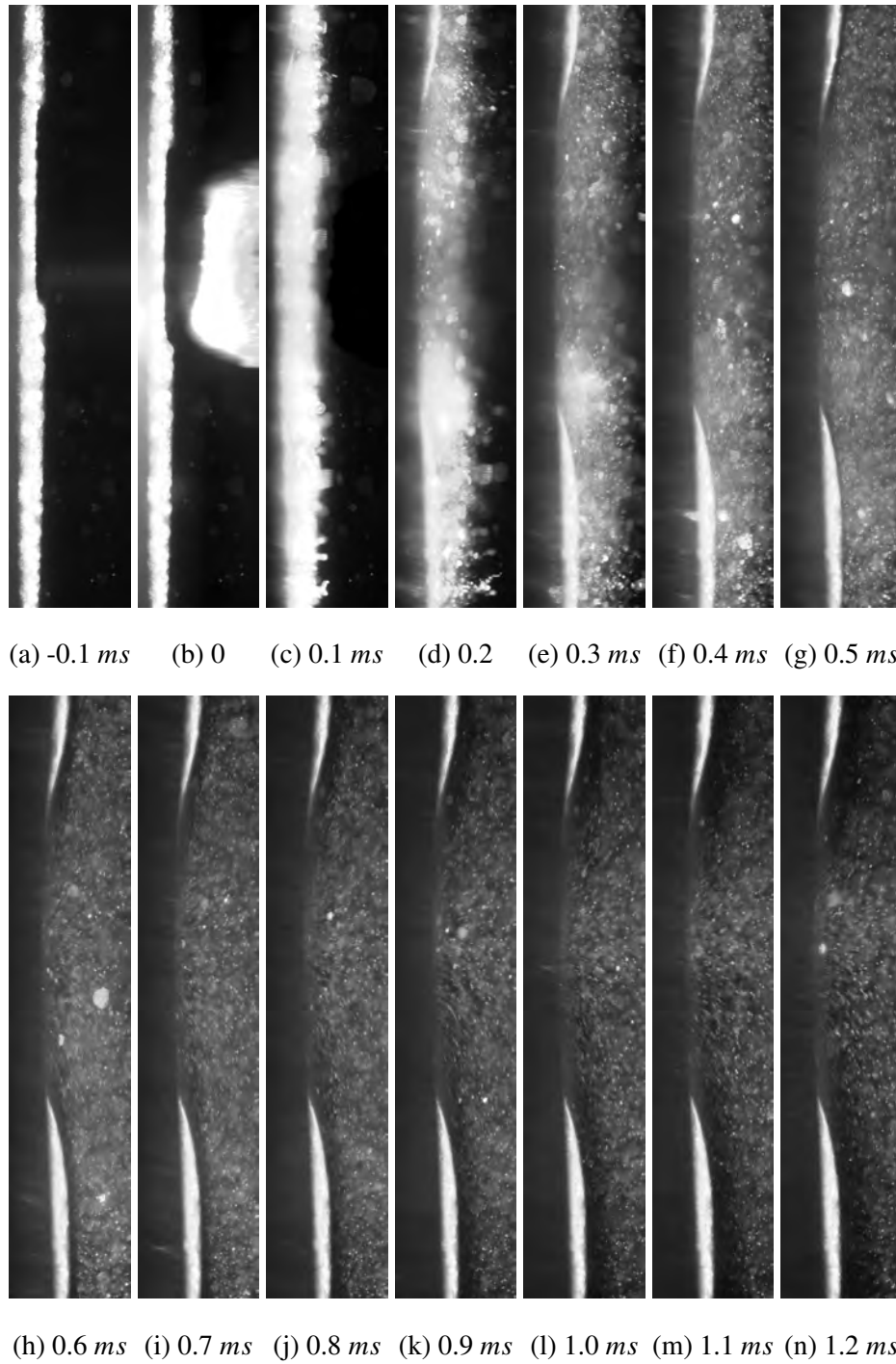
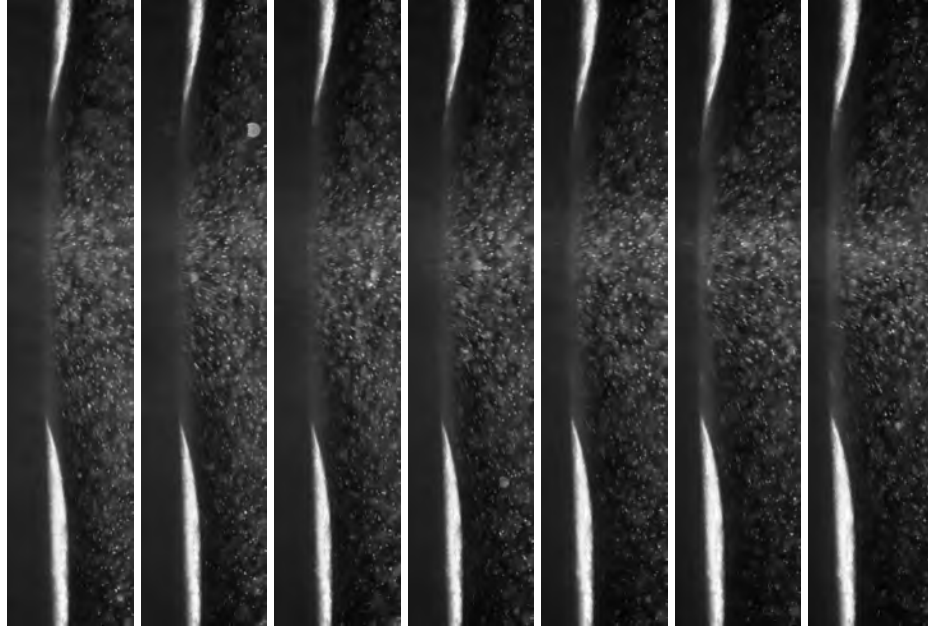
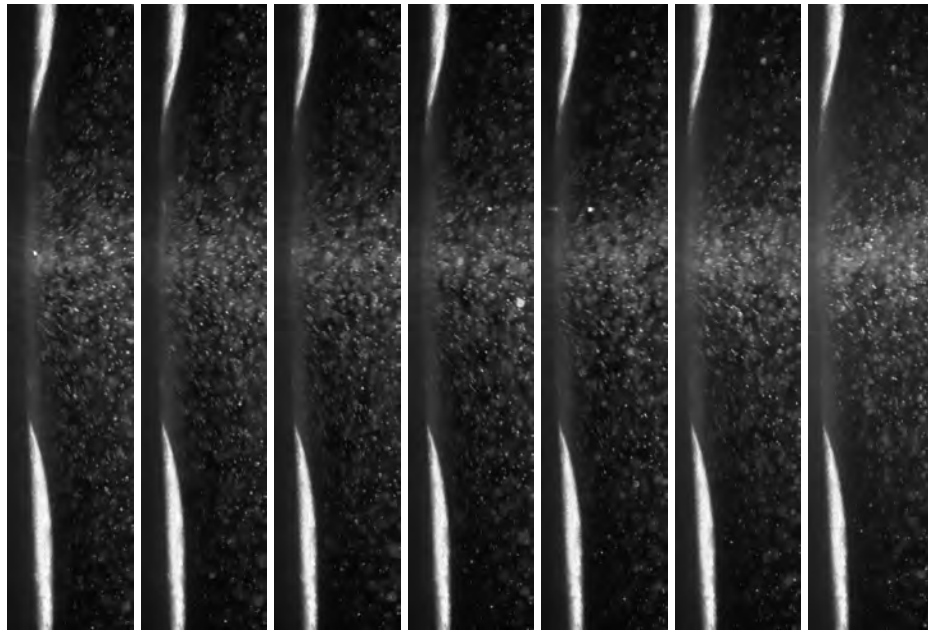


Figure A.12. Collected images depicting the evolution of entrained velocity measurements for  $135\text{ m/s}$  impact velocity from the first image prior to impact to  $1.2\text{ ms}$  after impact. Continuation of the event is shown in Fig. A.13.

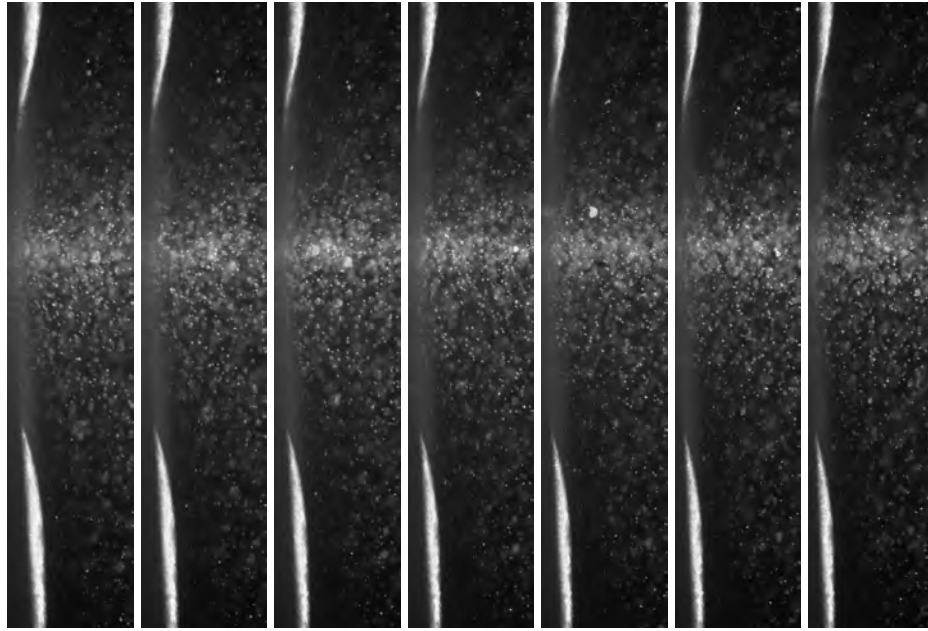


(a) 1.3 *ms* (b) 1.4 *ms* (c) 1.5 *ms* (d) 1.6 *ms* (e) 1.7 *ms* (f) 1.8 *ms* (g) 1.9 *ms*

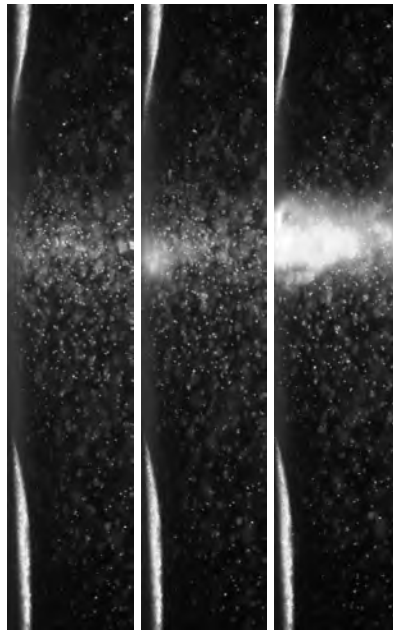


(h) 2.0 *ms* (i) 2.1 *ms* (j) 2.2 *ms* (k) 2.3 *ms* (l) 2.4 *ms* (m) 2.5 *ms* (n) 2.6 *ms*

Figure A.13. Collected images depicting the evolution of entrained velocity measurements for 135 *m/s* impact velocity from 1.3 to 2.6 *ms* after impact. Continuation of the event is shown in Fig. A.14.



(a)  $2.7\text{ ms}$  (b)  $2.8\text{ ms}$  (c)  $2.9\text{ ms}$  (d)  $3.0\text{ ms}$  (e)  $3.1\text{ ms}$  (f)  $3.2\text{ ms}$  (g)  $3.3\text{ ms}$



(h)  $3.4\text{ ms}$  (i)  $3.5\text{ ms}$  (j)  $3.6\text{ ms}$

Figure A.14. Collected images depicting the evolution of entrained velocity measurements for  $135\text{ m/s}$  impact velocity from  $2.7$  to  $3.5\text{ ms}$  after impact.

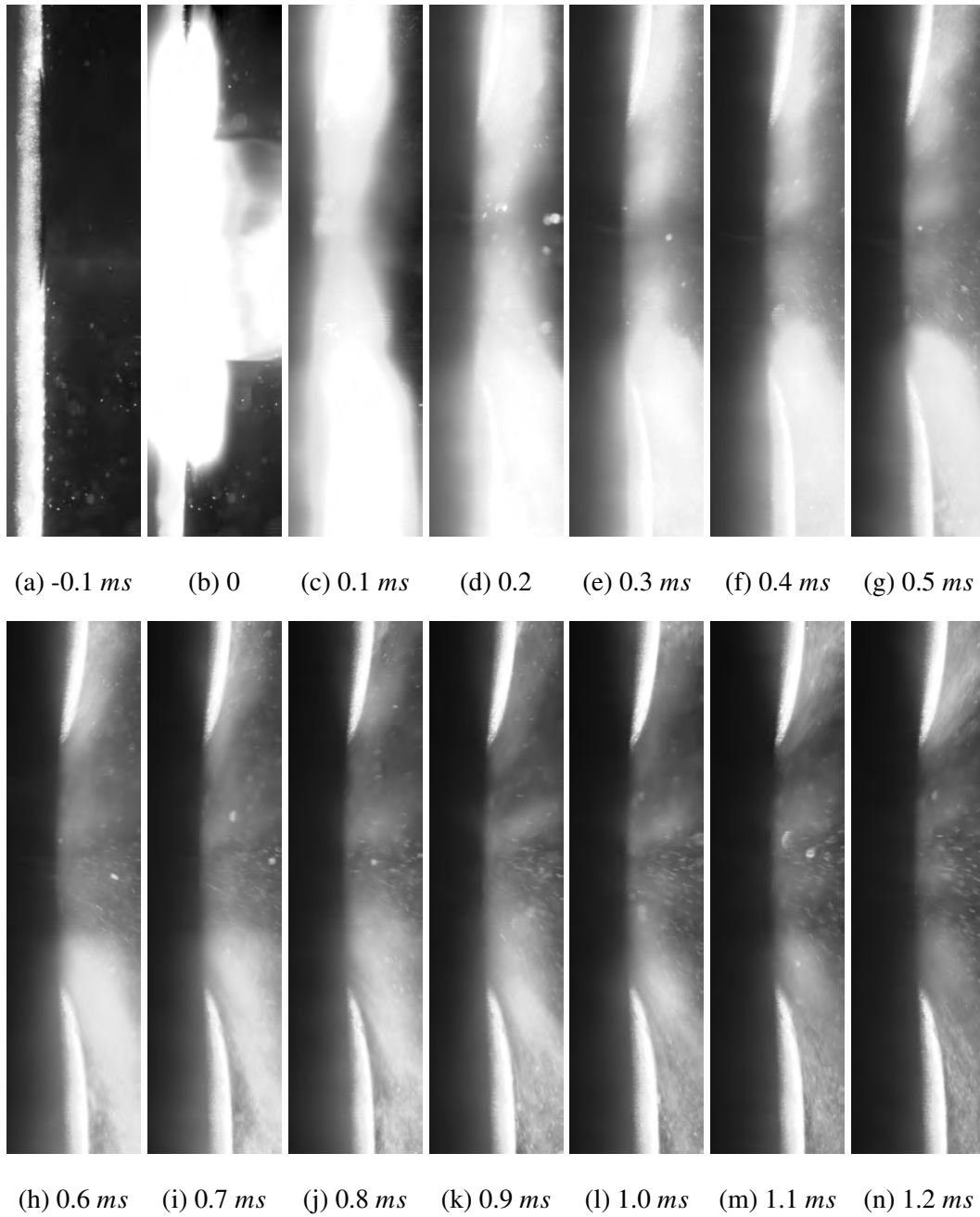


Figure A.15. Collected images depicting the evolution of entrained velocity measurements for  $176\text{ m/s}$  impact velocity from the first image prior to impact to  $1.2\text{ ms}$  after impact. Continuation of the event is shown in Fig. A.16.

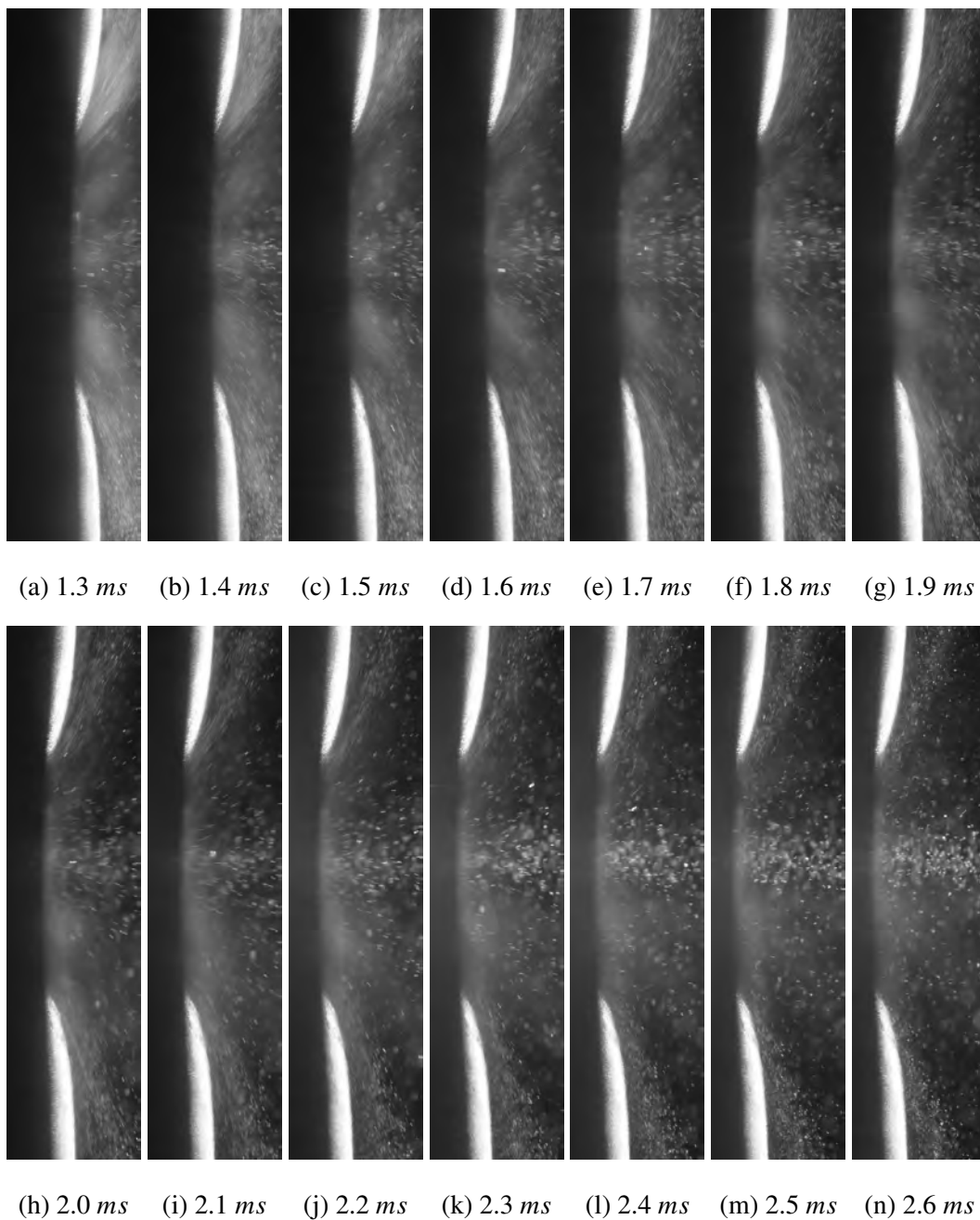
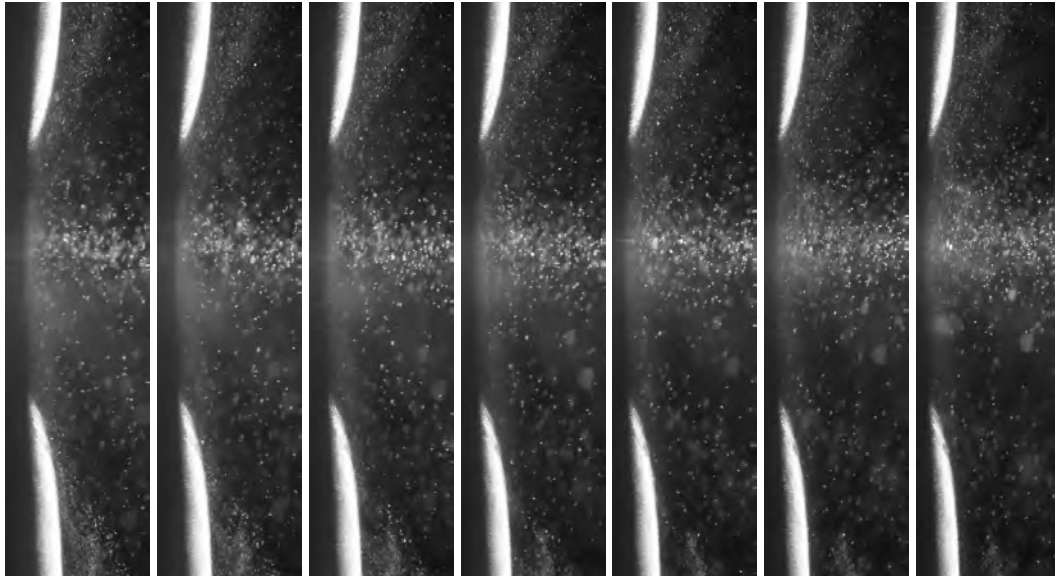


Figure A.16. Collected images depicting the evolution of entrained velocity measurements for 176 *m/s* impact velocity from 1.3 to 2.6 *ms* after impact. Continuation of the event is shown in Fig. A.17.



(a) 2.7 *ms*   (b) 2.8 *ms*   (c) 2.9 *ms*   (d) 3.0 *ms*   (e) 3.1 *ms*   (f) 3.2 *ms*   (g) 3.3 *ms*



(h) 3.4 *ms*

Figure A.17. Collected images depicting the evolution of entrained velocity measurements for 176 *m/s* impact velocity from 2.7 to 3.4 *ms* after impact.



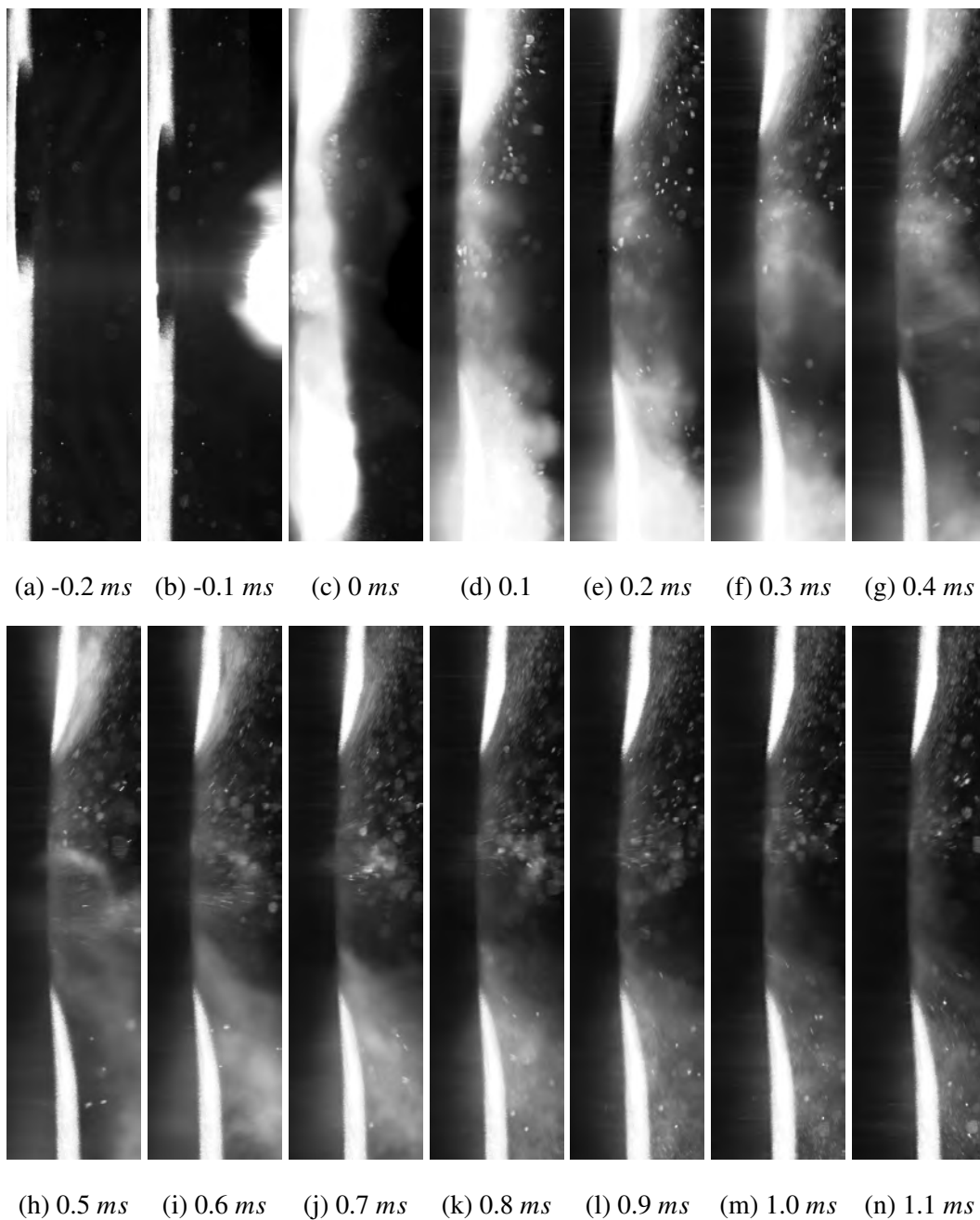


Figure A.18. Collected images depicting the evolution of entrained velocity measurements for  $176\ m/s$  impact velocity from the first image prior to impact to  $1.1\ ms$  after impact. Continuation of the event is shown in Fig. A.19.

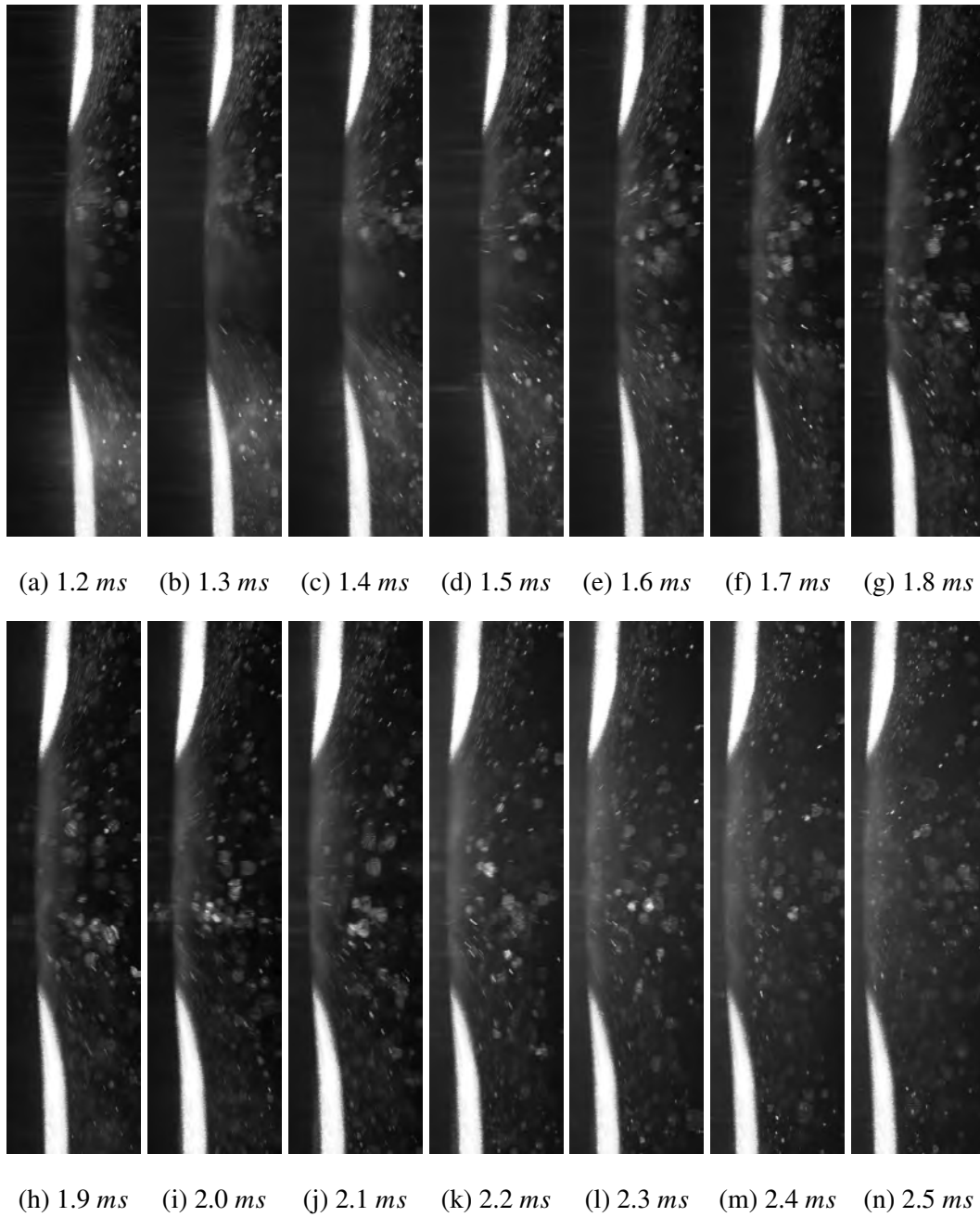


Figure A.19. Collected images depicting the evolution of entrained velocity measurements for 176 *m/s* impact velocity from 1.2 to 2.5 *ms* after impact. Continuation of the event is shown in Fig. A.20.

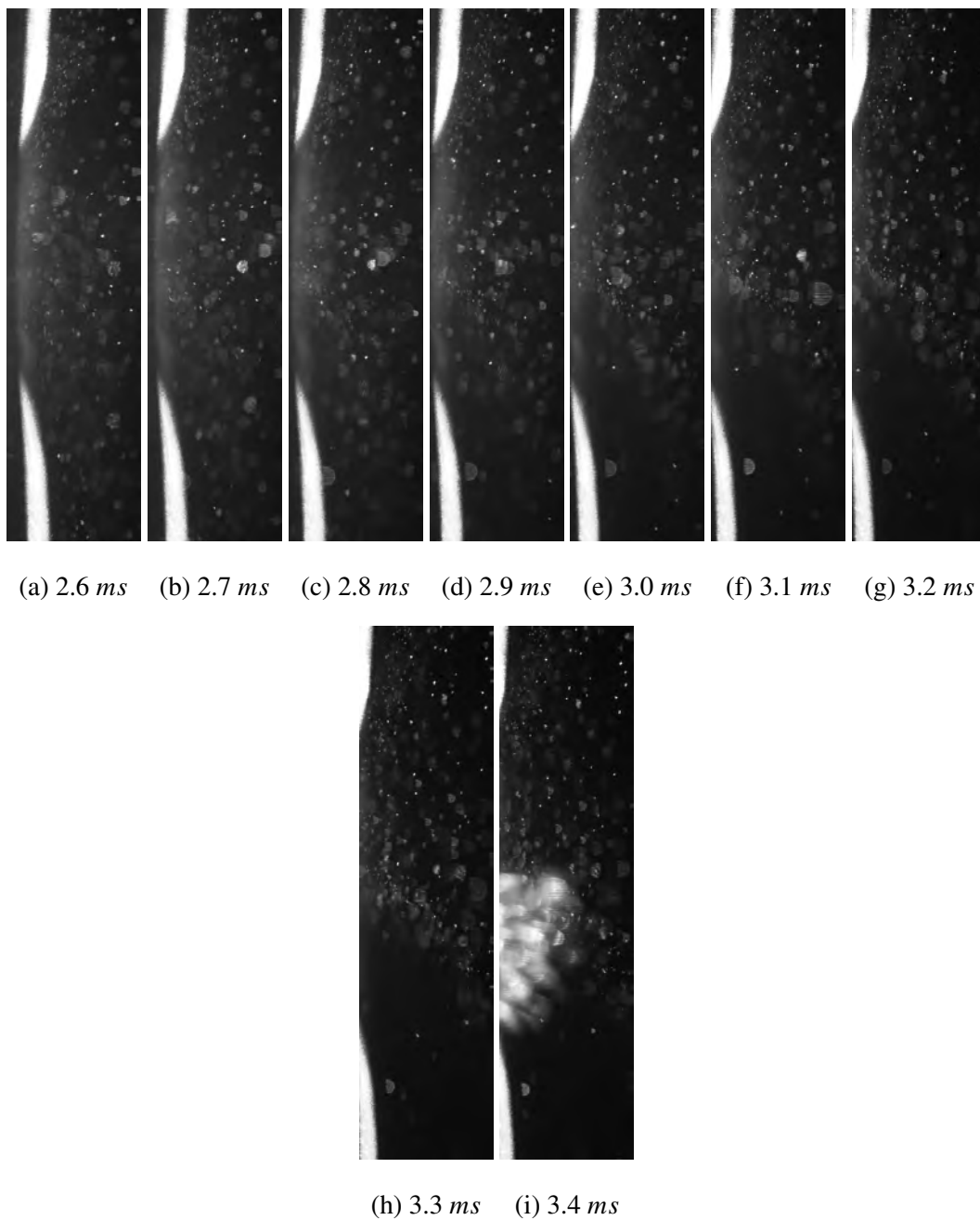


Figure A.20. Collected images depicting the evolution of entrained velocity measurements for 176 *m/s* impact velocity from 2.6 to 3.4 *ms* after impact.

## Appendix B: Entrained Mass and Velocity Plots

The mass flow through the orifice was calculated for projectile impact velocities of approximately 113, 114, 132, 135, 176, and 176  $m/s$ . The mass flow rate is very similar regardless of impact velocity as shown in Fig. 4.6. The similar mass flow rate was attributed to similar geometric cavity conditions and is discussed in Chapter IV. The velocity profile data, for the mass flow rate, was extracted from the raw imagery shown in Appendix A and the imagery analysis process is detailed in Chapter III. From the velocity profile, a trapezoidal approximation of a volume of revolution around the projectile's shot-line was used to calculate the mass flow assuming constant air density. Equations providing details on the trapezoidal approximation are provided in Chapter IV. Details about each specific shot are provided below.

### B.1 113 $m/s$ impact velocity

For the 113  $m/s$  shot, the mass flow rate is shown in Fig. B.1. The entrained mass calculation, shown in Fig. B.2 was obtained by performing a rectangular approximation of Fig. B.1's data to estimate the area under the curve. The entrained mass, along with the applicable cavity volume measurements in Appendix C, was used to compute the cavity's partial pressure as detailed in Section 4.4.3

The velocity profiles used to calculate the mass flow data points composing Fig. B.1 are shown in Fig. B.3 through B.8 at the applicable times. For example, in Fig. B.1, 0.5  $ms$  after projectile impact, the first mass flow data point's corresponding velocity profile is shown in Fig. B.3(a). The velocity profile in Fig. B.3(a) appears nominally symmetric about the projectile shot-line at zero. Based on knowledge of flow through nozzles and venturi, the symmetric velocity profile was expected for the flow through the orifice even though there is not an external "pipe" [49]. As the entrainment event proceeds, the flow

field continues to develop and increase its overall velocity magnitude as shown in Fig. B.3 through B.4 and to Fig. B.5(d) where the flow peaks at 2.0 *ms*.

Referring back to the mass flow plot in Fig. B.1, the mass flow begins to slow after 2.0 *ms*. The lower mass flow was attributed to the cavity contraction and the formation of the re-entrant jet as discussed in Chapter IV. The corresponding velocity profiles retain their symmetry indicating good flow field measurements.

In Fig. B.8(b) the symmetry of the flow field starts to break down indicating a potential sub-quality measurement. In particular, the flow field velocity increases noticeably at 1 diameter above and below the shot-line. This most likely contributes to the increase in mass flow rate at 3.6 and 3.7 *ms* in Fig. B.1.

For the 113 *m/s* shot, the first sign of fluid spurt occurred around 4.1 *ms* after impact as shown in Fig. A.4(a). The entrainment velocity calculations covered 0.5 *ms* to 3.5 *ms* accurately. The accuracy after 3.5 *ms* is questionable but the velocity plots were shown to provide a reference for future research or other potential unknown future uses. Regardless, the velocity profile data over the 0.5 to 3.5 *ms* window was sufficient to correlate back to the internal cavity geometric features as discussed in Chapter IV and provide the cavity composition necessary for partial pressure and pressure work calculations.

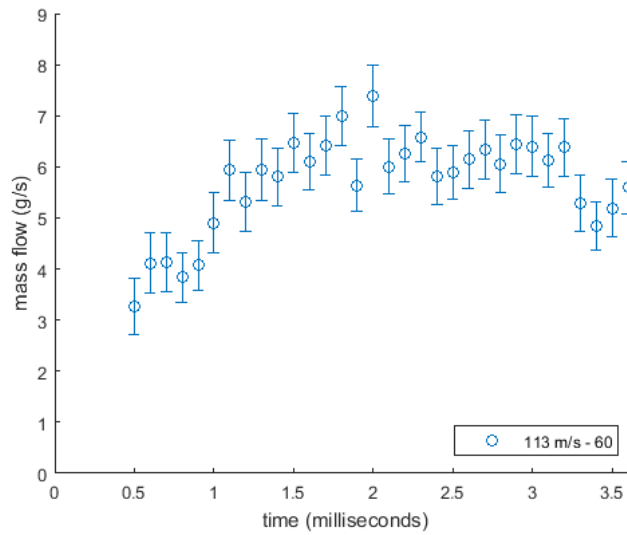


Figure B.1. Mass flow plot for the 113  $m/s$  shot obtained by performing a trapezoidal approximation of a volume of revolution around the projectile's shot-line. Each mass flow data point's corresponding velocity profile is shown in Fig. B.3 through B.8.

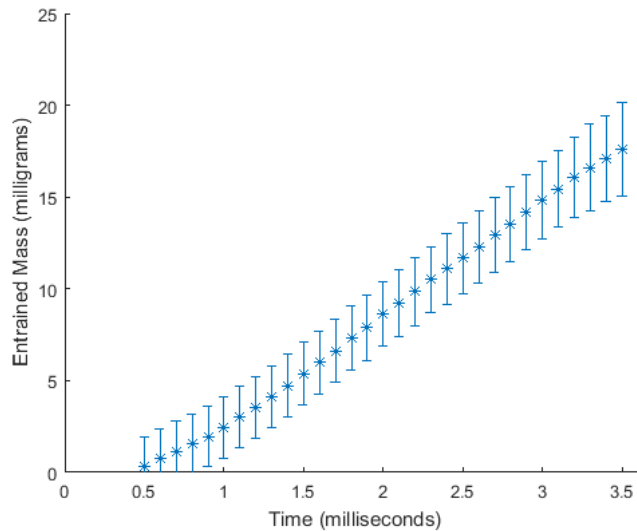
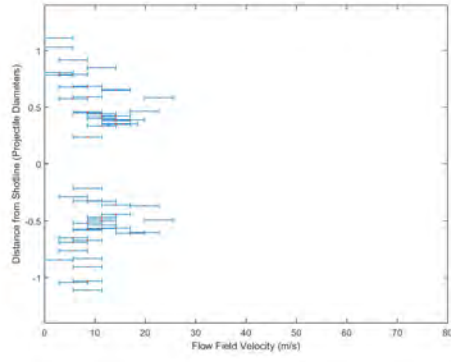
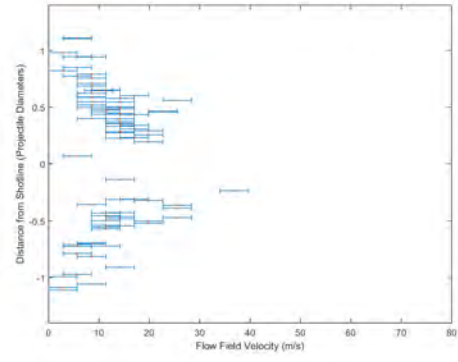


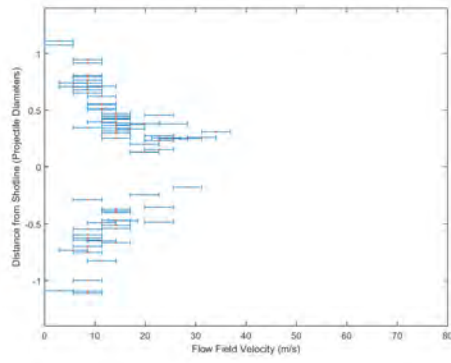
Figure B.2. Entrained mass calculation of ambient air into the HRAM cavity used for partial pressure calculations in Section 4.4.3 for the 113  $m/s$  shot. The entrained mass was calculated by performing a rectangular approximation of Fig. B.1's data to estimate the area under the curve.



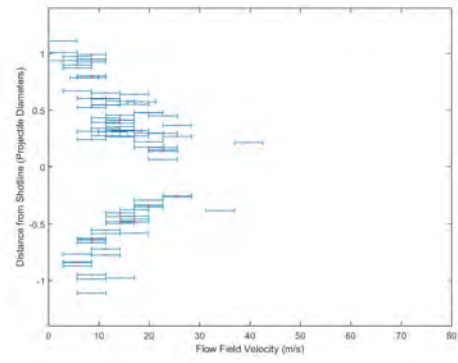
(a) 0.5 ms



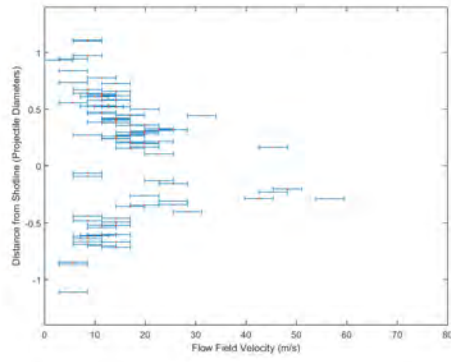
(b) 0.6 ms



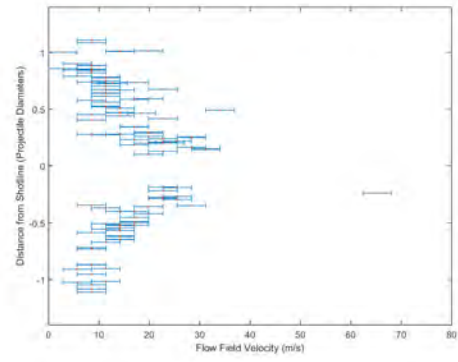
(c) 0.7 ms



(d) 0.8 ms

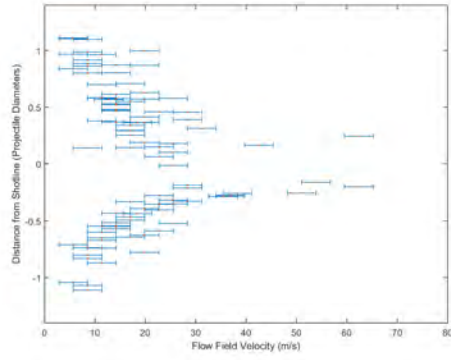


(e) 0.9 ms

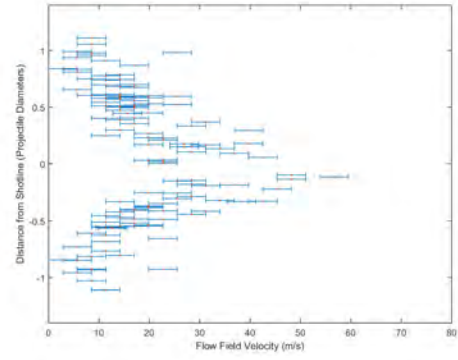


(f) 1.0 ms

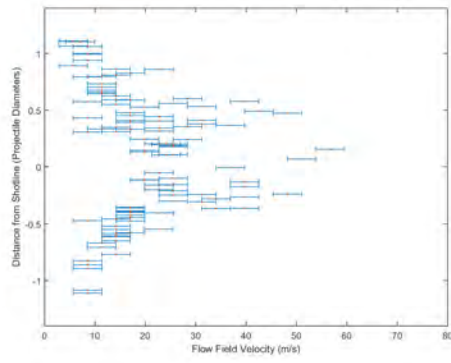
Figure B.3. Plotted horizontal component of the streak velocity across the funnel diameter 0.5 to 1.0 ms after impact for the 113 m/s impact velocity.



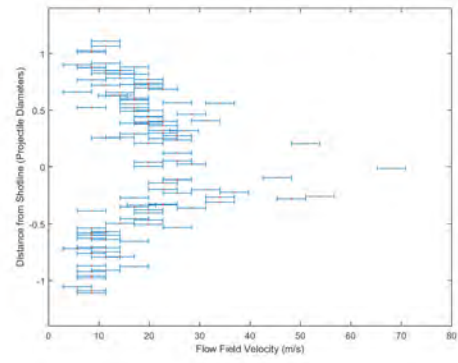
(a) 1.1 ms



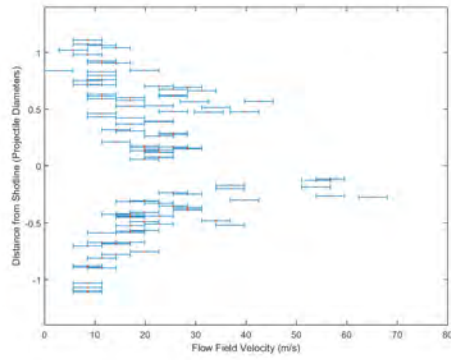
(b) 1.2 ms



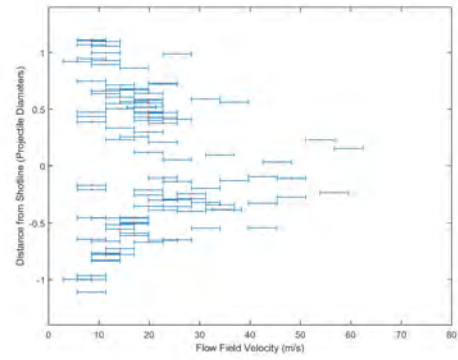
(c) 1.3 ms



(d) 1.4 ms



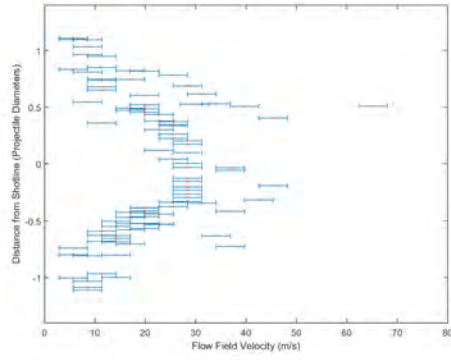
(e) 1.5 ms



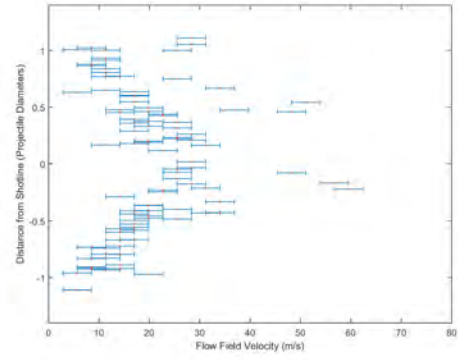
(f) 1.6 ms

Figure B.4. Plotted horizontal component of the streak velocity across the funnel diameter 1.1 to 1.6 ms after impact for the 113 m/s impact velocity.

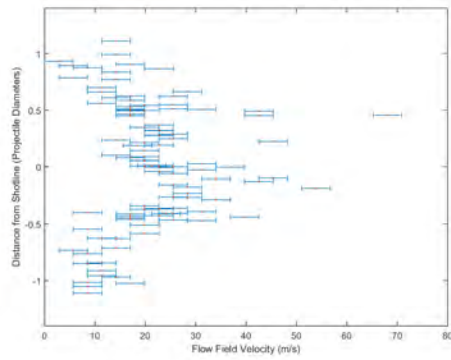




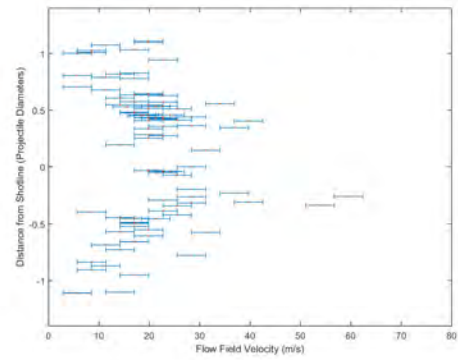
(a) 1.7 ms



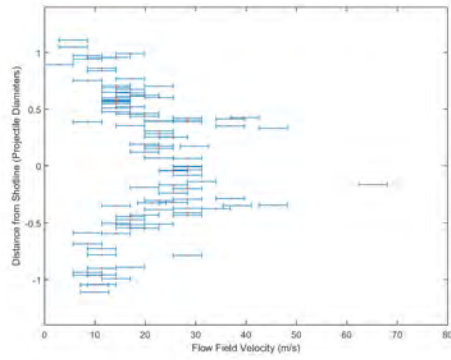
(b) 1.8 ms



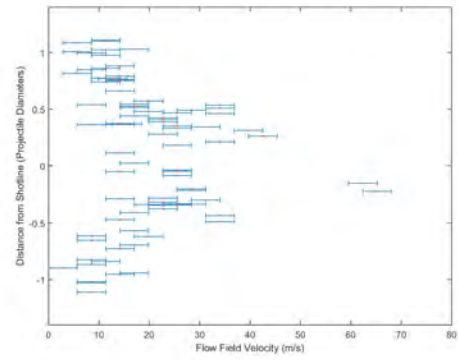
(c) 1.9 ms



(d) 2.0 ms

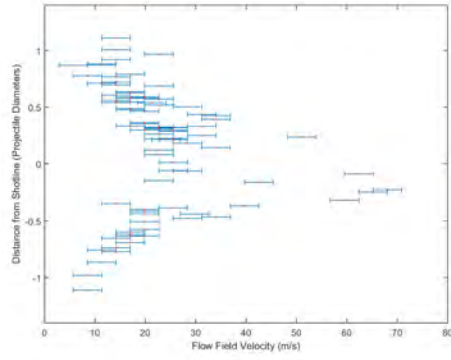


(e) 2.1 ms

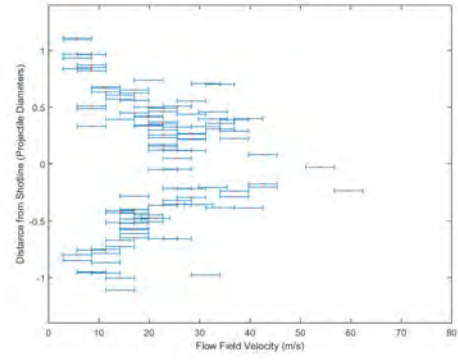


(f) 2.2 ms

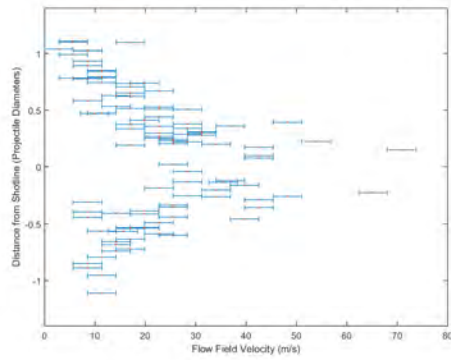
Figure B.5. Plotted horizontal component of the streak velocity across the funnel diameter 1.7 to 2.2 ms after impact for the 113 m/s impact velocity.



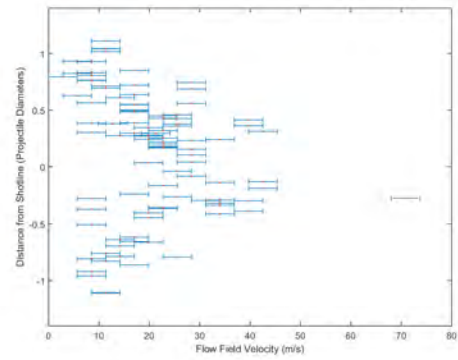
(a) 2.3 ms



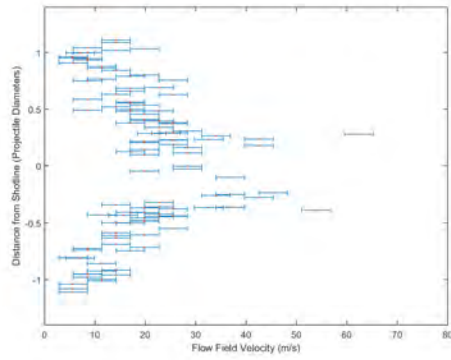
(b) 2.4 ms



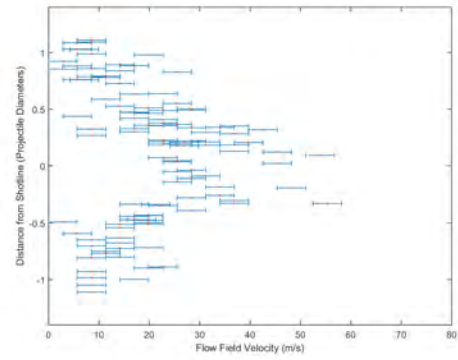
(c) 2.5 ms



(d) 2.6 ms

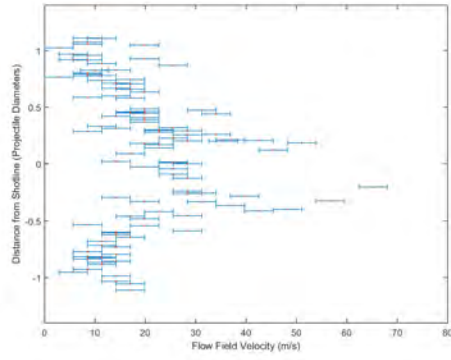


(e) 2.7 ms

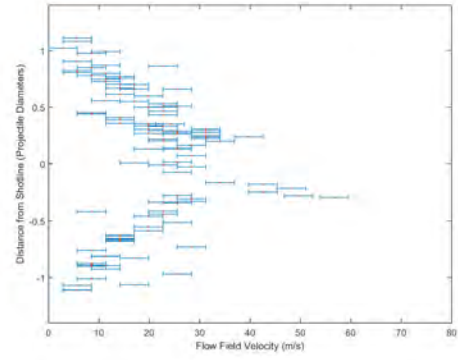


(f) 2.8 ms

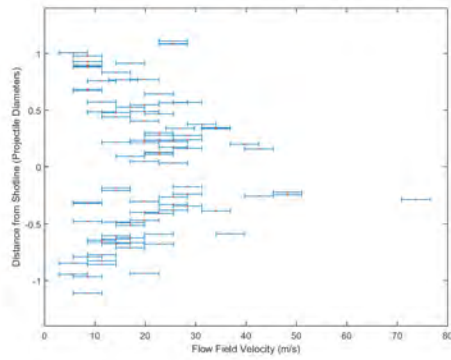
Figure B.6. Plotted horizontal component of the streak velocity across the funnel diameter 2.3 to 2.8 ms after impact for the 113 m/s impact velocity.



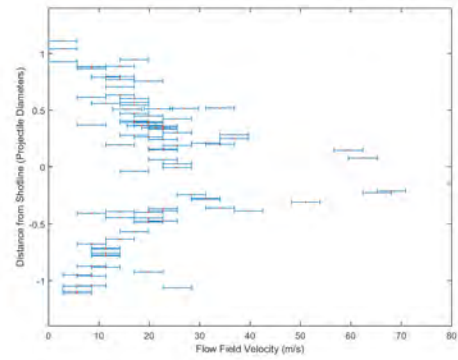
(a) 2.9 ms



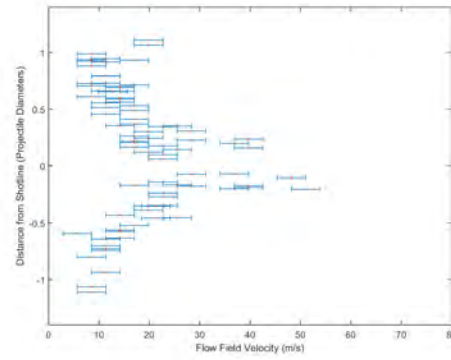
(b) 3.0 ms



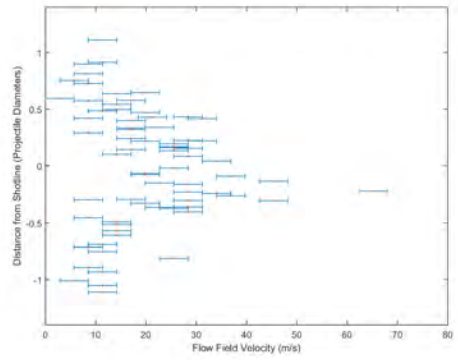
(c) 3.1 ms



(d) 3.2 ms

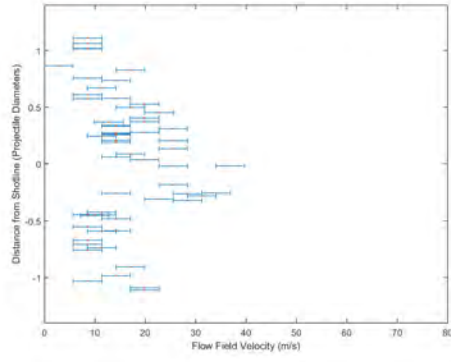


(e) 3.3 ms

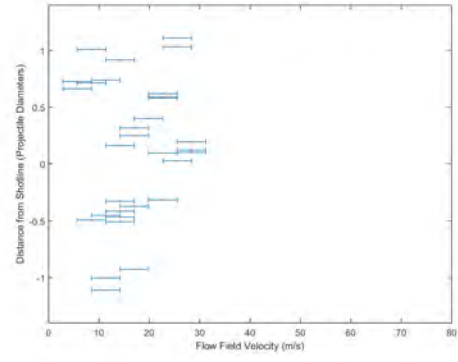


(f) 3.4 ms

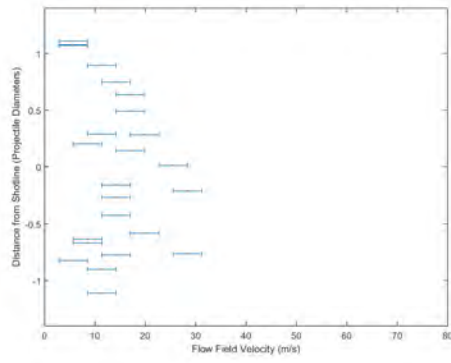
Figure B.7. Plotted horizontal component of the streak velocity across the funnel diameter 2.9 to 3.4 ms after impact for the 113 m/s impact velocity.



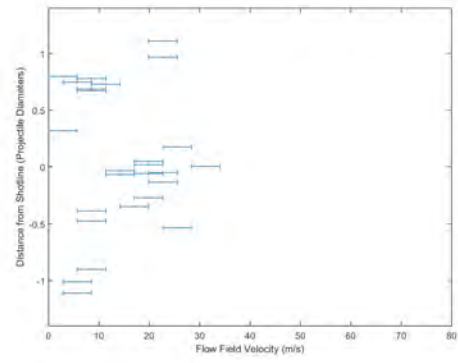
(a) 3.5 ms



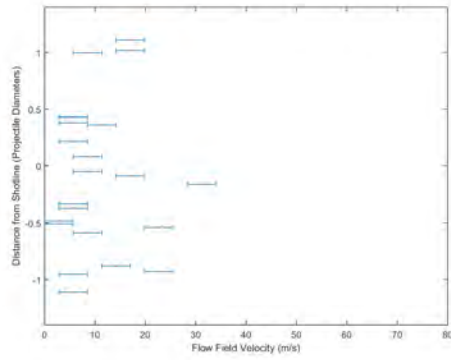
(b) 3.6 ms



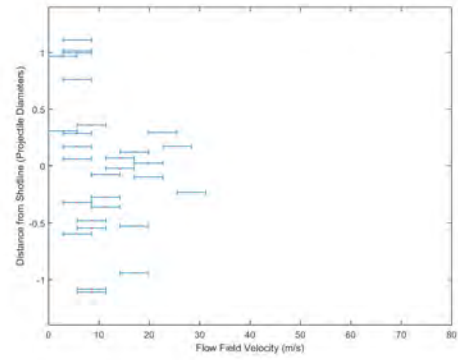
(c) 3.7 ms



(d) 3.8 ms



(e) 3.9 ms



(f) 4.0 ms

Figure B.8. Plotted horizontal component of the streak velocity across the funnel diameter 3.5 to 4.0 ms after impact for the 113 m/s impact velocity.

## B.2 114 m/s impact velocity

For the 114 *m/s* shot, the mass flow rate is shown in Fig. B.9. The entrained mass calculation, shown in Fig. B.10 was obtained by performing a rectangular approximation of Fig. B.9's data to estimate the area under the curve. The entrained mass, along with the applicable cavity volume measurements in Appendix C, was used to compute the cavity's partial pressure as detailed in Section 4.4.3

The velocity profiles used to calculate the mass flow data points composing Fig. B.9 are shown in Fig. B.11 through B.16 at the applicable times. For example, in Fig. B.9, 0.5 *ms* after projectile impact, the first mass flow data point's corresponding velocity profile is shown in Fig. B.11(a). The velocity profile in Fig. B.11(a) appears nominally symmetric about the projectile shot-line at zero even though the data points are sparse. Based on knowledge of flow through nozzles and venturi, the symmetric velocity profile was expected for the flow through the orifice even though there is not an external "pipe" [49]. As the entrainment event proceeds, the flow field continues to develop and increase its overall velocity magnitude as shown in Fig. B.11 through B.12 and to Fig. B.13(d) where the flow peaks around 2.0 *ms*.

The peak mass flow rate in Fig. B.9 is only around 6.5 g/s as compared to the peak mass flow rate of around 7.4 g/s shown in Fig. B.1. Looking back at Fig. A.7, there are a few relatively large saturated particles in the raw imagery approximately when peak mass flow should occur. It is not known the source of these large particles, but it is believed they are not water droplets. Filtering out these large particles during the imagery analysis process may have also filtered out some of the larger streaks necessary for obtaining mass flow calculations similar to the 113 *m/s* shot

Even though the mass flow has a lower peak as compared to the 113 *m/s* shot, similar flow rates of around 6.5 g/s was observed for both shots after 2.0 *ms*. The lower mass flow was attributed to the cavity contraction and the formation of the re-entrant jet as discussed

in Chapter IV. The corresponding velocity profiles still retain their symmetry indicating good flow field measurements.

The velocity profile shows a noticeable decrease in velocity away from the projectile shot-line shown in Fig. B.15(e) at 3.3 *ms* as the cavity continues to separate from the shot plate and form a conduit as shown in Fig. C.8. The slowing of the mass flow is potentially indicative of the HRAM event prior to spurt. For the 114 *m/s* shot, the first sign of fluid spurt occurred around 4.2 *ms* after impact as shown in Fig. A.8(b).

The entrainment velocity calculations covered 0.5 *ms* to 3.5 *ms* accurately enough to determine relationships to the cavity geometric features. Filtering out large particles may have unintentionally yielded a lower mass flow calculation around 2.0 *ms*. As the flow field slowed, the limitations of the streak technique potentially assign lengths based on the particle diameter even though particle may have negligible motion. Additional research and improvements on the measurement technique are needed to accurately measure the mass flow in the 4.0 and 4.1 *ms* images just prior to spurt. Regardless, the velocity profile data over the 0.5 to 3.5 *ms* window was sufficient to correlate back to the internal cavity geometric features as discussed in Chapter IV and provide the cavity composition necessary for partial pressure and pressure work calculations.

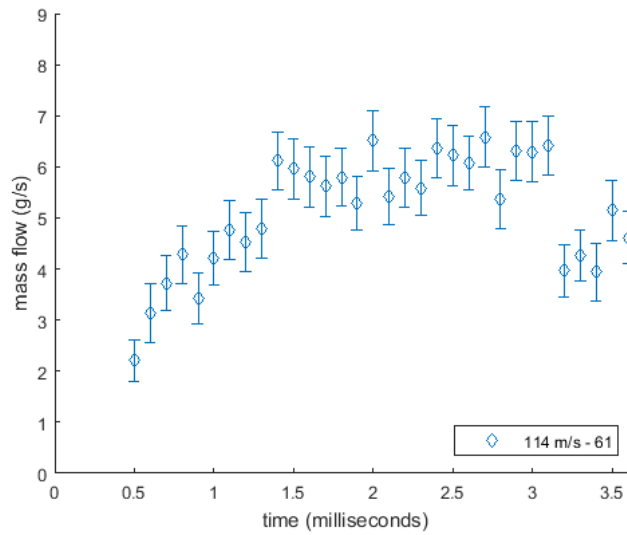


Figure B.9. Mass flow plot for the 114  $m/s$  shot obtained by performing a trapezoidal approximation of a volume of revolution around the projectile's shot-line. Each mass flow data point's corresponding velocity profile is shown in Fig. B.11 through B.16.

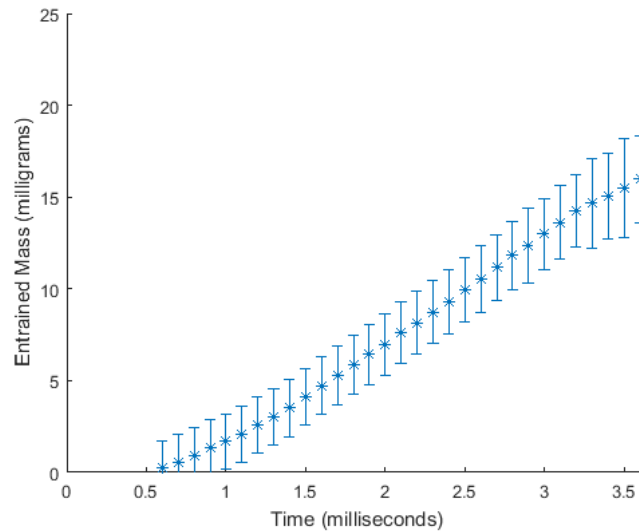
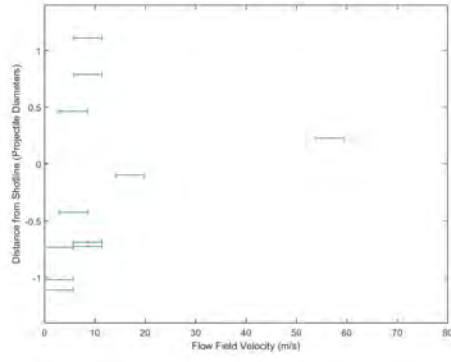
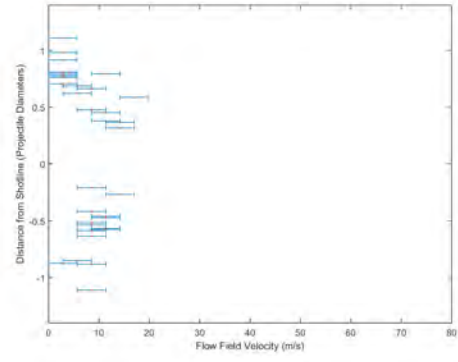


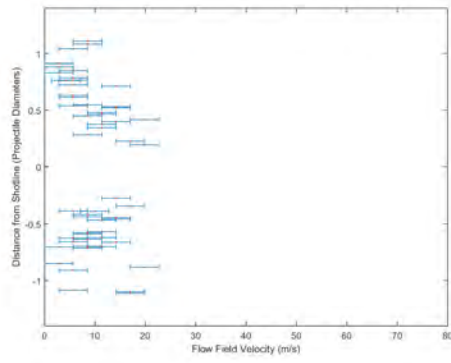
Figure B.10. Entrained mass calculation of ambient air into the HRAM cavity used for partial pressure calculations in Section 4.4.3 for the 114  $m/s$  shot. The entrained mass was calculated by performing a rectangular approximation of Fig. B.9's data to estimate the area under the curve.



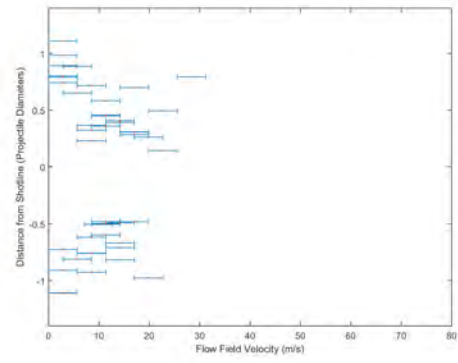
(a) 0.5 ms



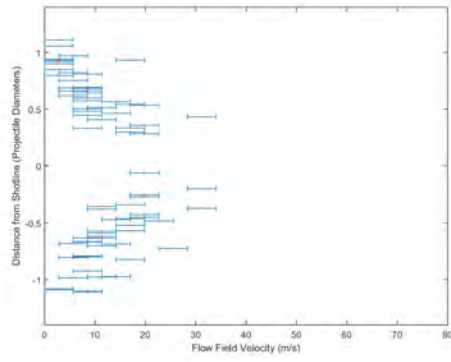
(b) 0.6 ms



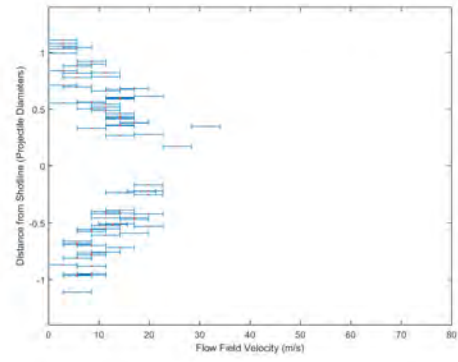
(c) 0.7 ms



(d) 0.8 ms



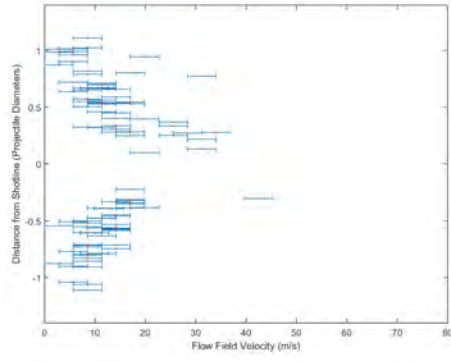
(e) 0.9 ms



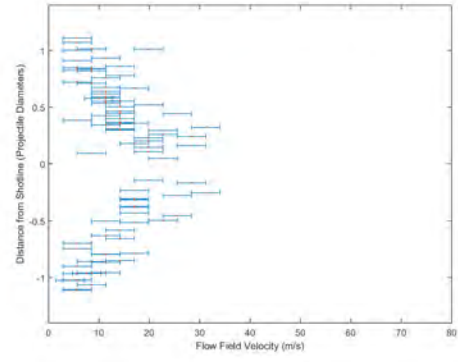
(f) 1.0 ms

Figure B.11. Plotted horizontal component of the streak velocity across the funnel diameter 0.5 to 1.0 ms after impact for the 114 m/s impact velocity.

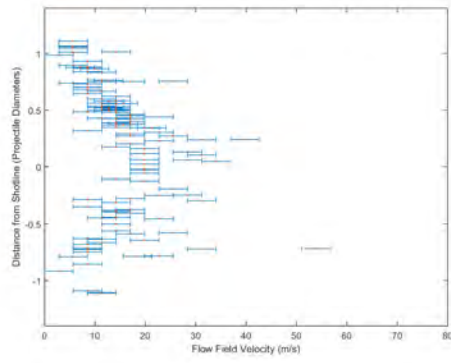




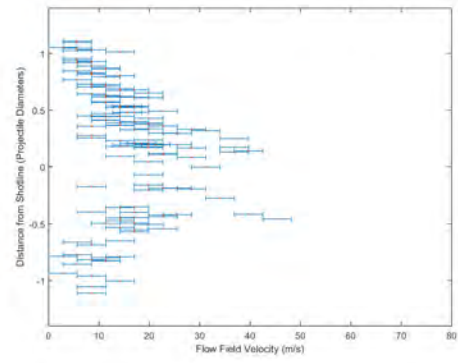
(a) 1.1 *ms*



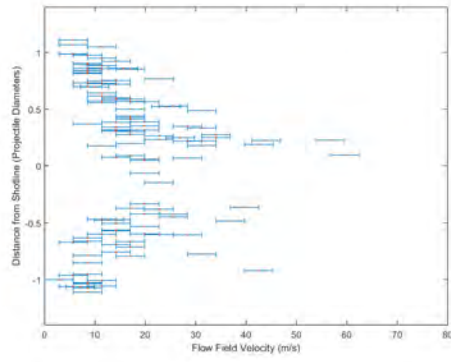
(b) 1.2 *ms*



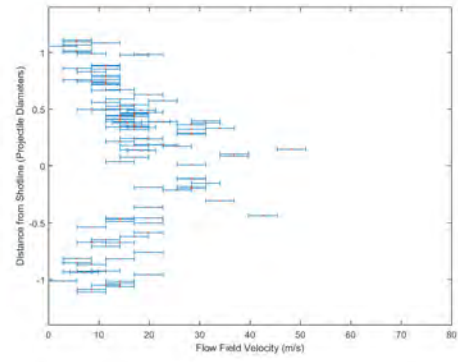
(c) 1.3 *ms*



(d) 1.4 *ms*

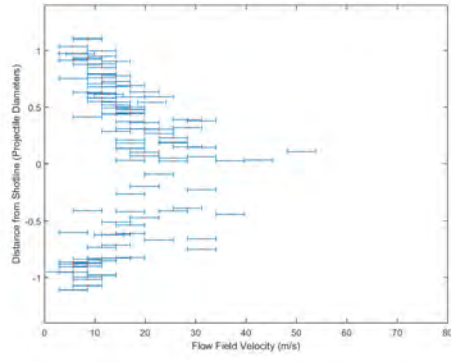


(e) 1.5 *ms*

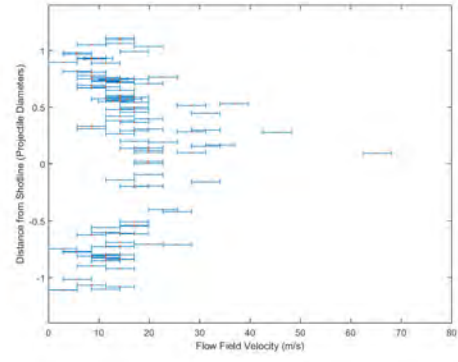


(f) 1.6 *ms*

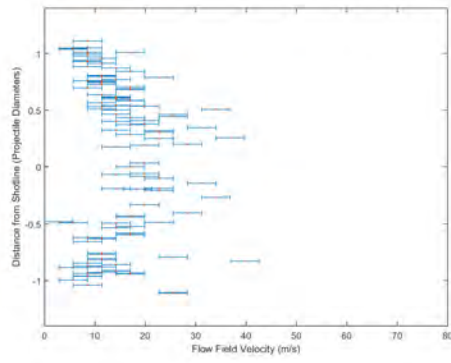
Figure B.12. Plotted horizontal component of the streak velocity across the funnel diameter 1.1 to 1.6 *ms* after impact for the 114 *m/s* impact velocity.



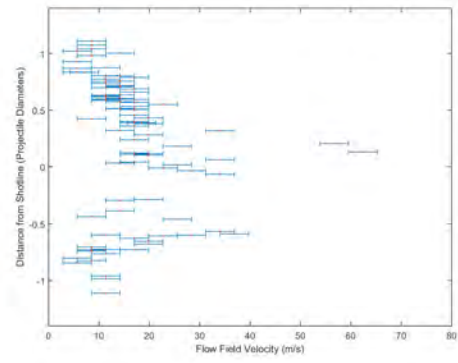
(a) 1.7 ms



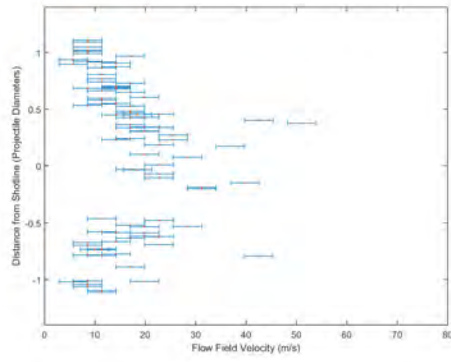
(b) 1.8 ms



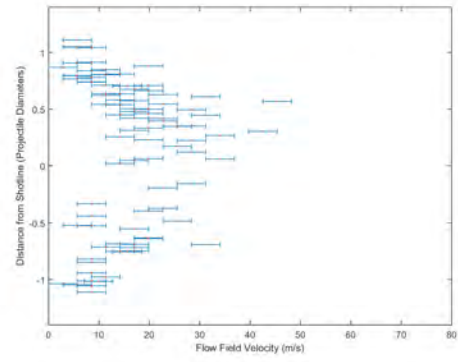
(c) 1.9 ms



(d) 2.0 ms

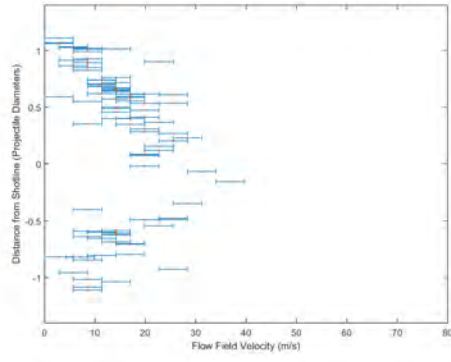


(e) 2.1 ms

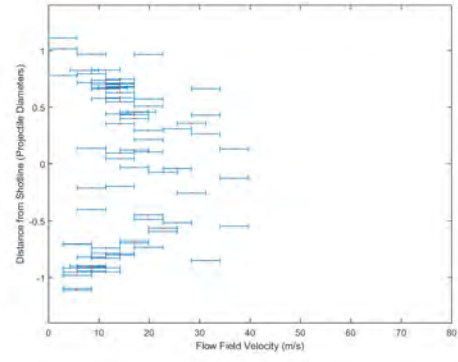


(f) 2.2 ms

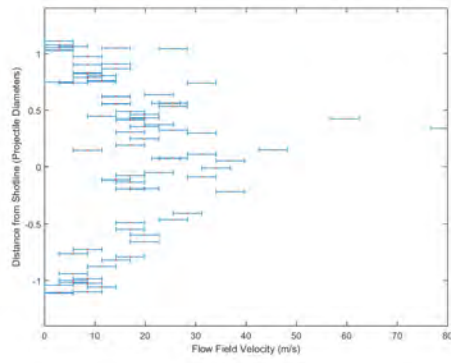
Figure B.13. Plotted horizontal component of the streak velocity across the funnel diameter 1.7 to 2.2 ms after impact for the 114 m/s impact velocity.



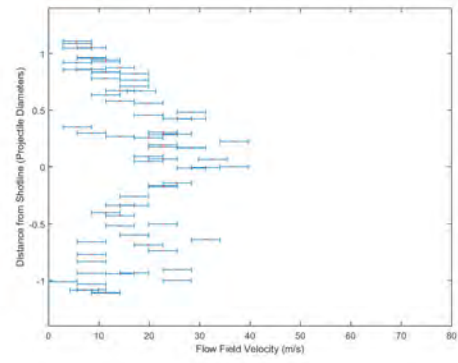
(a) 2.3 ms



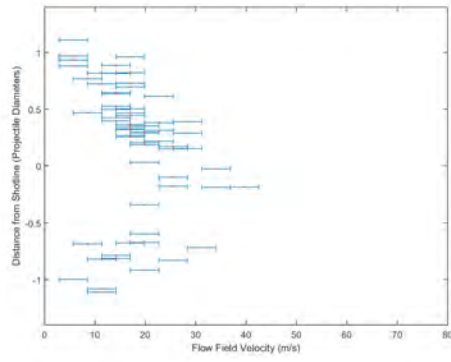
(b) 2.4 ms



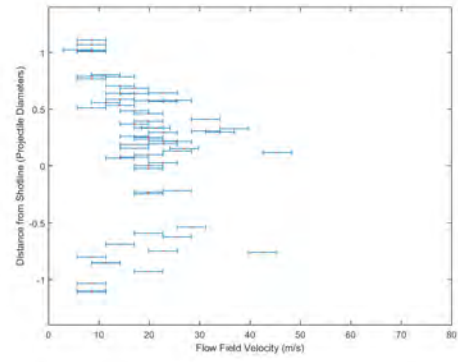
(c) 2.5 ms



(d) 2.6 ms

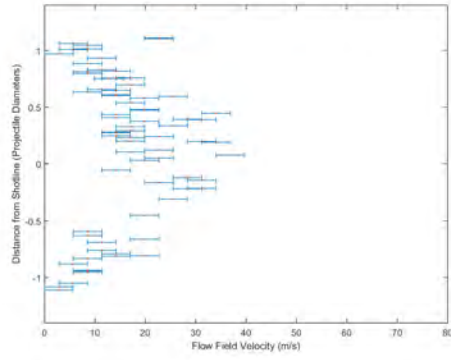


(e) 2.7 ms

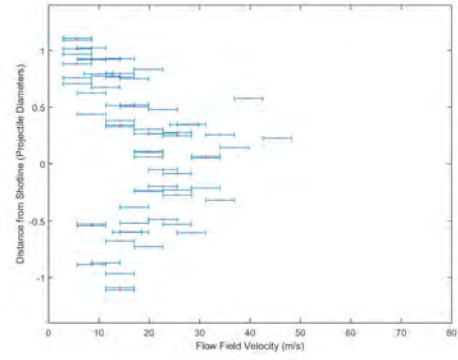


(f) 2.8 ms

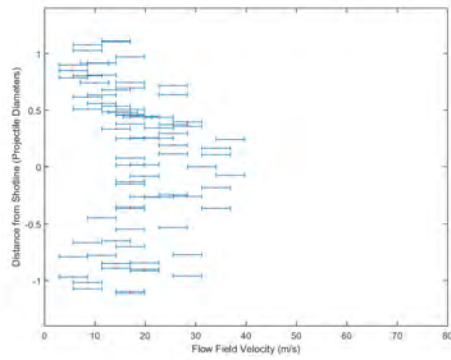
Figure B.14. Plotted horizontal component of the streak velocity across the funnel diameter 2.3 to 2.8 ms after impact for the 114 m/s impact velocity.



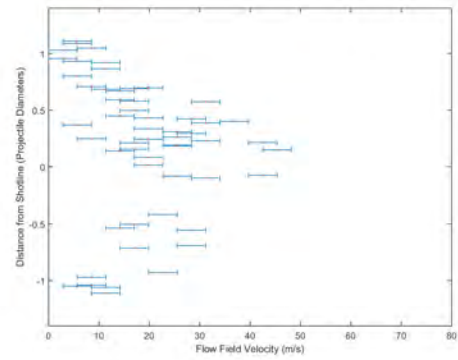
(a) 2.9 ms



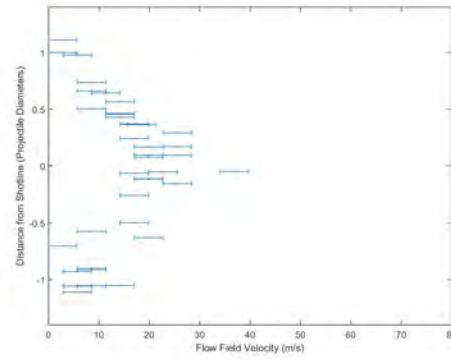
(b) 3.0 ms



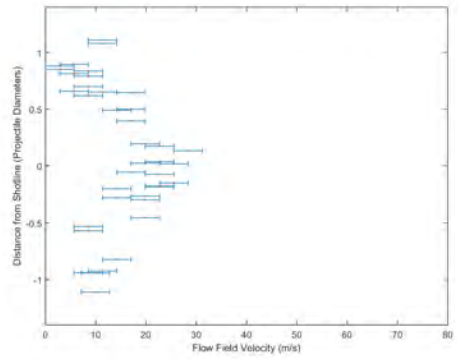
(c) 3.1 ms



(d) 3.2 ms

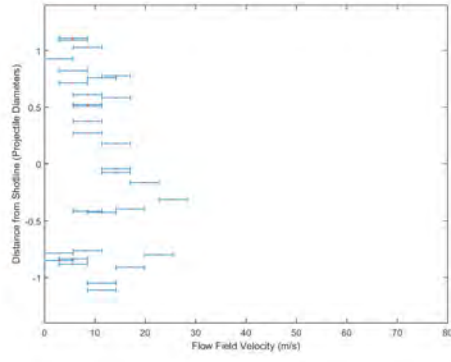


(e) 3.3 ms

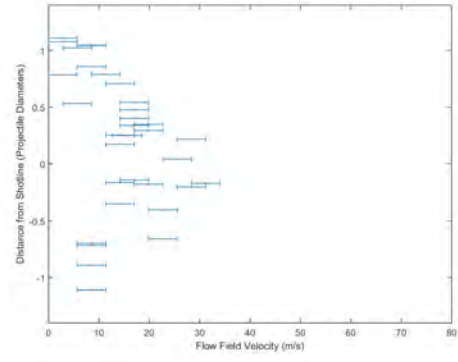


(f) 3.4 ms

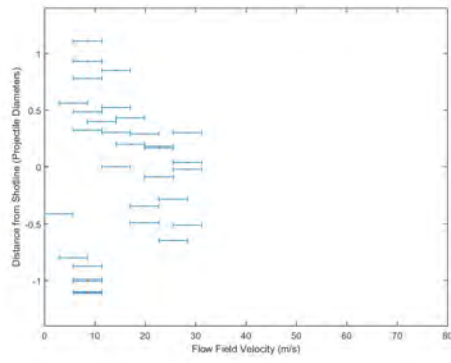
Figure B.15. Plotted horizontal component of the streak velocity across the funnel diameter 2.9 to 3.4 ms after impact for the 114 m/s impact velocity.



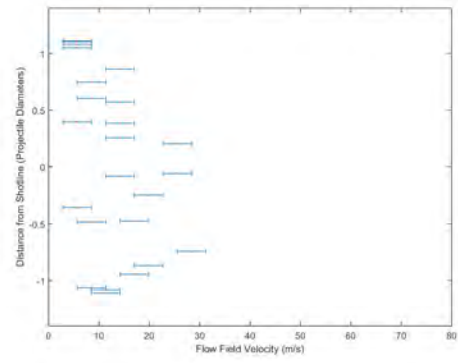
(a) 3.5 ms



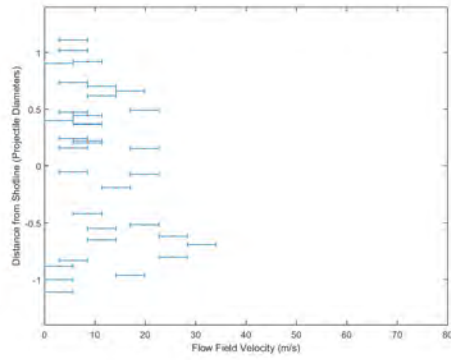
(b) 3.6 ms



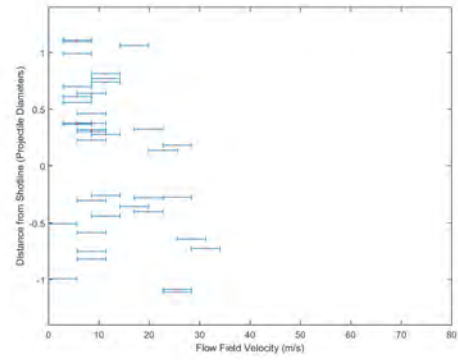
(c) 3.7 ms



(d) 3.8 ms



(e) 3.9 ms



(f) 4.0 ms

Figure B.16. Plotted horizontal component of the streak velocity across the funnel diameter 3.5 to 4.0 ms after impact for the 114 m/s impact velocity.

### B.3 132 m/s impact velocity

For the 132 *m/s* shot, the mass flow rate is shown in Fig. B.17. The entrained mass calculation, shown in Fig. B.18 was obtained by performing a rectangular approximation of Fig. B.17's data to estimate the area under the curve. The entrained mass, along with the applicable cavity volume measurements in Appendix C, was used to compute the cavity's partial pressure as detailed in Section 4.4.3

The velocity profiles used to calculate the mass flow data points composing Fig. B.17 are shown in Fig. B.19 through B.24 at the applicable times. For example, in Fig. B.17, 0.5 *ms* after projectile impact, the first mass flow data point's corresponding velocity profile is shown in Fig. B.19(a). The velocity profile in Fig. B.19(a) does not appear very symmetric about the projectile shot-line at zero. The first image with nominal symmetry appears in Fig. B.19(c). The velocity profiles at 0.5 and 0.6 *ms* are lacking the necessary vector measurements near the projectile shot-line to form a symmetrical velocity profile. The lacking measurements are most likely due to the particle density within the investigation region as discussed in Chapter III. Hence, the mass flow calculations at 0.5 and 0.6 *ms* are most likely under-representing the true mass flow rate. As the entrainment event proceeds, the flow field continues to develop and increase its overall velocity magnitude as shown in Fig. B.19 through B.20 and to Fig. B.21(d) where the flow peaks around 2.0 *ms*.

Referring back to the mass flow plot in Fig. B.17, the mass flow begins to slow after 2.2 *ms*. The lower mass flow was attributed to the cavity contraction and the formation of the re-entrant jet as discussed in Chapter IV. The corresponding velocity profiles retain their symmetry across the entire funnel diameter indicating good flow field measurements.

In Fig. B.23(c) the density of horizontal vectors is noticeably less. Lack of horizontal vectors may indicate a potential sub-quality measurement. The mass flow calculations after 3.0 *ms* are not used in this research to predict any of the corresponding cavity

geometric features discussed in Chapter IV. However, future research should use caution when applying the mass flow calculations after 3.0 *ms* as shown in Fig. B.17.

For the 132 *m/s* shot, the first sign of fluid spurt occurred around 3.7 *ms* after impact as shown in Fig. A.11(k). The entrainment velocity calculations covered 0.5 *ms* to 3.0 *ms* accurately enough to determine relationships to the cavity geometric features. The accuracy after 3.0 *ms* is questionable but the velocity plots were shown to provide a reference for future research or other potential unknown uses. Regardless, the velocity profile data over the 0.5 to 3.0 *ms* window was sufficient to correlate back to the internal cavity geometric features as discussed in Chapter IV and provide the cavity composition necessary for partial pressure and pressure work calculations.

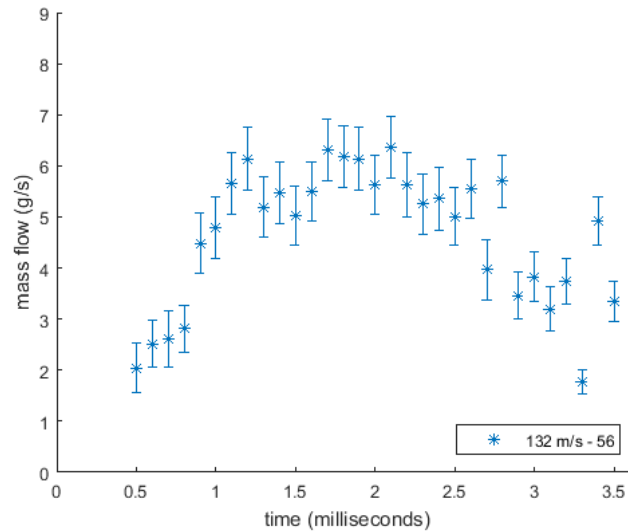


Figure B.17. Mass flow plot for the 132 *m/s* shot obtained by performing a trapezoidal approximation of a volume of revolution around the projectile's shot-line. Each mass flow data point's corresponding velocity profile is shown in Fig. B.19 through B.24.

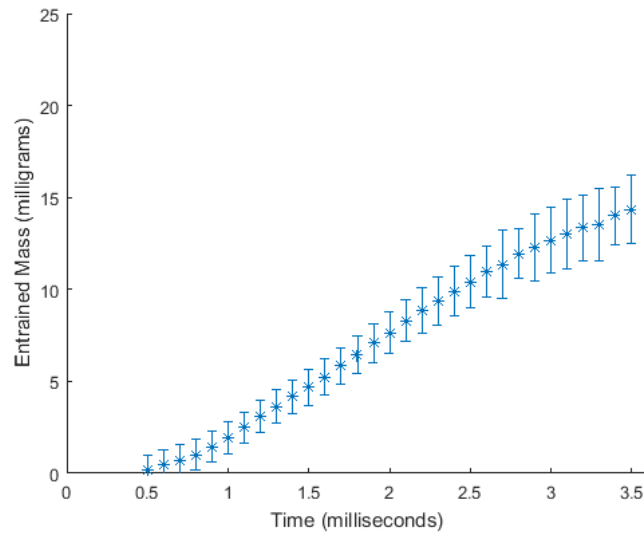
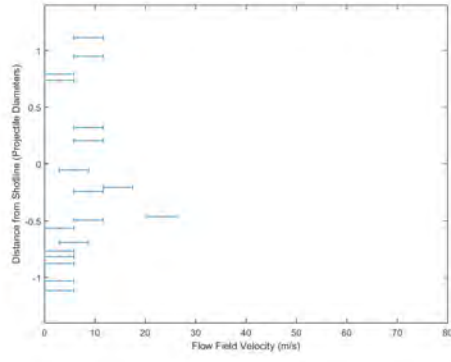
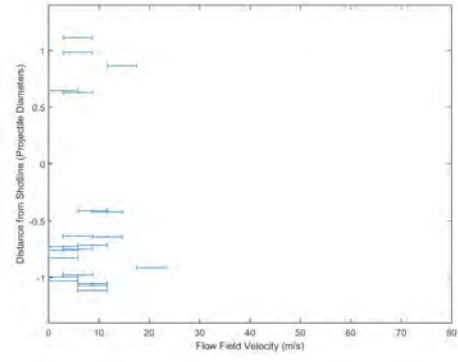


Figure B.18. Entrained mass calculation of ambient air into the HRAM cavity used for partial pressure calculations in Section 4.4.3 for the 132  $m/s$  shot. The entrained mass was calculated by performing a rectangular approximation of Fig. B.17's data to estimate the area under the curve.

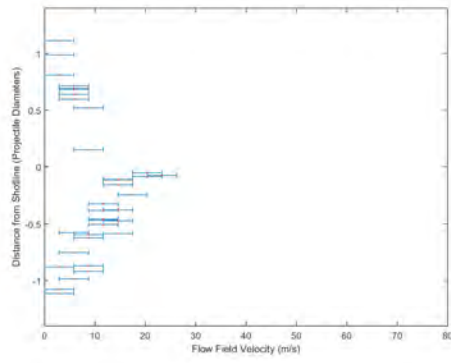




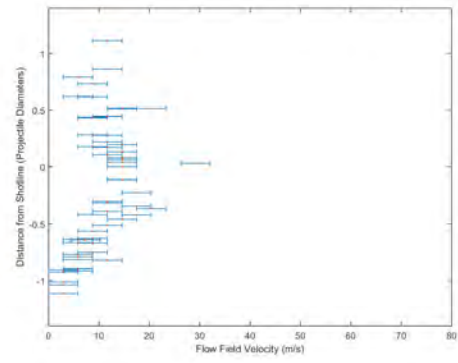
(a) 0.5 ms



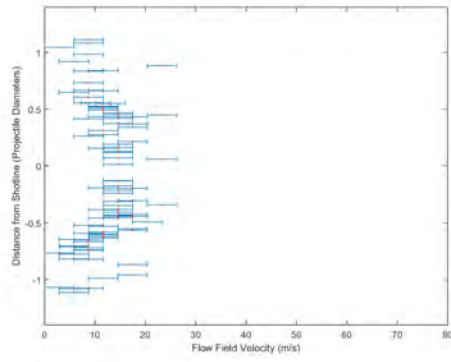
(b) 0.6 ms



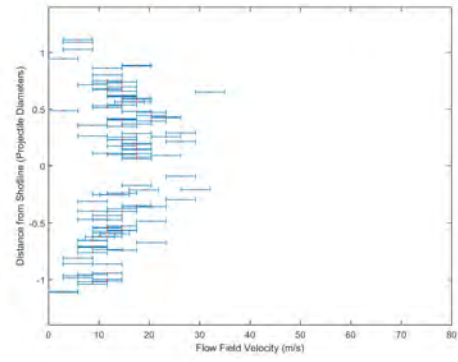
(c) 0.7 ms



(d) 0.8 ms

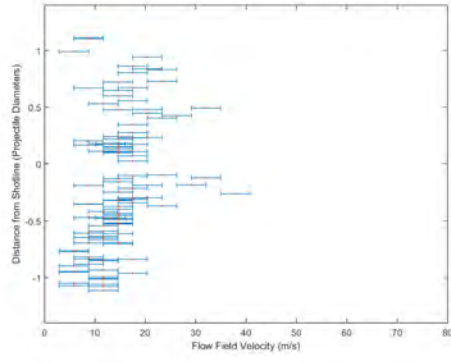


(e) 0.9 ms

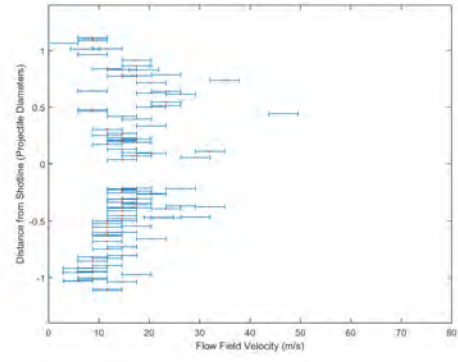


(f) 1.0 ms

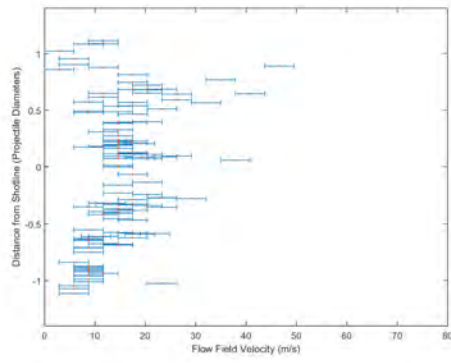
Figure B.19. Plotted horizontal component of the streak velocity across the funnel diameter 0.5 to 1.0 ms after impact for the 132 m/s impact velocity.



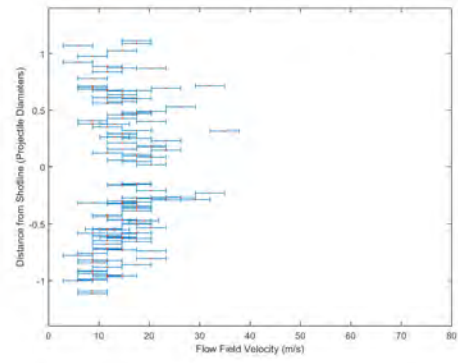
(a) 1.1 ms



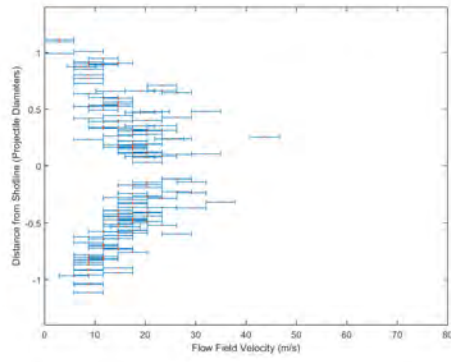
(b) 1.2 ms



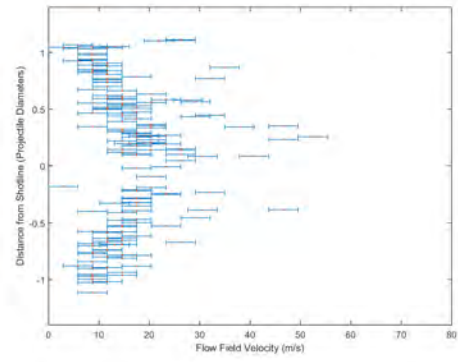
(c) 1.3 ms



(d) 1.4 ms

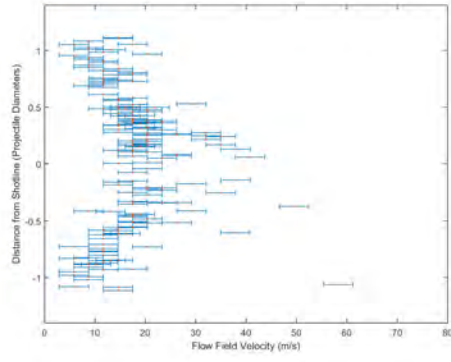


(e) 1.5 ms

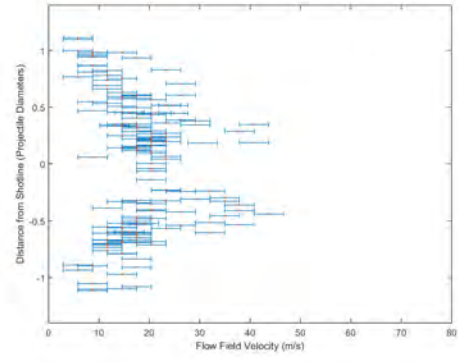


(f) 1.6 ms

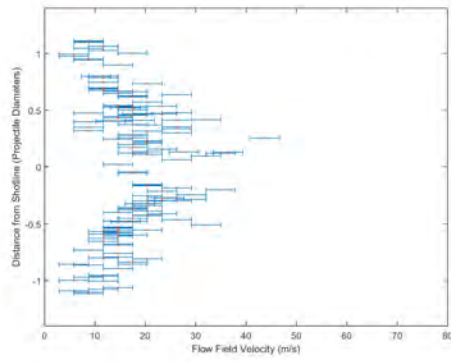
Figure B.20. Plotted horizontal component of the streak velocity across the funnel diameter 1.1 to 1.6 ms after impact for the 132 m/s impact velocity.



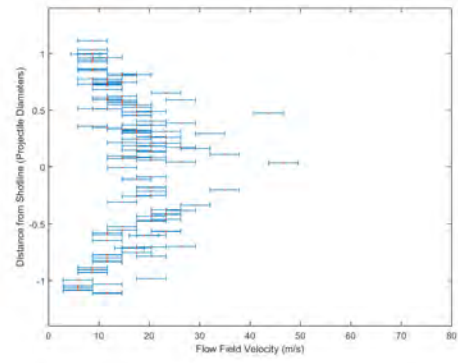
(a) 1.7 ms



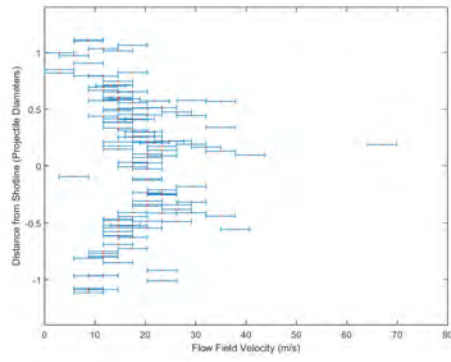
(b) 1.8 ms



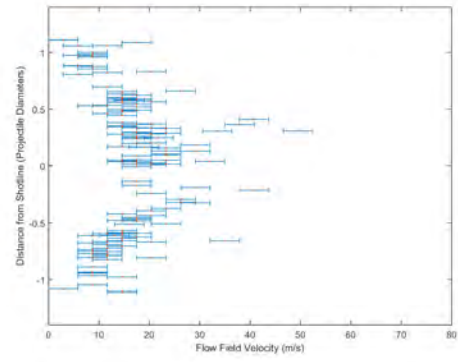
(c) 1.9 ms



(d) 2.0 ms

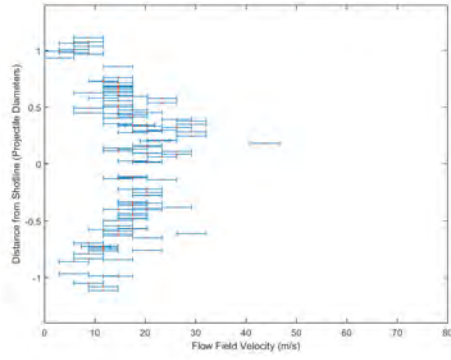


(e) 2.1 ms

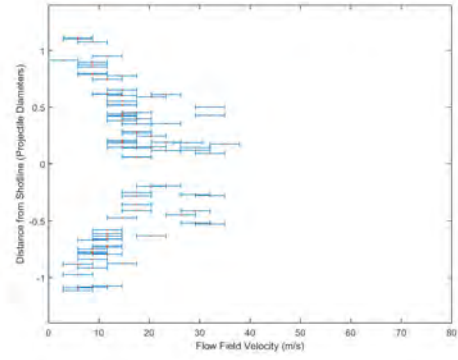


(f) 2.2 ms

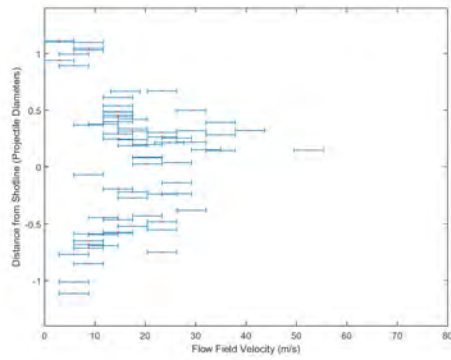
Figure B.21. Plotted horizontal component of the streak velocity across the funnel diameter 1.7 to 2.2 ms after impact for the 132 m/s impact velocity.



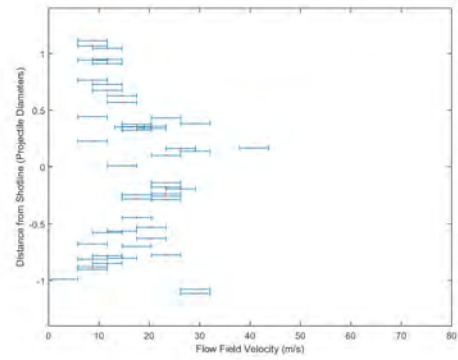
(a) 2.3 ms



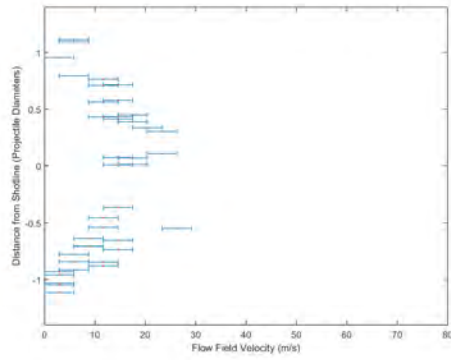
(b) 2.4 ms



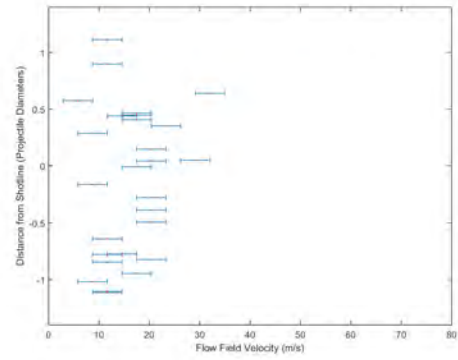
(c) 2.5 ms



(d) 2.6 ms

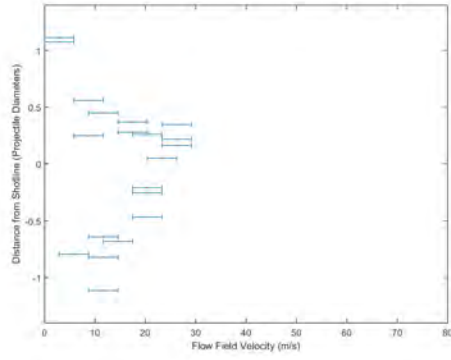


(e) 2.7 ms

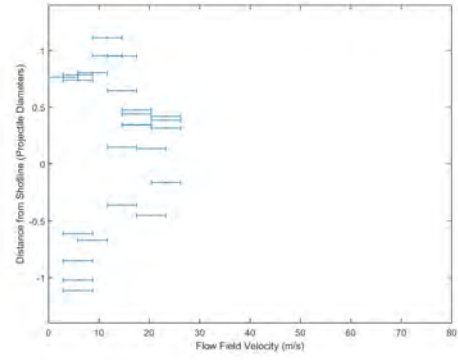


(f) 2.8 ms

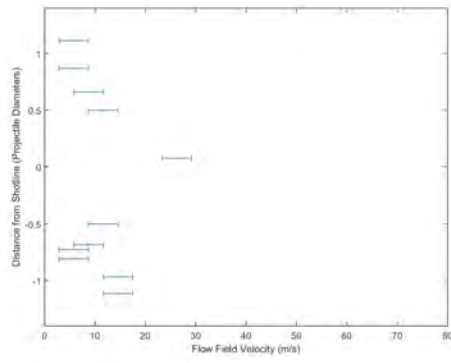
Figure B.22. Plotted horizontal component of the streak velocity across the funnel diameter 2.3 to 2.8 ms after impact for the 132 m/s impact velocity.



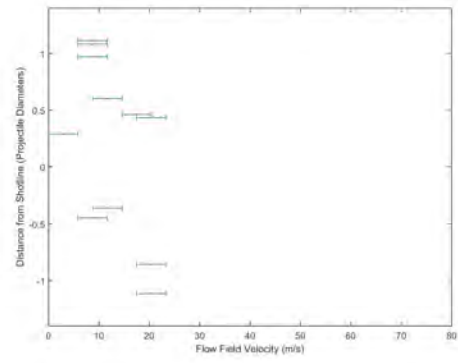
(a) 2.9 ms



(b) 3.0 ms

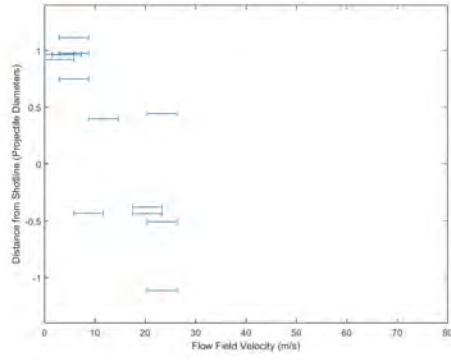


(c) 3.1 ms

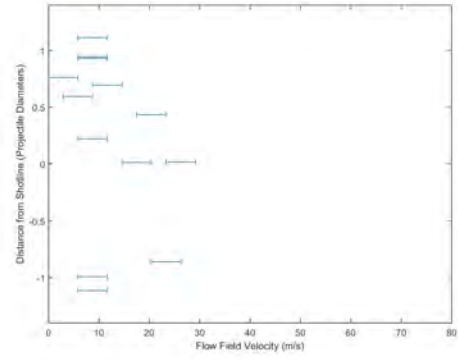


(d) 3.2 ms

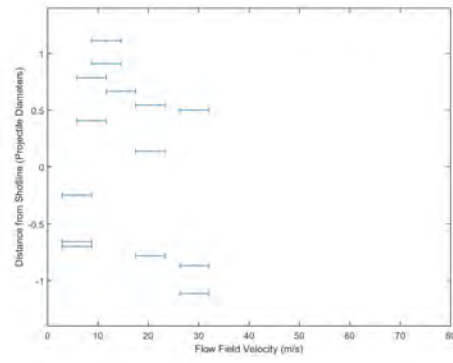
Figure B.23. Plotted horizontal component of the streak velocity across the funnel diameter 2.9 to 3.2 ms after impact for the 132 m/s impact velocity.



(a) 3.3 ms



(b) 3.4 ms



(c) 3.5 ms

Figure B.24. Plotted horizontal component of the streak velocity across the funnel diameter 3.3 to 3.5 ms after impact for the 132 m/s impact velocity.

#### B.4 135 m/s impact velocity

For the 135 *m/s* shot, the mass flow rate is shown in Fig. B.25. The entrained mass calculation, shown in Fig. B.26 was obtained by performing a rectangular approximation of Fig. B.25's data to estimate the area under the curve. The entrained mass, along with the applicable cavity volume measurements in Appendix C, was used to compute the cavity's partial pressure as detailed in Section 4.4.3

The velocity profiles used to calculate the mass flow data points composing Fig. B.25 are shown in Fig. B.27 through B.31 at the applicable times. For example, in Fig. B.25, 0.5 *ms* after projectile impact, the first mass flow data point's corresponding velocity profile is shown in Fig. B.27(a). The velocity profile in Fig. B.27 appears more symmetric and has velocity data close to the projectile shot-line as compared to Fig. B.19(a), which was missing data close to the projectile's shot-line. Therefore, the mass flow rate, shown in Fig. B.25 at 0.5 *ms*, is about 1.5 g/s larger than the corresponding mass flow rate shown in Fig. B.17. As the entrainment event proceeds, the flow field continues to develop and increase its overall velocity magnitude as shown in Fig. B.27 through B.28 and to Fig. B.29(e) where the flow peaks around 2.1 *ms*.

Referring back to the mass flow plot in Fig. B.25, the mass flow begins to slow after 2.4 *ms*. The lower mass flow was attributed to the cavity contraction and the formation of the re-entrant jet as discussed in Chapter IV. The corresponding velocity profiles retain their symmetry across the entire funnel diameter indicating good flow field measurements.

Lack of symmetry and density of horizontal vectors was shown in Fig. B.30(f). Some flow field symmetry was detected in some of the velocity measurements shown in Fig. B.31(a), (b), and (c). The lack of symmetry or vector density by themselves do not mean a measurement is poor and cannot be used. Lack of symmetry and horizontal vectors simply indicate a potential exists for a sub-quality measurement its application should use

caution. Regardless, the mass flow calculations after 2.8 *ms* were not used in this research to predict any of the corresponding cavity geometric features discussed in Chapter IV.

For the 135 *m/s* shot, the first sign of fluid spurt occurred around 3.6 *ms* after impact as shown in Fig. A.14(j). The entrainment velocity calculations covered 0.5 *ms* to 2.8 *ms* accurately enough to determine relationships to the cavity geometric features. The accuracy after 2.8 *ms* is questionable but the velocity plots were shown to provide a reference for future research or other potential unknown uses. Regardless, the velocity profile data over the 0.5 to 2.8 *ms* window was sufficient to correlate back to the internal cavity geometric features as discussed in Chapter IV and provide the cavity composition necessary for partial pressure and pressure work calculations.

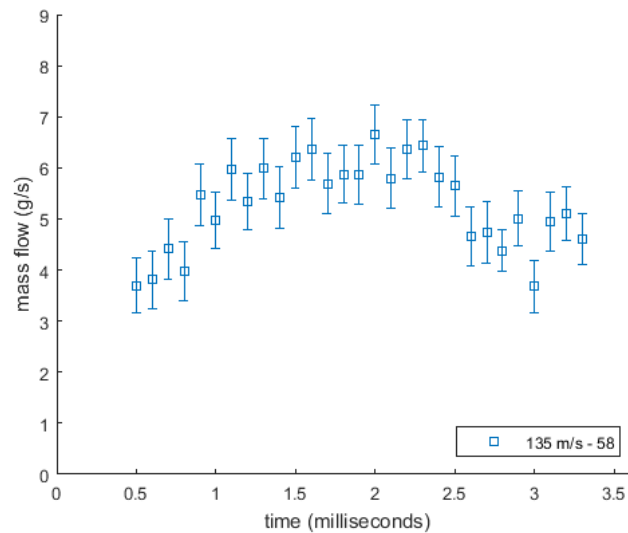


Figure B.25. Mass flow plot for the 135 *m/s* shot obtained by performing a trapezoidal approximation of a volume of revolution around the projectile's shot-line. Each mass flow data point's corresponding velocity profile is shown in Fig. B.27 through B.31.



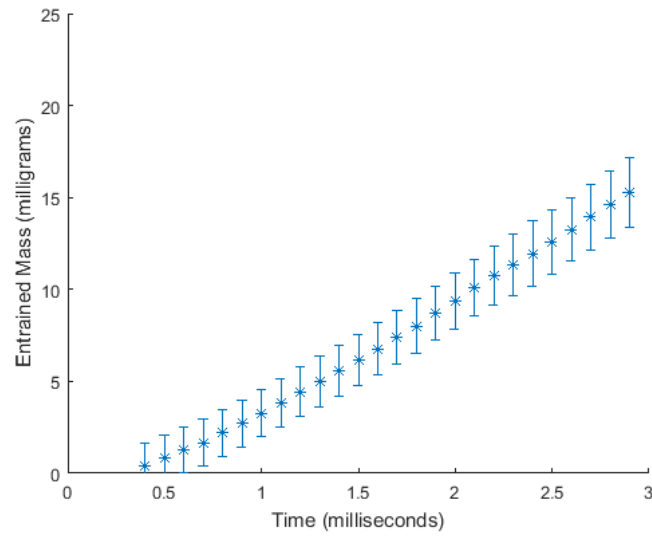
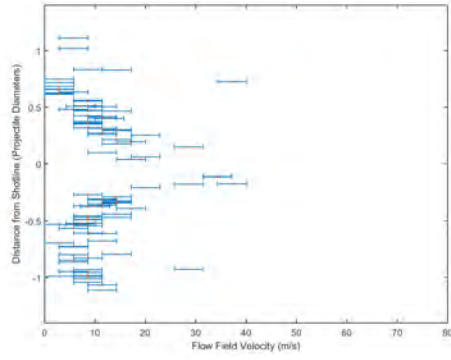
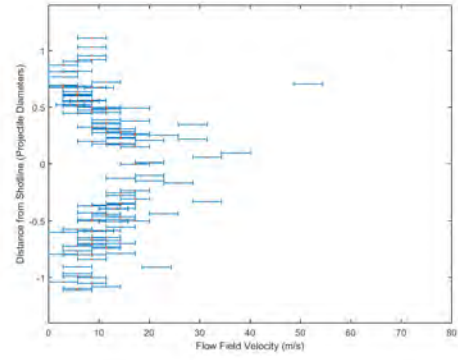


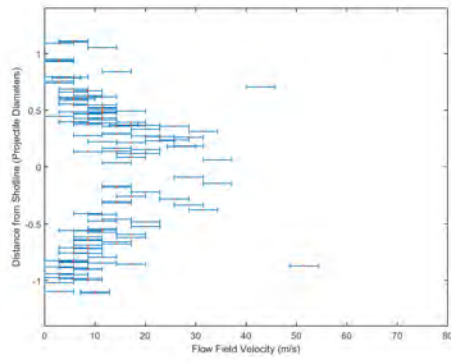
Figure B.26. Entrained mass calculation of ambient air into the HRAM cavity used for partial pressure calculations in Section 4.4.3 for the 135  $m/s$  shot. The entrained mass was calculated by performing a rectangular approximation of Fig. B.25's data to estimate the area under the curve.



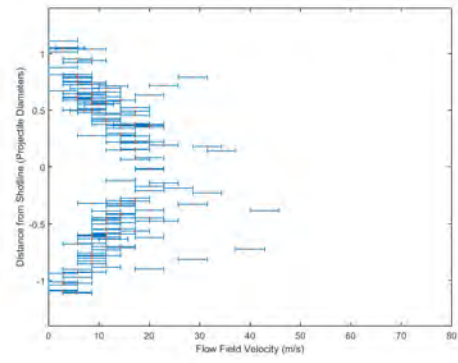
(a) 0.5 ms



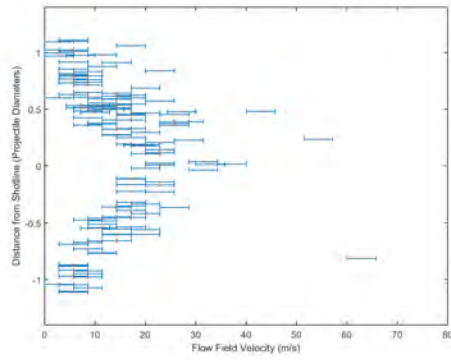
(b) 0.6 ms



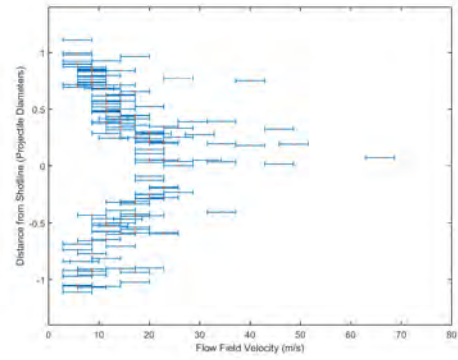
(c) 0.7 ms



(d) 0.8 ms

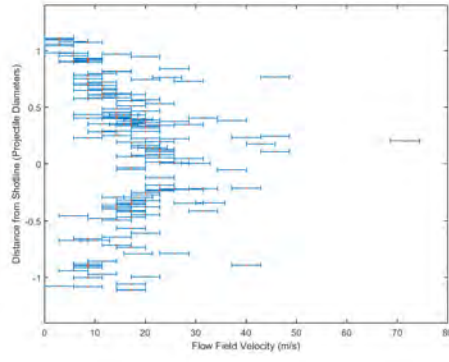


(e) 0.9 ms

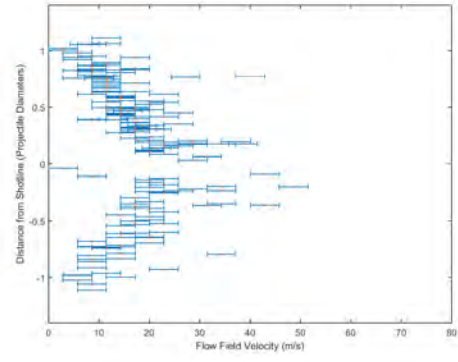


(f) 1.0 ms

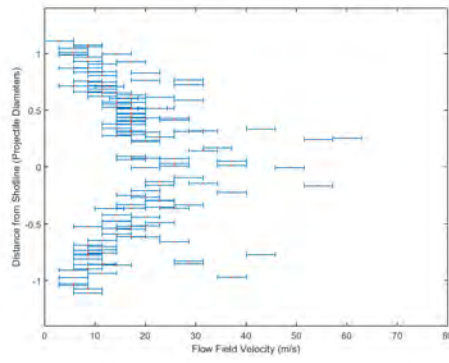
Figure B.27. Plotted horizontal component of the streak velocity across the funnel diameter 0.5 to 1.0 ms after impact for the 135 m/s impact velocity.



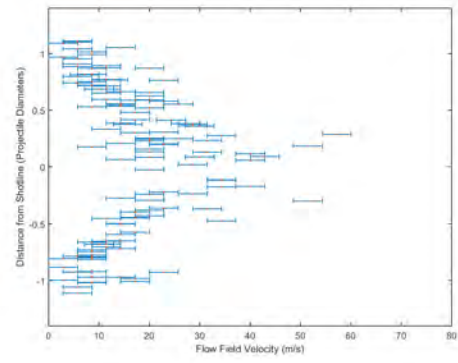
(a) 1.1 ms



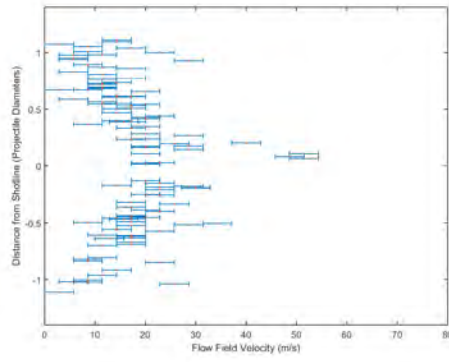
(b) 1.2 ms



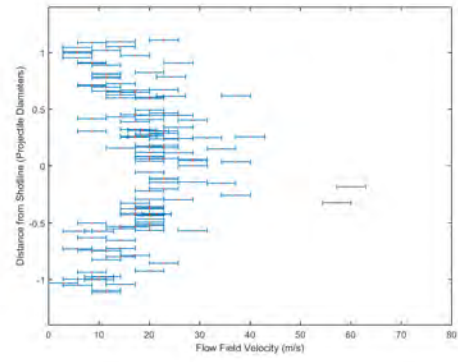
(c) 1.3 ms



(d) 1.4 ms

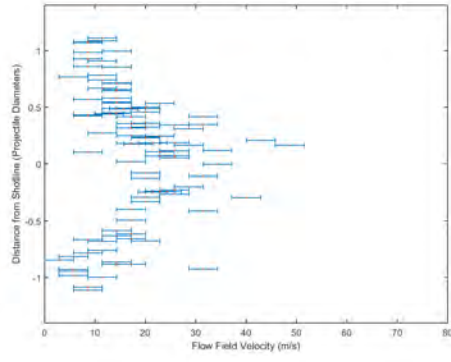


(e) 1.5 ms

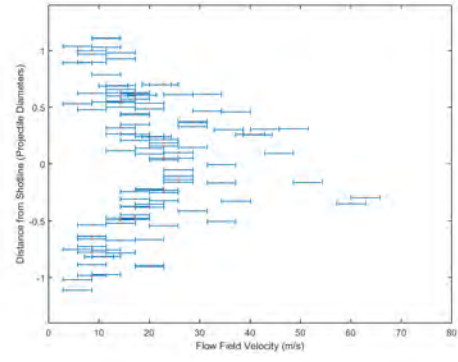


(f) 1.6 ms

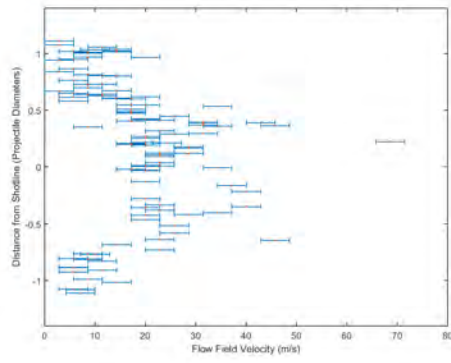
Figure B.28. Plotted horizontal component of the streak velocity across the funnel diameter 1.1 to 1.6 ms after impact for the 135 m/s impact velocity.



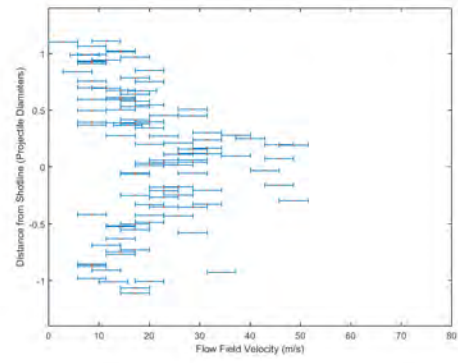
(a) 1.7 ms



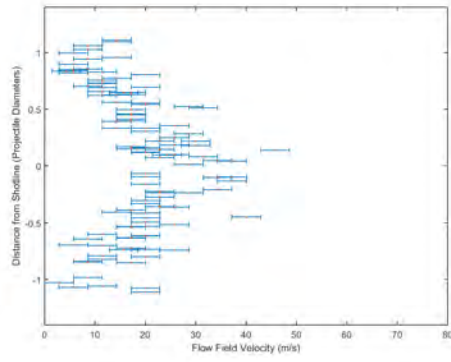
(b) 1.8 ms



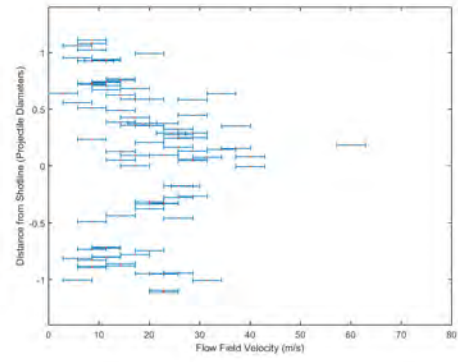
(c) 1.9 ms



(d) 2.0 ms

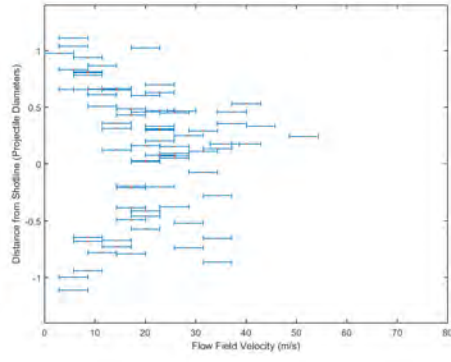


(e) 2.1 ms

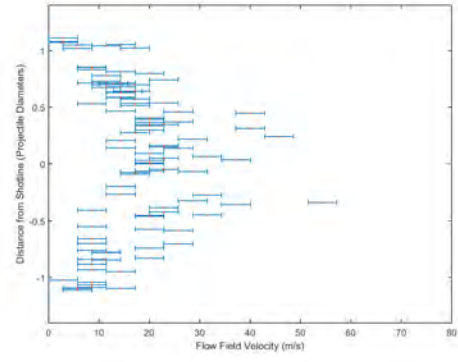


(f) 2.2 ms

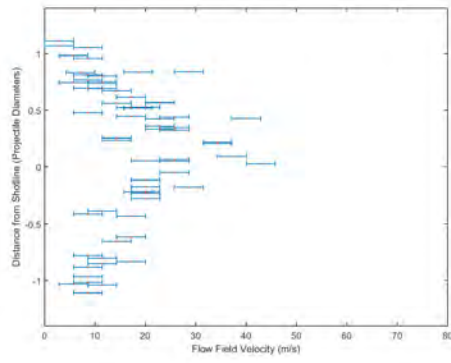
Figure B.29. Plotted horizontal component of the streak velocity across the funnel diameter 1.7 to 2.2 ms after impact for the 135 m/s impact velocity.



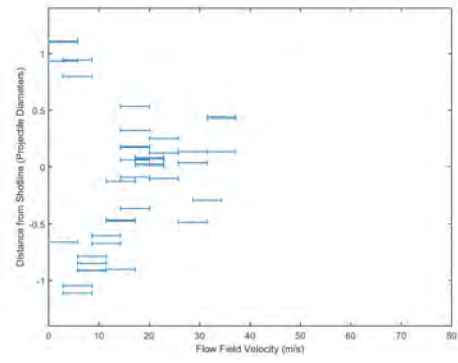
(a) 2.3 ms



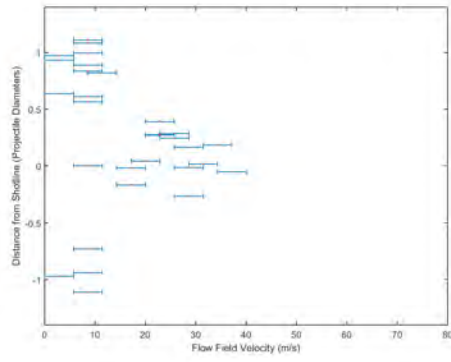
(b) 2.4 ms



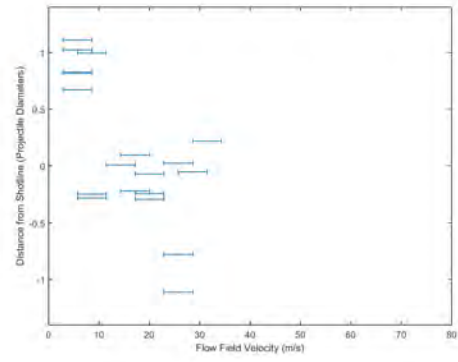
(c) 2.5 ms



(d) 2.6 ms

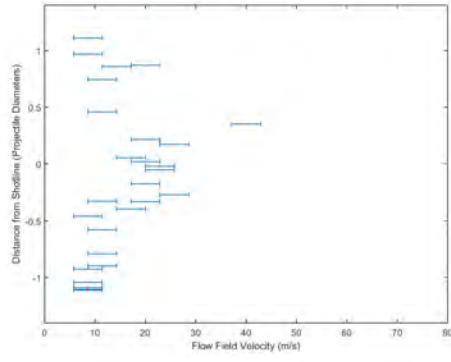


(e) 2.7 ms

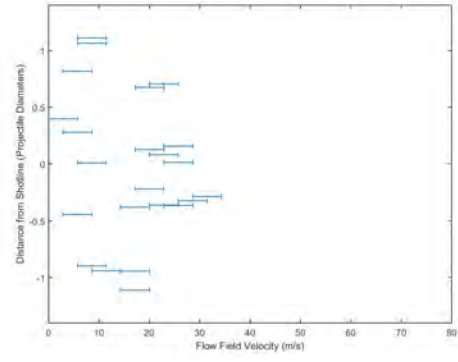


(f) 2.8 ms

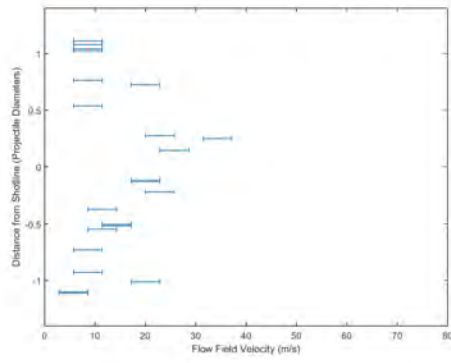
Figure B.30. Plotted horizontal component of the streak velocity across the funnel diameter 2.3 to 2.8 ms after impact for the 135 m/s impact velocity.



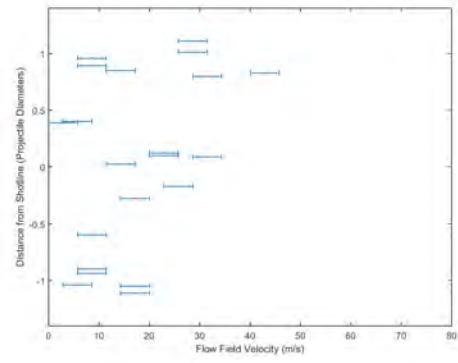
(a) 2.9 ms



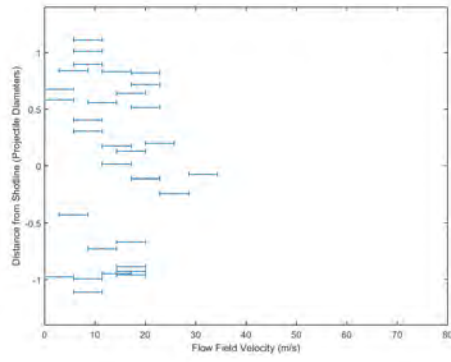
(b) 3.0 ms



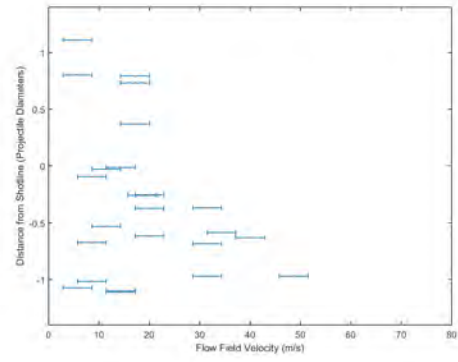
(c) 3.1 ms



(d) 3.2 ms



(e) 3.3 ms



(f) 3.4 ms

Figure B.31. Plotted horizontal component of the streak velocity across the funnel diameter 2.9 to 3.4 ms after impact for the 135 m/s impact velocity.

## B.5 176 m/s impact velocity

For the first 176 *m/s* shot, the mass flow rate is shown in Fig. B.32. The entrained mass calculation, shown in Fig. B.33 was obtained by performing a rectangular approximation of Fig. B.32's data to estimate the area under the curve. The entrained mass, along with the applicable cavity volume measurements in Appendix C, was used to compute the cavity's partial pressure as detailed in Section 4.4.3

The velocity profiles used to calculate the mass flow data points composing Fig. B.32 are shown in Fig. B.34 through B.38 at the applicable times. For example, in Fig. B.32, 0.5 *ms* after projectile impact, the first mass flow data point's corresponding velocity profile is shown in Fig. B.34(a). The velocity profile in Fig. B.34 appears somewhat symmetric but is lacking in vector density. Therefore, the mass flow rate, shown in Fig. B.32 at 0.5 *ms*, is potentially under-representing the true mass flow rate. As the entrainment event proceeds, the flow field continues to develop and increase its overall velocity magnitude as shown in Fig. B.35 through Fig. B.36(c), where the flow peaks around 1.9 *ms*.

Referring back to the mass flow plot in Fig. B.32, the mass flow begins to slow after 1.9 *ms*. The lower mass flow was attributed to the cavity contraction and the formation of the re-entrant jet as discussed in Chapter IV. The corresponding velocity profiles retain their symmetry across the entire funnel diameter indicating good flow field measurements.

The horizontal velocity vectors became more sparse 2.5 *ms* after impact, shown in Fig. B.37(c), but still retained their symmetry about the shot-line. Symmetry about the shot line appeared in Fig. B.37(e). The lack of symmetry or vector density by themselves do not mean a measurement is poor and cannot be used. Lack of symmetry and horizontal vectors simply indicate a potential exists for a sub-quality measurement its application should use caution. Regardless, the mass flow calculations after 2.5 *ms* were not used in this research to predict any of the corresponding cavity geometric features discussed in Chapter IV.

For the 135  $m/s$  shot, the first sign of fluid spurt occurred around 3.4  $ms$  after impact as shown in Fig. A.17(h). The entrainment velocity calculations covered 0.5  $ms$  to 2.5  $ms$  accurately enough to determine relationships to the cavity geometric features. The accuracy after 2.5  $ms$  is questionable but the velocity plots were shown to provide a reference for future research or other potential unknown uses. Regardless, the velocity profile data over the 0.5 to 2.5  $ms$  window was sufficient to correlate back to the internal cavity geometric features as discussed in Chapter IV and provide the cavity composition necessary for partial pressure and pressure work calculations.

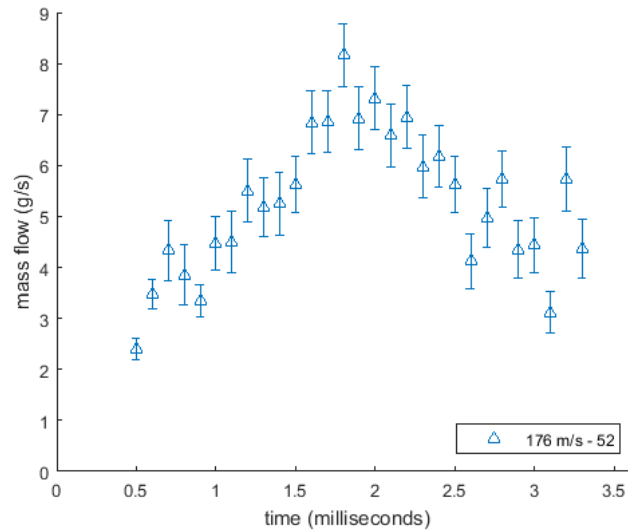


Figure B.32. Mass flow plot for the 176  $m/s$  shot obtained by performing a trapezoidal approximation of a volume of revolution around the projectile's shot-line. Each mass flow data point's corresponding velocity profile is shown in Fig. B.34 through B.45.



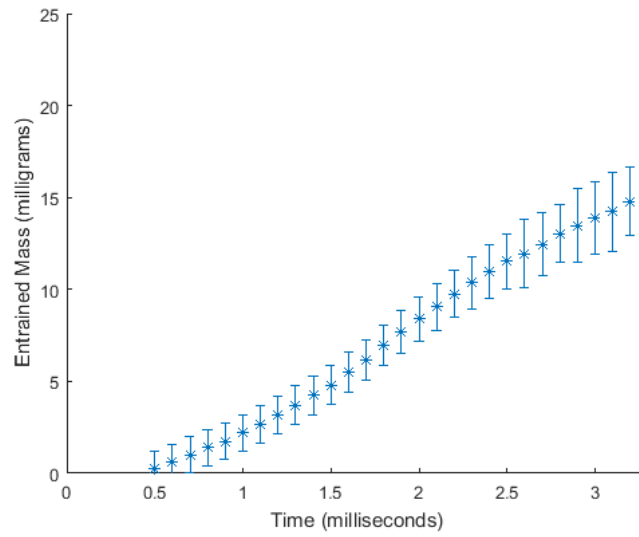
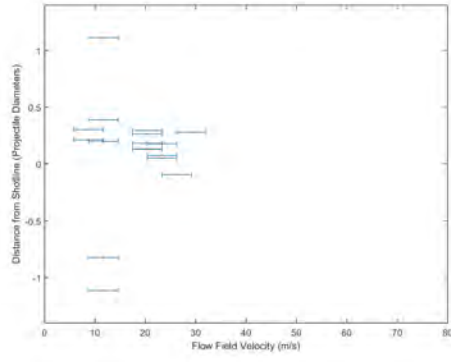
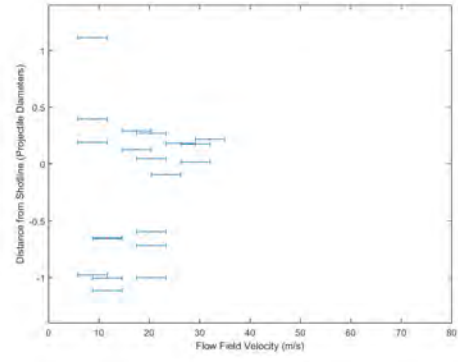


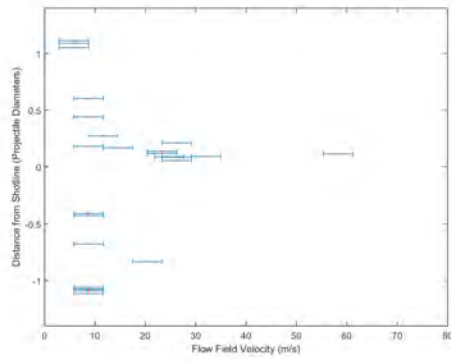
Figure B.33. Entrained mass calculation of ambient air into the HRAM cavity used for partial pressure calculations in Section 4.4.3 for the 176  $m/s$  shot. The entrained mass was calculated by performing a rectangular approximation of Fig. B.32's data to estimate the area under the curve.



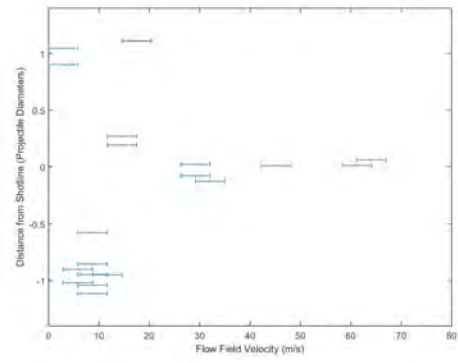
(a) 0.5 ms



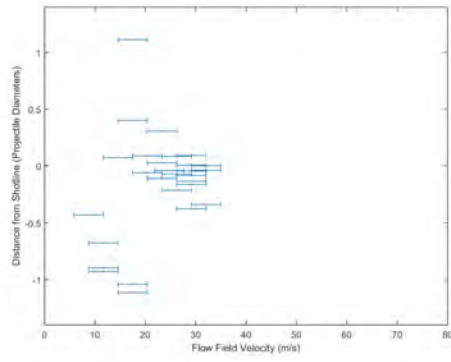
(b) 0.6 ms



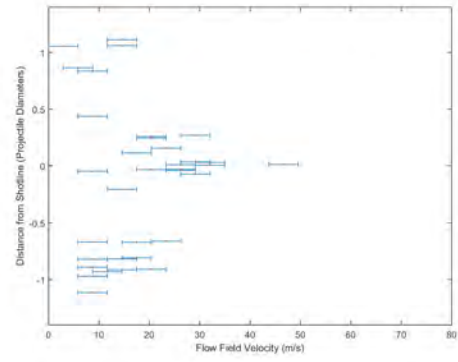
(c) 0.7 ms



(d) 0.8 ms

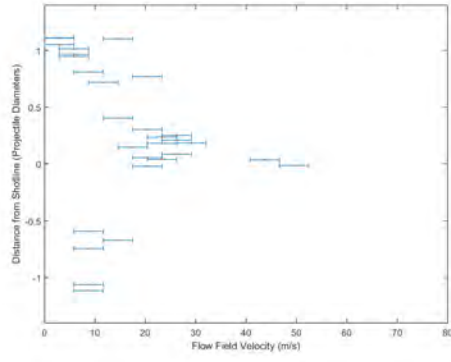


(e) 0.9 ms

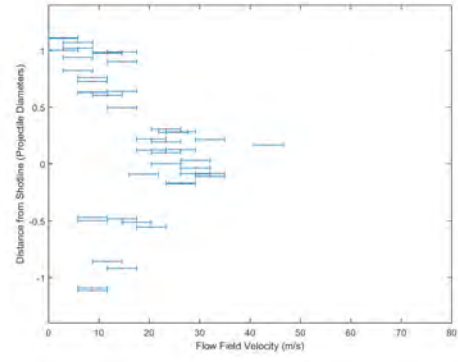


(f) 1.0 ms

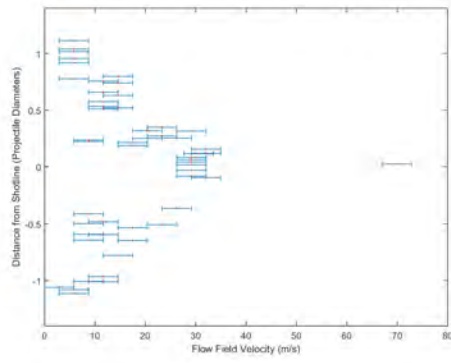
Figure B.34. Plotted horizontal component of the streak velocity across the funnel diameter for 176 m/s impact velocity from 0.5 to 1.0 ms after impact.



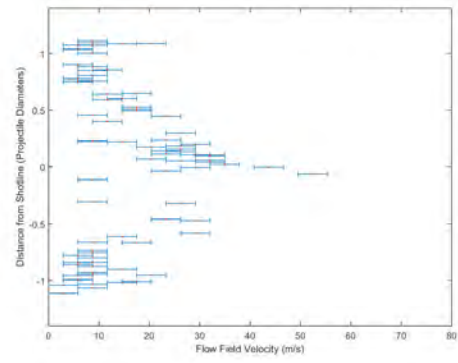
(a) 1.1 ms



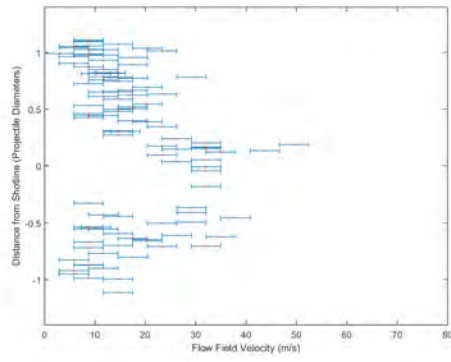
(b) 1.2 ms



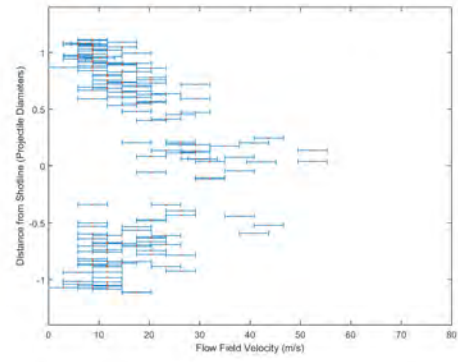
(c) 1.3 ms



(d) 1.4 ms

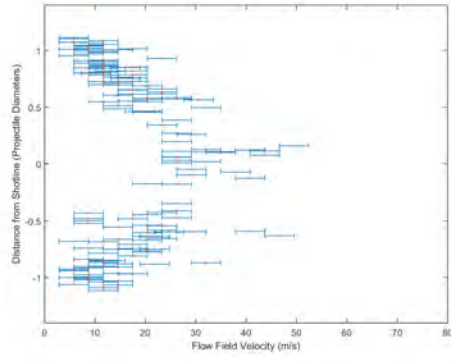


(e) 1.5 ms

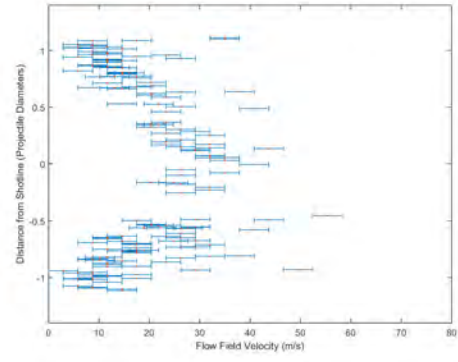


(f) 1.6 ms

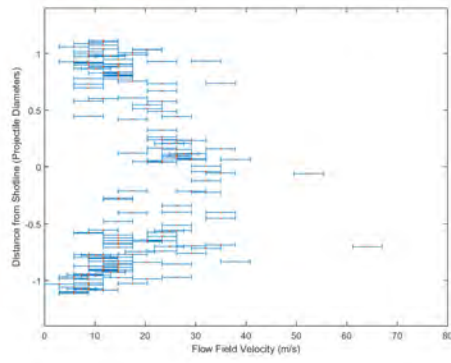
Figure B.35. Plotted horizontal component of the streak velocity across the funnel diameter 1.1 to 1.6 ms after impact.



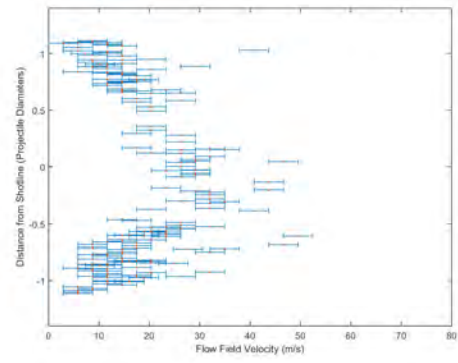
(a) 1.7 ms



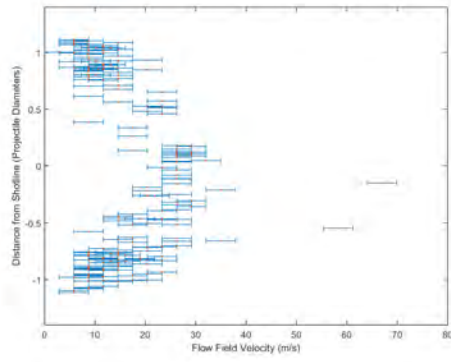
(b) 1.8 ms



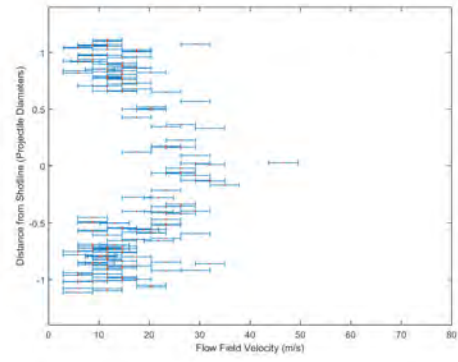
(c) 1.9 ms



(d) 2.0 ms

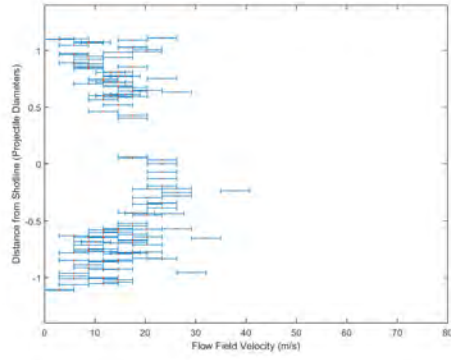


(e) 2.1 ms

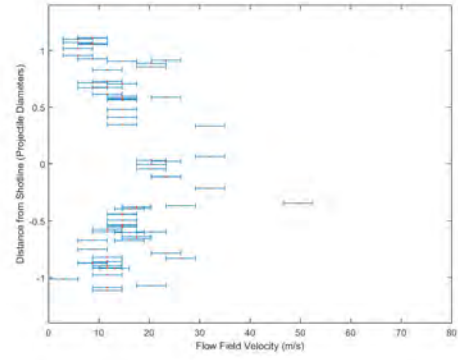


(f) 2.2 ms

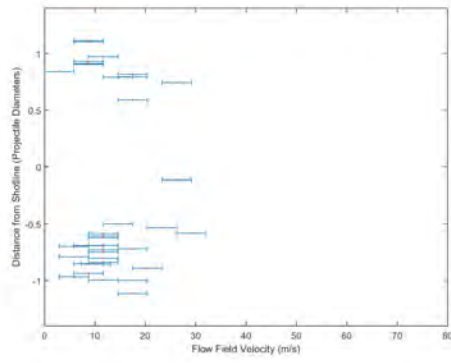
Figure B.36. Plotted horizontal component of the streak velocity across the funnel diameter 1.7 to 2.2 ms after impact.



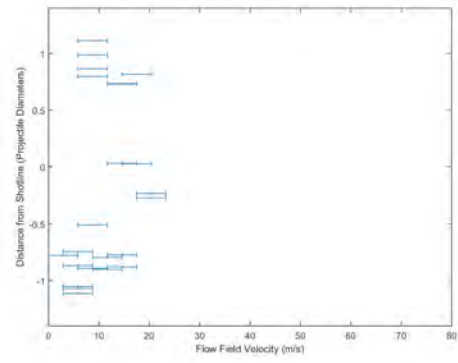
(a) 2.3 ms



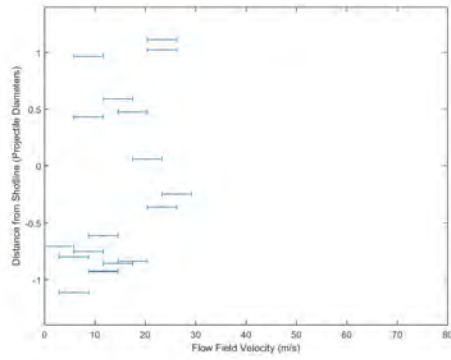
(b) 2.4 ms



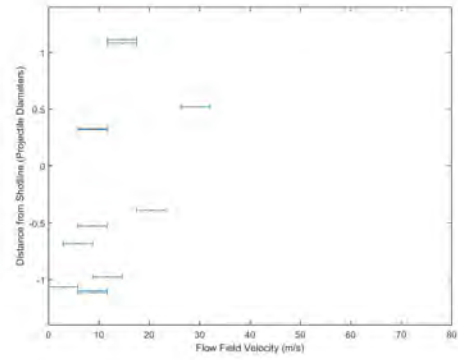
(c) 2.5 ms



(d) 2.6 ms

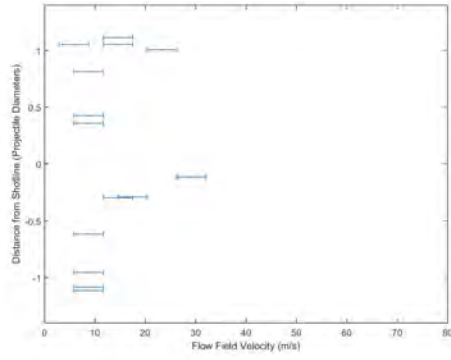


(e) 2.7 ms

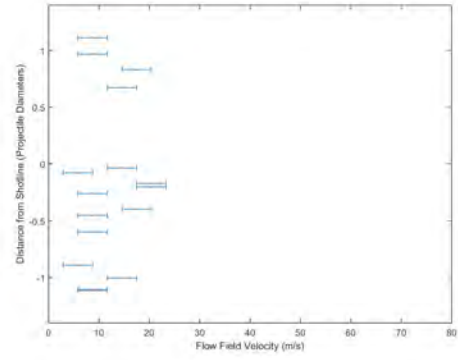


(f) 2.8 ms

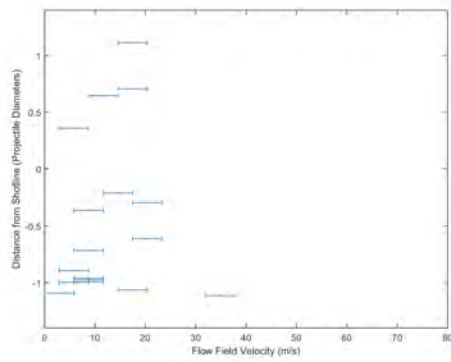
Figure B.37. Plotted horizontal component of the streak velocity across the funnel diameter 2.3 to 2.8 ms after impact.



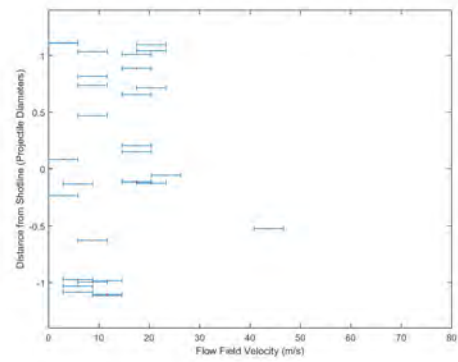
(a) 2.9 ms



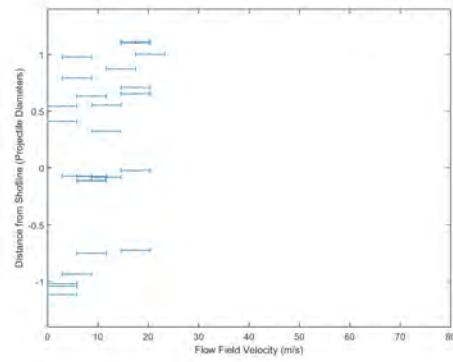
(b) 3.0 ms



(c) 3.1 ms



(d) 3.2 ms



(e) 3.3 ms

Figure B.38. Plotted horizontal component of the streak velocity across the funnel diameter 2.9 to 3.3 ms after impact.

## B.6 176 m/s impact velocity

For the second 176 *m/s* shot, the mass flow rate is shown in Fig. B.39. The entrained mass calculation, shown in Fig. B.40 was obtained by performing a rectangular approximation of Fig. B.39's data to estimate the area under the curve. The entrained mass, along with the applicable cavity volume measurements in Appendix C, was used to compute the cavity's partial pressure as detailed in Section 4.4.3

The velocity profiles used to calculate the mass flow data points composing Fig. B.39 are shown in Fig. B.41 through B.45 at the applicable times. For example, in Fig. B.39, 0.6 *ms* after projectile impact, the first mass flow data point's corresponding velocity profile is shown in Fig. B.41(a). The velocity profile in Fig. B.41(a) through (e) appears somewhat symmetric but is lacking in vector density on the upper half of the funnel. The lacking vector density can potentially lead to over or under representing the mass flow rate depending on the remaining vectors that did get detected. In this case, it appears the vectors on the upper half of the funnel could be potentially over representing the velocity at this radial position. Therefore, the mass flow rate, shown in Fig. B.39 at 0.6 *ms*, is potentially over representing the true mass flow rate, especially when compared to the other test cases. Regardless, it was difficult to measure the entrained flow field velocity even after waiting 0.5 to 0.6 *ms* after impact.

As the entrainment event proceeds, the flow field continues to develop and increase its overall velocity magnitude and symmetry as shown in Fig. B.41. For this test case the peak mass flow occurs over a range of approximately 1.6 to 2.1 *ms*, which corresponds to Fig. B.42(e) through Fig. B.43(d). Then the mass flow begins to slow as shown in Fig. B.32 after 2.1 *ms*. The decline in mass flow was attributed to the cavity contraction and the formation of the re-entrant jet as discussed in Chapter IV.

The flow field measurement begins to lose its symmetry at approximately 2.9 *ms* shown in Fig. B.44(f). The horizontal velocity vectors remain reasonably dense for the

remainder of the event but indicated a velocity profile of approximately  $8\text{ m/s}$  across the entire funnel as shown in Fig. B.45. The lack of symmetry or vector density by themselves do not mean a measurement is poor and cannot be used. Lack of symmetry and horizontal vectors simply indicate a potential exists for a sub-quality measurement its application should use caution. Regardless, the mass flow calculations after 2.9

*ms*

were not used in this research to predict any of the corresponding cavity geometric features discussed in Chapter IV.

For the second  $176\text{ m/s}$  shot, the first sign of fluid spurt occurred around  $3.4\text{ ms}$  after impact as shown in Fig. A.20(i). The entrainment velocity calculations covered  $0.6\text{ ms}$  to  $2.9\text{ ms}$  accurately enough to determine relationships to the cavity geometric features. The accuracy after  $2.9\text{ ms}$  is questionable but the velocity plots were shown to provide a reference for future research or other potential unknown uses. Regardless, the velocity profile data over the  $0.6$  to  $2.9\text{ ms}$  window was sufficient to correlate back to the internal cavity geometric features as discussed in Chapter IV and provide the cavity composition necessary for partial pressure and pressure work calculations.



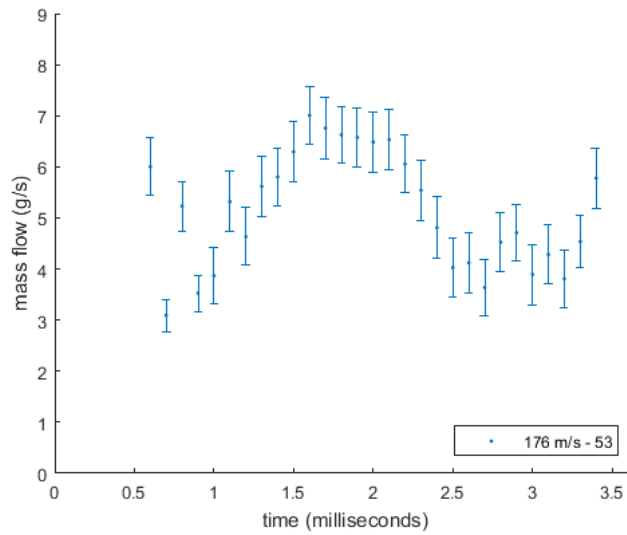


Figure B.39. Mass flow plot for the 176  $m/s$  shot obtained by performing a trapezoidal approximation of a volume of revolution around the projectile's shot-line. Each mass flow data point's corresponding velocity profile is shown in Fig. B.41 through B.45.

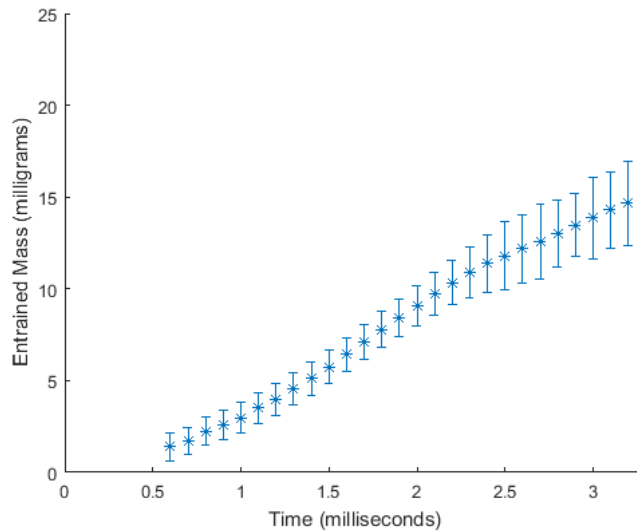
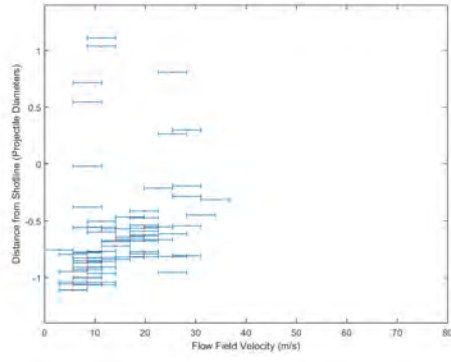
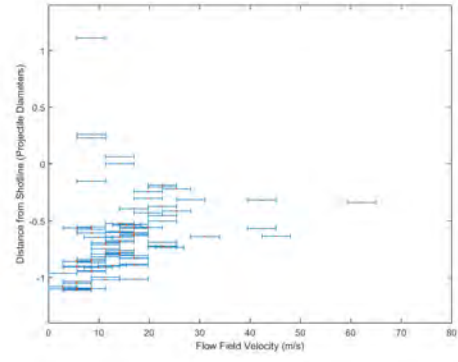


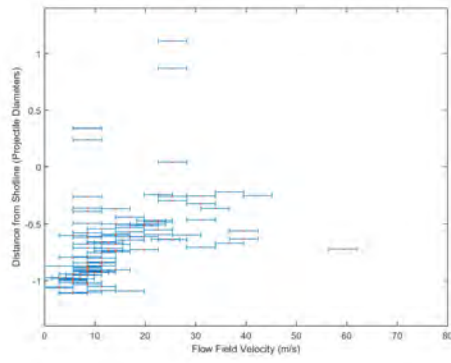
Figure B.40. Entrained mass calculation of ambient air into the HRAM cavity used for partial pressure calculations in Section 4.4.3 for the 176  $m/s$  shot. The entrained mass was calculated by performing a rectangular approximation of Fig. B.39's data to estimate the area under the curve.



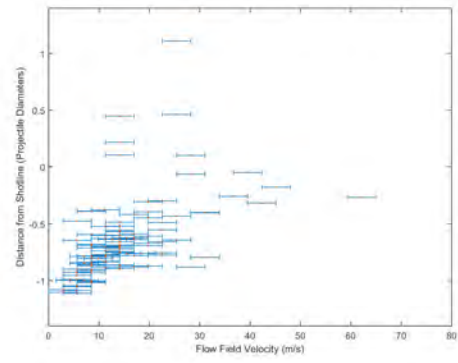
(a) 0.6 ms



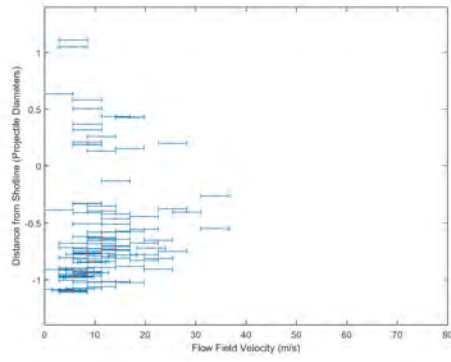
(b) 0.7 ms



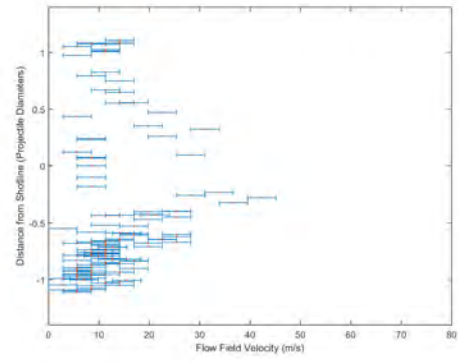
(c) 0.8 ms



(d) 0.9 ms

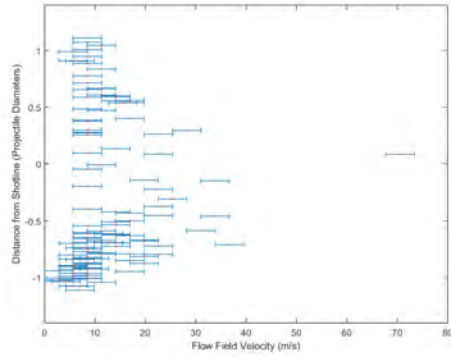


(e) 1.0 ms

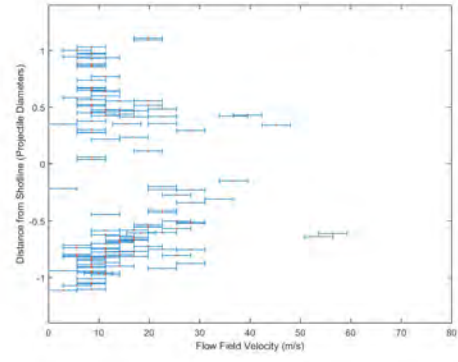


(f) 1.1 ms

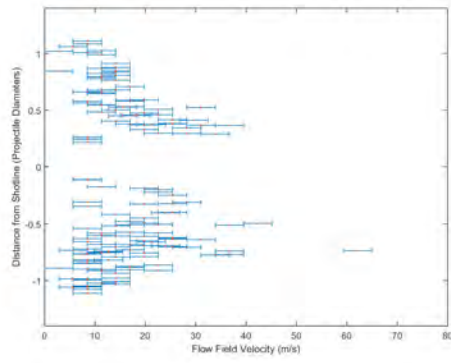
Figure B.41. Plotted horizontal component of the streak velocity across the funnel diameter 0.6 to 1.1 ms after impact.



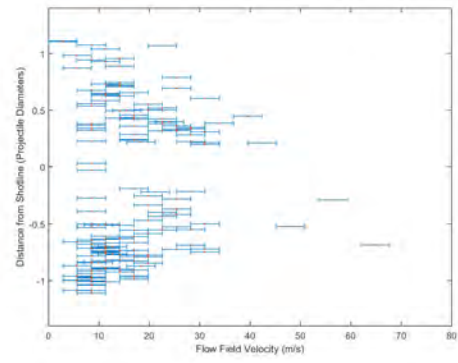
(a) 1.2 ms



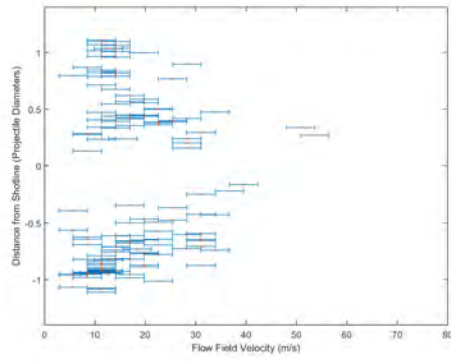
(b) 1.3 ms



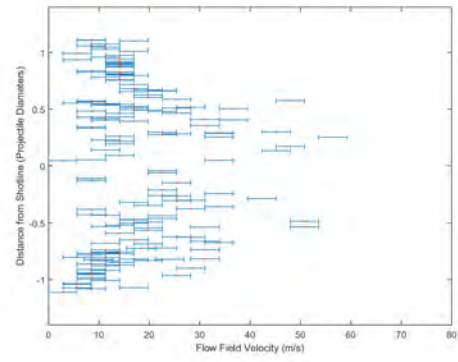
(c) 1.4 ms



(d) 1.5 ms

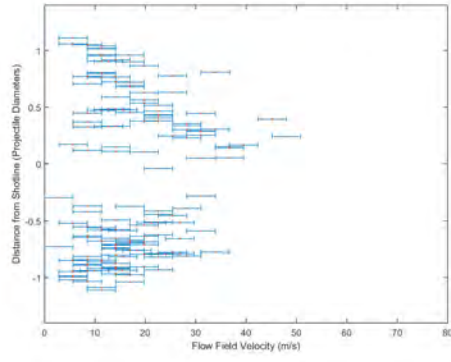


(e) 1.6 ms

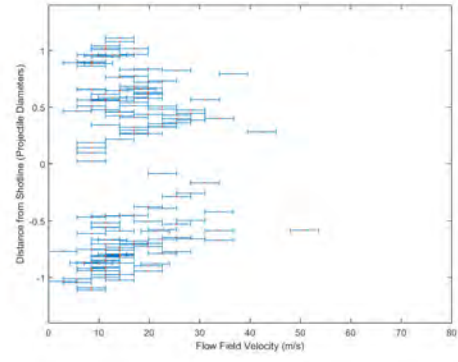


(f) 1.7 ms

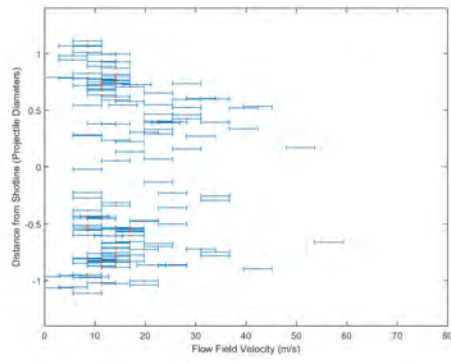
Figure B.42. Plotted horizontal component of the streak velocity across the funnel diameter 1.2 to 1.7 ms after impact.



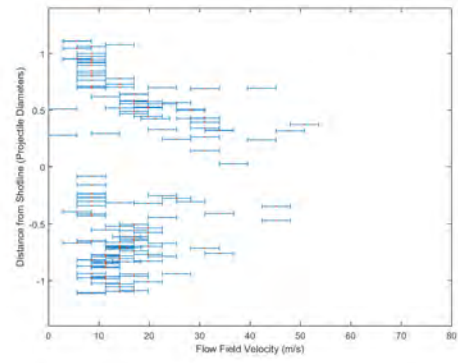
(a) 1.8 ms



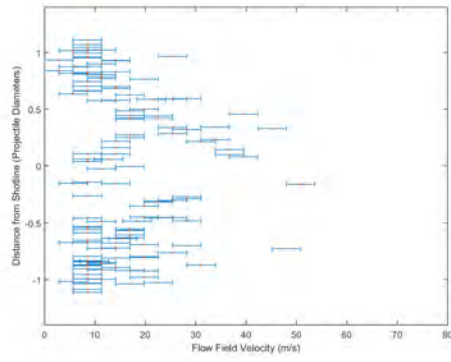
(b) 1.9 ms



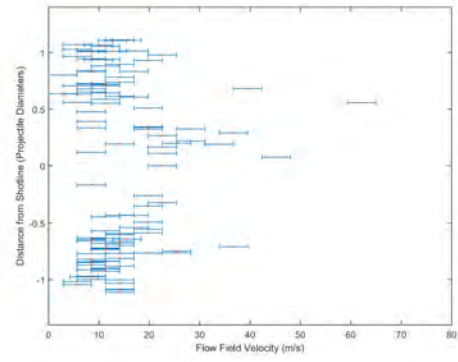
(c) 2.0 ms



(d) 2.1 ms

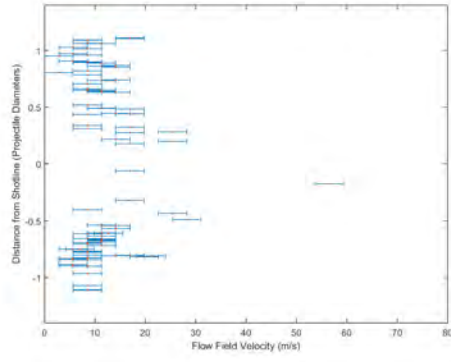


(e) 2.2 ms

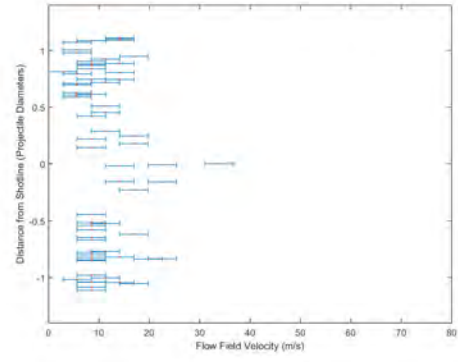


(f) 2.3 ms

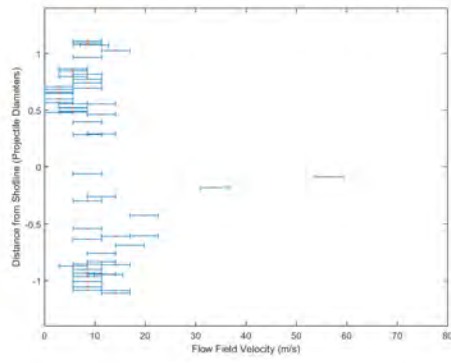
Figure B.43. Plotted horizontal component of the streak velocity across the funnel diameter 1.8 to 2.3 ms after impact.



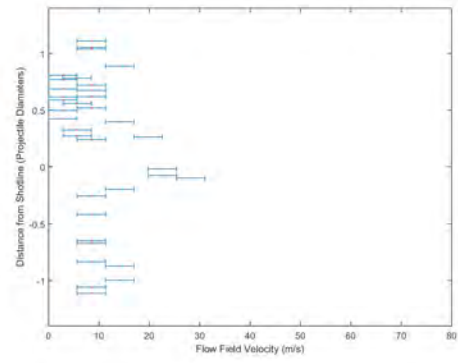
(a) 2.4 ms



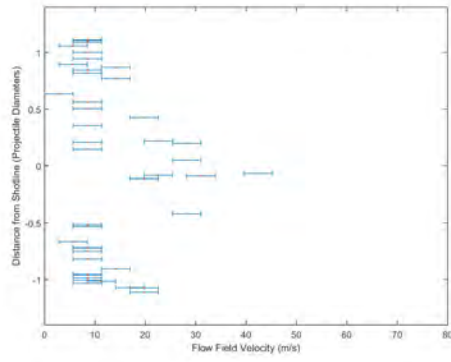
(b) 2.5 ms



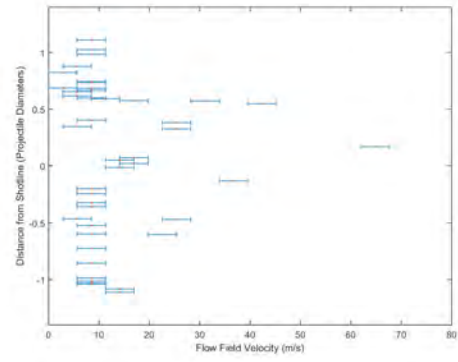
(c) 2.6 ms



(d) 2.7 ms

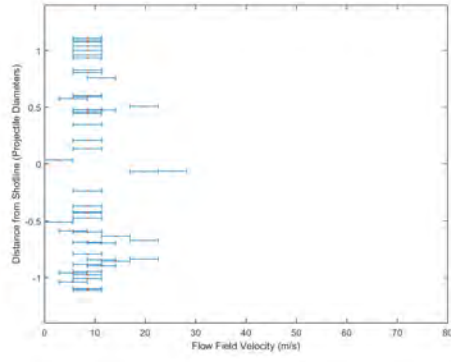


(e) 2.8 ms

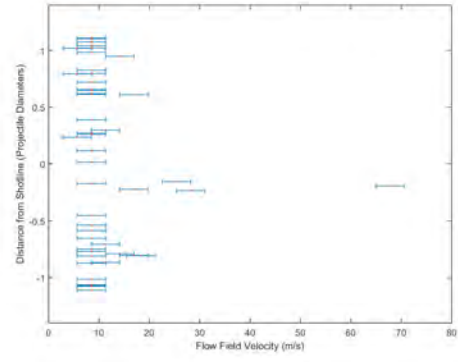


(f) 2.9 ms

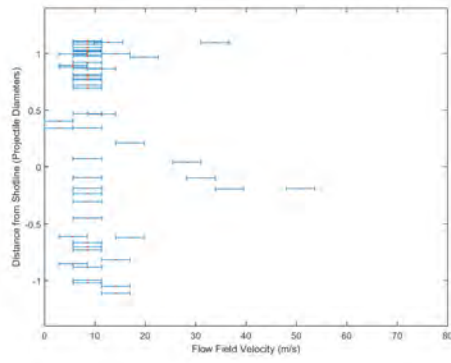
Figure B.44. Plotted horizontal component of the streak velocity across the funnel diameter 2.4 to 2.9 ms after impact.



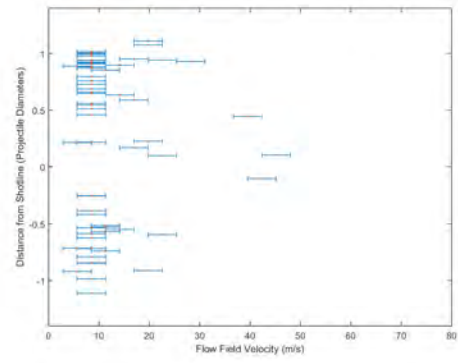
(a) 3.0 ms



(b) 3.1 ms



(c) 3.2 ms



(d) 3.3 ms

Figure B.45. Plotted horizontal component of the streak velocity across the funnel diameter 3.0 to 3.3 ms after impact.

## Appendix C: Cavity Imagery

The cavity images shown in Figs. C.1 through C.26 were used for two purposes. The first purpose was for volumetric measurements of the cavity. The second purpose was for projectile position measurements. All cavity imagery was taken at 20,000  $Hz$  with a 4  $\mu s$  exposure time using a brightfield imaging technique [34]. Each image had a resolution of 786 by 1024 pixels.

To measure the projectile position, the Image Cube technique, detailed in Chapter III, was used. The position measurements relative to the orifice were recorded and the camera's frame rate was used as a time source for velocity calculations. Each of the impact velocity's position measurements are recorded in Table C.1, C.2, and C.3.

### C.1 111 m/s impact velocity

The 111  $m/s$  shot was taken to approximate the cavity volume and projectile kinetic energy losses corresponding to the 113 and 114  $m/s$  entrainment shots. The cavity imagery was collected at 20,000  $Hz$  to increase the probability of obtaining a similar starting position for correlation with the 113 and 114  $m/s$  entrainment velocity experiments. Hence, Figs. C.3 through C.9 are shown at 10,000  $Hz$  to match the measurement rate for the entrainment velocity shots.

The image cube technique used the imagery collected at 20,000  $Hz$  to generate the slice shown in Fig. C.1. Therefore, not all the imagery data used for the position measurements is shown in Fig. C.3 through C.9. However, the corresponding images to the frame number is referenced in Table C.1 as available.

Projectile position data utilized the Image Cube technique at  $S_{417}$ . The data in Table C.1 was then used to fit a second order polynomial. A second order polynomial was chosen based on curve's shape in Fig. C.1, and to ultimately overcome the issues

associated with pixel locking. Pixel locking arises since pixel values are discrete responses. Fitting a curve approximated a continuous response for the discretely measured values. It is commonplace to use curve fitting or data smoothing to alleviate the issues associated with pixel locking [22].

A second order polynomial cannot predict the projectile position location during for the entire duration of the event, but it is sufficient for the first 4 *ms*. It is hypothesized, the approximate constant acceleration is due to the fluid contact area remaining relatively even during the time range of interest. Eventually, the cavity collapses and the fluid around the projectile contacts a larger portion of the surface area. When the fluid contacts a larger portion of the projectile, the acceleration profile changes. This hypothesis is based on observations and further research is required to determine the true acceleration profile of the projectile throughout the HRAM event. Regardless, the second order polynomial is sufficient at determining projectile position since cavity contraction and separation occur within the time frame shown in Fig. C.1.



Figure C.1. Image slice at  $S_{417}$  using the Image Cube technique detailed in Chapter III. The positional information resides on the horizontal while the frame number information resides on the vertical. The images composing the vertical were collected over a 4.0 *ms* duration after projectile impact. The position data pulled from this slice is shown in Table C.1.

The measured cavity volume for the 111 *m/s* shot is shown in Fig. C.2. The cavity's boundary was detected by using a Sobel edge detection algorithm. Assuming axial symmetry, the cavity's volume is approximated by breaking the cavity into small



Table C.1. Projectile Position Data for 111 *m/s* shot

Pixel Location	Frame Number	Figure Reference Number
992	1	Fig. C.3(a)
981	2	NS
972	3	Fig. C.3 (b)
967	4	NS
960	5	Fig. C.3 (c)
952	6	NS
930	9	Fig. C.3 (e)
894	14	NS
867	18	NS
834	23	Fig. C.4(f)
821	25	Fig. C.5(a)
796	29	Fig. C.5(c)
771	33	Fig. C.5(e)
731	40	NS
703	45	Fig. C.6(e)
679	49	Fig. C.7(a)
669	51	Fig. C.7(b)
638	57	Fig. C.7(e)
608	63	Fig. C.8(b)
574	70	NS
541	77	Fig. C.9(c)

cylinders. Each cylinder's diameter is measured by detecting and computing the cavity's boundary across each column of pixels. The width of the cylinder is simply 1 pixel where each cavity diameter is detected. For example, if the cavity is 100 pixels long, there are 100 small cylinders, with varying diameter and a 1 pixel width, at each 100 column locations. Summing the small cylinders throughout the cavity provide the necessary volume measurements. Details on the process and assumptions to calculate the cavity volume in each image is provided in Chapter III and detailed in "Development of Methods for Characterizing Hydrodynamic Ram Cavity Dynamics" [36].

The cavity's volume measurements were also calculated using the imagery at 20,000  $Hz$ . However, the necessary cavity volume measurements were extracted from the 20,000  $Hz$  measurement to match the 10,000  $Hz$  entrainment measurement. The volume measurements needed to match in time with the entrainment measurements to facilitate the calculation of the cavity's partial pressure, and the maximum pressure work potential. Chapter IV provides details and results regarding the cavity's partial pressure and pressure work potential.

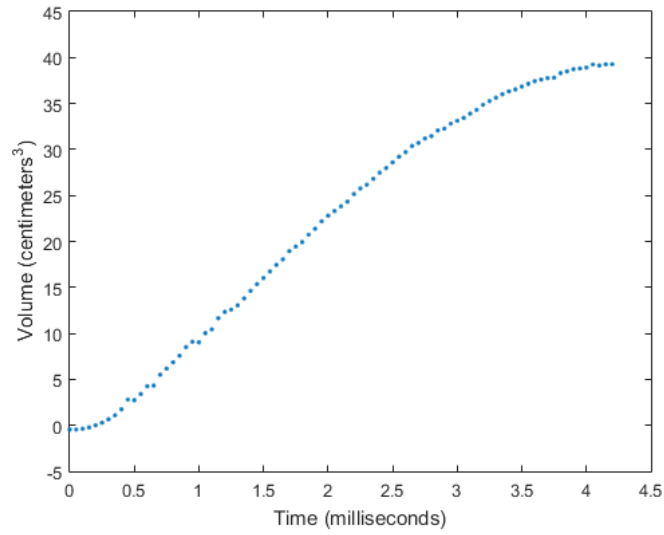
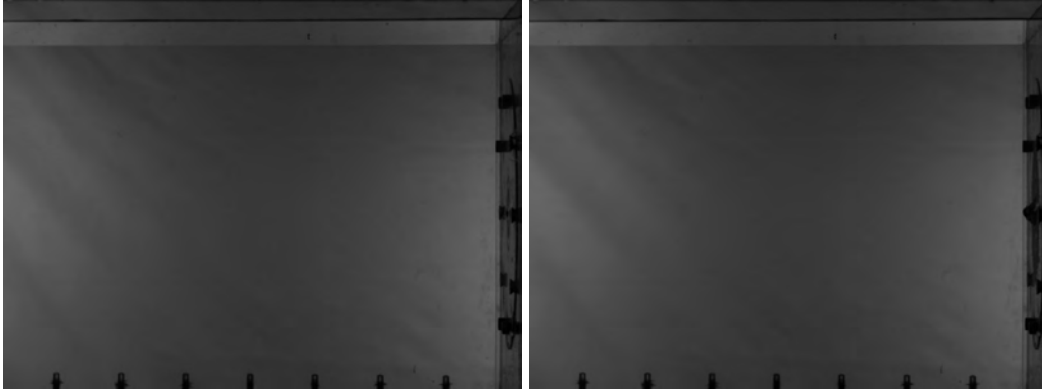
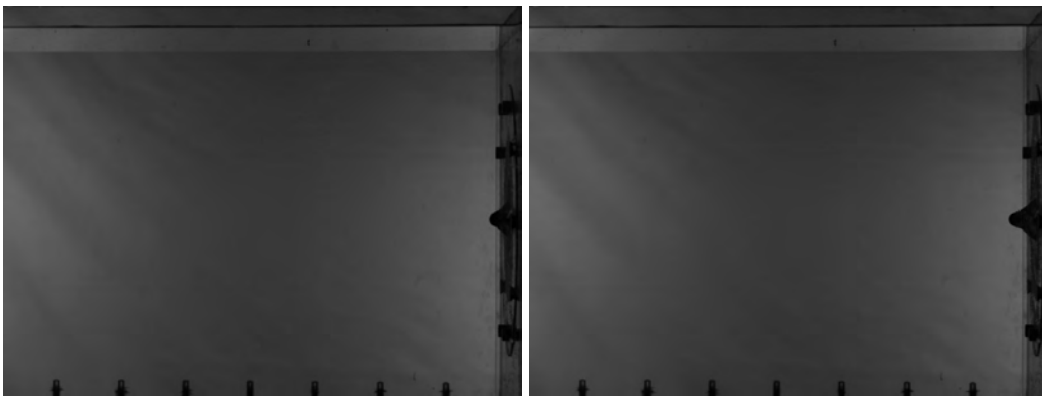


Figure C.2. Cavity volume calculations for the 111  $m/s$  shot plotted at 20,000  $Hz$ . The necessary volume data was extracted from the above figure and used to match the entrainment measurement rate of 10,000  $Hz$ . Details on the process and assumptions to compute the cavity volume are provided in Chapter III and in “Development of Methods for Characterizing Hydrodynamic Ram Cavity Dynamics” [36].



(a) 0.0 *ms*

(b) 0.1 *ms*



(c) 0.2 *ms*

(d) 0.3 *ms*



(e) 0.4 *ms*

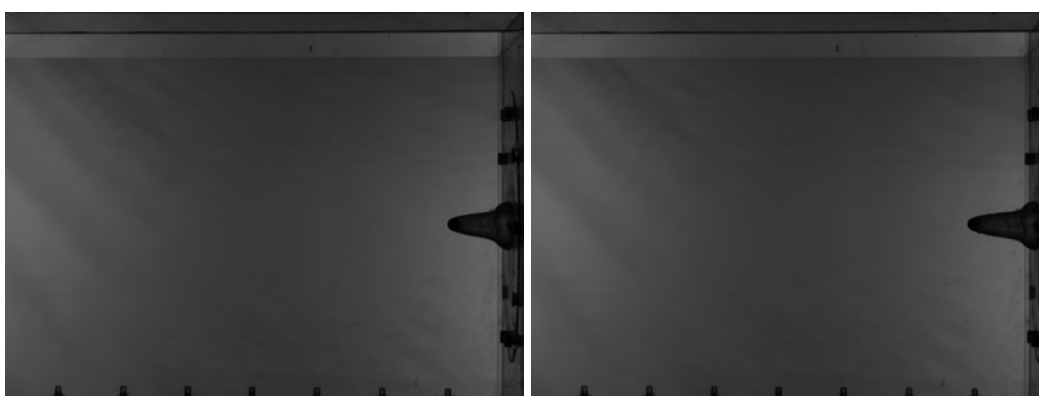
(f) 0.5 *ms*

Figure C.3. Raw cavity images for 111 *m/s* impact velocity for 0.0 to 0.5 *ms* after impact.



(a) 0.6 *ms*

(b) 0.7 *ms*



(c) 0.8 *ms*

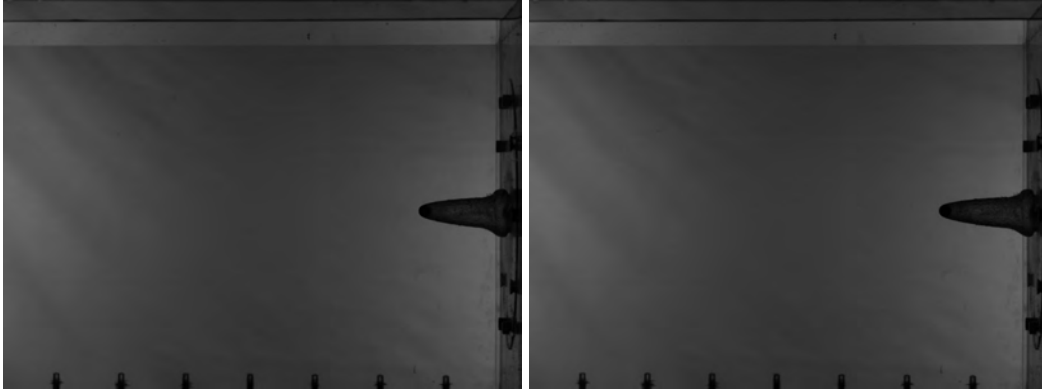
(d) 0.9 *ms*



(e) 1.0 *ms*

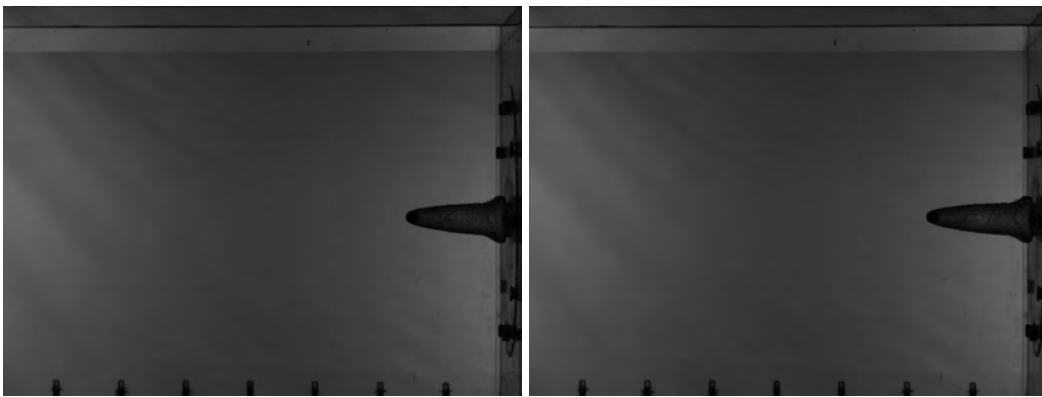
(f) 1.1 *ms*

Figure C.4. Raw cavity images for 111 *m/s* impact velocity for 0.6 to 1.1 *ms* after impact.



(a) 1.2 *ms*

(b) 1.3 *ms*



(c) 1.4 *ms*

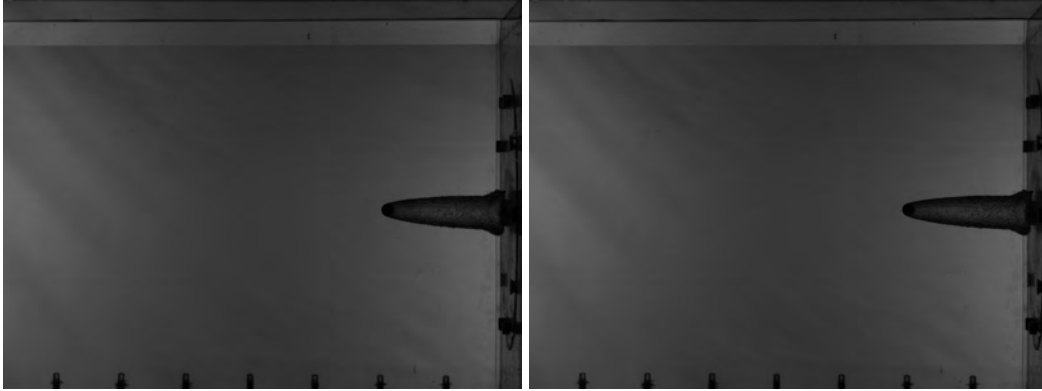
(d) 1.5 *ms*



(e) 1.6 *ms*

(f) 1.7 *ms*

Figure C.5. Raw cavity images for 111 *m/s* impact velocity for 1.2 to 1.7 *ms* after impact.



(a) 1.8 *ms*

(b) 1.9 *ms*



(c) 2.0 *ms*

(d) 2.1 *ms*



(e) 2.2 *ms*

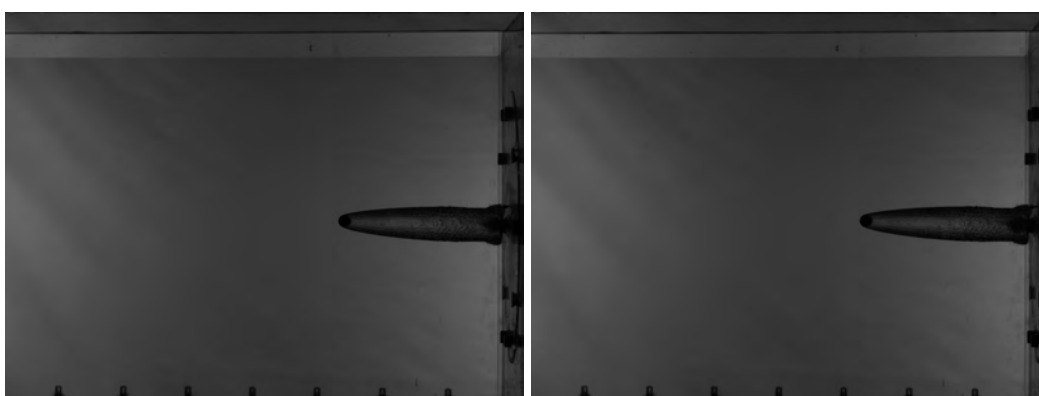
(f) 2.3 *ms*

Figure C.6. Raw cavity images for 111 *m/s* impact velocity for 1.8 to 2.3 *ms* after impact.



(a) 2.4 *ms*

(b) 2.5 *ms*



(c) 2.6 *ms*

(d) 2.7 *ms*

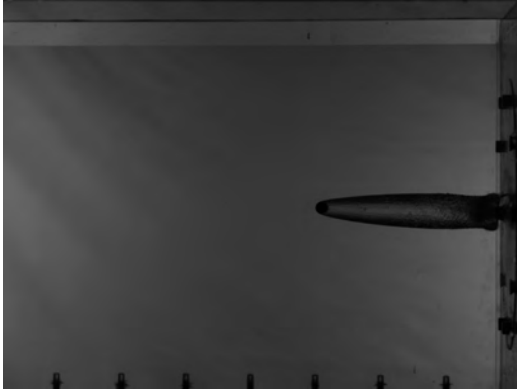


(e) 2.8 *ms*

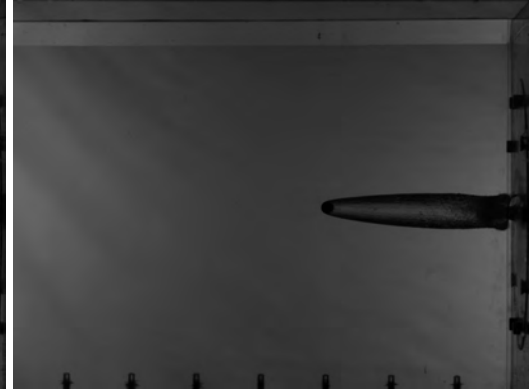
(f) 2.9 *ms*

Figure C.7. Raw cavity images for 111 *m/s* impact velocity for 2.4 to 2.9 *ms* after impact.





(a) 3.1 *ms*



(b) 3.2 *ms*



(c) 3.3 *ms*



(d) 3.4 *ms*

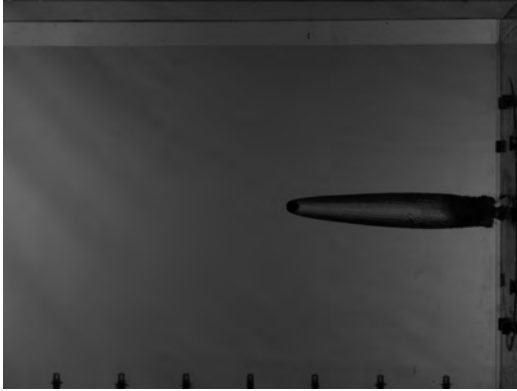


(e) 3.5 *ms*

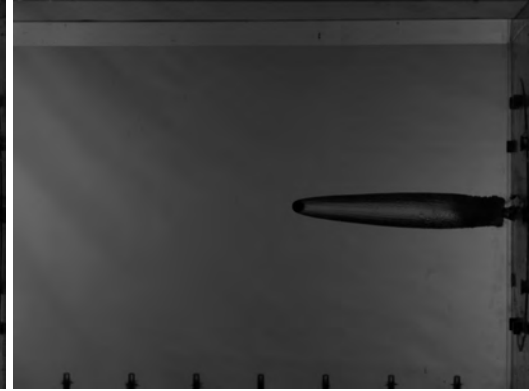


(f) 3.6 *ms*

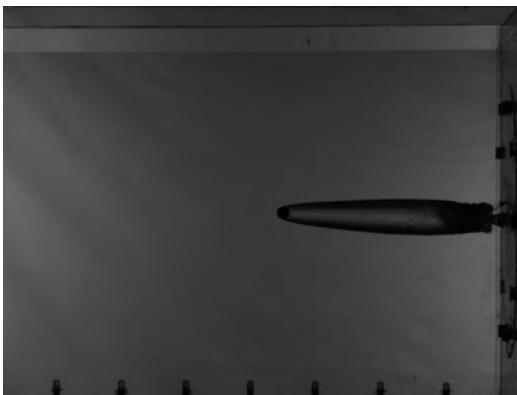
Figure C.8. Raw cavity images for 111 *m/s* impact velocity for 3.1 to 3.6 *ms* after impact.



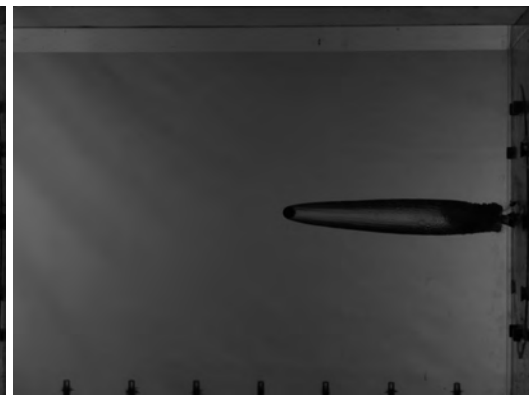
(a) 3.7 *ms*



(b) 3.8 *ms*



(c) 3.9 *ms*



(d) 4.0 *ms*



(e) 4.1 *ms*



(f) 4.2 *ms*

Figure C.9. Raw cavity images for 111 *m/s* impact velocity for 3.7 to 4.2 *ms* after impact.

## C.2 136 m/s impact velocity

The 136 *m/s* shot was taken to approximate the cavity volume and projectile kinetic energy losses corresponding to the 132 and 135 *m/s* entrainment shots. The cavity imagery was collected at 20,000 *Hz* to increase the probability of obtaining a similar starting position for correlation with the 132 and 135 *m/s* entrainment velocity experiments. Hence, Figs. C.12 through C.18 are shown at 10,000 *Hz* to match the measurement rate for the entrainment velocity shots.

The image cube technique used the imagery collected at 20,000 *Hz* to generate the slice shown in Fig. C.10. Therefore, not all the imagery data used for the position measurements is shown in Fig. C.12 through C.18. However, the corresponding images to the frame number is referenced in Table C.2 as applicable.

Projectile position data utilized the Image Cube technique at  $S_{432}$ . The data in Table C.2 was then used to fit a second order polynomial. A second order polynomial was chosen based on curve's shape in Fig. C.10, and to ultimately overcome the issues associated with pixel locking. Pixel locking arises since pixel values are discrete responses. Fitting a curve approximated a continuous response for the discretely measured values. It is commonplace to use curve fitting or data smoothing to alleviate the issues associated with pixel locking [22].

A second order polynomial cannot predict the projectile position location during for the entire duration of the event, but it is sufficient for the first 4 *ms*. It is hypothesized, the approximate constant acceleration is due to the fluid contact area remaining relatively even during the time range of interest. Eventually, the cavity collapses and the fluid around the projectile contacts a larger portion of the surface area. When the fluid contacts a larger portion of the projectile, the acceleration profile changes. This hypothesis is based on observations and further research is required to determine the true acceleration profile of the projectile throughout the HRAM event. Regardless, the second order polynomial is

sufficient at determining projectile position since cavity contraction and separation occur within the time frame shown in Fig. C.10.



Figure C.10. Image slice at  $S_{432}$  using the Image Cube technique detailed in Chapter III. The positional information resides on the horizontal while the frame number information resides on the vertical. The images composing the vertical were collected over a 4.0 *ms* duration after projectile impact. The position data pulled from this slice is shown in Table C.2.

The measured cavity volume for the 136 *m/s* shot is shown in Fig. C.2. The cavity's boundary was detected by using a Sobel edge detection algorithm. Assuming axial symmetry, the cavity's volume is approximated by breaking the cavity into small cylinders. Each cylinder's diameter is measured by detecting and computing the cavity's boundary across each column of pixels. The width of the cylinder is simply 1 pixel where each cavity diameter is detected. For example, if the cavity is 100 pixels long, there are 100 small cylinders, with varying diameter and a 1 pixel width, at each 100 column locations. Summing the small cylinders throughout the cavity provide the necessary volume measurements. Details on the process and assumptions to calculate the cavity volume in each image is provided in Chapter III and detailed in "Development of Methods for Characterizing Hydrodynamic Ram Cavity Dynamics" [36].

The cavity's volume measurements were also calculated using the imagery at 20,000 *Hz*. However, the necessary cavity volume measurements were extracted from the 20,000 *Hz* measurement to match the 10,000 *Hz* entrainment measurement. The volume measurements needed to match in time with the entrainment measurements to facilitate

Table C.2. Projectile Position Data for 136 *m/s* shot

Pixel Location	Frame Number	Figure Reference Number
986	1	Fig. C.12(a)
974	2	NS
964	3	Fig. C.12(b)
953	4	NS
943	5	Fig. C.12(c)
932	6	NS
921	7	Fig. C.12(d)
911	8	NS
890	10	NS
841	15	Fig. C.13(b)
804	19	Fig. C.13(d)
760	24	NS
718	29	Fig. C.14(c)
641	39	Fig. C.15(b)
577	48	NS
481	63	Fig. C.17(b)
457	67	Fig. C.17(d)
385	80	NS

the calculation of the cavity's partial pressure, and the maximum pressure work potential. Chapter IV provides details and results regarding the cavity's partial pressure and pressure work potential.

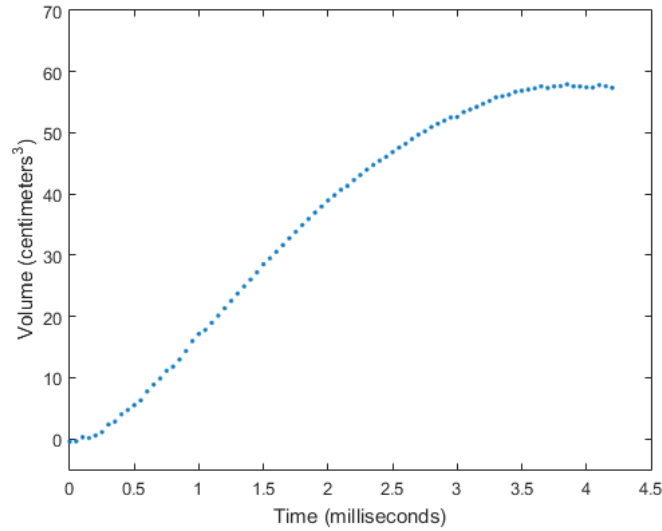


Figure C.11. Cavity volume calculations for the 136 *m/s* shot plotted at 20,000 *Hz*. The necessary volume data was extracted from the above figure and used to match the entrainment measurement rate of 10,000 *Hz*. Details on the process and assumptions to compute the cavity volume are provided in Chapter III and in “Development of Methods for Characterizing Hydrodynamic Ram Cavity Dynamics” [36].



(a) 0.0 *ms*

(b) 0.1 *ms*



(c) 0.2 *ms*

(d) 0.3 *ms*



(e) 0.4 *ms*

(f) 0.5 *ms*

Figure C.12. Raw cavity images for 136 *m/s* impact velocity for 0.0 to 0.5 *ms* after impact.



(a) 0.6 *ms*

(b) 0.7 *ms*



(c) 0.8 *ms*

(d) 0.9 *ms*

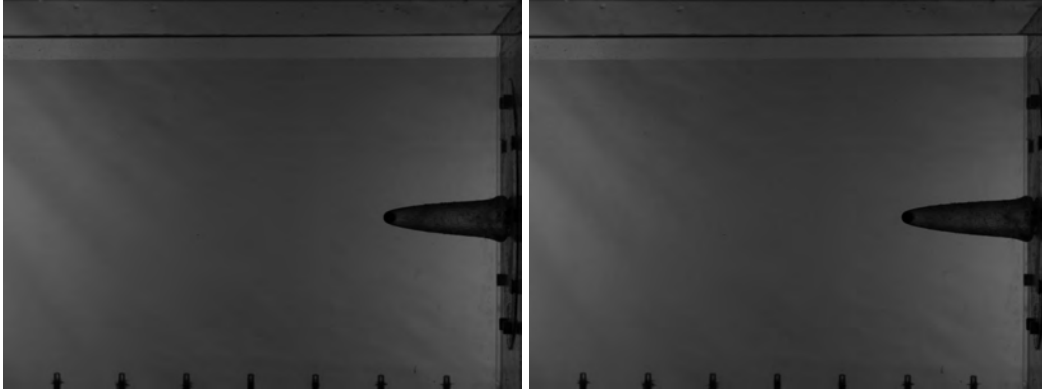


(e) 1.0 *ms*

(f) 1.1 *ms*

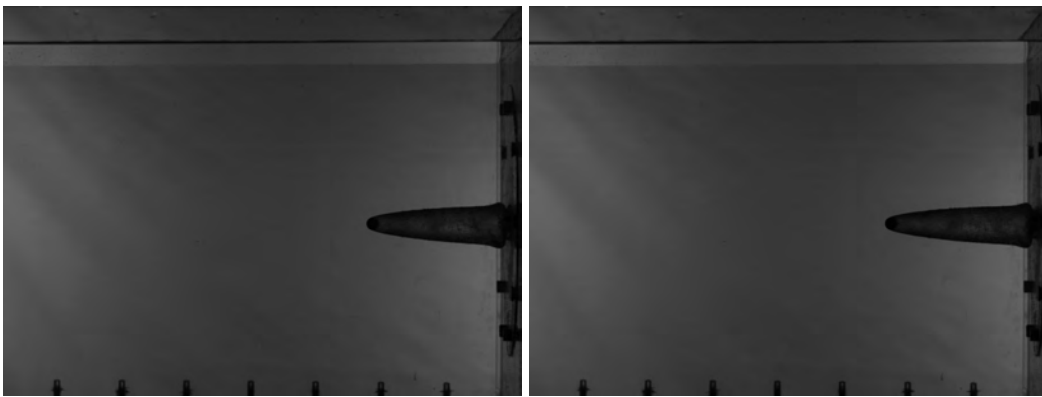
Figure C.13. Raw cavity images for 136 *m/s* impact velocity for 0.6 to 1.1 *ms* after impact.





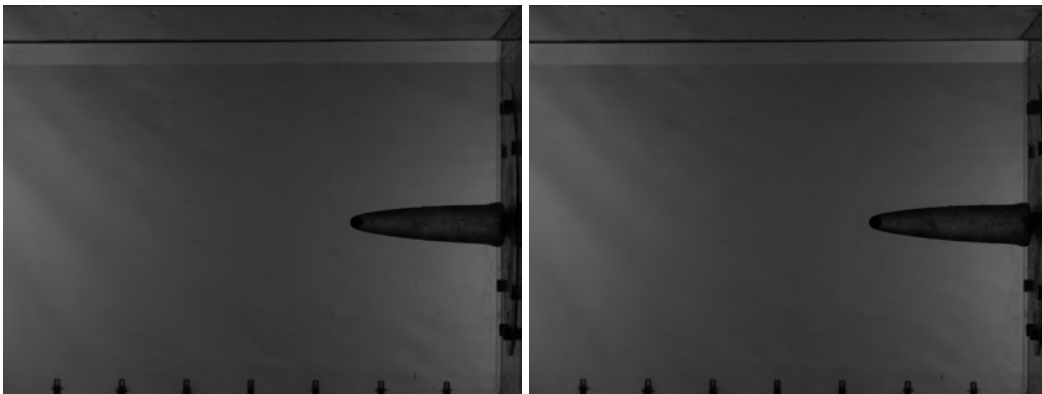
(a) 1.2 *ms*

(b) 1.3 *ms*



(c) 1.4 *ms*

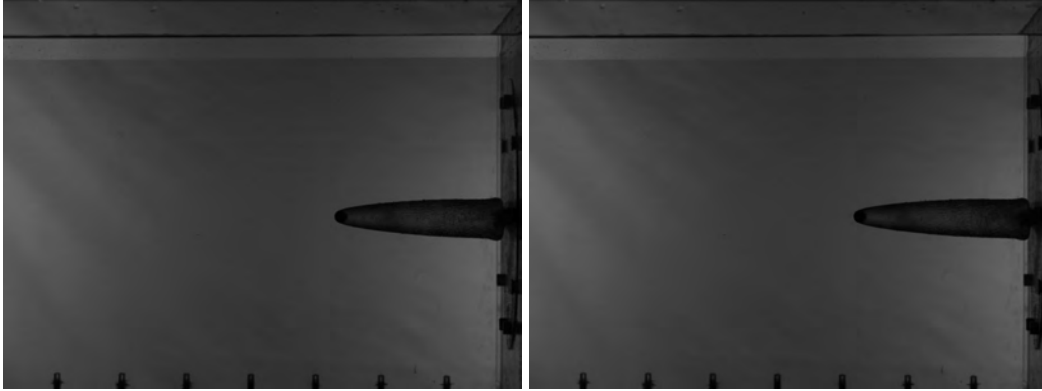
(d) 1.5 *ms*



(e) 1.6 *ms*

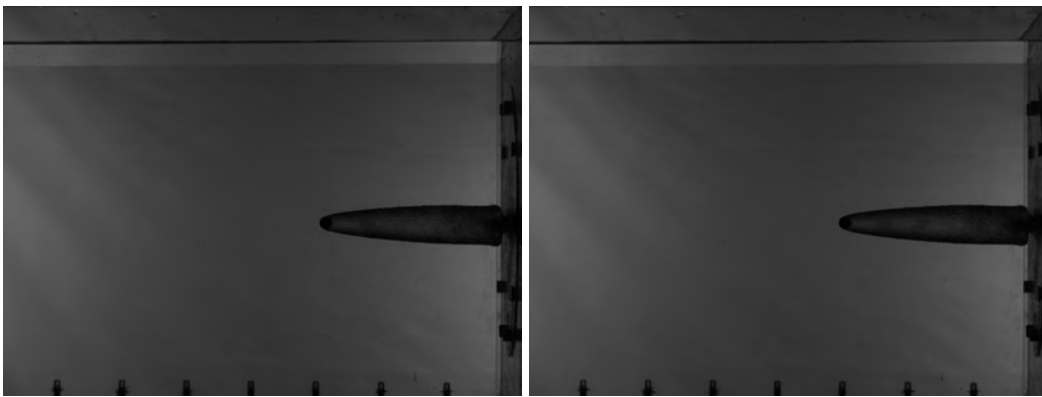
(f) 1.7 *ms*

Figure C.14. Raw cavity images for 136 *m/s* impact velocity for 1.2 to 1.7 *ms* after impact.



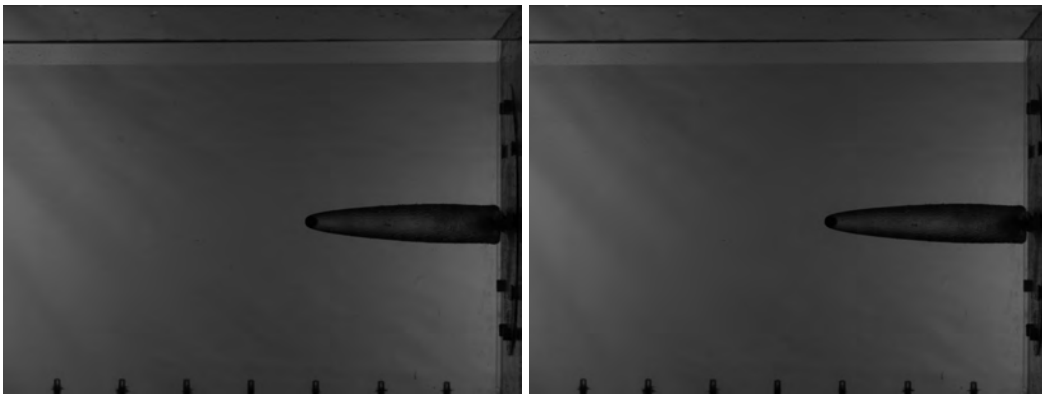
(a) 1.8 *ms*

(b) 1.9 *ms*



(c) 2.0 *ms*

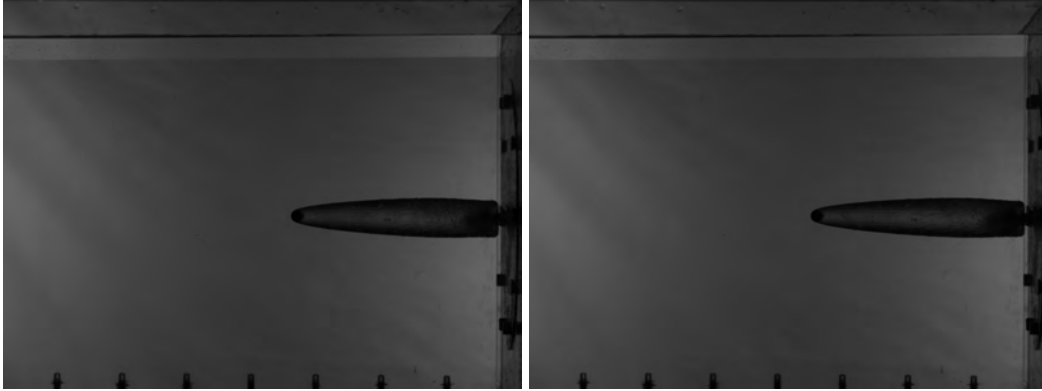
(d) 2.1 *ms*



(e) 2.2 *ms*

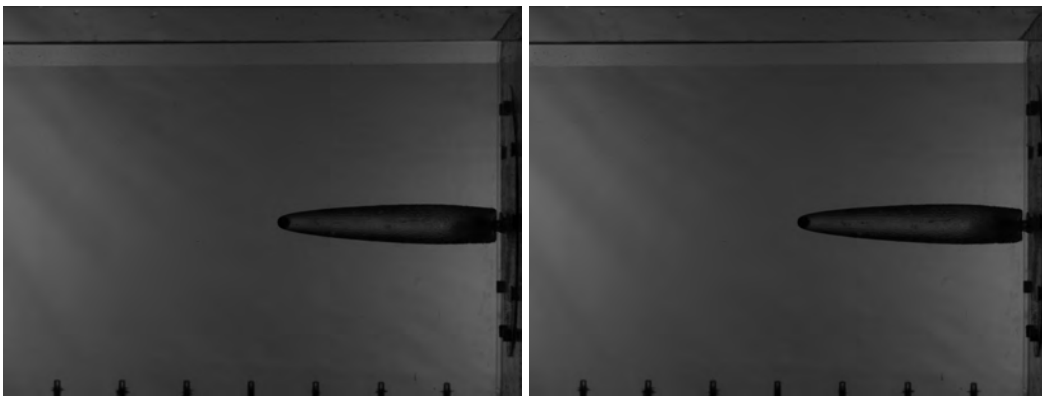
(f) 2.3 *ms*

Figure C.15. Raw cavity images for 136 *m/s* impact velocity for 1.8 to 2.3 *ms* after impact.



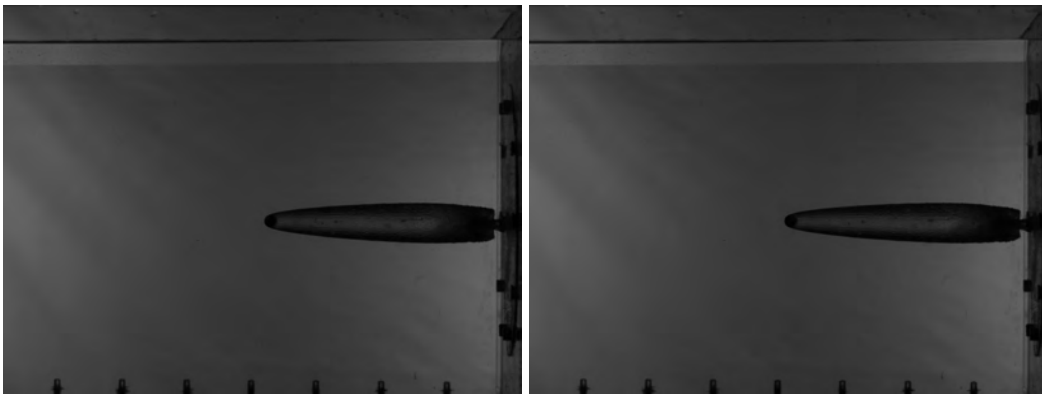
(a)  $2.4\text{ ms}$

(b)  $2.5\text{ ms}$



(c)  $2.6\text{ ms}$

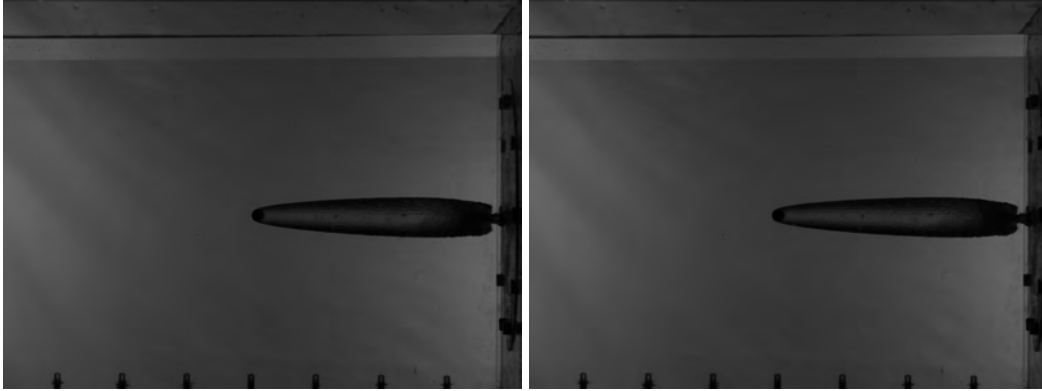
(d)  $2.7\text{ ms}$



(e)  $2.8\text{ ms}$

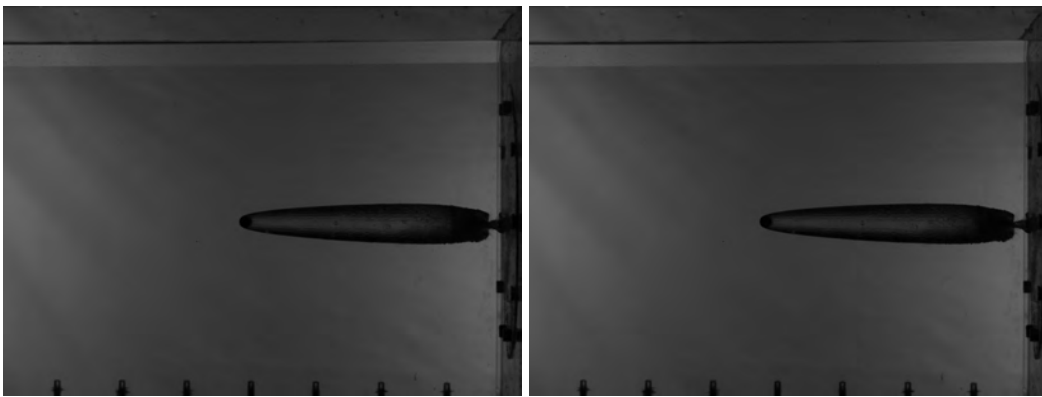
(f)  $2.9\text{ ms}$

Figure C.16. Raw cavity images for  $136\text{ m/s}$  impact velocity for  $2.4$  to  $2.9\text{ ms}$  after impact.



(a) 3.1 *ms*

(b) 3.2 *ms*



(c) 3.3 *ms*

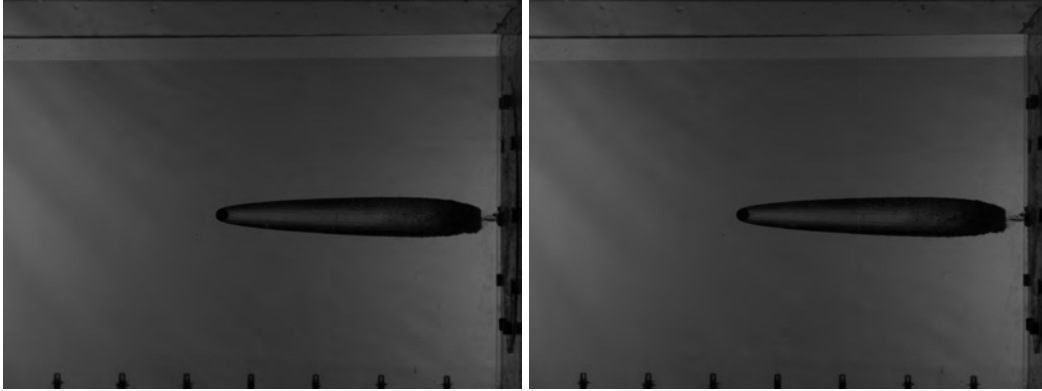
(d) 3.4 *ms*



(e) 3.5 *ms*

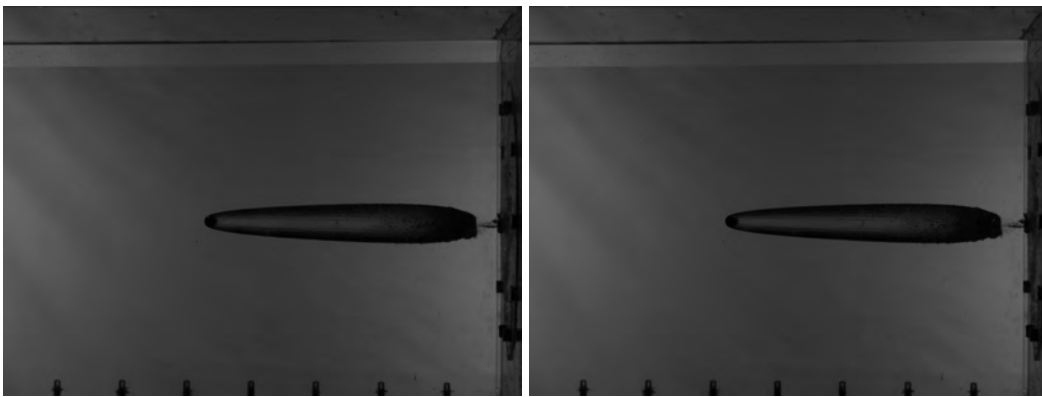
(f) 3.6 *ms*

Figure C.17. Raw cavity images for 136 *m/s* impact velocity for 3.1 to 3.6 *ms* after impact.



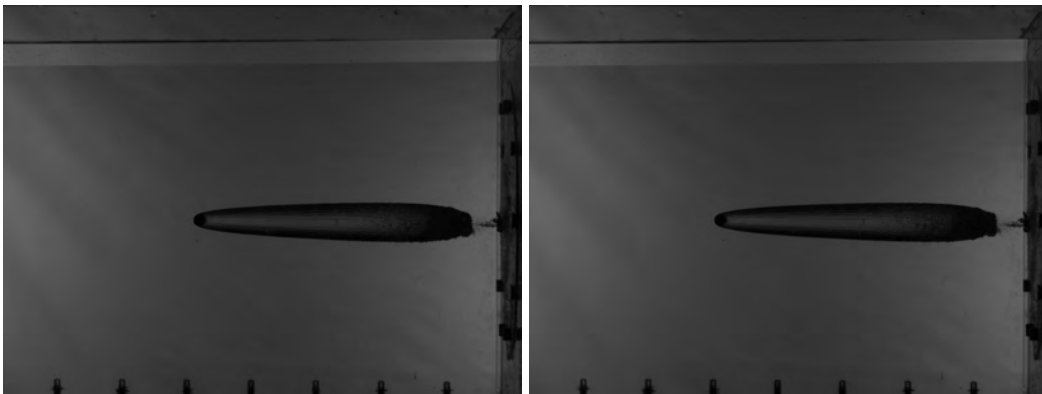
(a) 3.7 *ms*

(b) 3.8 *ms*



(c) 3.9 *ms*

(d) 4.0 *ms*



(e) 4.1 *ms*

(f) 4.2 *ms*

Figure C.18. Raw cavity images for 136 *m/s* impact velocity for 3.7 to 4.2 *ms* after impact.

### C.3 174 m/s impact velocity

The 174 *m/s* shot was taken to approximate the cavity volume and projectile kinetic energy losses corresponding to each of the 176 *m/s* entrainment shots. The cavity imagery was collected at 20,000 *Hz* to increase the probability of obtaining a similar starting position for correlation with the 176 *m/s* entrainment velocity experiments. Hence, Figs. C.21 through C.27 are shown at 10,000 *Hz* to match the measurement rate for the entrainment velocity shots.

The image cube technique used the imagery collected at 20,000 *Hz* to generate the slice shown in Fig. C.19. Therefore, not all the imagery data used for the position measurements is shown in Fig. C.21 through C.27. However, the corresponding images to the frame number is referenced in Table C.3 as available.

Projectile position data utilized the Image Cube technique at  $S_{428}$ . The data in Table C.3 was then used to fit a second order polynomial. A second order polynomial was chosen based on curve's shape in Fig. C.19, and to ultimately overcome the issues associated with pixel locking. Pixel locking arises since pixel values are discrete responses. Fitting a curve approximated a continuous response for the discretely measured values. It is commonplace to use curve fitting or data smoothing to alleviate the issues associated with pixel locking [22].

A second order polynomial cannot predict the projectile position location during for the entire duration of the event, but it is sufficient for the first 2.85 *ms*. Something interesting happened with the 174 *m/s* shot that did not happen in the 111 and 136 *m/s* shot. A piece of the aluminum shot plate remained attached to the front of the projectile after penetration. At approximately 1.0 *ms*, shown in Fig. C.23(e), the aluminum shot plate begins to peel off the front of the projectile. In Figs. C.24(a) through (f), the piece of aluminum is left behind and creates a small ripple seen on the bottom of the cavity.

Two things changed when the aluminum peeled off the front of the projectile. The first change occurs with regards to the fluid contact area on the projectile. With the aluminum attached, the fluid contacts both the projectile and the rough aluminum. The aluminum has rough edges from being plugged from the thin shot plate during projectile penetration. The aluminum's surface is also considerably more rough when compared to the projectile's polished finish. The second change occurs with regards to the system's mass. For the first  $1.0\text{ ms}$ , the projectile is moving with the aluminum attached, essentially combining their mass. As the aluminum peels, the mass of the system returns to that of the projectile. Therefore, the HRAM cavity and fluid forces acting on the projectile experience a mass change. In summary, the contact area and mass change cause the second order polynomial to fit poorly after approximately  $2.85\text{ ms}$ . However, this also lends credence to the hypothesis regarding changing acceleration as fluid contact area on the projectile changes.

The shortened window for projectile penetration has some follow-on effects, mainly with regards to the projectile kinetic energy and dimensionless kinetic energy. Since the time window for projectile position was shortened, the time window is also shortened for the projectile's kinetic energy and dimensionless kinetic energy. Even though the window is shortened, the kinetic energy dissipation rate is greater for projectiles at higher impact velocities. Hence, cavity contraction and separation occur well within the  $2.85\text{ ms}$  after impact, especially for the  $174\text{ m/s}$  shot, as shown in Fig. C.21 through C.27. Therefore, the prediction of cavity geometric features, per Fig. 4.27, 4.28, and 4.32 are still valid even when using making kinetic energy calculations over a shorter time duration.

It is hypothesized, the approximate constant acceleration is due to the fluid contact area remaining relatively even during the time range of interest. Eventually, the cavity collapses and the fluid around the projectile contacts a larger portion of the surface area. When the fluid contacts a larger portion of the projectile, the acceleration profile changes. This

hypothesis is based on observations and further research is required to determine the true acceleration profile of the projectile throughout the HRAM event. Regardless, the second order polynomial is sufficient at determining projectile position since cavity contraction and separation occur within the time frame shown in Fig. C.19.



Figure C.19. Image slice at  $S_{428}$  using the Image Cube technique detailed in Chapter III. The positional information resides on the horizontal while the frame number information resides on the vertical. The images composing the vertical were collected over a 4.0 *ms* duration after projectile impact. The position data pulled from this slice is shown in Table C.3.

The measured cavity volume for the 174 *m/s* shot is shown in Fig. C.20. The cavity's boundary was detected by using a Sobel edge detection algorithm. Assuming axial symmetry, the cavity's volume is approximated by breaking the cavity into small cylinders. Each cylinder's diameter is measured by detecting and computing the cavity's boundary across each column of pixels. The width of the cylinder is simply 1 pixel where each cavity diameter is detected. For example, if the cavity is 100 pixels long, there are 100 small cylinders, with varying diameter and a 1 pixel width, at each 100 column locations. Summing the small cylinders throughout the cavity provide the necessary volume measurements. Full details on the process and assumptions to calculate the cavity volume in each image is provided in Chapter III and detailed in "Development of Methods for Characterizing Hydrodynamic Ram Cavity Dynamics" [36].

The cavity's volume measurements were also calculated using the imagery at 20,000 *Hz*. However, the necessary cavity volume measurements were extracted from the



Table C.3. Projectile Position Data for 174 *m/s* shot

Pixel	Frame	Figure Reference	Pixel	Frame	Figure Reference
Location	Number	Number	Location	Number	Number
978	1	Fig. C.21(a)	741	15	Fig. C.22(b)
958	2	NS	727	16	NS
938	3	Fig. C.21(b)	700	18	NS
920	4	NS	673	20	NS
902	5	Fig. C.21(c)	635	23	Fig. C.22(f)
885	6	NS	597	26	NS
867	7	Fig. C.21(d)	549	30	NS
851	8	NS	527	32	NS
834	9	Fig. C.21(e)	505	34	NS
818	10	NS	463	38	NS
802	11	Fig. C.21(f)	394	45	Fig. C.24(e)
786	12	NS	366	48	NS
771	13	Fig. C.22(a)	322	53	Fig. C.25(c)
756	14	NS	289	57	Fig. C.25(e)

20,000  $Hz$  measurement to match the 10,000  $Hz$  entrainment measurement. The volume measurements needed to match in time with the entrainment measurements to facilitate the calculation of the cavity's partial pressure, and the maximum pressure work potential. Chapter IV provides details and results regarding the cavity's partial pressure and pressure work potential.

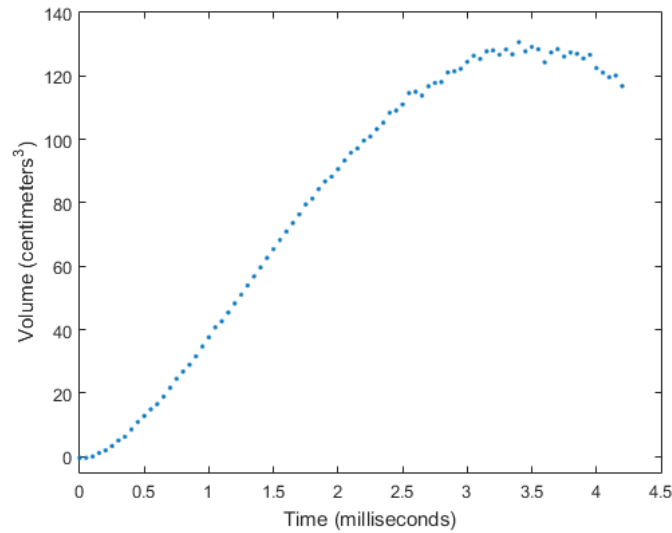


Figure C.20. Cavity volume calculations for the 174  $m/s$  shot plotted at 20,000  $Hz$ . The necessary volume data was extracted from the above figure and used to match the entrainment measurement rate of 10,000  $Hz$ . Details on the process and assumptions to compute the cavity volume are provided in Chapter III and in “Development of Methods for Characterizing Hydrodynamic Ram Cavity Dynamics” [36].



(a) 0.0 *ms*

(b) 0.1 *ms*



(c) 0.2 *ms*

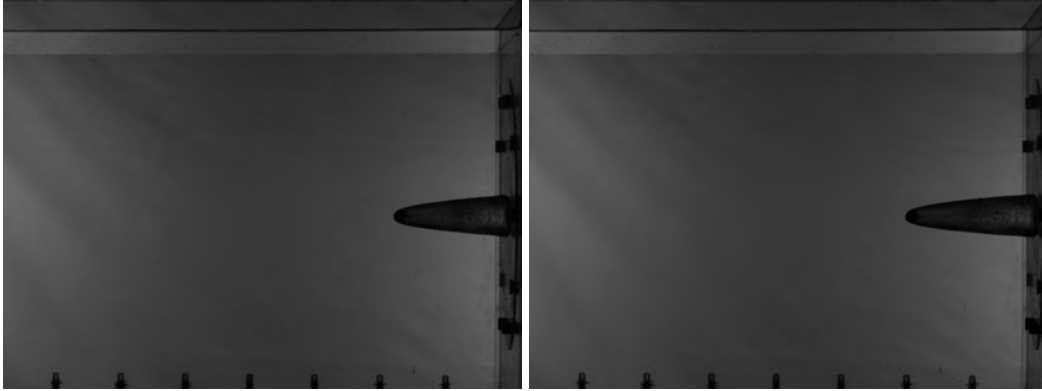
(d) 0.3 *ms*



(e) 0.4 *ms*

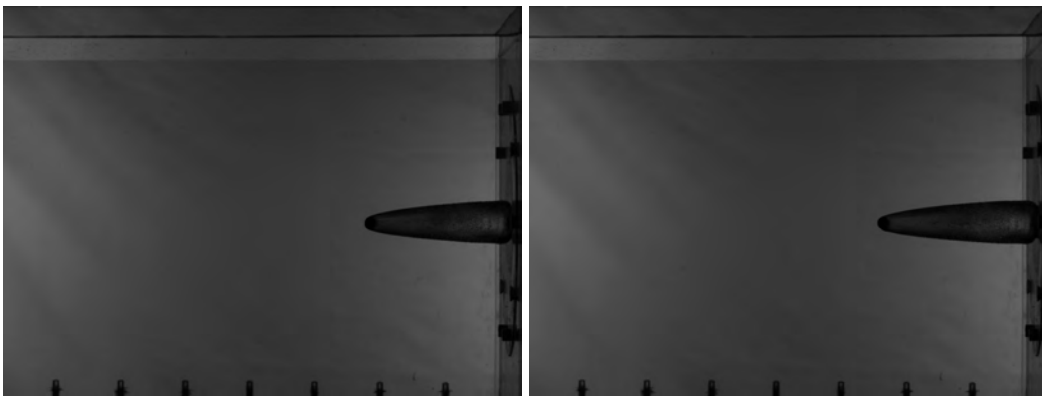
(f) 0.5 *ms*

Figure C.21. Raw cavity images for 174 *m/s* impact velocity for 0.0 to 0.5 *ms* after impact.



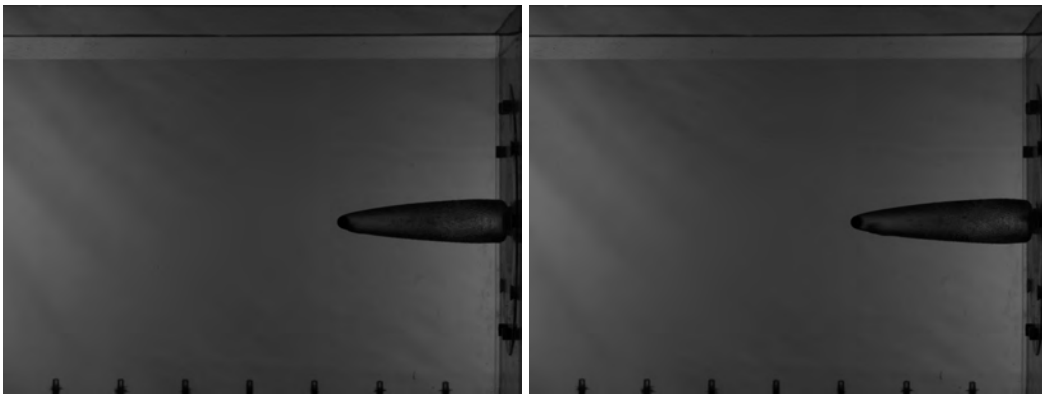
(a) 0.6 *ms*

(b) 0.7 *ms*



(c) 0.8 *ms*

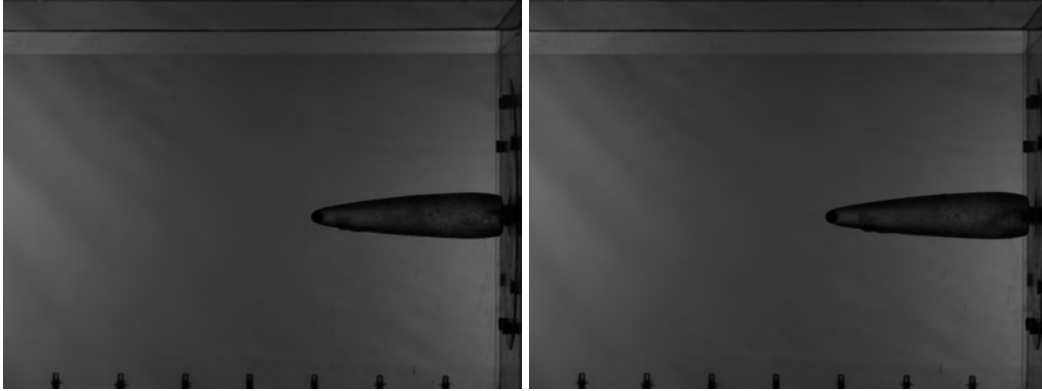
(d) 0.9 *ms*



(e) 1.0 *ms*

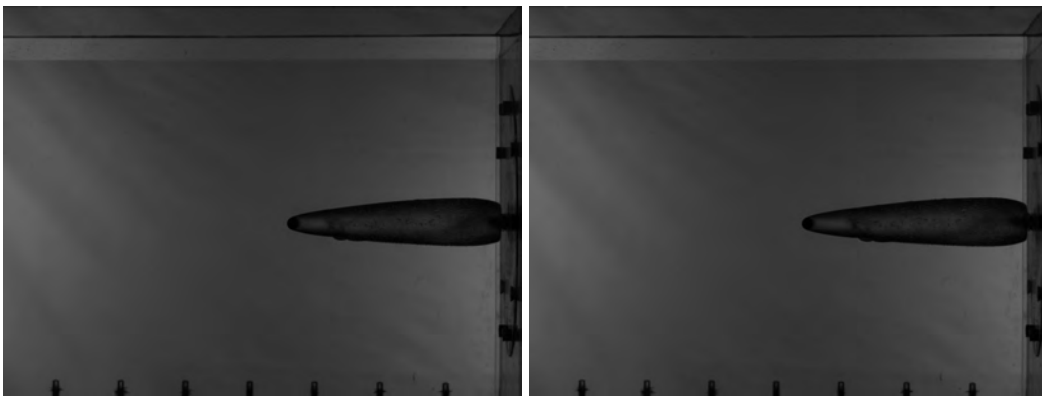
(f) 1.1 *ms*

Figure C.22. Raw cavity images for 174 *m/s* impact velocity for 0.6 to 1.1 *ms* after impact.



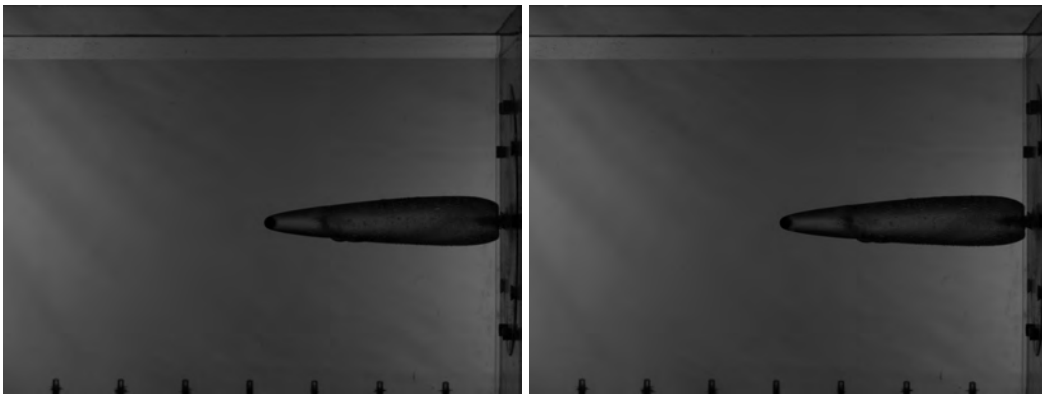
(a) 1.2 *ms*

(b) 1.3 *ms*



(c) 1.4 *ms*

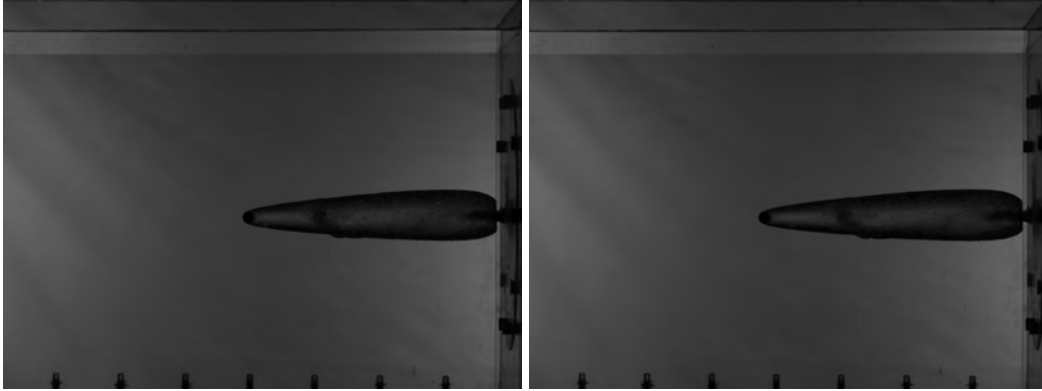
(d) 1.5 *ms*



(e) 1.6 *ms*

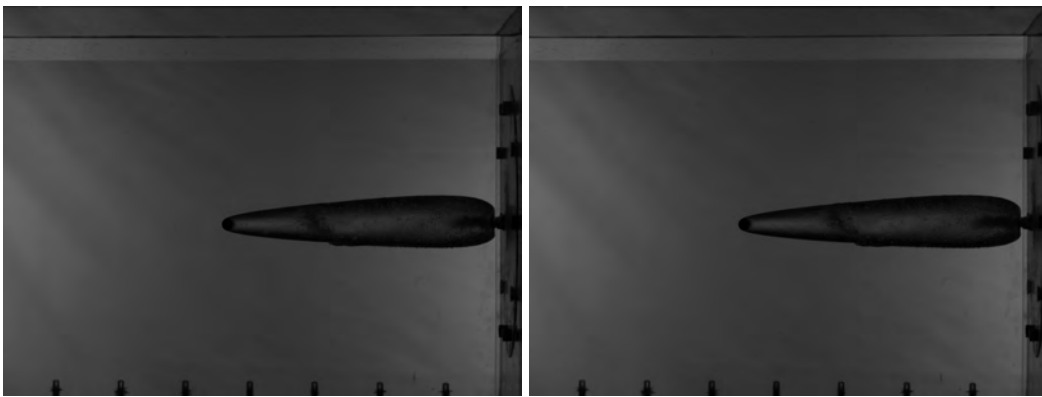
(f) 1.7 *ms*

Figure C.23. Raw cavity images for 174 *m/s* impact velocity for 1.2 to 1.7 *ms* after impact.



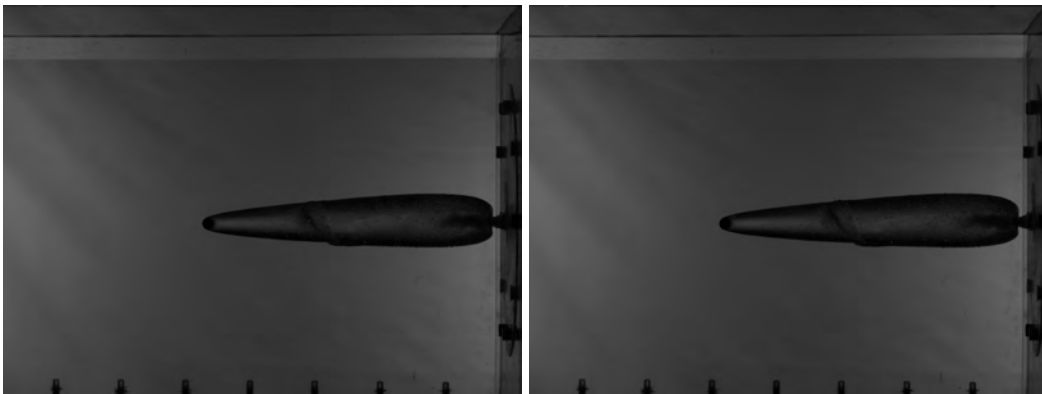
(a) 1.8 *ms*

(b) 1.9 *ms*



(c) 2.0 *ms*

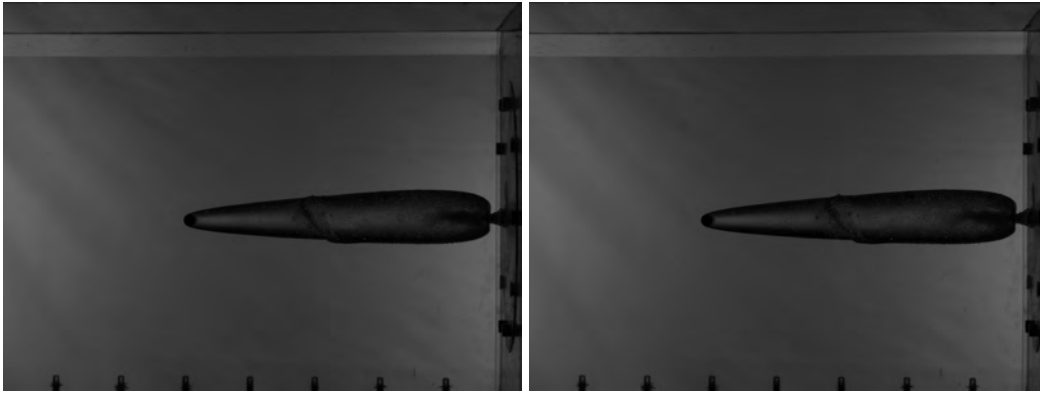
(d) 2.1 *ms*



(e) 2.2 *ms*

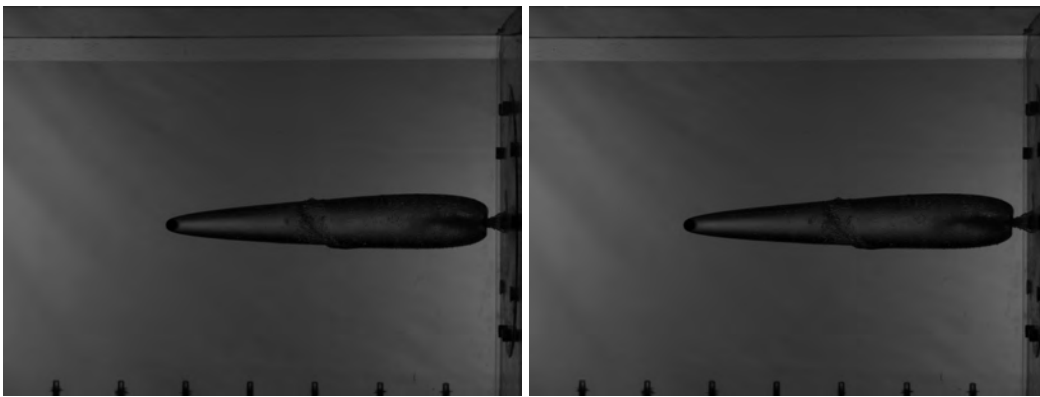
(f) 2.3 *ms*

Figure C.24. Raw cavity images for 174 *m/s* impact velocity for 1.8 to 2.3 *ms* after impact.



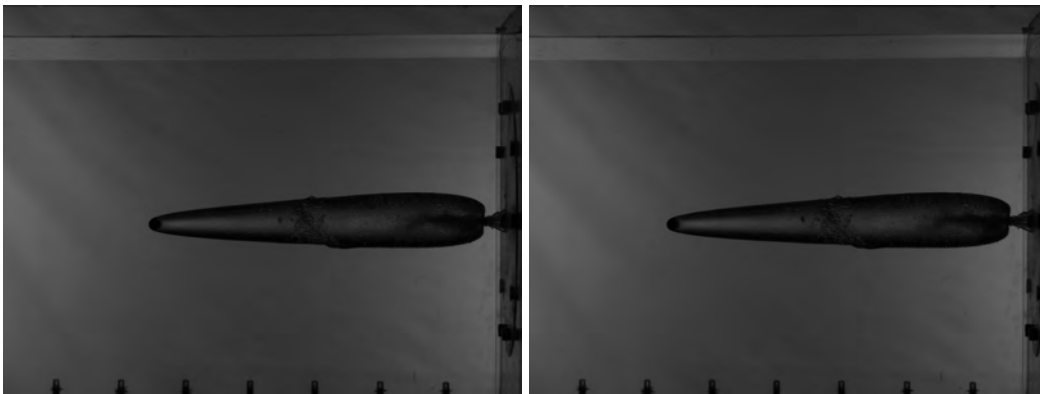
(a) 2.4 *ms*

(b) 2.5 *ms*



(c) 2.6 *ms*

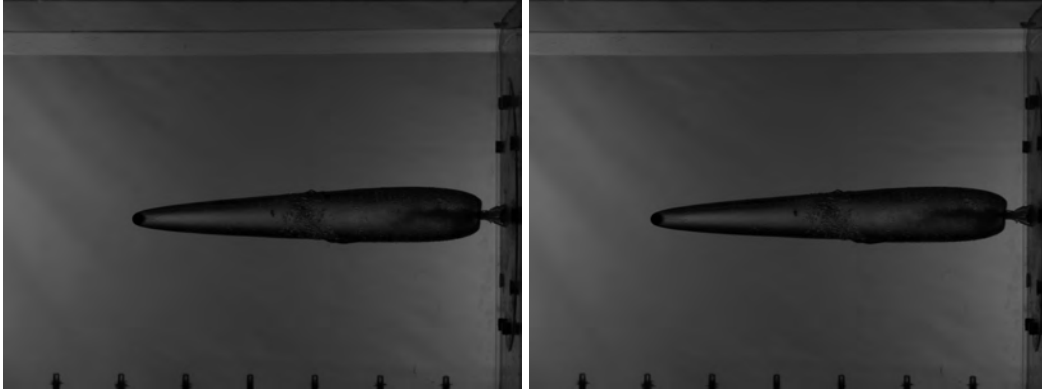
(d) 2.7 *ms*



(e) 2.8 *ms*

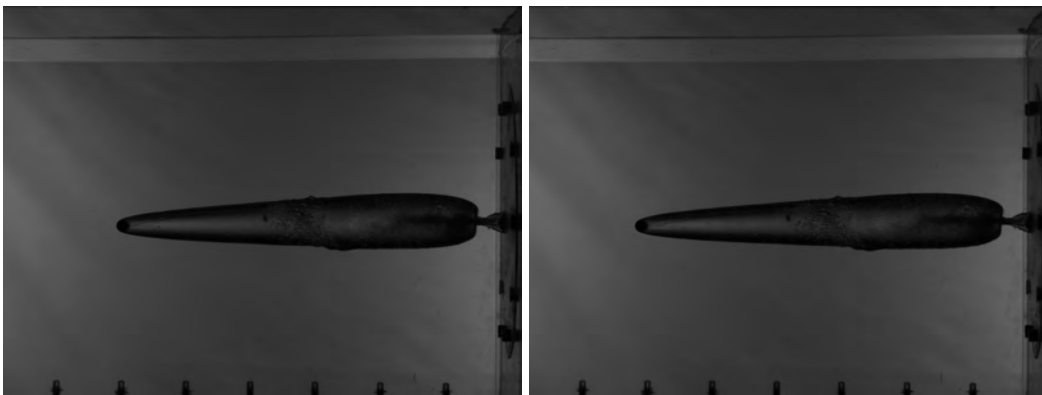
(f) 2.9 *ms*

Figure C.25. Raw cavity images for 174 *m/s* impact velocity for 2.4 to 2.9 *ms* after impact.



(a) 3.1 *ms*

(b) 3.2 *ms*



(c) 3.3 *ms*

(d) 3.4 *ms*

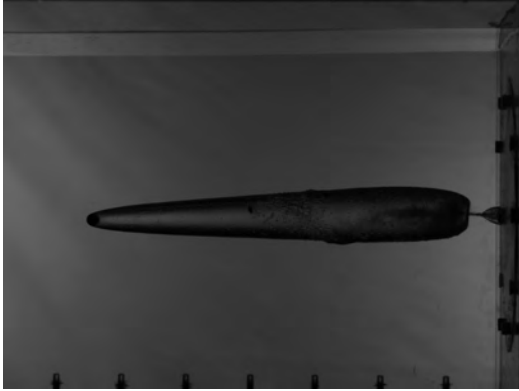


(e) 3.5 *ms*

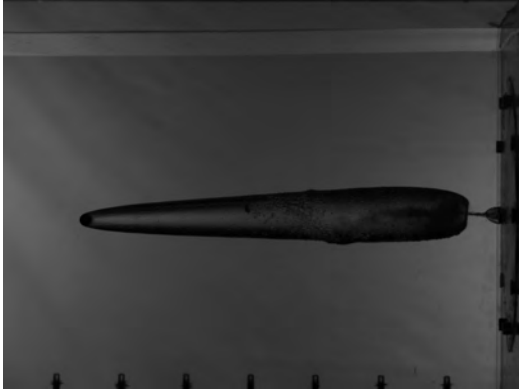
(f) 3.6 *ms*

Figure C.26. Raw cavity images for 174 *m/s* impact velocity for 3.1 to 3.6 *ms* after impact.

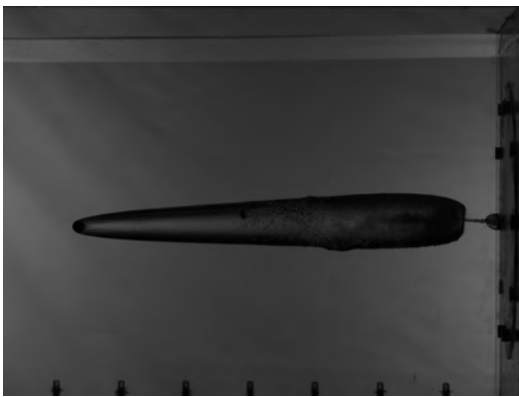




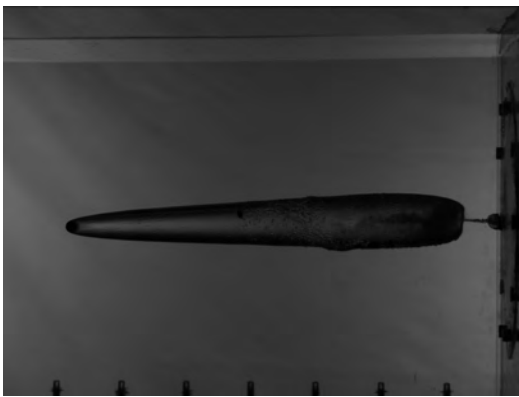
(a) 3.7 *ms*



(b) 3.8 *ms*



(c) 3.9 *ms*



(d) 4.0 *ms*



(e) 4.1 *ms*



(f) 4.2 *ms*

Figure C.27. Raw cavity images for 174 *m/s* impact velocity for 3.7 to 4.2 *ms* after impact.

## **Appendix D: Extrapolated Imagery from Research with 96th Test Group**

Imagery was collected at 28,000  $Hz$  for the 1,200, 1,495, and 1,800  $m/s$  impact velocities. The collected imagery did not have sufficient field of view to capture the entire cavity volume while cavity contraction and separation were occurring. Note, the objective of the research was not to measure the entire cavity volume, but to determine which cavity geometric features contributed to the transient spray phases. However, by predicting the projectile's position and extrapolating the cavity's volume, cavity volume calculations are possible and relationships between the relatively low projectile velocities are discussed.

The raw imagery did not have sufficient contrast to consistently detect the cavity's boundary using the Sobel edge detection algorithm. Therefore, the cavity's boundary was enhanced by visual inspection by placing black pixels along the approximate location of the cavity boundary. Additionally, the projectile position was predicted and extrapolated outside the camera's field of view. Once the cavity's boundaries were enhanced and connected to the the predicted projectile's position, the cavity volume was calculated using the processing techniques as detailed in Chapter III, for the 1,200, 1,495, and 1,800  $m/s$  shots.

Cavity volume calculations assume axial symmetry about the projectile's shot line. The camera was not perpendicular to the projectile's shot line indicating the imagery collected is skewed by the camera's offset angle. Camera calibration, to obtain the pixel to length conversion, was not performed. Therefore, to convert the imagery data from pixels to standard units, the 0.375  $in$  projectile was approximated as having a diameter of 14 pixels. Additionally, to reduce the visual inspection efforts, every 3<sup>rd</sup> image from the collected data was used giving the cavity volume calculations an effective rate of approximately 9,333  $Hz$ .

Users should apply caution when using the extrapolated data. This data was used to make broad observations between the low and high velocity impacts as provided in

Chapter IV. The accuracy of the data limited due to the unknown errors associated with the camera's offset angle, the camera calibration, prediction of the projectile's position, and the visual inspection of the cavity. Regardless, the data was useful in drawing similarities and differences between the low impact velocity research conducted within AFIT's laboratories.

The calculated cavity volume from the extrapolated imagery data for the 1,200, 1,495, and 1,800  $m/s$  shot is shown in Fig. D.1, D.2, and D.3, respectively. A 3<sup>rd</sup> order polynomial was fit to the extrapolated data and an inflection point at 1.653, 1.881, and 1.954  $ms$  was calculated for the 1,200, 1,495, and 1,800  $m/s$  shots, respectively. The extrapolated images used for the volume calculations are shown in Figs. D.4 through D.16, Figs. D.17 through D.29, and Figs. D.30 through D.41 for the 1,200, 1,495, and 1,800  $m/s$  shots, respectively.

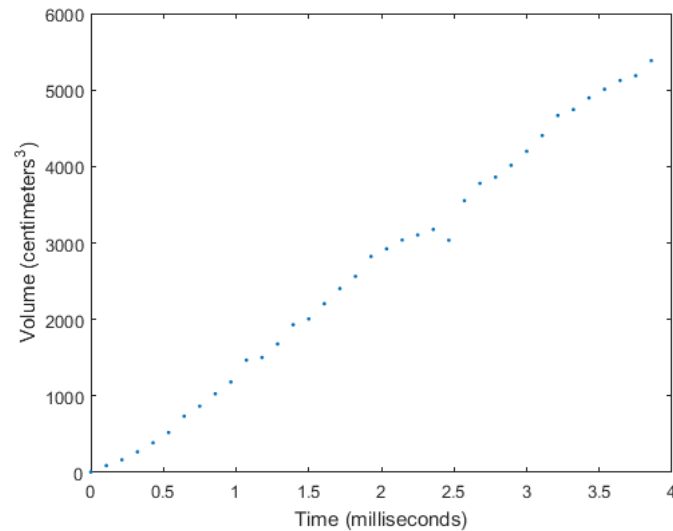


Figure D.1. Volume plot resulting from extrapolated images shown in Figs. D.4 through D.16.

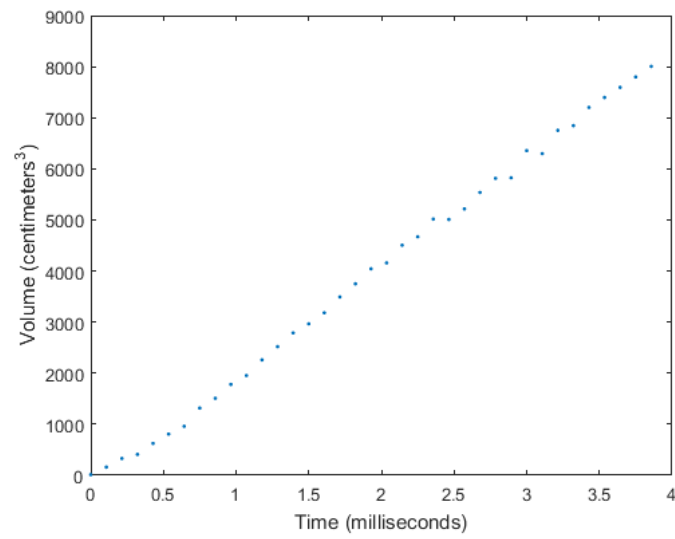


Figure D.2. Volume plot resulting from extrapolated images shown in Figs. D.17 through D.29.

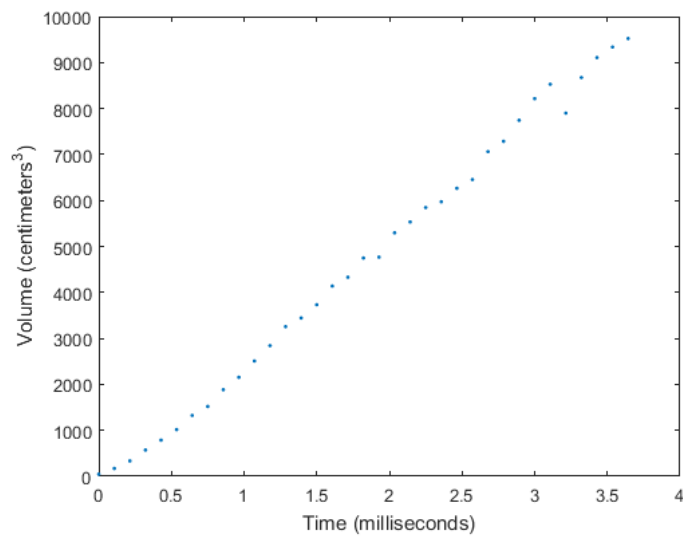


Figure D.3. Volume plot resulting from extrapolated images shown in Figs. D.30 through D.41.

### D.1 Extrapolated Cavity Volume Imagery Data for the 1,200 m/s impact velocity



(a) 0.0 *ms*



(b) 0.0357 *ms*



(c) 0.1429 *ms*

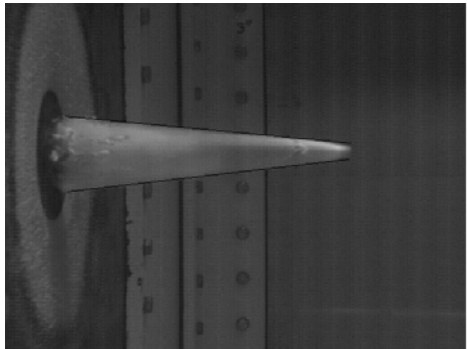
Figure D.4. Extrapolated cavity images for 1,200 *m/s* impact velocity for 0.0 to 0.1429 *ms* after impact.



(a) 0.2500 *ms*

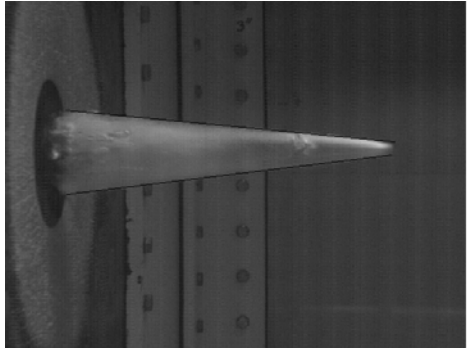


(b) 0.3571 *ms*

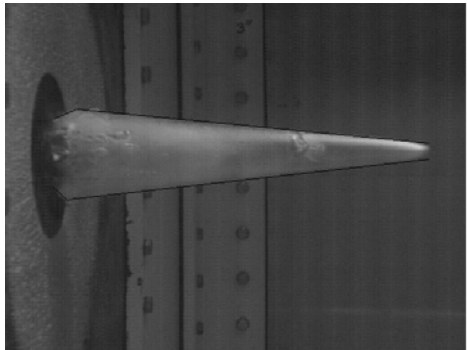


(c) 0.4643 *ms*

Figure D.5. Extrapolated cavity images for 1,200 *m/s* impact velocity for 0.2500 to 0.4643 *ms* after impact.



(a) 0.5714 *ms*

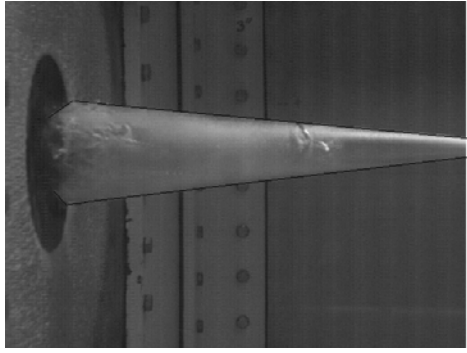


(b) 0.6786 *ms*

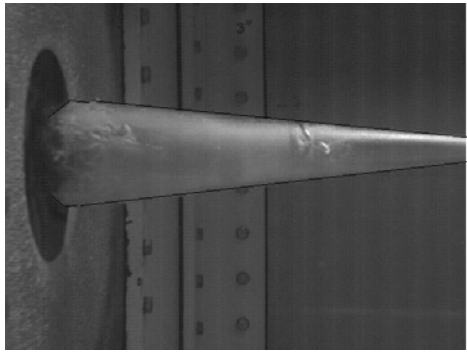


(c) 0.7857 *ms*

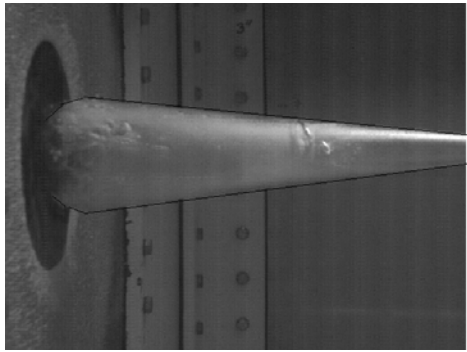
Figure D.6. Extrapolated cavity images for 1,200 *m/s* impact velocity for 0.5714 to 0.7857 *ms* after impact.



(a) 0.8929 *ms*



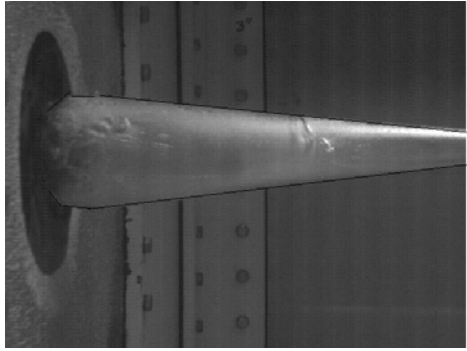
(b) 1.0000 *ms*



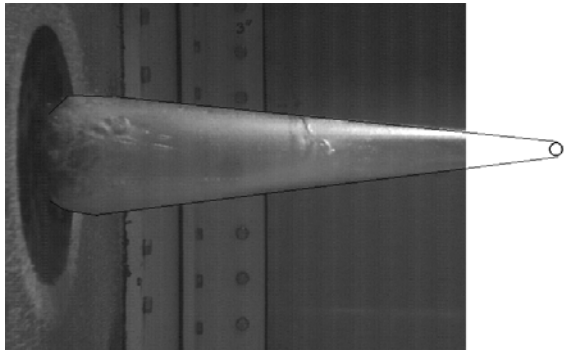
(c) 1.1071 *ms*

Figure D.7. Extrapolated cavity images for 1,200 *m/s* impact velocity for 0.8929 to 1.1071 *ms* after impact.

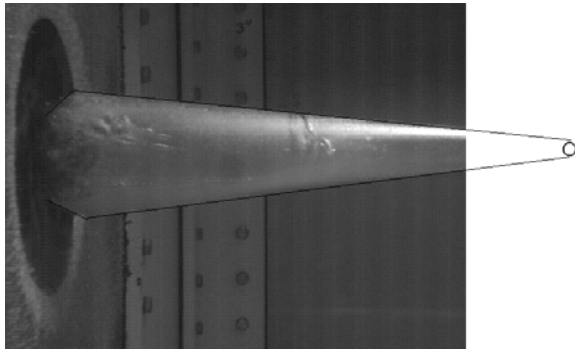




(a) 1.2143 *ms*

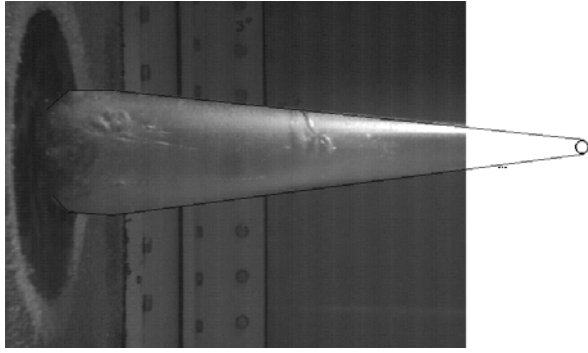


(b) 1.3214 *ms*

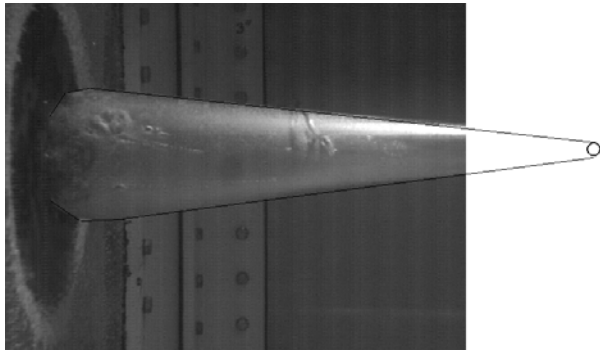


(c) 1.4286 *ms*

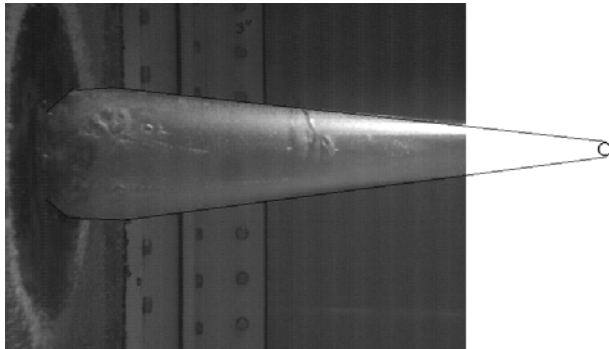
Figure D.8. Extrapolated cavity images for 1,200 *m/s* impact velocity for 1.2143 to 1.4286 *ms* after impact.



(a) 1.5357 *ms*

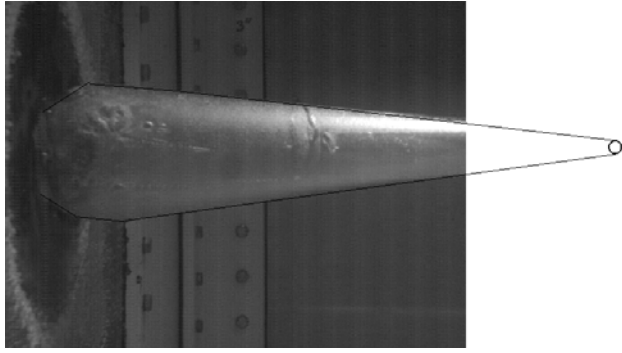


(b) 1.6429 *ms*

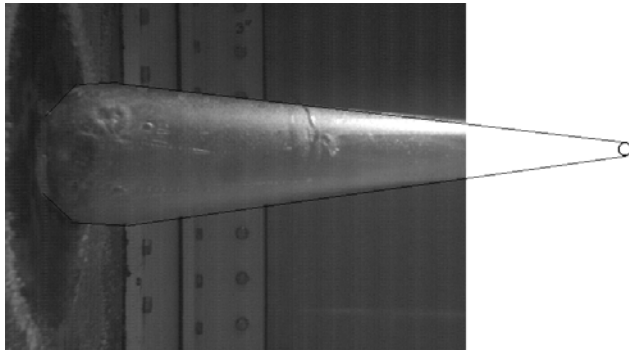


(c) 1.7500 *ms*

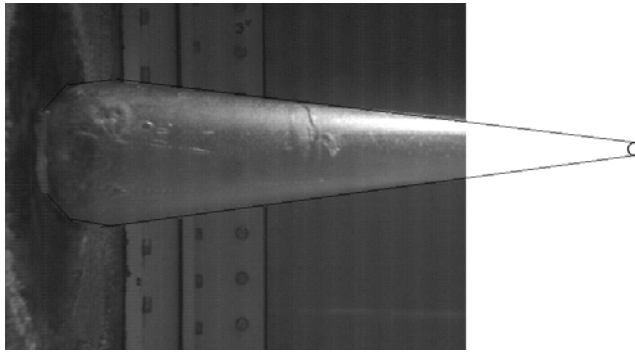
Figure D.9. Extrapolated cavity images for 1,200 *m/s* impact velocity for 1.5357 to 1.7500 *ms* after impact.



(a) 1.8571 *ms*

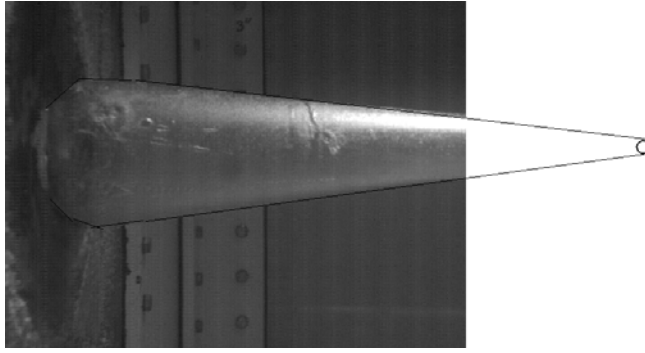


(b) 1.9643 *ms*

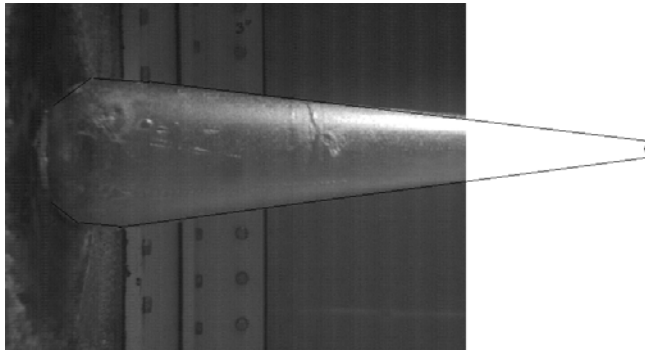


(c) 2.0714 *ms*

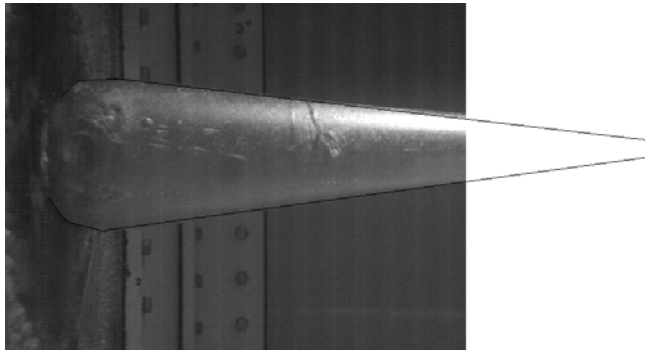
Figure D.10. Raw cavity images for 1,200 *m/s* impact velocity for 1.8571 to 2.3929 *ms* after impact.



(a) 2.1786 *ms*

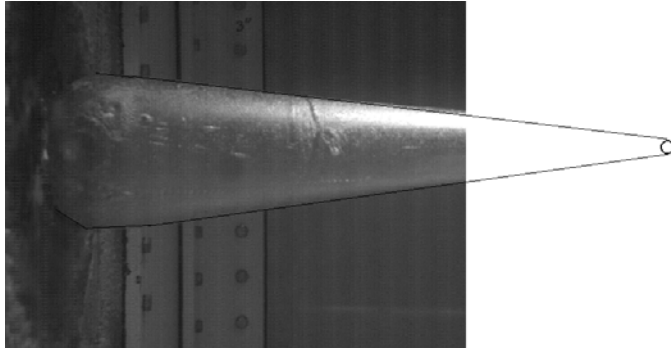


(b) 2.2857 *ms*

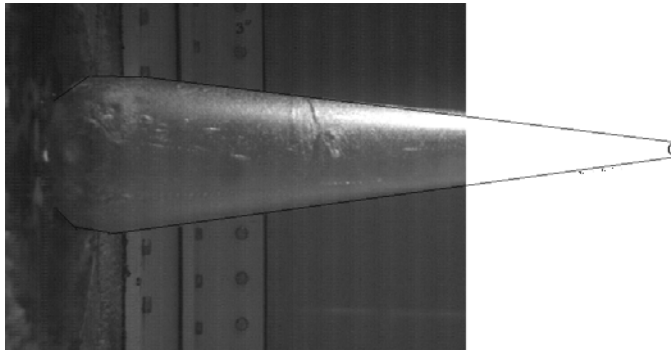


(c) 2.3929 *ms*

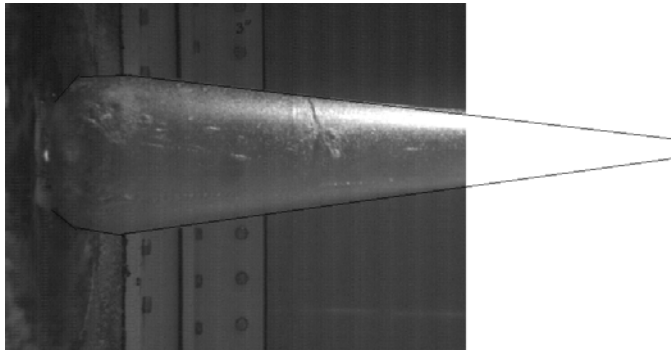
Figure D.11. Raw cavity images for 1,200 *m/s* impact velocity for 2.1786 to 2.3929 *ms* after impact.



(a) 2.5000 *ms*

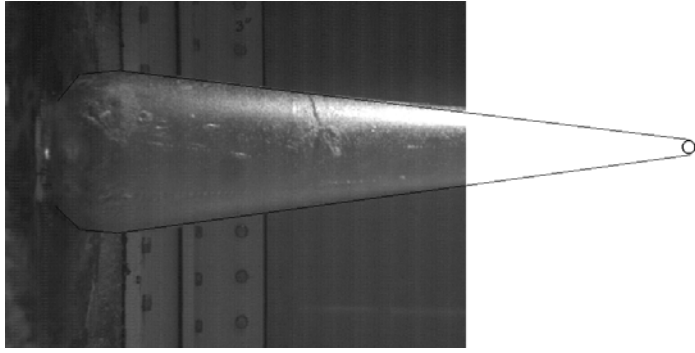


(b) 2.6071 *ms*

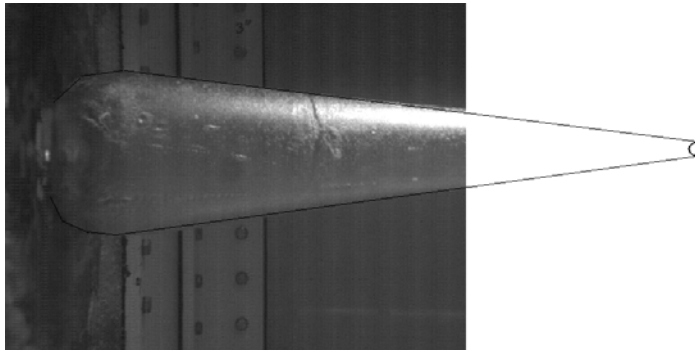


(c) 2.7143 *ms*

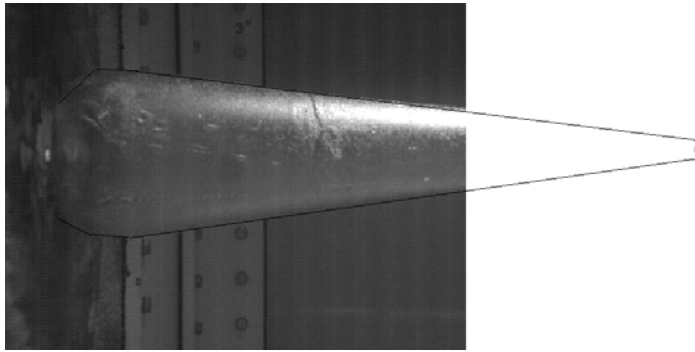
Figure D.12. Raw cavity images for 1,200 *m/s* impact velocity for 2.5000 to 3.0357 *ms* after impact.



(a) 2.8214 *ms*

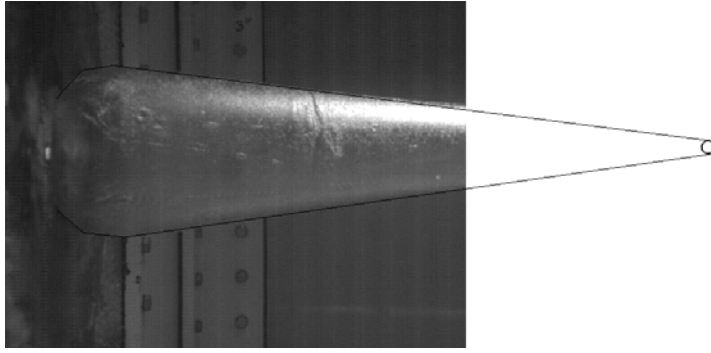


(b) 2.9286 *ms*

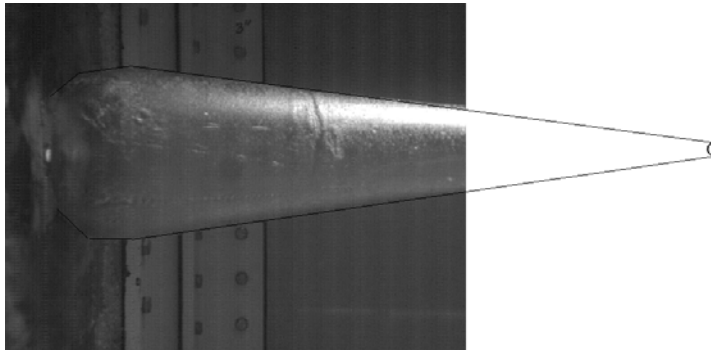


(c) 3.0357 *ms*

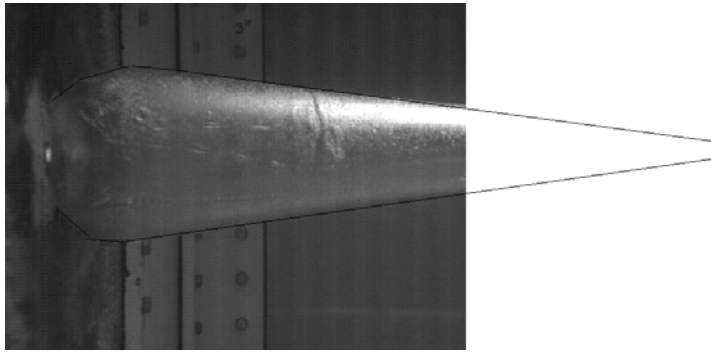
Figure D.13. Raw cavity images for 1,200 *m/s* impact velocity for 2.5000 to 3.0357 *ms* after impact.



(a) 3.1429 *ms*

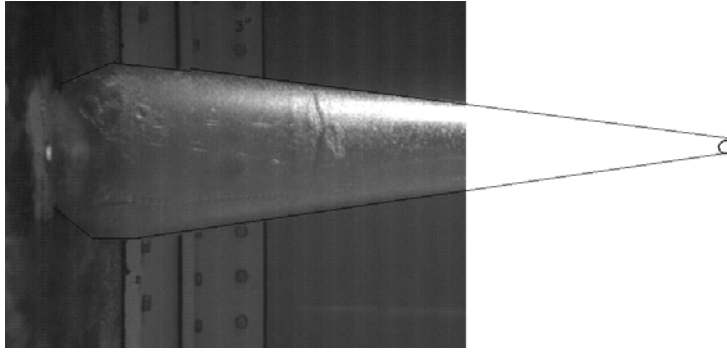


(b) 3.2500 *ms*

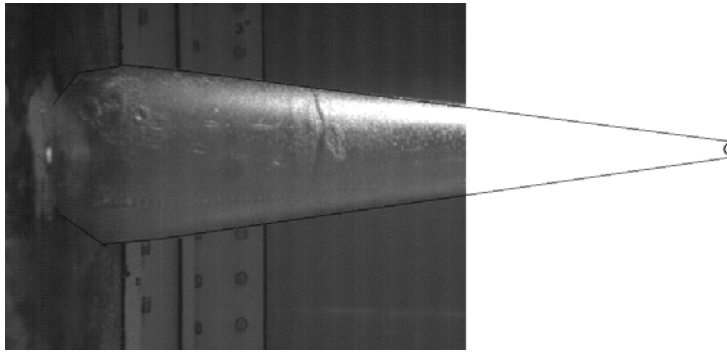


(c) 3.3571 *ms*

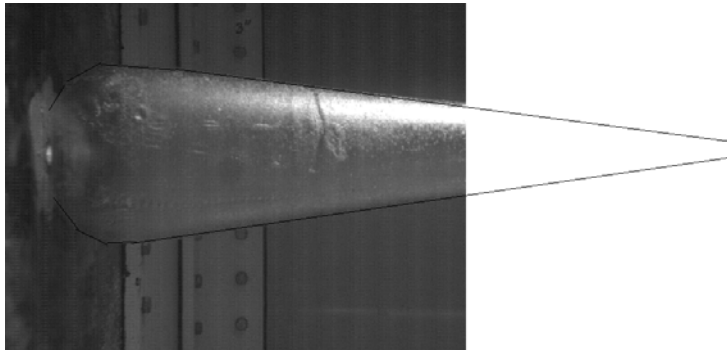
Figure D.14. Raw cavity images for 1,200 *m/s* impact velocity for 3.1429 to 3.6786 *ms* after impact.



(a) 3.4643 *ms*



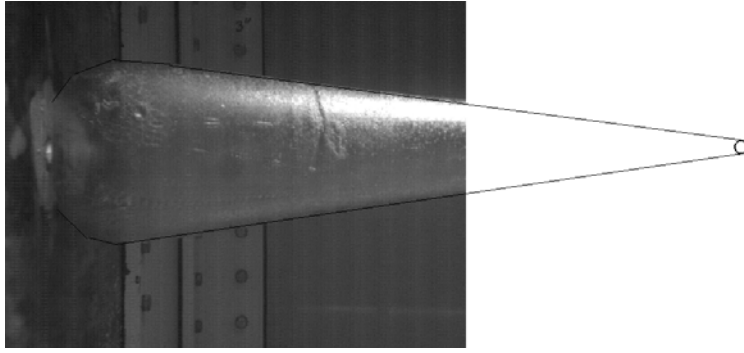
(b) 3.5714 *ms*



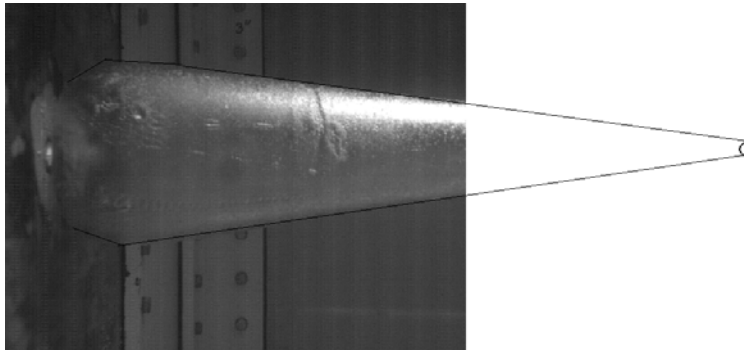
(c) 3.6786 *ms*

Figure D.15. Raw cavity images for 1,200 *m/s* impact velocity for 3.1429 to 3.6786 *ms* after impact.





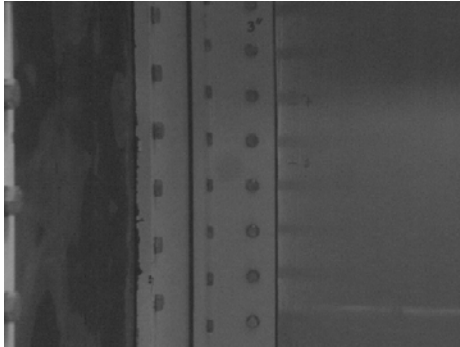
(a) 3.7857 *ms*



(b) 3.8929 *ms*

Figure D.16. Raw cavity images for 1,200 *m/s* impact velocity for 3.7857 to 3.8929 *ms* after impact.

## D.2 Extrapolated Cavity Volume Imagery Data for the 1,495 m/s impact velocity



(a) 0.0 *ms*

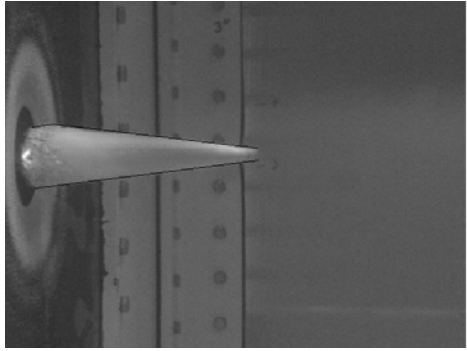


(b) 0.0357 *ms*

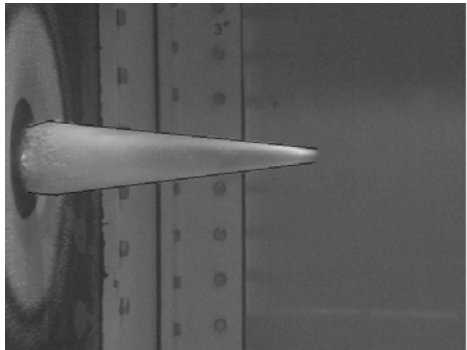


(c) 0.1429 *ms*

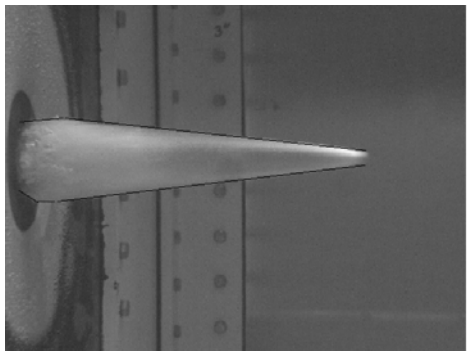
Figure D.17. Extrapolated cavity images for 1,485 *m/s* impact velocity for 0.0 to 0.1429 *ms* after impact.



(a) 0.2500 *ms*

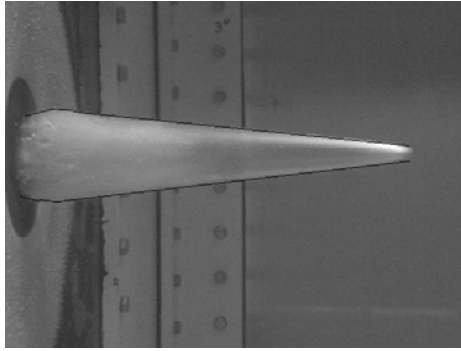


(b) 0.3571 *ms*

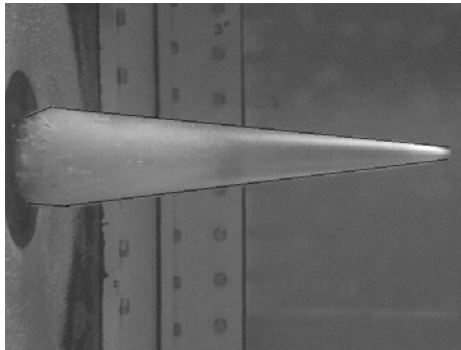


(c) 0.4643 *ms*

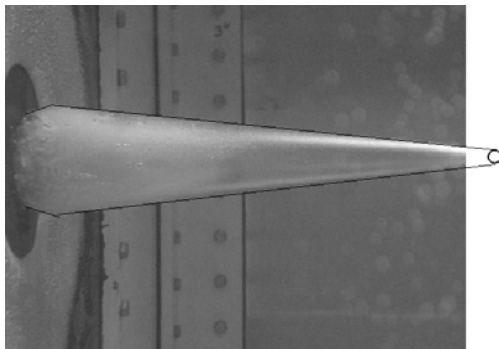
Figure D.18. Extrapolated cavity images for 1,485 *m/s* impact velocity for 0.2500 to 0.4643 *ms* after impact.



(a) 0.5714 *ms*

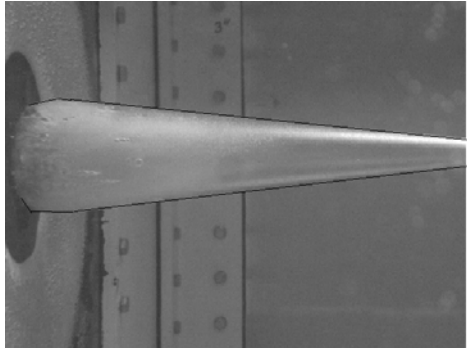


(b) 0.6786 *ms*

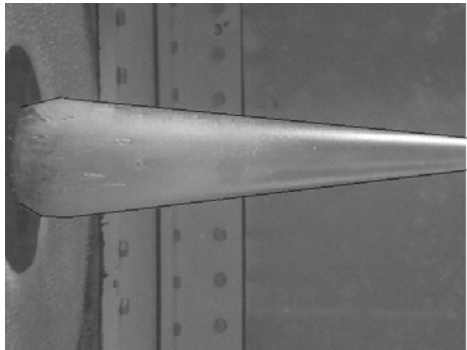


(c) 0.7857 *ms*

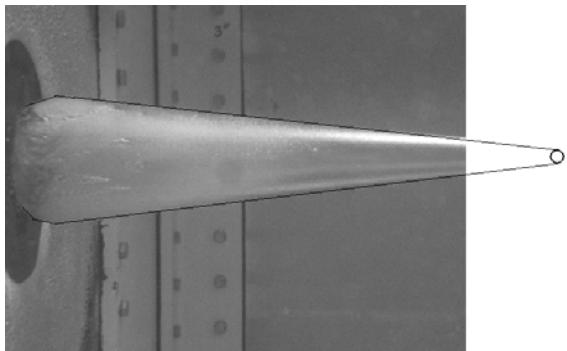
Figure D.19. Extrapolated cavity images for 1,485 *m/s* impact velocity for 0.5714 to 0.7857 *ms* after impact.



(a) 0.8929 *ms*

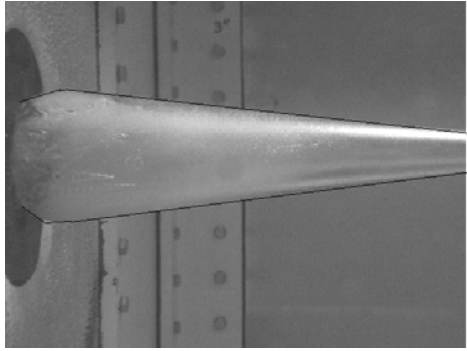


(b) 1.0000 *ms*

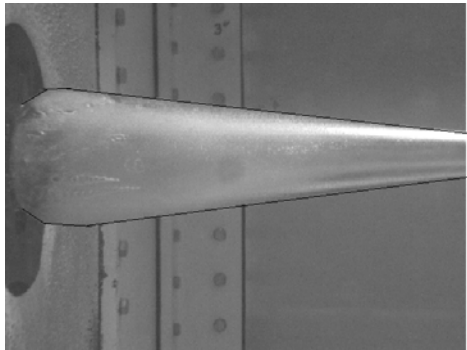


(c) 1.1071 *ms*

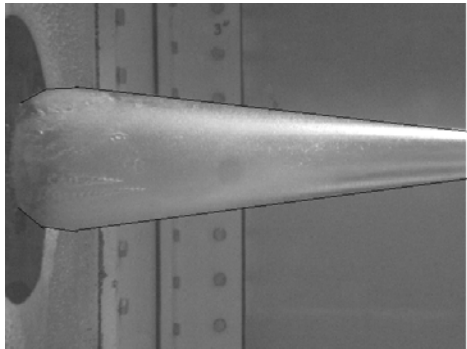
Figure D.20. Extrapolated cavity images for 1,485 *m/s* impact velocity for 0.8929 to 1.1071 *ms* after impact.



(a) 1.2143 *ms*

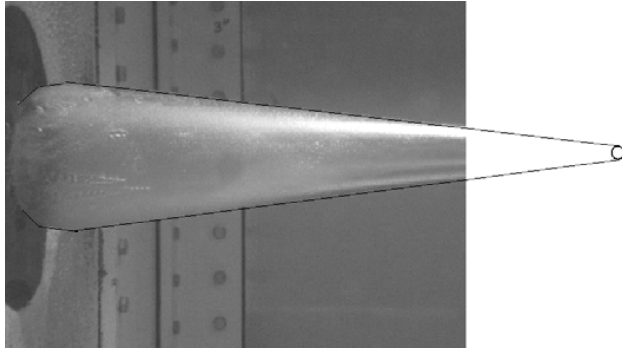


(b) 1.3214 *ms*

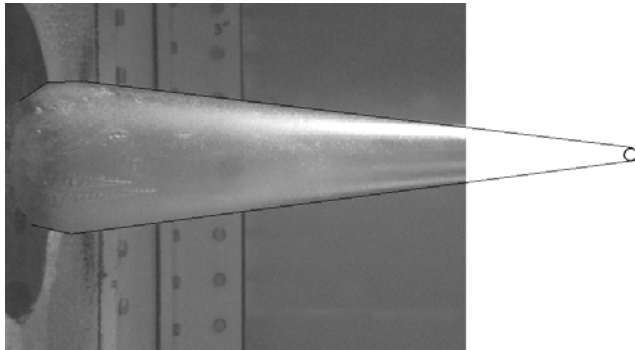


(c) 1.4286 *ms*

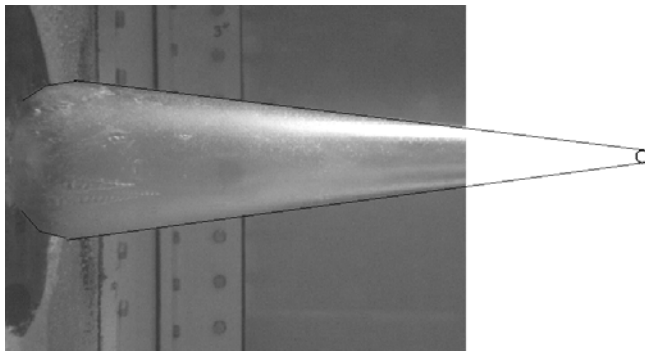
Figure D.21. Extrapolated cavity images for 1,485 *m/s* impact velocity for 1.2143 to 1.4286 *ms* after impact.



(a) 1.5357 *ms*

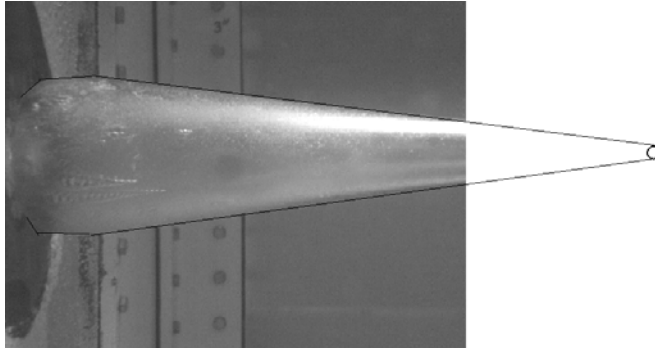


(b) 1.6429 *ms*

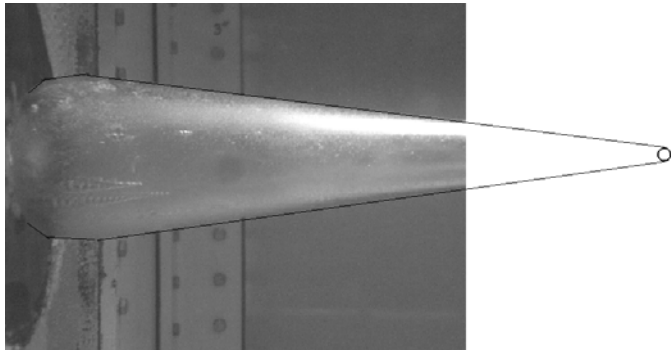


(c) 1.7500 *ms*

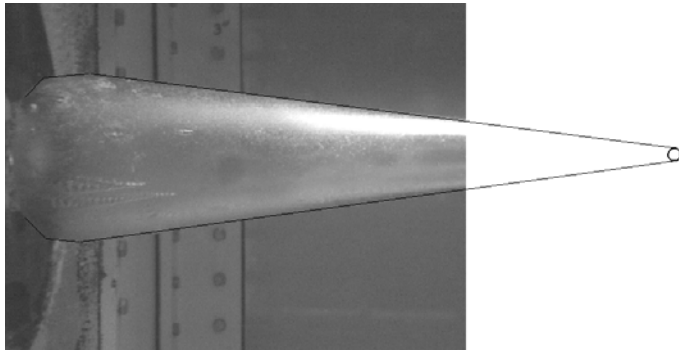
Figure D.22. Extrapolated cavity images for 1,485 *m/s* impact velocity for 1.5357 to 1.7500 *ms* after impact.



(a) 1.8571 *ms*



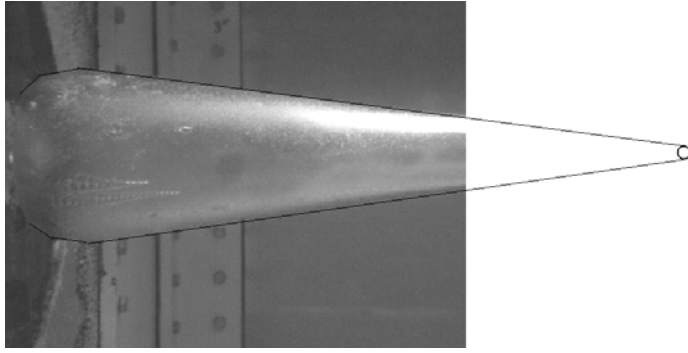
(b) 1.9643 *ms*



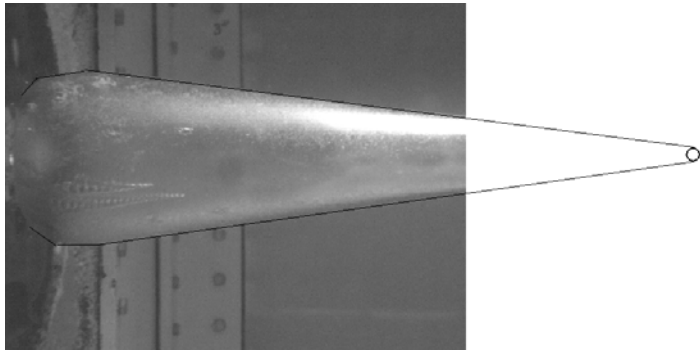
(c) 2.0714 *ms*

Figure D.23. Raw cavity images for 1,485 *m/s* impact velocity for 1.8571 to 2.0714 *ms* after impact.

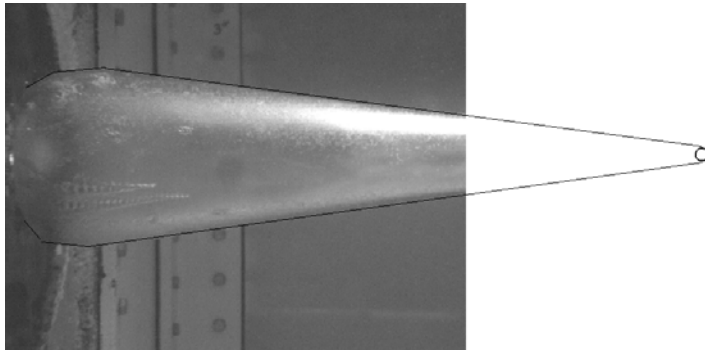




(a) 2.1786 *ms*

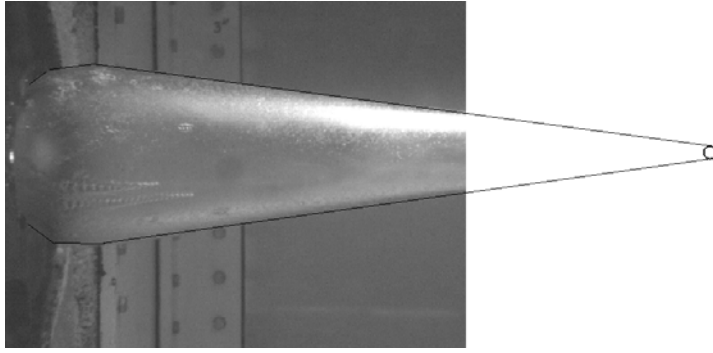


(b) 2.2857 *ms*

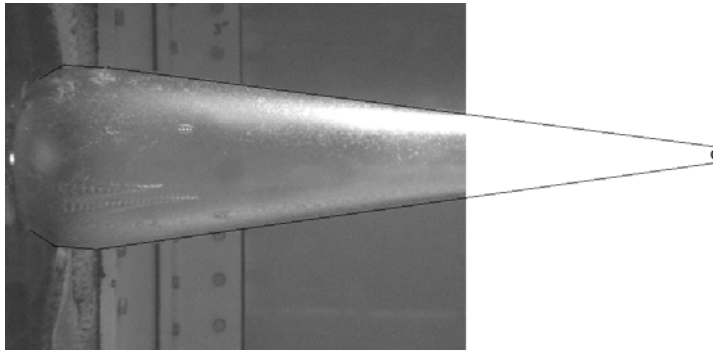


(c) 2.3929 *ms*

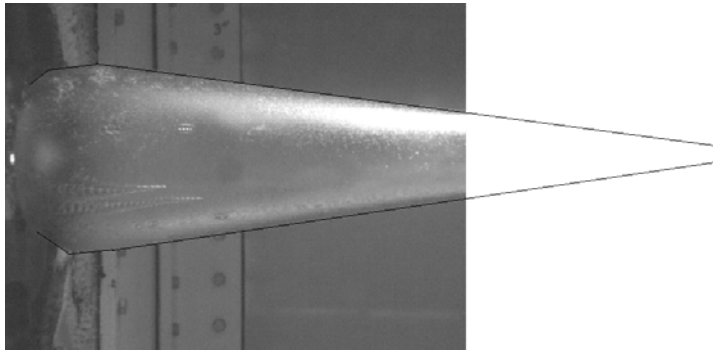
Figure D.24. Raw cavity images for 1,485 *m/s* impact velocity for 1.8571 to 2.3929 *ms* after impact.



(a) 2.5000 *ms*

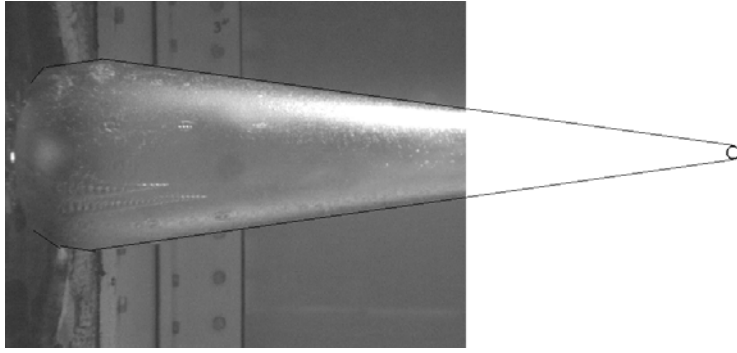


(b) 2.6071 *ms*

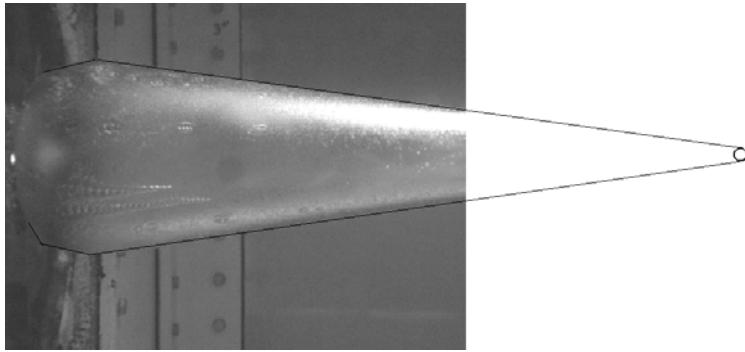


(c) 2.7143 *ms*

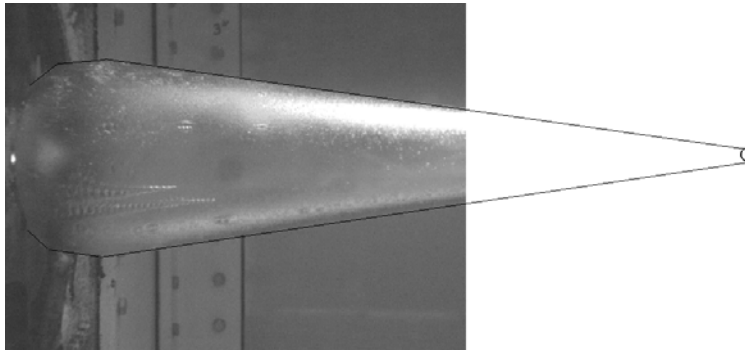
Figure D.25. Raw cavity images for 1,485 *m/s* impact velocity for 2.5000 to 2.7143 *ms* after impact.



(a) 2.8214 *ms*

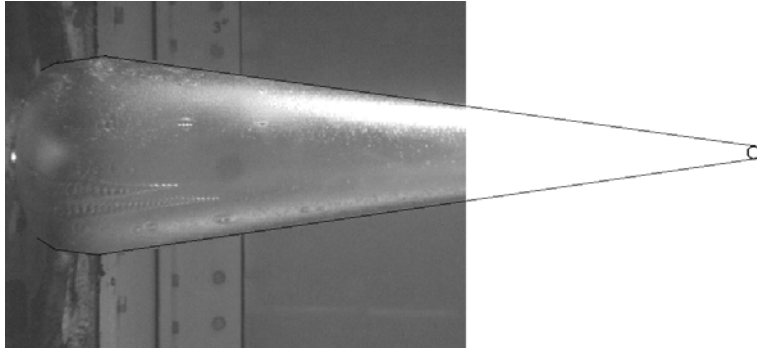


(b) 2.9286 *ms*

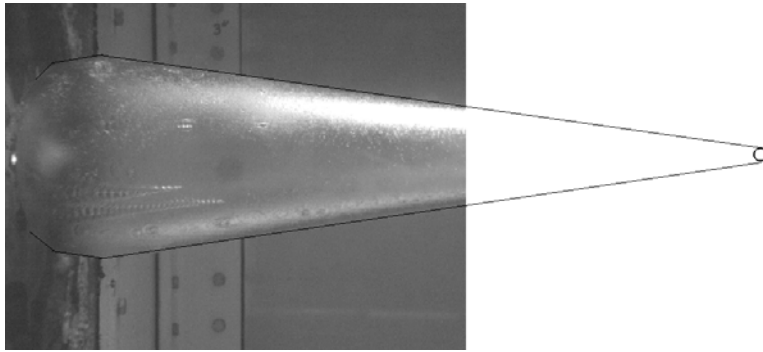


(c) 3.0357 *ms*

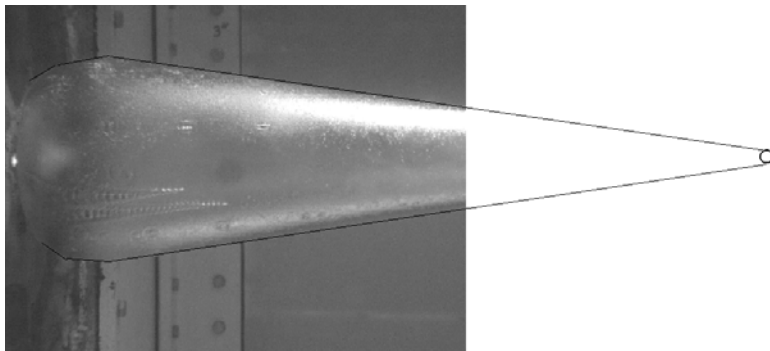
Figure D.26. Raw cavity images for 1,485 *m/s* impact velocity for 2.8214 to 3.0357 *ms* after impact.



(a) 3.1429 *ms*

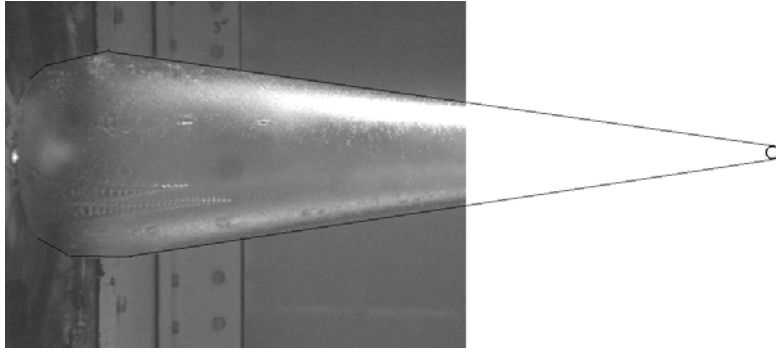


(b) 3.2500 *ms*

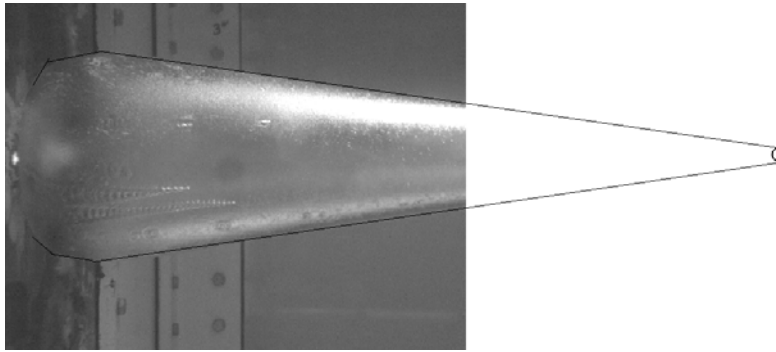


(c) 3.3571 *ms*

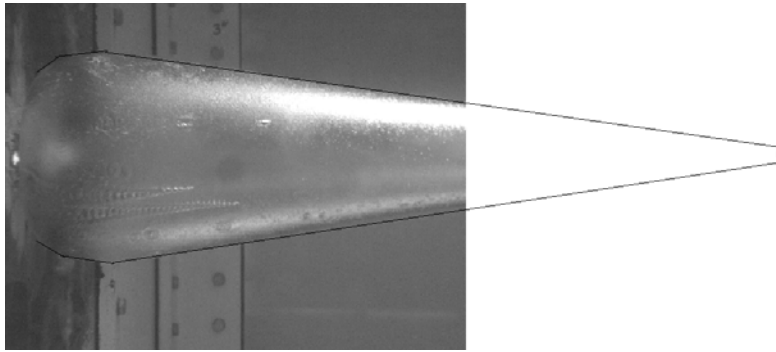
Figure D.27. Raw cavity images for 1,485 *m/s* impact velocity for 3.1429 to 3.3571 *ms* after impact.



(a) 3.4643 *ms*

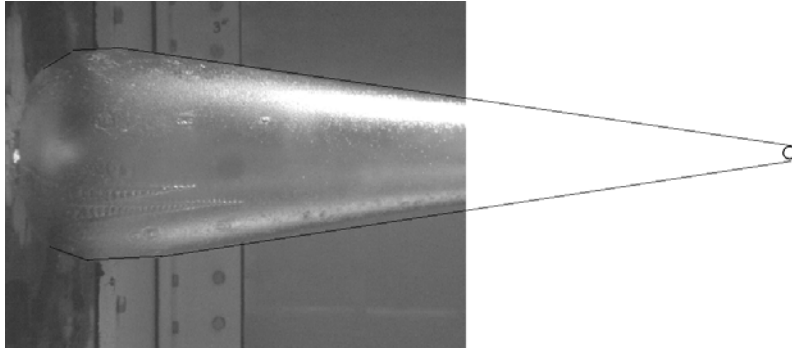


(b) 3.5714 *ms*

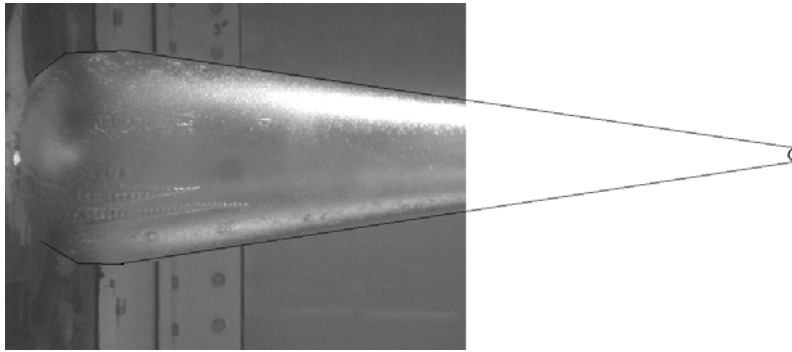


(c) 3.6786 *ms*

Figure D.28. Raw cavity images for 1,485 *m/s* impact velocity for 3.4643 to 3.6786 *ms* after impact.



(a) 3.7857 *ms*



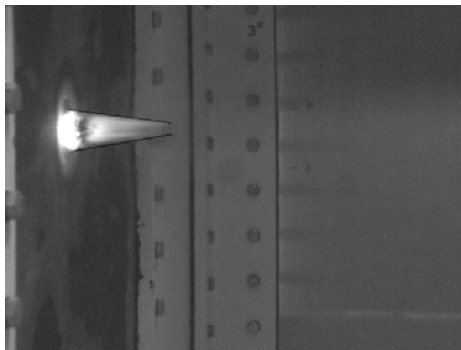
(b) 3.8929 *ms*

Figure D.29. Raw cavity images for 1,485 *m/s* impact velocity for 3.7857 to 3.8929 *ms* after impact.

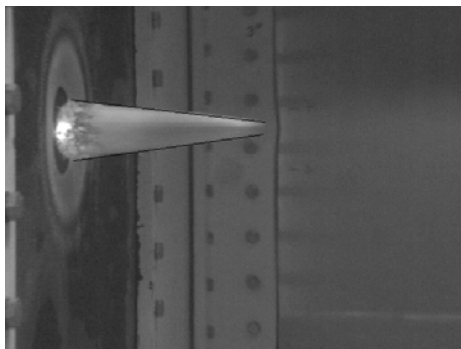
### D.3 Extrapolated Cavity Volume Imagery Data for the 1,800 m/s impact velocity



(a) 0.0 *ms*



(b) 0.0357 *ms*



(c) 0.1429 *ms*

Figure D.30. Extrapolated cavity images for 1,800 *m/s* impact velocity for 0.0 to 0.1429 *ms* after impact.



(a) 0.2500 *ms*



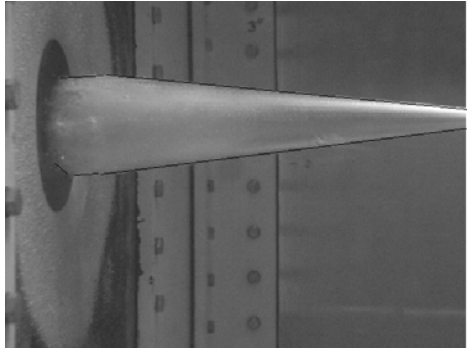
(b) 0.3571 *ms*



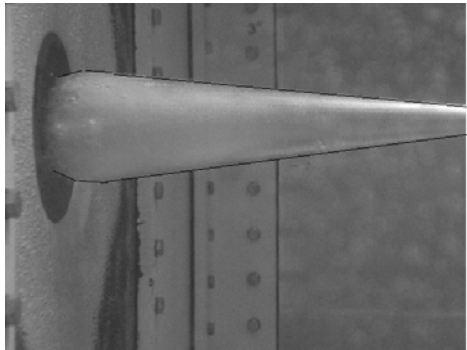
(c) 0.4643 *ms*

Figure D.31. Extrapolated cavity images for 1,800 *m/s* impact velocity for 0.2500 to 0.4643 *ms* after impact.

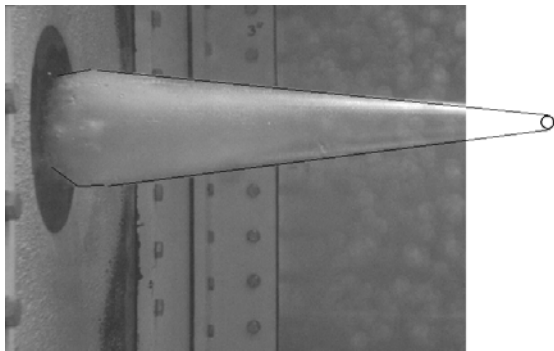




(a) 0.5714 *ms*

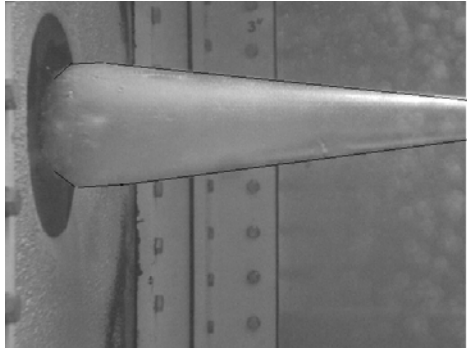


(b) 0.6786 *ms*

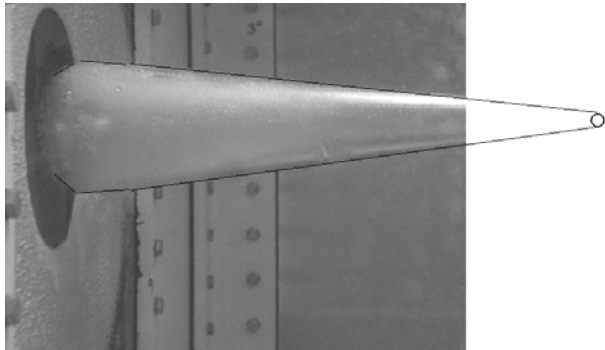


(c) 0.7857 *ms*

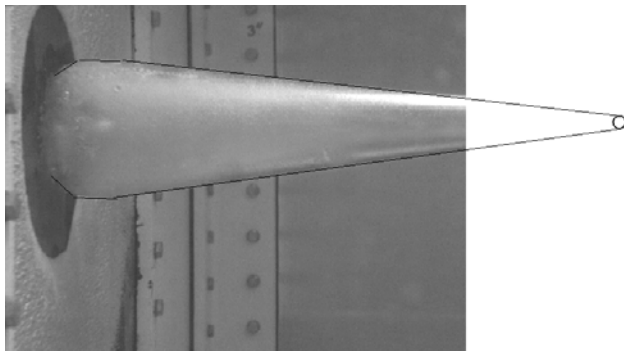
Figure D.32. Extrapolated cavity images for 1,800 *m/s* impact velocity for 0.5714 to 0.7857 *ms* after impact.



(a) 0.8929 *ms*

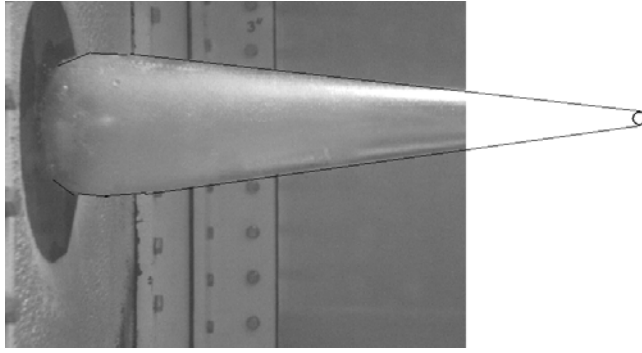


(b) 1.0000 *ms*

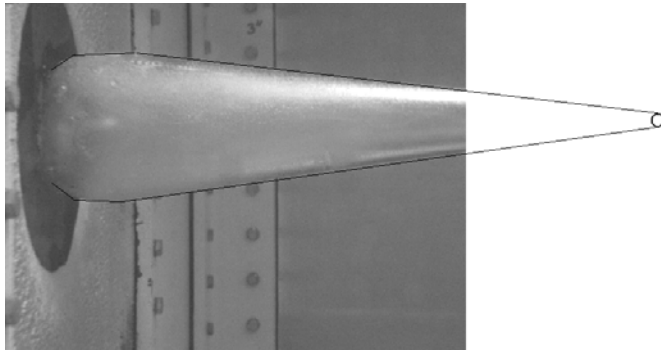


(c) 1.1071 *ms*

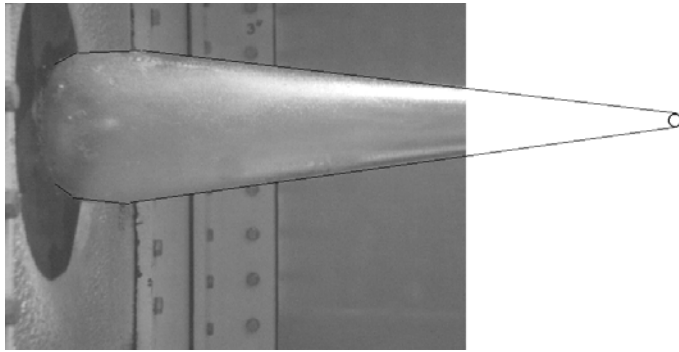
Figure D.33. Extrapolated cavity images for 1,800 *m/s* impact velocity for 0.8929 to 1.1071 *ms* after impact.



(a) 1.2143 *ms*

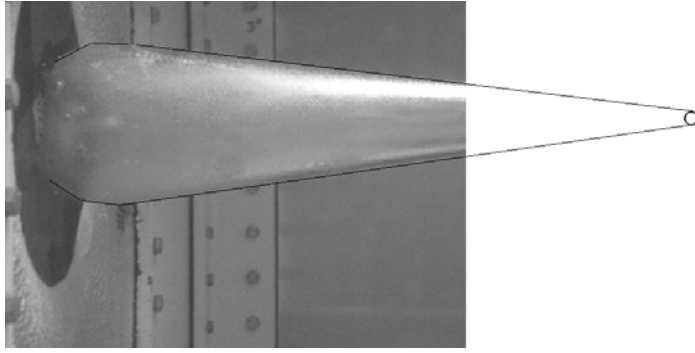


(b) 1.3214 *ms*

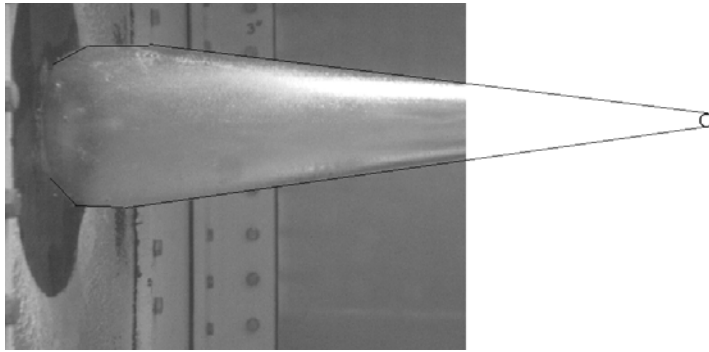


(c) 1.4286 *ms*

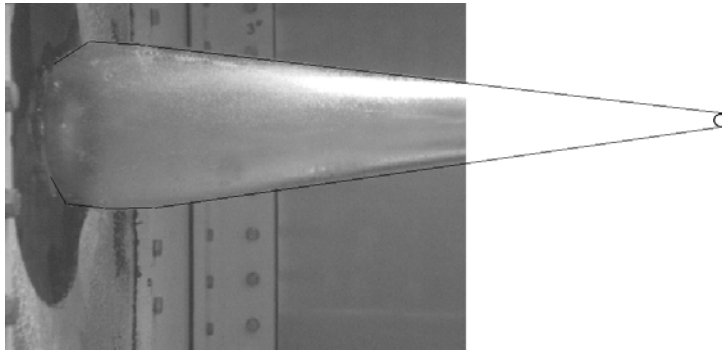
Figure D.34. Extrapolated cavity images for 1,800 *m/s* impact velocity for 1.2143 to 1.4286 *ms* after impact.



(a) 1.5357 *ms*

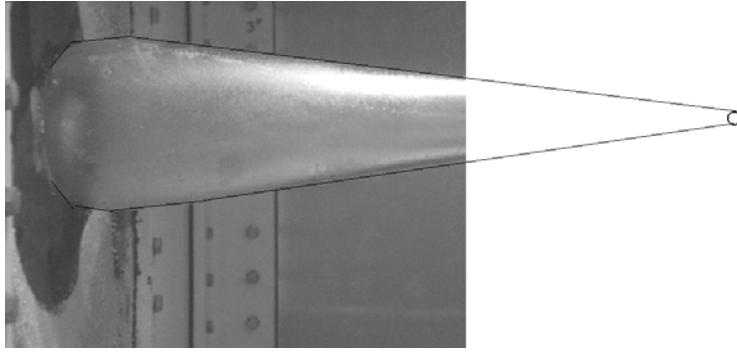


(b) 1.6429 *ms*

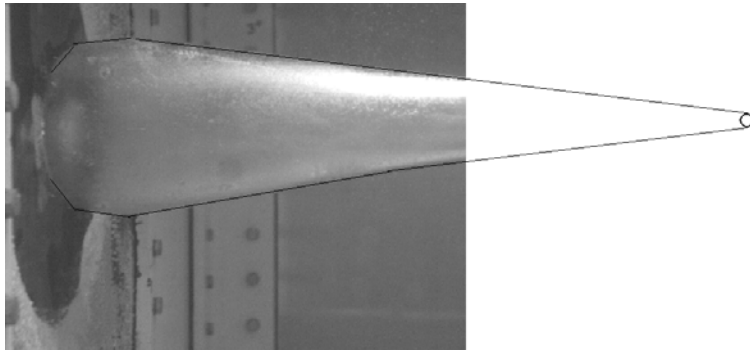


(c) 1.7500 *ms*

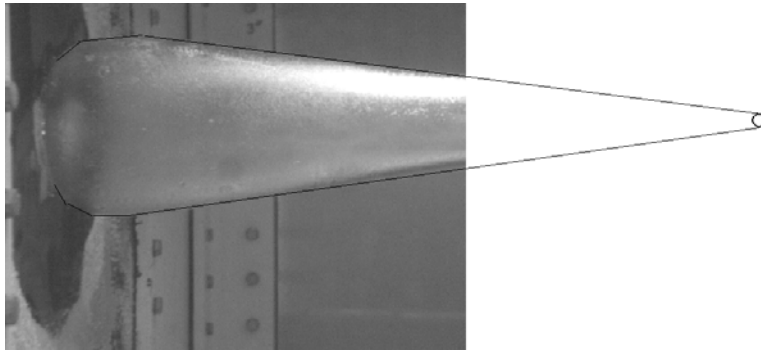
Figure D.35. Extrapolated cavity images for 1,800 *m/s* impact velocity for 1.5357 to 1.7500 *ms* after impact.



(a) 1.8571 *ms*

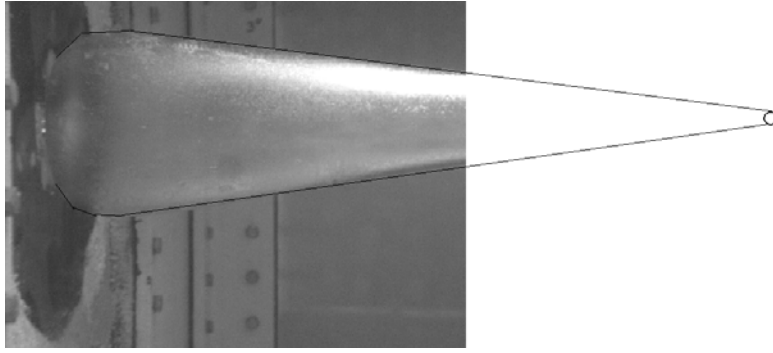


(b) 1.9643 *ms*

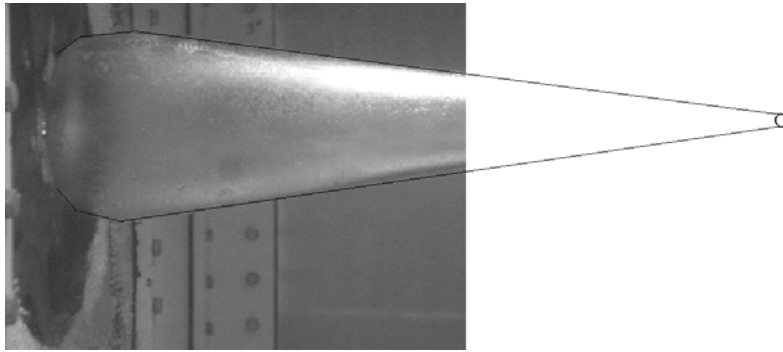


(c) 2.0714 *ms*

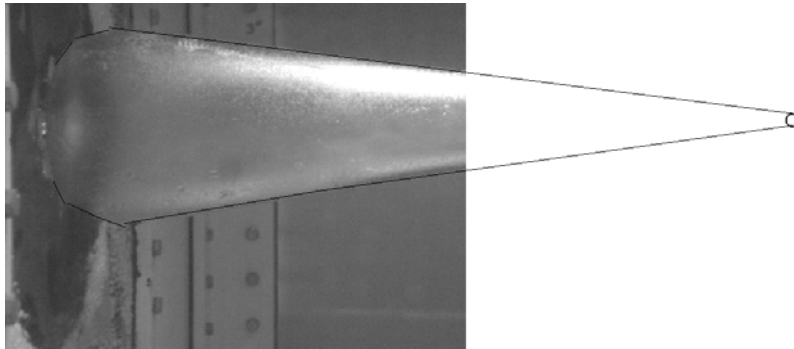
Figure D.36. Raw cavity images for 1,800 *m/s* impact velocity for 1.8571 to 2.0714 *ms* after impact.



(a) 2.1786 *ms*

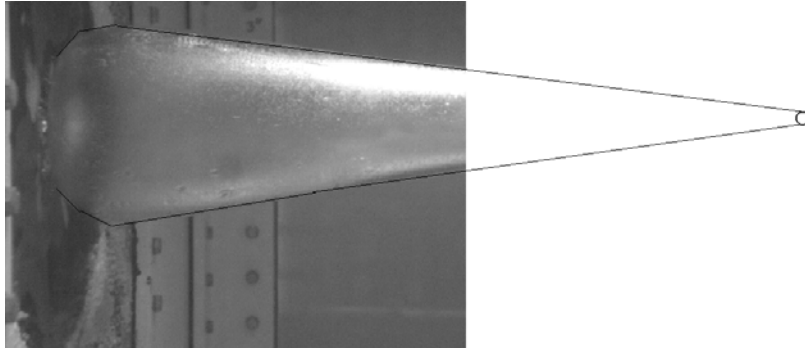


(b) 2.2857 *ms*

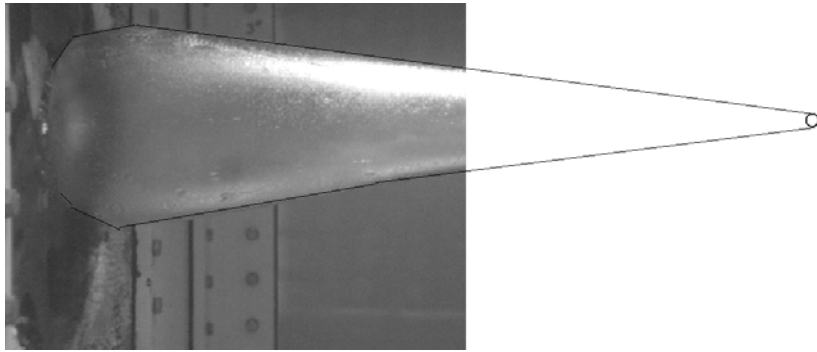


(c) 2.3929 *ms*

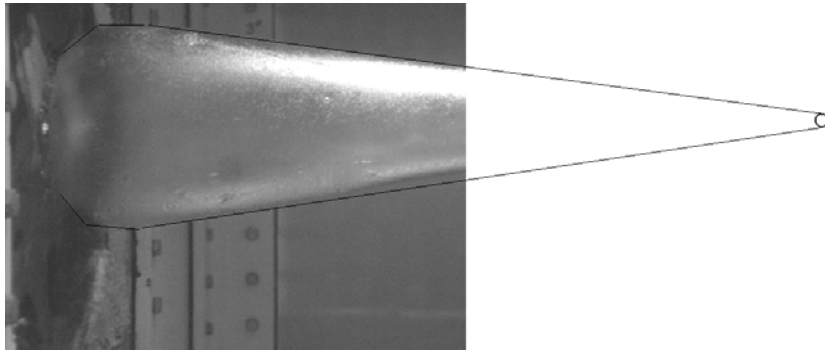
Figure D.37. Raw cavity images for 1,800 *m/s* impact velocity for 1.1786 to 2.3929 *ms* after impact.



(a) 2.5000 *ms*

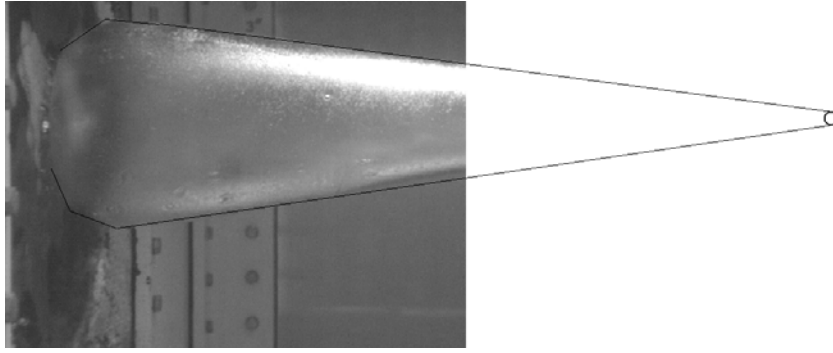


(b) 2.6071 *ms*

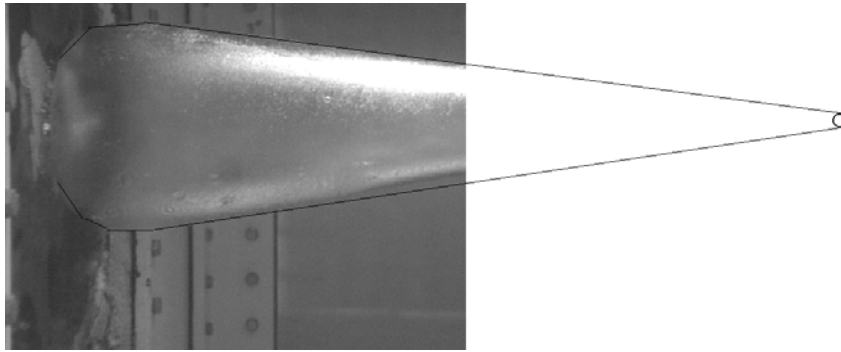


(c) 2.7143 *ms*

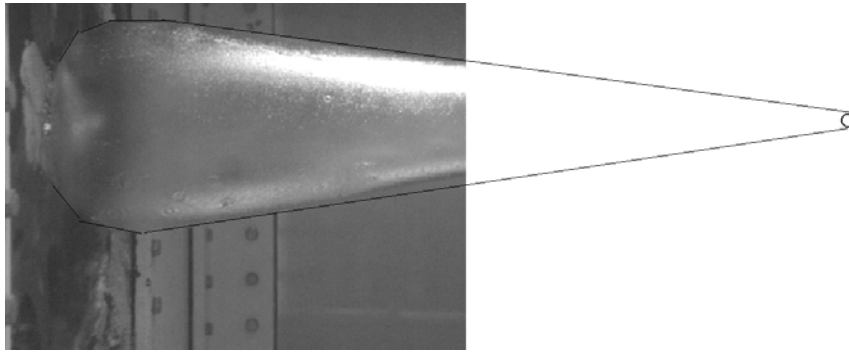
Figure D.38. Raw cavity images for 1,800 *m/s* impact velocity for 2.5000 to 2.7143 *ms* after impact.



(a) 2.8214 *ms*



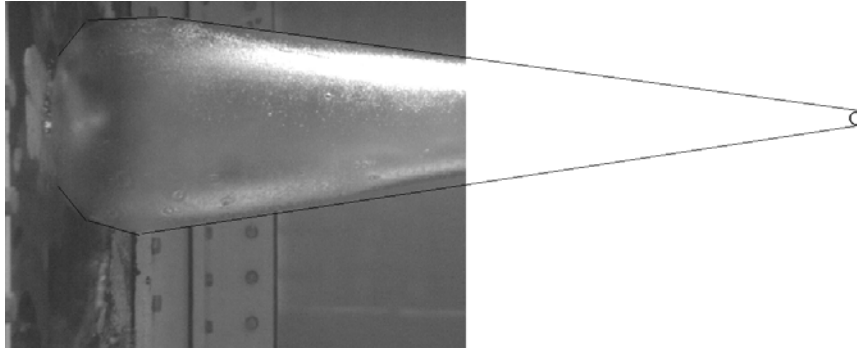
(b) 2.9286 *ms*



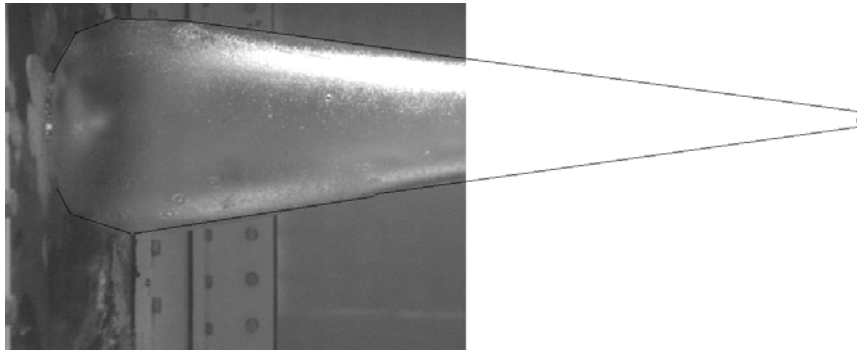
(c) 3.0357 *ms*

Figure D.39. Raw cavity images for 1,800 *m/s* impact velocity for 2.8214 to 3.0357 *ms* after impact.

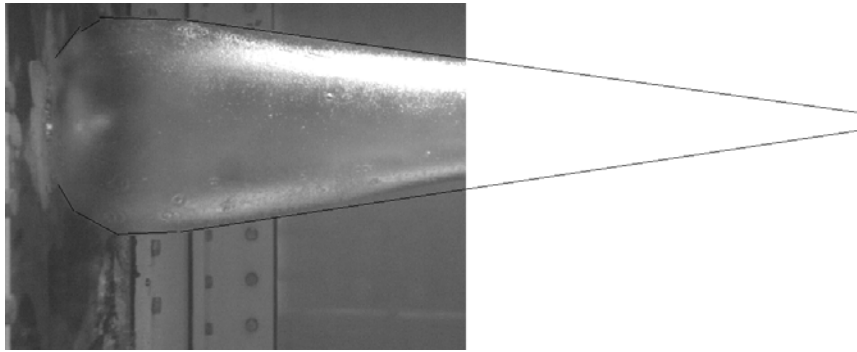




(a) 3.1429 *ms*

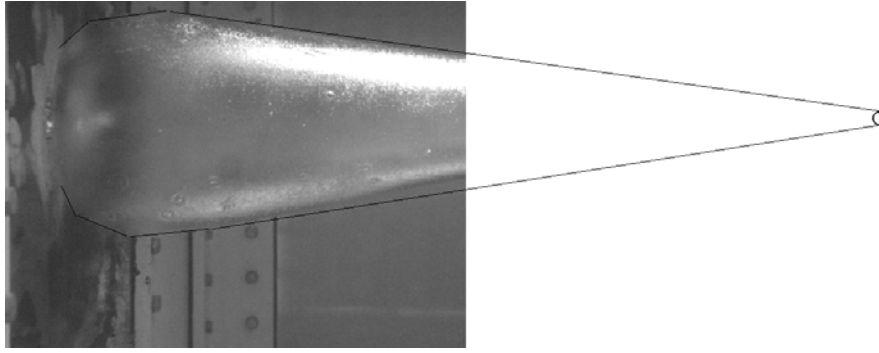


(b) 3.2500 *ms*

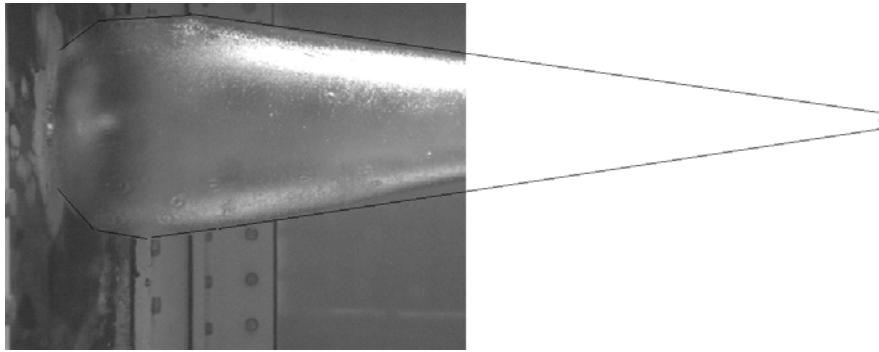


(c) 3.3571 *ms*

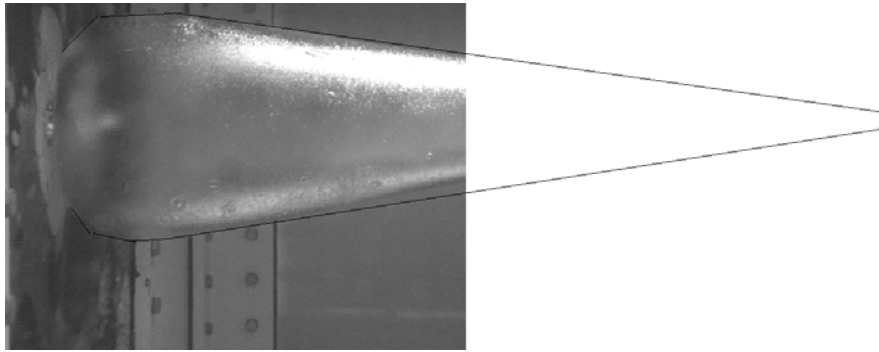
Figure D.40. Raw cavity images for 1,800 *m/s* impact velocity for 3.1429 to 3.3571 *ms* after impact.



(a) 3.4643 *ms*



(b) 3.5714 *ms*



(c) 3.6786 *ms*

Figure D.41. Raw cavity images for 1,800 *m/s* impact velocity for 3.4643 to 3.6786 *ms* after impact.

## Bibliography

- [1] Disimile, P. J., Davis, J. M., and Pyles, J. M., “Qualitative Assessment of a Transient Spray Caused by a Hydrodynamic Ram Event,” *Journal of Flow Visualization and Image Processing*, Vol. 14, No. 3, 2007, pp. 287–303.
- [2] O’Connell, P. J., “Dry Bay Fire Test and Evaluation For Representative Large Commercial Aircraft,” Tech. rep., 46th Test Group, 2012.
- [3] Yang, H. Q., Disimile, P. J., and Czarnecki, G. J., “A Multiphase and Multiphysics CFD Technique for Fuel Spurt Prediction with Cavitation and Fluid-Structure Interaction,” *22nd AIAA Computational Fluid Dynamics Conference*, 2015, p. 3419.
- [4] Ball, R. E., *The Fundamentals of Aircraft Combat Survivability Analysis*, American Institute of Aeronautics and Astronautics, Inc., second edition ed., 2003.
- [5] Disimile, P. J., Swanson, L. A., and Toy, N., “The Hydrodynamic Ram Pressure Generated by Spherical Projectiles,” *International Journal of Impact Engineering*, Vol. 36, No. 6, 2009, pp. 821–829.
- [6] Lecysyn, N., Bony-Dandrieux, A., Aprin, L., Heymes, F., Slangen, P., Dusserre, G., Munier, L., and Gallic, C. L., “Experimental study of hydraulic ram effects on a liquid storage tank: Analysis of overpressure and cavitation induced by a high-speed projectile,” *Journal of Hazardous Materials*, Vol. 178.1, 2010, pp. 635 – 643.
- [7] Guo, Z., Zhang, W., and Wang, C., “Experimental and Theoretical Study on the High-Speed Horizontal Water Entry Behaviors of Cylindrical Projectiles,” *Journal of Hydrodynamics, Ser. B*, Vol. 24, No. 2, 2012, pp. 217 – 225.
- [8] Guo, Z., Zhang, W., Xiao, X., Wei, G., and Ren, P., “An Investigation into Horizontal Water Entry Behaviors of Projectiles with Different Nose Shapes,” *International Journal of Impact Engineering*, Vol. 49, No. 0, 2012, pp. 43 – 60.
- [9] Varas, D., Z. R. L.-P. J., “Numerical Modelling of the Hydrodynamic Ram Phenomenon,” *International Journal of Impact Engineering*, Vol. 36, 2009, pp. 363–374.
- [10] Varas, D., Zaera, R., and Lpez-Puente, J., “Numerical Modelling of Partially Filled Aircraft Fuel Tanks Submitted to Hydrodynamic Ram,” *Aerospace Science and Technology*, Vol. 16, No. 1, 2012, pp. 19 – 28.
- [11] Bureau d’Enquetes et d’Analysis Translated: Office of Investigations and Analysis, “Accident to the Concorde registered F-BTSC operated by Air France occurred on 07/25/00 at Gonesse: Final Report f-sc000725 1/16/2002,” Tech. rep., 2002.

- [12] Campbell, I. and Hilborne, D., “Air Entrainment Behind Artificially Inflated Cavities,” *Proceedings of the Second Symposium on Naval Hydrodynamics*, 1958.
- [13] Hoerner, S. F., *Fluid Dynamic Drag*, Hoerner Fluid Dynamics, 1965.
- [14] May, A., “Water Entry and the Cavity-Running Behavior of Missiles,” Tech. rep., DTIC Document, 1975.
- [15] Cardea, G. C., *The Cavitation Phase of Hydraulic Ram Described by Equations Derived for Underwater Explosions*, Master’s thesis, Air Force Institute of Technology, 2950 Hobson Way, WPAFB OH, 45433, 1973.
- [16] Bless, S., “Fuel Tank Survivability for Hydrodynamic Ram Induced by High Velocity Fragments: Part I. Experimental Results and Design Summary,” Tech. rep., DTIC Document, 1979.
- [17] Fourest, T., Laurens, J.-M., Deletombe, E., Dupas, J., and Arrigoni, M., “Confined Rayleigh–Plesset Equation for Hydrodynamic Ram Analysis in Thin-Walled Containers Under Ballistic Impacts,” *Thin-Walled Structures*, Vol. 86, 2015, pp. 67–72.
- [18] May, A., “On the Entry of Missiles into Water,” *NOL NABORD Report 1809*, 1951.
- [19] Hrubec, J. D., “High-speed Imaging of Supercavitating Underwater Projectiles,” *Experiments in Fluids*, Vol. 30, No. 1, 2001, pp. 57–64.
- [20] Lingenfelter, A. J. and Liu, D., “Characterization of Hydrodynamic Ram Cavity Dynamics to Transient Spray,” *57th AIAA/ASCE/AHS/ASC Structures, Structural Dynamics, and Materials Conference*, American Institute of Aeronautics and Astronautics, 2016.
- [21] Lingenfelter, A. J. and Liu, D., “Multidimensional Tensor Array Analysis of Multiphase Flow During a Hydrodynamic Ram Event,” *Accepted to: 9th International Symposium on Cavitation*, Journal of Physics: Conference Series, 2015.
- [22] Prasad, A. K., “Particle Image Velocimetry,” *Current Science*, Vol. 79, No. 1, 2000, pp. 51–60.
- [23] Aristoff, J. M., Truscott, T. T., and Techet, Alexandra H. and Bush, J. W. M., “The Water Entry of Decelerating Spheres,” *Physics of Fluids*, Vol. 22, 2010, pp. 032102–1:032102–8.
- [24] Zhao, C.-G., Wang, C., Wei, Y.-J., and Zhang, X.-S., “An Experimental Study on Characteristics of Cavitation and Ballistics of Axisymmetric Slender Body Underwater Movement,” *Journal of Physics: Conference Series*, Vol. 656, IOP Publishing, 2015, p. 012175.
- [25] Abelson, H., “Pressure Measurements in the Water-Entry Cavity,” *Journal of Fluid Mechanics*, Vol. 44, No. 01, 1970, pp. 129–144.

- [26] Brandner, P., Walker, G., Niekamp, P., and Anderson, B., “An Investigation of Cloud Cavitation about a Sphere,” *16th Australasian Fluid Mechanics Conference (AFMC)*, School of Engineering, The University of Queensland, 2007, pp. 1392–1398.
- [27] Brandner, P., Walker, G., Niekamp, P., and Anderson, B., “An Experimental Investigation of Cloud Cavitation about a Sphere,” *Journal of Fluid Mechanics*, Vol. 656, 2010, pp. 147–176.
- [28] Washio, S., *Recent Developments in Cavitation Mechanisms: A Guide for Scientists and Engineers*, Woodhead Publishing, 2014.
- [29] Varas, D., López-Puente, J., and Zaera, R., “Numerical Analysis of the Hydrodynamic Ram Phenomenon in Aircraft Fuel Tanks,” *AIAA journal*, Vol. 50, No. 7, 2012, pp. 1621–1630.
- [30] Gibson, A. H., *Hydraulics and its Applications*, Constable, 1947.
- [31] Crane, *Flow of Fluids: through valves, fittings, and pipe*, 1977.
- [32] Achenbach, E., “Experiments on the Flow Past Spheres at Very High Reynolds Numbers,” *Journal of Fluid Mechanics*, Vol. 54, No. 03, 1972, pp. 565–575.
- [33] ASME, “Fluid Meters,” *American Society of Mechanical Engineers, Part 1 - 6th Edition*, 1971.
- [34] Settles, G. S., “Schlieren and Shadowgraph Techniques for Fluid Physics Experiments - A Brief Tutorial,” *61st Annual Meeting of the APS Division of Fluid Dynamics*, 2008.
- [35] Settles, G. S., *Schlieren and Shadowgraph Techniques: Visualizing Phenomena in Transparent Media*, Springer, first edition ed., 2001.
- [36] Lingenfelter, A. J. and Liu, D., “Development of Methods for Characterizing Hydrodynamic Ram Cavity Dynamics,” *56th AIAA/ASCE/AHS/ASC Structures, Structural Dynamics, and Materials Conference*, American Institute of Aeronautics and Astronautics, 2015.
- [37] Sobel, I. and Feldman, G., “A 3x3 Isotropic Gradient Operator for Image Processing (1968),” *A talk at the Stanford Artificial Intelligence Project*.
- [38] Weisstein, E., “Tensor,” <http://mathworld.wolfram.com/Tensor.html>, Accessed: 2016-07.
- [39] Schowengerdt, R. A., *Remote sensing: models and methods for image processing*, Academic press, 2006.

- [40] Lingenfelter, A. J. and Liu, D., “Development for Orifice Entrainment Velocity Characterization during a Hydrodynamic Ram Event,” *57th AIAA/ASCE/AHS/ASC Structures, Structural Dynamics, and Materials Conference*, American Institute of Aeronautics and Astronautics, 2016.
- [41] Lingenfelter, A. J., Liu, D., and Reeder, M. F., “Time Resolved Flow Field Measurements of Orifice Entrainment During a Hydrodynamic Ram Event,” *Journal of Visualization*, 2016, pp. 1–12.
- [42] Tropea, C., Yarin, A. L., and Foss, J. F., *Springer Handbook of Experimental Fluid Mechanics*, Vol. 1, Springer Science & Business Media, 2007.
- [43] Clemens, N. T., “Flow Imaging,” *Encyclopedia of Imaging Science and Technology*, 2002.
- [44] Holman, J., *Thermodynamics: Third Edition*, McGraw-Hill, 1980.
- [45] ImageJ, “ImageJ Software Download and Description,” <https://imagej.nih.gov/ij/>, Accessed: 2016-03.
- [46] Stearns, R., Johnson, R., Jackson, R., and Larson, C., *Flow Measurements with Orifice Meters*, D. Van Nostrand company, LTD., 1951.
- [47] Aristoff, J. M. and Bush, J. W., “Water Entry of Small Hydrophobic Spheres,” *Journal of Fluid Mechanics*, Vol. 619, 2009, pp. 45–78.
- [48] Truscott, T. T., Epps, B. P., and Belden, J., “Water Entry of Projectiles,” *Annual Review of Fluid Mechanics*, Vol. 46, 2014, pp. 355–378.
- [49] Anderson, J., *Modern Compressible Flow: With Historical Perspective*, McGraw-Hill series in aeronautical and aerospace engineering, McGraw-Hill, 1990.

## **Vita**

Captain Andrew J. Lingenfelter graduated from Plainview Public Schools in Plainview, Nebraska in May 2004. He entered undergraduate studies at the University of Nebraska-Lincoln where he graduated with a Bachelors of Science degree in Mechanical Engineering in December 2008. He was commissioned through the Detachment 465 AFROTC at the University of Nebraska-Lincoln.

His first assignment was at Eglin AFB as a program systems engineer on the BQM-167A. In November 2010 he began work for the 53d Test Wing conducting operational testing on HH-60, MC-12, U-2, and RQ-4 weapon systems. While stationed at Eglin, he also attended the University of Florida, where he obtained a Masters of Engineering in Industrial and Systems Engineering in August 2011. In August 2013, he entered the Graduate School of Engineering and Management, Air Force Institute of Technology. Upon graduation, he will join the Aeronautics and Astronautics faculty at the Air Force Institute of Technology.

REPORT DOCUMENTATION PAGE					Form Approved OMB No. 0704-0188	
<p>The public reporting burden for this collection of information is estimated to average 1 hour per response, including the time for reviewing instructions, searching existing data sources, gathering and maintaining the data needed, and completing and reviewing the collection of information. Send comments regarding this burden estimate or any other aspect of this collection of information, including suggestions for reducing this burden to Department of Defense, Washington Headquarters Services, Directorate for Information Operations and Reports (0704-0188), 1215 Jefferson Davis Highway, Suite 1204, Arlington, VA 22202-4302. Respondents should be aware that notwithstanding any other provision of law, no person shall be subject to any penalty for failing to comply with a collection of information if it does not display a currently valid OMB control number. PLEASE DO NOT RETURN YOUR FORM TO THE ABOVE ADDRESS.</p>						
1. REPORT DATE (DD-MM-YYYY)		2. REPORT TYPE		3. DATES COVERED (From — To)		
15-09-2016		Doctoral Dissertation		Oct 2013-Sep 2016		
4. TITLE AND SUBTITLE  Cavity geometric features and entrainment characterization resulting from a ballistically induced hydrodynamic ram event				5a. CONTRACT NUMBER		
				NA		
				5b. GRANT NUMBER		
				NA		
6. AUTHOR(S)  Lingenfelter, Andrew J. , Captain, USAF				5c. PROGRAM ELEMENT NUMBER		
				JASPO: P-17-G-08-01		
				5d. PROJECT NUMBER		
				ENY-102		
				5e. TASK NUMBER		
				NA		
				5f. WORK UNIT NUMBER		
				NA		
7. PERFORMING ORGANIZATION NAME(S) AND ADDRESS(ES) Air Force Institute of Technology Graduate School of Engineering and Management (AFIT/EN) 2950 Hobson Way WPAFB, OH 45433-7765				8. PERFORMING ORGANIZATION REPORT NUMBER  AFIT-ENY-DS-16-S-065		
9. SPONSORING / MONITORING AGENCY NAME(S) AND ADDRESS(ES) Mr. Dennis Lindell Joint Aircraft Survivability Program Office 701 South Courthouse Road B15, Ste 1G140 Arlington, VA 22204				10. SPONSOR/MONITOR'S ACRONYM(S)  JASP, JASPO		
				11. SPONSOR/MONITOR'S REPORT NUMBER(S)  NA		
12. DISTRIBUTION / AVAILABILITY STATEMENT DISTRIBUTION STATEMENT A: APPROVED FOR PUBLIC RELEASE; DISTRIBUTION UNLIMITED						
13. SUPPLEMENTARY NOTES  This work is declared a work of the U.S. Government and is not subject to copyright protection in the United States. NA						
14. ABSTRACT  Hydrodynamic Ram can cause damage to industrial and aircraft systems. The resulting transient spray increases the probability of fire. To better understand the driving mechanisms behind transient spray, internal, and external measurements of the cavity geometry, and entrained flow field were accomplished. Research determined cavity contraction and separation are pre-cursors to the initiation of the transient spray phases. The entrained flow measurement required development of a new and novel technique using a continuous wave laser and atomized water particles. The peak mass flow correlated well with cavity geometric features, such as cavity contraction. Using the mass flow, cavity diameter at the orifice, and cavity length, projectile kinetic energy dissipation was related to cavity contraction. A relationship was developed for a range of impact velocities for the expected kinetic energy dissipation to occur prior to cavity contraction. Design of safer systems is possible by relating cavity contraction to the projectile's kinetic energy, and understanding how the transient spray is related to the cavity geometric features and the entrained mass flow.						
15. SUBJECT TERMS  Hydrodynamic Ram, HRAM, Transient Spray, Entrainment, Kinetic, Ballistic, Cavity, Energy, Pressure Work						
16. SECURITY CLASSIFICATION OF:			17. LIMITATION OF ABSTRACT	18. NUMBER OF PAGES	19a. NAME OF RESPONSIBLE PERSON	
a. REPORT	b. ABSTRACT	c. THIS PAGE			Dr. David. Liu (ENY)	
U	U	U	UU	324	19b. TELEPHONE NUMBER (include area code) (850) 883-0438 david.liu@us.af.mil	